ESPOO 2005 VTT PUBLICATIONS 591

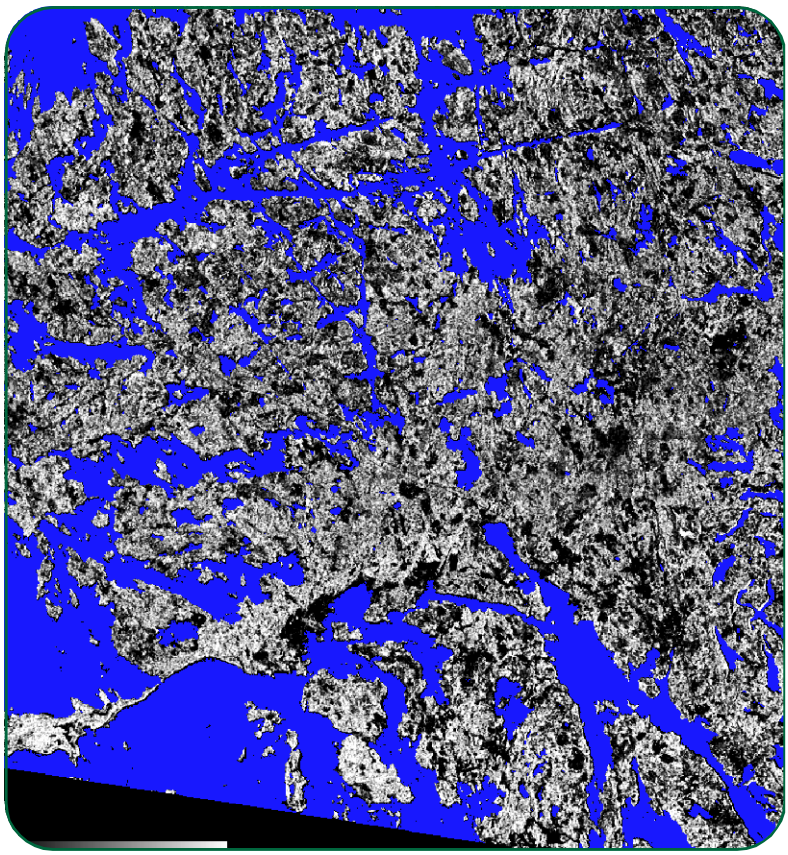

Yrjö Rauste

Techniques for wide-area mapping of forest biomass using radar data

VTT PUBLICATIONS 591

Techniques for wide-area mapping of forest biomass using radar data

Yrjö Rauste

VTT Information Technology

Dissertation for the degree of Doctor of Science in Technology to be presented with due permission of the Department of Surveying for public examination and debate in Auditorium M1 (Otakaari 1) at Helsinki University of Technology (Espoo, Finland) on the 17th of February, 2006, at 12 noon.

ISBN 951–38–6694–7 (soft back ed.)
ISSN 1235–0621 (soft back ed.)

ISBN 951–38–6695–5 (URL: http://www.vtt.fi/inf/pdf/)
ISSN 1455–0849 (URL: http://www.vtt.fi/inf/pdf/)

JULKAISIJA – UTGIVARE – PUBLISHER

VTT, Vuorimiehentie 3, PL 1000, 02044 VTT
puh. vaihde 020 722 111, faksi 020 722 4374

VTT, Bergsmansvägen 3, PB 1000, 02044 VTT
tel. växel 020 722 111, fax 020 722 4374

VTT Technical Research Centre of Finland, Vuorimiehentie 3, P.O. Box 1000, FI-02044 VTT, Finland
phone internat. +358 20 722 111, fax + 358 20 722 4374

VTT Tietotekniikka, Vuorimiehentie 3, PL 1000, 02044 VTT
puh. vaihde 020 722 111, faksi 020 722 7024

VTT Informationsteknik, Vuorimiehentie 3, PB 1000, 02044 VTT
tel. växel 020 722 111, fax 020 722 7024

VTT Information Technology, Vuorimiehentie 3, P.O. Box 1000, FI-02044 VTT, Finland
phone internat. +358 20 722 111, fax +358 20 722 7024

Otamedia Oy, Espoo 2006

Rauste, Yrjö. Techniques for wide-area mapping of forest biomass using radar data. Espoo 2005. VTT Publications 591. 103 p. + app. 77 p.

Keywords wide-area mapping, remote sensing, Synthetic Aperture Radar, forest biomass, SAR, Polarimetry, mosaicking, forests, backscattering

Abstract

Aspects of forest biomass mapping using SAR (Synthetic Aperture Radar) data were studied in study sites in northern Sweden, Germany, and south-eastern Finland. Terrain topography – via the area of a resolution cell – accounted for 61 percent of the total variation in a Seasat (L-band) SAR scene in a hilly and mountainous study site.

A methodology – based on least squares adjustment of tie point and ground control point observations in a multi-temporal SAR mosaic dataset – produced a tie point RMSE (Root Mean Square Error) of 56 m and a GCP RMSE of 240 m in the African mosaic of the GRFM (Global Rain Forest Mapping) project. The mosaic consisted of 3624 JERS SAR scenes. A calibration revision methodology – also based on least squares adjustment and points in overlap areas between scenes – removed a calibration artifact of about 1 dB.

A systematic search of the highest correlation between forest stem volume and backscattering amplitude was conducted over all combinations of transmit and receive polarisations in three AIRSAR scenes in a German study site. In the P-band, a high and narrow peak around HV-polarisation was found, where the correlation coefficient was 0.75, 0.59, and 0.71 in scenes acquired in August 1989, June 1991, and July 1991, respectively. In other polarisations of P-band, the correlation coefficient was lower. In L-band, the polarisation response was more flat and correlations lower, between 0.54 and 0.70 for stands with a stem volume 100 m^3/ha or less.

Three summer-time JERS SAR scenes produced very similar regression models between forest stem volume and backscattering amplitude in a study site in south-eastern Finland. A model was proposed for wide area biomass mapping when biomass accuracy requirements are not high. A multi-date regression model employing three summer scenes and three winter scenes produced a multiple correlation coefficient of 0.85 and a stem volume estimation RMSE of 41.3m^3/ha. JERS SAR scenes that were acquired in cold winter conditions produced very low correlations between stem volume and backscattering amplitude.

Preface

This thesis summarizes the work published in six papers over the period 1990–2005. All six papers can be considered to contribute to a theme "Techniques for wide-area mapping of forest biomass using radar data". The term "wide-area mapping" here is understood to cover such mapping situations where the whole mapping area cannot be covered by a single space-borne SAR scene.

The supervisor of the work is Professor Henrik Haggren of the Laboratory of Photogrammetry and Remote Sensing in the Department of Surveying, Helsinki University of Technology, Finland. The work has been carried out at the VTT Technical Research Centre of Finland (Espoo, Finland) and the Joint Research Centre (JRC, Ispra, Italy) of the European Union.

I want to express my gratitude to my bosses – Risto Kuittinen, Einar-Arne Herland, and Tuomas Häme at VTT as well as Frank De Grandi at JRC – for encouragement and support in various phases of the work. I also want to thank all co-workers in the VTT Remote Sensing group and in the Global Vegetation Monitoring (GVM) group at JRC for many fruitful discussions in a scientific atmosphere during the work.

I want to thank the funding organisations of the projects in which the papers of this thesis were produced: VTT, Tekes, the Central Association of Finnish Forest Industries (Suomen Metsäteollisuuden Keskusliitto), and the Human Capital and Mobility program of the European Union.

I also thank my wife Erja and my children Turo and Noora for their understanding and patience during the years of this work.

List of Appended Papers

This thesis is based on six papers published between the years 1990 and 2005:

1. Rauste, Y. 1990. Incidence-angle dependence in forested and non-forested areas in Seasat SAR data, International Journal of Remote Sensing, Vol. 11, No. 7, p. 1267–1276, reprinted with permission from Taylor and Francis Journals UK, (http://www.tandf.co.uk).

2. Rauste, Y., De Grandi, G., Richards, T., Rosenqvist, Å., Perna, G., Franchino, E., Holecz, F., and Pasquali, P. 1999. Compilation of a bi-temporal JERS SAR mosaic over the African rain forest belt in the GRFM project, Proceedings of IGARSS'99, 28 June–2 July 1999, Hamburg, Germany, p. 750–752, reprinted with permission from IEEE.

3. De Grandi, G., Mayaux, P., Rauste, Y., Rosenqvist, Å., Simard, M., and Saatchi, S. 2000. The global rain forest mapping project JERS-1 radar mosaic of tropical Africa: Development and product characterization aspects, IEEE Transactions on Geoscience and Remote Sensing, Vol. 38, No. 5, September 2000, p. 2218–2233, reprinted with permission from IEEE.

4. Rauste, Y., Häme, T., Pulliainen, J., Heiska, K., and Hallikainen, M. 1994. Radar-based forest biomass estimation, International Journal of Remote Sensing, Vol. 15, No. 14, p. 2797–2808, reprinted with permission from Taylor and Francis Journals UK, (http://www.tandf.co.uk).

5. Rauste, Y. 1993. Multitemporal analysis of forest biomass using AIR-SAR data, Proceedings of the 25th International Symposium, Remote Sensing and Global Environmental Change, 4–8 April, 1993, Graz, Austria, p. I-328–I-338, reprinted with permission from Altarum Institute.

6. Rauste, Y. 2005. Multi-temporal JERS SAR data in boreal forest biomass mapping, Remote Sensing of Environment, Vol. 97, p. 263–275, reprinted with permission from Elsevier[1].

[1]Reprinted from Remote Sensing of Environment, Vol. 97, Rauste, Y., Multi-temporal JERS SAR data in boreal forest biomass mapping, p. 263–275, Copyright(2005), with permission from Elsevier.

The work can be divided into four themes:

- Incidence-angle effects on radar backscatter in forests (Paper 1),
- Pre-processing techniques – block adjustment in mosaicking and block adjustment in calibration revision of SAR images (Papers 2 and 3),
- Radar backscatter of forests in various wavelengths and polarisations (Papers 4 and 5), and
- Multi-temporal L-band radar backscatter in forest biomass mapping (Paper 6).

Paper 1 was written in VTT in project SLARSAR. I was the sole author of Paper 1.

Papers 2 and 3 were written at the Joint Research Centre (JRC) of the European Union while I was a post doctoral grant holder in 1997–1999. In Paper 2, my responsibility was the development of the methodology for tie point production, block adjustment for SAR mosaicking, application of these techniques to the GRFM dataset of Africa, and evaluation of the results obtained in terms of mosaic geometry. In Paper 3, my contribution was the development of geometry revision and calibration methods and experimental results described in sections V, VI, and VII of Paper 3.

Paper 4 was written in VTT during project MAESTRO. My contribution to Paper 4 was the development of methods and obtaining the experimental results using AIRSAR polarimetric SAR data.

Paper 5 was written in VTT during project MAC-Europe. I was the sole author of Paper 5.

Paper 6 was written in VTT during project MODIS Biomass. I was the sole author of Paper 6.

Contents

List of Figures

List of Tables

1 Introduction

The synthetic aperture radar (SAR) satellites Seasat (Lewis *et al.* 1983, Moore *et al.* 1983), ERS-1 and 2 (ESA 1988), JERS-1 (NASDA 1988), Radarsat-1 (Williamson 1990), and Envisat (Louet 2001) have created an opportunity to map various properties of the earth's surface at high resolution using microwave radiation. Future SAR satellites such as ALOS (Shimada *et al.* 2005 and Shimada *et al.* 2002a) will further extend the capabilities of space-borne microwave remote sensing. Vegetation cover is an important characteristic of the earth's surface. Mapping forest and vegetation cover using radar has been studied extensively since Morain and Simonett (1967). The biomass of vegetation cover is needed especially in environmental and climatological studies, where the greatest amount of uncertainty arises from lack of information on biomass density (*e.g.,* Sader *et al.* 1989 and Häme *et al.* 2003). Since tree trunks are the most important raw material of the Paper and timber industries, information on forest biomass is also needed in sustainable forestry.

In many countries, fertile low-lying flat areas are typically in agricultural use. Forests tend to be in areas with more pronounced topography. When mapping forest biomass – or other forest characteristics – the influence of topography on the radar signal needs to be known. Paper 1 studies the influence of topography (via incidence angle) on the radar signal that scatters back from various forest areas.

When mapping forest biomass for large areas, large numbers of SAR scenes must be used to cover the area. Individual scenes must be mosaicked together. This can be done in two ways: SAR scenes can be mosaicked before image analysis or the results from single-scene analysis can be mosaicked after the image analysis. In this mosaicking process, various sensor-specific geometric and radiometric characteristics must be taken into account. Mosaicking of SAR data and geometric and radiometric techniques needed in mosaicking are studied in Papers 2 and 3.

Radar signals from various radars interact with the forest canopy in different ways. When mapping forest biomass, the accuracy of results depends on the type of radar data used. In Papers 4 and 5, the use of various radar wavelengths and polarisations in forest biomass mapping is studied.

Even if a radar sensor is considered accurate and efficient in forest biomass mapping, practical space-borne mapping is restricted to those radar sensors that are available on satellites in the foreseeable future. In Paper 6,

the temporal development of L-band radar signal of forests and the possibilities of using multi-temporal methods in forest biomass mapping are studied.

The following sections describe the context in which the themes mentioned above were studied. Samples of relevant literature are mentioned until the year of submission of the corresponding paper. More recent literature is cited where this is necessary for understanding the relevance of the paper today.

Interferometric techniques (*e.g.*, Pulliainen *et al.* 2003, Wagner *et al.* 2003, Shimada *et al.* 2002b, Koskinen *et al.* 2001) in forest biomass mapping have been investigated in recent years. Repeat pass interferometry poses some additional requirements on image acquisition conditions (*e.g.,* low wind). Interferometric techniques at least double the number of image acquisitions (compared to techniques that can work with backscattering amplitude data only). For these reasons, interferometric techniques are not very attractive when aiming at covering large areas with homogeneous mapping results. Interferometric techniques are left outside the scope of this thesis.

Forest biomass is a quantity that is difficult to measure. In boreal forests, the biomass is tightly coupled to forest stem volume (Häme *et al.* 1992, Kauppi *et al.* 1995, and Häme *et al.* 1997). Häme *et al.* (1992) presented an (approximate) analytical form for this relation in boreal forest:

$$B = 0.6 \cdot V \tag{1}$$

where V is forest stem volume (m^3/ha) and B is dry biomass (tons/ha). Equation (1) ignores differences between species (see *e.g.* Kauppi *et al.* 1995). Equation (1) may underestimate the biomass by up to 20 percent. In the absence of large datasets of biomass measurements, forest stem volume data were converted into forest biomass using Equation (1).

Radars measure the return of a signal emitted by the radar. The strength of this signal can be expressed as a power or amplitude. The amplitude is the square root of the received power. In the following, the term backscattering amplitude is used to refer to the square root of received power. In case of SAR, the radar does not measure directly the power backscattered from a resolution unit, but the final signal is derived in a computational process called SAR processing. In SAR data, the backscattering amplitude can be defined as the square root of the power that would have been measured by a real aperture radar that has the same resolution as the SAR. The term

backscatter is used in a more general context without making assumptions on power or amplitude formats.

Table 1. SAR sensors used in Papers 1 through 6.

Sensor	Band(Wave-length in cm)	Pols.	Res. (m) /Looks	Inc. (deg)	Launch	End of Life
Seasat	L(23)	HH	25/4	23	1978-06-28	1978-10-10
JERS	L(23)	HH	18/3	39	1992-02-11	1998-10-12
AIRSAR	C(6), L(23) P(63)	Full	12/4	30-70	N/A	N/A

Table 1 lists the main characteristics of radar systems used in this thesis. The column “Pols.” lists the polarisations of the sensors. AIRSAR is a fully polarimetric sensor (measuring HH, HV, VH, and VV polarisations) in all three wavelength bands. Column “Res.” gives the ground resolution and the number of looks for which the resolution is given. The AIRSAR resolution is approximate. Held *et al.* (1988) report a pixel spacing of 12.1 m in azimuth and 6.67 m in slant range. Column “Inc.” gives the incidence angle. This is the mid-swath incidence angle for space-borne sensors and the minimum and maximum incidence angles over flat earth for the air-borne AIRSAR sensor. A nominal incidence angle of 38 degrees is mentioned in some literature for JERS SAR. The nominal orbit elevation of 570 km and mid-swath off-nadir angle of 35° (NASDA 1988) give a mid-swath incidence angle of 38.68 degrees.

1.1 Incidence Angle Effects on Radar Backscatter in Forests

Topographic effects have been observed to influence or even dominate SAR images of forests (*e.g.* Drieman 1987). Few studies have evaluated the topographic effects on SAR images of forests in quantitative terms.

Teillet *et al.* (1985) studied terrain effects in a rugged forested study site in Canada using data from the Canadian Convair-580 SAR. This SAR operates in X- and L-bands and can record in both bands four polarisations: HH, VV, HV, and VV. The terrain topography has its influence on radar backscattering amplitude by the (local) incidence angle (θ). Terrain elevation varied between 330 and 1100 m above sea level. In a shallow mode

scene (nominal incidence angle 22°), $cos(\theta)$ accounted for 26 to 38 percent of the total variation in HH- and HV-polarisations of X- and L-bands (in forested areas). In a steep mode scene (nominal incidence angle 43°), $cos^2(\theta)$ accounted for 8 to 27 percent.

Foody (1986) studied terrain effects in an undulating study site in England. A set of 227 grass covered fields were divided into seven zones (a minimum of 30 fields per zone) to minimize the variation due to antenna gain and sensor look angle. This grass-land study is included here because early works in forested areas are so rare in the published literature. The SAR data were acquired by the Canadian Convair-580 SAR system. The polarisation was HH in both X- and L-bands. The SAR had the nominal incidence angle range 32° to 63° (aircraft altitude 5.4 km, swath width 7 km in ground range). The square of the multiple correlation coefficient (R^2) was used to measure the effect (on radar backscatter) of two variables: slope and aspect (relative to the SAR look direction). The R^2 statistic was derived from zero and first order partial correlations using the formula: $R^2_{0.12} = r^2_{01} + r^2_{02.1}(1 - r^2_{01})$ where subscript 0 was image tone and subscripts 1 and 2 slope and aspect respectively. $R^2_{0.12}$ was the proportion of variance in image tone (0) accounted for by the variables 1 and 2 both jointly and separately and r was the correlation coefficient. The proportion of variation in L-band that was explained by slope and aspect was between 3 and 30 percent, except in the two zones furthest away from the radar, where 50 and 38 percent of the total variation was accounted for by these variables. In X-band, the proportion of variation that was explained by slope and aspect was between 3 and 30 percent in all zones.

Hinse *et al.* (1988) reported a reduction between 3 and 9.5 percent in the variance of spectral signatures of land cover types (variance in backscatter amplitude within a land cover type) after terrain corrections of an air-borne C-band (Convair-580 SAR) HH-polarised scene. The land cover types were deciduous, coniferous, corn, agriculture, and combined. The variance in backscatter amplitude in the corn land cover increased slightly in the terrain corrections. The study site (in Canada) had moderate relief (elevation variation of 210 m within the study site). The corrections were based on the total incidence angle (not an explicit calculation of scattering area).

In newer remote sensing literature, Small *et al.* (2004b) reported error histograms on the estimation of backscattering coefficient γ^o as a function of DEM resolution. The backscattering coefficient γ^o is related to the more widely used backscattering coefficient σ^o by: $\gamma^o = \sigma^o / cos(\theta)$. Small *et al.*

(2004b) produced a (radiometrically normalized) γ^o mosaic of Switzerland using five ASAR (C-band) wide-swath scenes (nominal incidence angle 19° to 38°) with opposing look directions.

Goering *et al.* (1995) reported a reduction of 30 and 13 percent in pixel value variance in an ascending and descending ERS-1 SAR scene, respectively, after removal of terrain effects, which included the effect of the size of a resolution cell. The study site was a tundra site (in Alaska) with moderate relief and elevations between 410 and 490 m. The nominal incidence angle in the 1.5 km by 1.5 km study site was 23.1319° for the ascending scene and 23.1619° for the descending scene.

Bayer *et al.* (1991) reported that local incidence angle accounted for 36 percent of the total variation in forested areas and the range component of local incidence angle 33 percent in a Seasat SAR scene in a German study site. The nominal incidence angle for the Seasat SAR was 23°. The regression analysis did not include a scattering area as an independent variable. The study site had terrain slopes of up to 53 degrees. The elevation varied between 46 and 180 m.

Sun *et al.* (2000 and 2002) presented a technique for radiometric correction of terrain topography when using polarimetric SAR data. Because the resolution of an available DEM (DTED level 1) was too low for radiometric corrections the dependence of backscatter on the incidence angle was estimated from model calculations for HH- and HV-polarised L-band data separately. The local incidence angle was estimated from HH-polarised data. The incidence angle was used to correct the HV-polarised data to the nominal incidence angle of the SIR-C SAR. The terrain-corrected L-band HV-polarised data were used to derive a forest biomass model ($\sqrt[3]{B} = 8.45 + 0.67\sigma^o$). The estimates produced by this model had an r^2 value of 0.91 with the ground data in a stand-wise forest biomass dataset, where the biomass varied between 11.6 and 240 tons/ha. The RMSE (root mean square error) was 18.1 tons/ha. 28 stands were used for model development and another 28 stands for testing.

Goyal *et al.* (1999) combined the incidence angle and soil roughness into a linear correction function when mapping soil moisture in a mountainous grass-land area. They used L-band HH-polarised data from the AIRSAR sensor. Elevation in the study site (56.25 km^2) varied between 1097 and 2252 m). The nominal incidence angle in the study site varied from 38° to 54°. The use of the regression model between radar backscattering intensity, incidence angle, and soil roughness (root mean square height) reduced the variance in σ^o by 85 percent.

The power measured by a radar can be described by the radar equation (here for real aperture radar, a fully focused SAR has R^3 instead of R^4, *e.g.* Rosisch and Meadows 2004):

$$P_r = \frac{P_t G^2 \lambda^2 \sigma}{(4\pi)^3 R^4} \tag{2}$$

where

P_r = received power,
P_t = transmitted power,
G = antenna gain,
λ = radar wavelength,
σ = radar cross-section of the target, and
R = distance between the radar and the target.

In earth observation radars, where the target is a spatially extended piece of earth's surface, the radar cross-section σ can be expressed:

$$\sigma = \sigma^o A \tag{3}$$

where

σ^o = radar cross-section per unit surface area,
A = surface area of a resolution cell.

The term σ^o is called the backscattering coefficient.

The radar equation can be written:

$$P_r = \frac{P_t G^2 \lambda^2 \sigma^o A}{(4\pi)^3 R^4}. \tag{4}$$

The terms by which terrain topography affects the power measured by radars are the backscattering coefficient σ^o and the area of the resolution cell A.

The incidence angle (or angle of incidence) θ is defined as the angle (in 3-dimensional space) between the propagation direction of the radar signal and the normal vector of an (assumed planar) resolution cell.

The backscattering coefficient $\sigma^o(\theta)$ of smooth targets (in terms of radar wavelength) decreases steeply with an increasing incidence angle. The backscattering coefficient of rough targets does not decrease so steeply with the increasing incidence angle (Ulaby *et al.* 1982).

The area of resolution cell A depends not only on the total incidence angle, but on its components in azimuth (along track) direction θ_a and in range (cross track) direction θ_r.

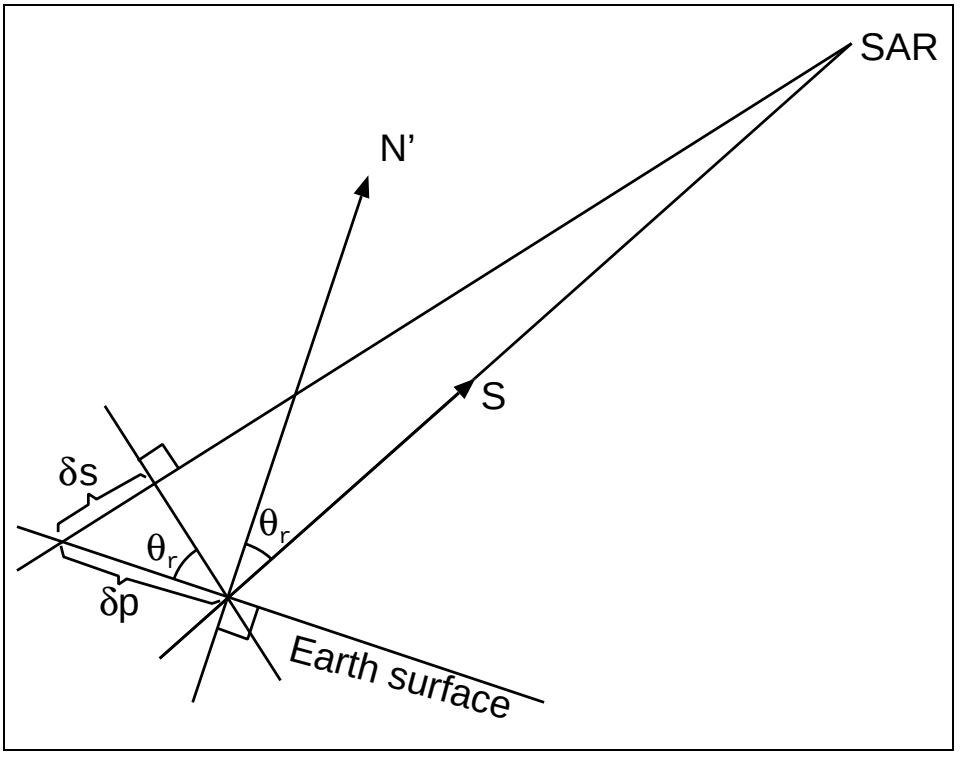

Figure 1. Dimension of a resolution cell in range direction.

Figure 1 shows a vertical cross-section plane that goes through the SAR and a pixel. N' is the orthogonal projection of the surface normal vector on the vertical plane. Angle θ_r is the angle between the vector S (pointing to the SAR) and N' in the vertical plane of Figure 1.

A space-borne SAR produces its resolution in the range direction using a pulse of finite duration (which is determined by the pulse compression technique utilized). Since the pulse length is constant, slant range resolution δ_s is constant through the image swath. As can be read in Figure 1, the range dimension δp of a resolution cell can be calculated:

$$\delta p = \frac{\delta s}{sin(\theta_r)} \tag{5}$$

Figure 2 shows a vertical cross-section plane that goes through a pixel and is parallel to the SAR orbit. N" is the orthogonal projection of the surface normal vector on the vertical plane (of Figure 2). Angle θ_a is the angle between a vertical line and vector N" in the vertical plane of Figure 2. Angle θ_a is also the terrain slope in the orbit direction of the SAR.

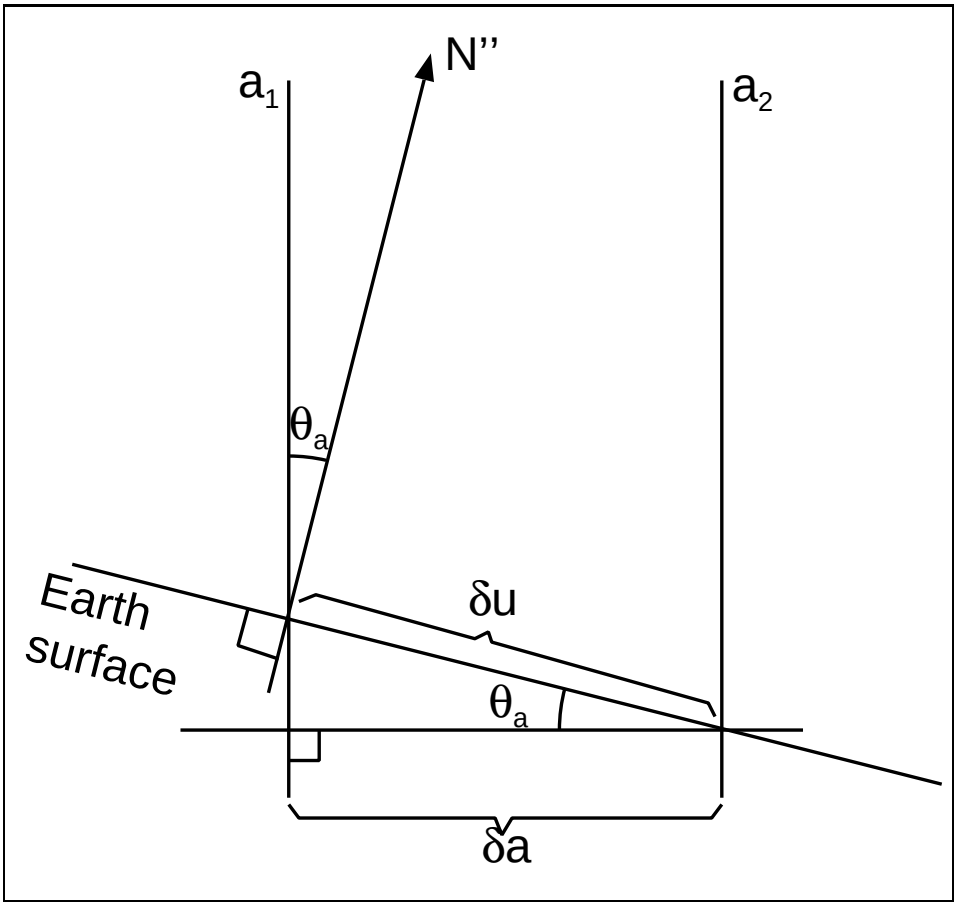

Figure 2. Dimension of a resolution cell in azimuth direction.

In a SAR scene, the azimuth resolution (on a horizontal surface) is constant through the image swath. The azimuth dimension of a (tilted) planar resolution cell is determined by two vertical planes (a_1 and a_2 in Figure 2, separated by azimuth resolution δa) that are orthogonal to the SAR orbit (unless the SAR scene has been acquired and processed in squint mode). The azimuth dimension of a tilted pixel δu can be calculated (see Figure 2):

$$\delta u = \frac{\delta a}{cos(\theta_a)} \tag{6}$$

The surface area A (in Equation 4) of a resolution cell is the product of range and azimuth dimensions:

$$A = \delta p \cdot \delta u = \frac{\delta s}{sin(\theta_r)} \frac{\delta a}{cos(\theta_a)} \tag{7}$$

In more recent literature, Ulander (1996) has presented an approach for terrain slope correction that takes into account the simultaneous effects of pixel tilting in azimuth and range directions. This approach is equal to the case where the plane of Figure 2 is not horizontal but tilted by θ_r. In this formulation, θ_a is no longer equal to the slope in the azimuth direction (unless θ_r equals zero). The angle θ_a can be defined as the angle between two planes: the vertical plane containing the sensor and the pixel (= plane 1), and the plane that contains the terrain normal vector and intersects plane 1 along the intersection of the terrain plane and plane 1. If θ_a is defined this way, Equation (7) is equal to the pixel area of Ulander (1996). As Ulander (1996) points out, the difference between these two approaches is insignificant (less than 0.01 dB) unless the terrain slope is higher than 20 degrees (and less than 0.1 dB within slopes between -40 and +40 degrees). In such high-relief landscapes lay-over seriously reduces the usefulness of SAR data regardless of terrain correction methods (unless multiple scenes with opposing look directions can be used as by Small *et al.* 2004a).

An alternative way for the backscattering coefficient σ^o is the (gamma) backscattering coefficient γ^o

$$\sigma = \gamma^o O \tag{8}$$

where
γ^o = radar cross-section per unit projected area,
O = projected area of a resolution cell.
As γ^o is directly proportional to the projected area of a resolution cell, and

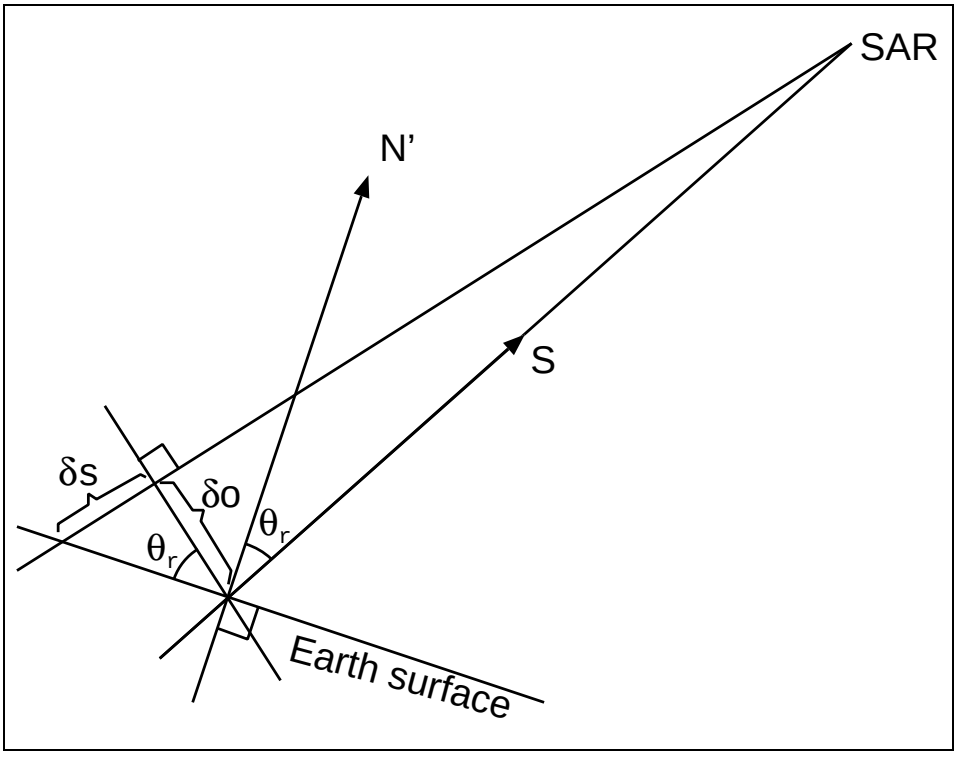

Figure 3. Projected dimension of a resolution cell in range direction.

consequently to the power intercepted by the resolution cell, the effects of terrain tilt components in range and azimuth directions are more uniform. In this alternative, the radar equation can be written:

$$P_r = \frac{P_t G^2 \lambda^2 \gamma^o O}{(4\pi)^3 R^4} \tag{9}$$

The projected resolution cell area O can be calculated (Figure 3, the same vertical plane as in Figure 1):

$$O = \delta o \cdot \delta a = \frac{\delta s \cdot \delta a}{tan(\theta_r)} \tag{10}$$

Noting that the received power must be the same in both Equations (4) and (9), the relation between σ^o and γ^o is:

$$\gamma^o = \frac{\sigma^o}{cos(\theta_r) cos(\theta_a)}. \tag{11}$$

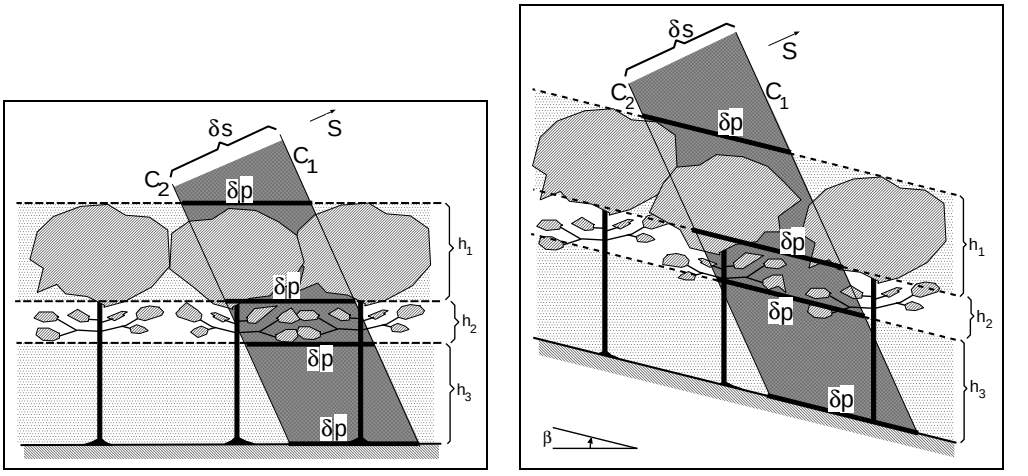

Figure 4. Resolution cell size for scattering volume. The scattering volume is proportional to the resolution surface area both with horizontal ground, a) and with sloping ground, b).

Because θ_r and θ_a are two orthogonal components of the total incidence angle θ, Equation (11) is equivalent to:

$$\gamma^o = \frac{\sigma^o}{cos(\theta)}. \tag{12}$$

Leclerc *et al.* (2001) describe in addition to σ^o and γ^o the backscatter relative to Lambertian scatterer ($\sigma^o cos^2\theta$). They used C-band HH- and VV-polarized data from the Convair-580 SAR in the so-called narrow mode (nominal incidence angles typically 45° to 76°). Slopes of up to 40° were present in the study site. After terrain correction relative to the Lambertian scatterer, forest and banana plantations could be distinguished from coffee plantations on slopes facing towards the radar.

The surface area of a resolution cell A and projected area O can be computed if a digital elevation model (DEM) is available. Small *et al.* (2004a) note that the assumption of a planar pixel has the disadvantage that it does not account for fore-shortening, lay-over, and radar shadow.

When correcting radar images for the area of resolution cell, the the same correction can be applied in areas dominated by surface scattering and those dominated by volume scattering. In most forest scattering models, the forest canopy is divided into layers of constant thickness that can be considered as homogeneous in terms of backscattering. The equidistant

circles (C_1 and C_2 in Figure 4, drawn as straight lines to describe the long distance to space-borne SAR sensors) that define the range resolution of a radar intersect an equal area ($\delta p \cdot \delta u$) of all boundary surfaces between the canopy layers and the ground surface. This is true for horizontal and tilted pixels (Figure 4). The size of scattering volume (the volume from which the scattering that contributes to a single resolution unit originates) is

$$V_{scat} = \delta p \cdot \delta u \cdot h \cdot cos(\beta), \tag{13}$$

where h is the vertical thickness of the layer and β (Figure 4) is the terrain slope component in range direction (*i.e.* in the cross track vertical plane). Normalisation to a constant unit scattering volume is not feasible because the balance of backscattering and absorption can vary widely in forest canopies of varying age. Normalisation to a constant unit scattering volume would also require that the thickensses of the layers within the canopy are known (or the tree heigth if the canopy is considered as a single layer). This is difficult to map with high resoltion using today's earth observation instruments. The application of the $cos(\beta)$ term in radiometric correction would require information on where the backscattering is dominated by surface scattering and where by volume scattering. This information is also difficult to map. The difference would also be small. For example for a terrain slope of 20° (36 percent slope), the $cos(\beta)$ term is 0.97 for amplitude images. The most varying term (excluding the layer thickness) in the expression of scattering volume (13) is the area of the (upper and lower) surface of the scattering layer. Radiometric correction by this term leads to a correction procedure that is identical to the corecction that is approporiate for areas dominated by surface scattering.

Similar to the surface area of volume scattering layers, the projected area of all layer boundaries is constant from boundary to boundary (Figure 5).

Backscatter modelling studies (*e.g.,* Richards *et al.* 1987, Sun and Simonett 1988) indicate that the so-called double-bounce scattering mechanism is important in L-band SAR data. This phenomenon should be visible in the angular backscatter curve $\sigma^o(\theta)$.

1.2 SAR Mosaicking Techniques

When several images are mosaicked together, the geo-location of individual scenes must fit on the image boundaries within a sub-pixel. If this is not the case, discontinuities – like rivers that do not flow continuously –

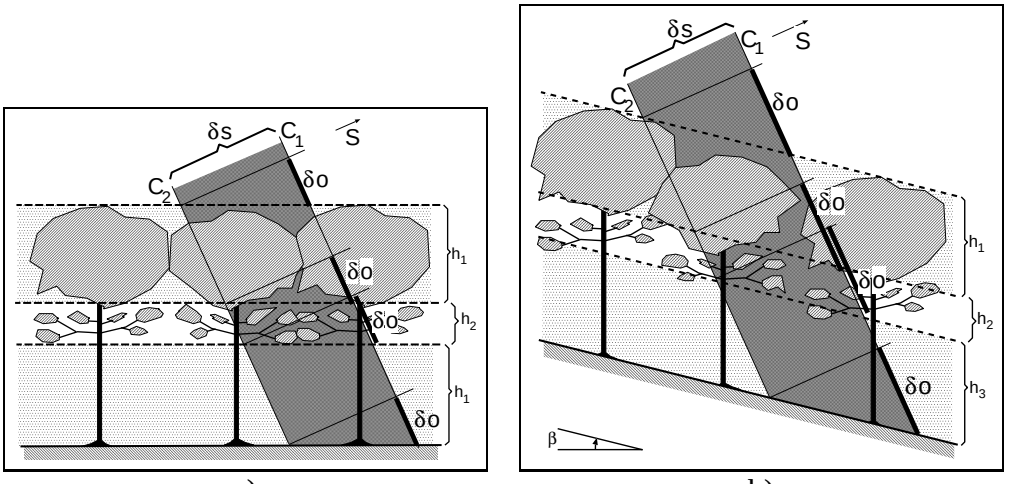

Figure 5. Projected area for volume scattering elements. The projected area of layer boundaries is constant from boundary to boundary both for horizontal ground, a) and for sloping ground, b).

occur at image seams. If a multi-temporal mosaic is compiled, the temporal components of the mosaic must also fit together within a fraction of a pixel. Otherwise mis-registration of mosaic components produces artifacts around high-contrast edges in multi-temporal image analysis techniques.

The scene radiometry must also be calibrated in such a way that no abrupt changes occur between individual scenes of the mosaic. Very sophisticated calibration methods have been developed for SAR data (*e.g.*, Menges *et al.* 2001). This approach makes a frequency table of backscatter values separately for each range co-ordinate in a SAR image. This table is then used as a look-up table in the actual calibration phase. The approach, which was applied to AIRSAR C-, L-, and P-band polarimetric dataset, assumes uniform distribution of land cover classes across image swath. The calibration method in mosaicking must be robust and free of restrictive requirements on scene contents.

The error sources of space-borne SAR data are different from those of air-borne data, and different methods are optimal for space-borne data, where the orbit information is usually more accurate. However, the orbit control and measurement accuracy of, for example, the JERS satellite was not very high. The initial (orbit-data based) geo-location accuracy of the SAR scenes was, consequently, also low. This emphasizes the need for adequate geometry revision techniques when mosaicking JERS SAR scenes.

Leberl (1975) studied mosaicking methods using a simulated set of 20 air-borne SAR strips (600 km long, 37 km wide, 63 percent sidelap). Sequential block formation with splines, followed by external interpolative adjustment, was found to be more robust and accurate than various forms of simultaneous block adjustment. The main error source in the simulation of the air-borne SAR data was the periodic error of the inertial navigation system that was used in the mosaic construction.

The GRFM (Global Rain Forest Mapping) project was launched by the Japanese space agency (NASDA) using the JERS SAR for rain forest mapping (Rosenqvist 1996). The major objectives of the project were to create spatially and temporally consistent JERS SAR image mosaics at 100-m resolution covering the entire equatorial belt and to provide these as 'ready-to-use' datasets freely and openly to the international science community and educational institutions as tools to help improve our understanding of the tropical ecosystems (Rosenqvist *et al.* 2000). In this international project, NASDA and NASA (Alaskan SAR Facility) processed raw SAR signals into image form. NASDA, JRC, and JPL produced SAR mosaics in South-East Asia, Africa, and South and Central America, respectively. The GRFM project was followed by the GBFM project. One of its main objectives was the generation of extensive, pan-boreal, SAR image mosaics to provide snap-shots of the forest, wetland, and open water status in the mid-1990'ies in the boreal forest zone of Eurasia and North America (Rosenqvist *et al.* 2004).

Rosaz *et al.* (1994) describe a methodology for using least squares adjustment in the compilation of a SAR mosaic. This technique was used when compiling a mosaic of 15 ERS-1 SAR scenes over the territory of French Guiana. Tie points between scenes were first measured manually and then refined using image correlation. SAR images of the same orbit were first combined into an image strip. A similarity transformation of the form:

$$\begin{bmatrix} x' \\ y' \end{bmatrix} = \begin{bmatrix} \cos\alpha & -\sin\alpha \\ \sin\alpha & \cos\alpha \end{bmatrix} \cdot \begin{bmatrix} x \\ y \end{bmatrix} + \begin{bmatrix} T_x \\ T_y \end{bmatrix} \tag{14}$$

was determined between two neighbouring strips. This was done using tie points and a least squares adjustment. One of the two strips was resampled to the geometry of the other strip using the parameters (rotation α and translations T_x and T_y in x and y) of the similarity transformation. The pair-wise combination of strips was repeated until all strips were combined into a mosaic.

Rosaz *et al.* (1994) made the mosaic compilation in a co-ordinate system

that was aligned with the azimuth-range (line-column) co-ordinate system of one of the image strips. In this approach, the need for the rotation angle α comes from the difference of the orbit heading of the reference scene and the orbit heading of the other scene where the latter heading is taken with respect to the meridian of the reference scene. The expected value of α is a non-zero function of scene latitude and depends on the imaging geometry of the (ERS-1) SAR sensor.

Rosaz *et al.* (1994) also normalized image radiometry in a pair-wise manner. One scene was modified on the basis of a transformation determined by a least squares estimation over a set of points in the overlap area between the two scenes.

Siqueira *et al.* (2000) presented a geometry revision methodology, which was also based on similarity transformation. The methodology was applied to the South-American JERS SAR dataset of the GRFM project. In this methodology, the transformation parameters were determined in a global least squares adjustment comprising all scenes in the mosaic, which included one acquisition layer. This methodology treats ground control points like adding a single, pan-continental scene that is not allowed to undergo any transformation (regarded as a “truth scene”). This treatment disturbs the structure of the normal equation coefficient matrix by adding an extended row and column since the “truth scene” has common elements with a large number of other scenes in the mosaic.

Shimada and Isoguchi (2002) presented a methodology for mosaicking long JERS SAR scenes (over 1000 km long path images) produced by the so-called Sigma-SAR processor. As the sensor yaw angle is known with high accuracy, this methodology uses only translations to make neighbouring scenes fit. Ground control points and an affine transformation are used to prevent error propagation due to path integration.

Shimada and Isoguchi (2002) used second-degree polynomials to normalize the range dependency of backscatter. Additional gain correction was determined on the basis of points in overlap areas between scenes and a least squares estimation.

Hutton *et al.* (2000) compiled a Radarsat-1 mosaic of Canada. Over 100 image strips (4 to 7 scenes each, 300 km by 300 km scenes, scanSAR narrow B beam mode, 50 m resolution) were mosaicked using approximately 3000 ground control points measured from 1:50 000 and 1:250 000 topographic maps. Radiometric balancing within image strips was performed when necessary. An algorithm was designed to automatically calculate ra-

diometric variations across a scene and to produce more consistent gray values in the output image. The global elevation model GTOPO30 was used in ortho-rectification. The output mosaic was produced in Lambert's conformal conical map projection with a pixel spacing of 250 m.

Noltimier *et al.* (1999) compiled a Radarsat-1 mosaic of Antarctica. The mosaic consisted of approximately 4000 Radarsat images acquired in standard beam modes 2 to 7 and extended high beam 4. The scenes, which had a ground resolution of 25 m, covered an area of 100 km by 100 km. The mosaic was constructed in blocks consisting of approximately 150 scenes. Ground control points, tie points (between image swaths), and satellite ephemeris data were used in block adjustment. A digital elevation model was used to ortho-rectify images. The ensemble of ortho-rectified images was radiometrically balanced to remove seams and other artifacts. Individual blocks were combined in the final processing stages including block to block balancing and grand geometric correction.

In Siberia project (Wagner *et al.* 2003), mosaicking was done after (interferometric) image analysis. ERS scenes acquired at the same track-frame co-ordinates were co-registered by cross-correlation. JERS scenes were co-registered to ERS-frames. A total of 122 ERS-JERS "stacks" were then mosaicked to a larger coverage after image analysis.

1.3 Radar Wavelength and Polarisation in Forest Biomass Mapping

The interaction between the electromagnetic radiation of a radar signal and components of forest canopy and forest floor depend strongly on the wavelength and polarisation of the radar (*e.g.*, Ulaby *et al.* 1982).

The electric field of a radar pulse oscillates in two dimensions that are orthogonal to each other and to the propagation direction of the radar pulse. These oscillations have a constant phase difference in such a way that the electric field vector draws an ellipse on the plane perpendicular to the propagation direction (Figure 6). The polarisation of the pulse can be described by two angles: the orientation angle ψ between the vertical and the semi-major axis of the ellipse and the ellipticity angle χ (van Zyl *et al.* 1987). The ellipticity angle χ is the angle between two end points of the semi-minor axis of the ellipse seen from the end point of the major axis (Figure 6).

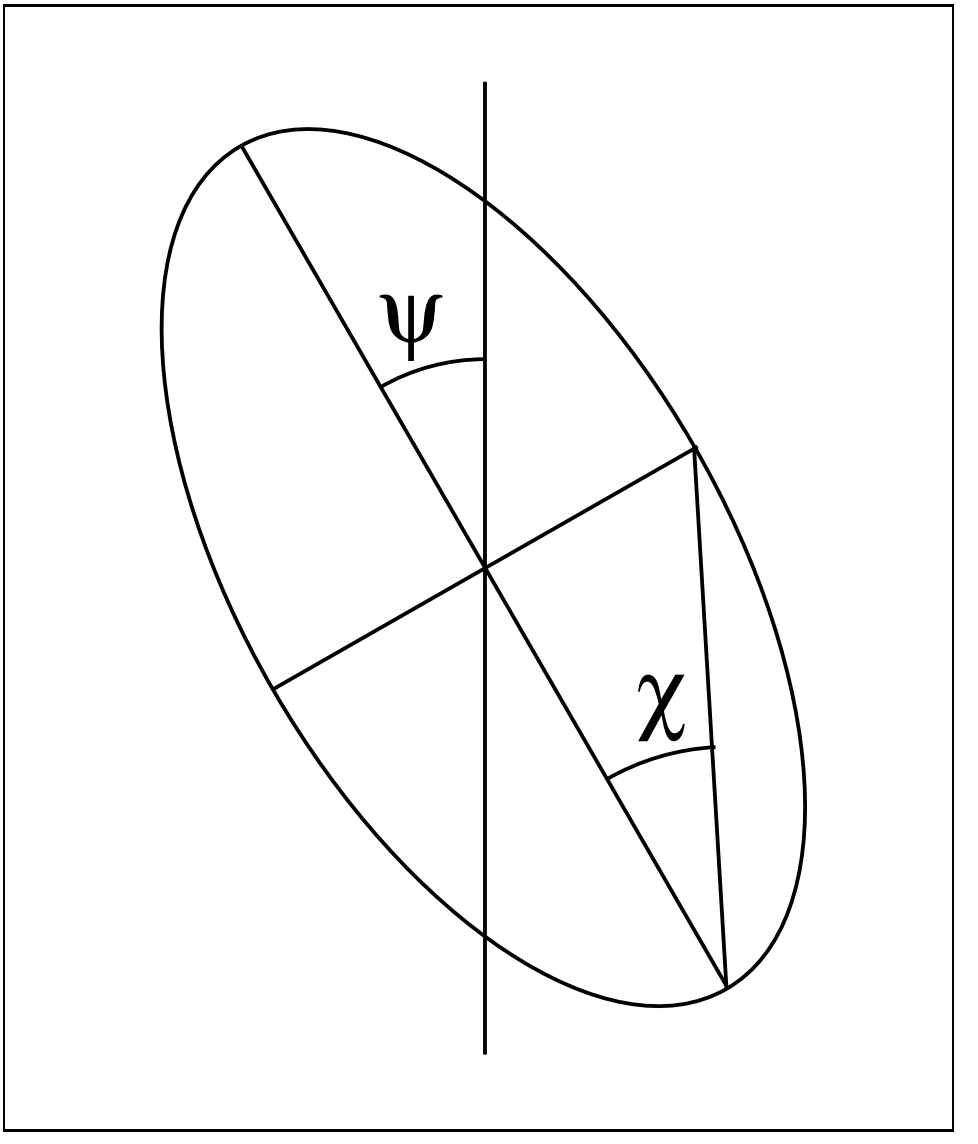

Figure 6. Orientation and ellipticity angles of an electromagnetic radar pulse on a plane orthogonal to the propagation direction of the pulse.

The ellipticity angle χ varies between -45° and 45°. The orientation angle ψ varies between -90° and 90°. An ellipticity angle of 0° produces a linear polarisation (where the electric field oscillates in one dimension only) and χ of 45° (or -45°) produces a circular polarisation.

Sader (1987) studied L-band SAR polarimetric data in forest biomass mapping. The sensor was a JPL-developed predecessor of the AIRSAR sensor (nominal incidence angle 15° to 60°), which was operated on a Convair 990 aircraft. A correlation coefficient of 0.76 was obtained in a dataset of nine forest stands between the biomass and HV-polarisation digital number. The HH- and VV-polarisations were not significantly correlated with biomass. The stands included two pine species: longleaf pine (*Pinus palustris* Mill.) and slash pine (*Pinus elliotti* Englem.) in a relatively flat study site (elevation 3 to 15 m). The green weight biomass varied from 25 to 230 tons/ha.

Hussin *et al.* (1991) also studied slash pine biomass and L-band polarimetric SAR data. The sensor was the JPL-developed polarimetric L-band SAR before the AIRSAR sensor (on-board a Convair 990 aircraft). A coefficient of determination (R^2) of 0.97 was obtained between HV-polarised SAR data and biomass data that had been transformed by the Box-Cox power transformation. The dataset contained 35 stands with an age of between 4 and 31 years. The biomass varied between 35 and 428 tons/ha.

Le Toan *et al.* (1991) studied forest biomass with AIRSAR multi-band polarimetric radar. High correlations (R^2 values of 0.95, 0.90, and 0.88) were obtained between stem biomass and P-band data in VH-, HH-, and VV-polarisations. The study site was on flat soil. The stem biomass varied between 0 and 105 tons/ha and stand age between 0 and 42 years. Tree species was mainly maritime pine (*Pinus pinaster* (Ait.)). The dataset consisted of 24 forest stands and 9 clear-cut stands.

In more recent literature, Hoekman and Quinones (1998 and 2000) studied AIRSAR data in forest biomass mapping in a tropical study site in Colombia. The ground data set consisted of 13 plots of primary forest, 10 plots of secondary forest, and 5 plots of grassland with bushes. The size of primary and secondary forest plots was 1000 m^2. The biomass varied between a few tons/ha and 315 tons/ha. The non-linear regression model (3 parameters) was between the logarithm of γ^o (dependent variable) and the exponential of the logarithm of biomass. C-band produced the lowest coefficient of determination, followed by L-band, and P-band, which produced the highest. In both L- and P-bands, the HV-polarisation produced the highest R^2 values (0.93 and 0.94). Hoekman and Quinones (2000, p.

693) note that the biomass map is useful for land and forest degradation assessment. The biomass map is of limited value for foresters who want to assess parameters such as timber volume.

Ranson and Sun (1994) studied forest biomass mapping in a study site in Maine, USA using AIRSAR data. The elevation varied only within 68 m. The ground dataset consisted of 39 stands with above-ground dry biomass between 0 and 350 tons/ha. The natural forest stands consisted of mixtures of hemlock-spruce-fir, hemlock-hardwoods and hardwood stands (mixtures of aspen, birch, maple and beech). Ranson and Sun (1994) used only HV-polarised data because earlier studies suggested HV-polarisation to be most correlated with forest biomass. In linear regression between the logarithm of biomass and backscatter, P-band produced an R^2 value of 0.81 and L-band 0.75. Using the band ratios P/C and L/C improved the R^2 values slightly.

Saatchi and Moghaddam (2000) used an AIRSAR mosaic (C-, L-, and P-bands, all in HH-, HV-, and VV-polarisations) for forest biomass mapping in a boreal study site in Canada. Elevation in the study site was between 550 and 730 m. The method started with estimating (using an iterative non-linear least squares estimation method) the parameters for a semi-empirical forest backscatter model for four homogeneous stands of trembling aspen, old jack pine, old black spruce, and young jack pine. The parameters included crown moisture content, stem moisture content, rms height of (ground) surface roughness, surface reflectivity (a function of soil moisture), and 11 attenuation or scattering cross-section coefficients. The crown and stem moisture content were used to estimate the crown and stem biomass (by a conversion factor). The method required at least seven independent radar measurements that were sensitive to these parameters. This condition was met in the AIRSAR polarimetric 3-band dataset. When applying the method in forest biomass estimation, a land cover map was included. For mixed stands, a separate set of structural model parameters was computed. A dataset of 18 stands (with biomass between 7.42 and 153.52 tons/ha) was used to evaluate the accuracy of forest biomass mapping. The total biomass mapping accuracy was 91 percent for a set of P-, L-, and C-bands (P-HH, P-HV, L-HV, and C-HV). The accuracies for polarimetric (HH-, HV-, and VV-polarised data) P-band and L-band datasets were 92 percent and 86 percent, respectively.

Balzter *et al.* (2002) studied forest biomass mapping in a Finnish study site using polarimetric EMISAR (C- and L-band) data. Landsat-derived forest inventory data were used as surrogate ground data. The most com-

mon tree species were pine (*Pinus sylvestris* L.), spruce (*Picea abies* L.), and birch (*Betula spp.*). The average forest stem volume was 50.5 m^3/ha (variation 0–140 m^3/ha). Pixel values averaged over 100 m by 100m pixels (20 by 20 averaging) were used as observations instead of the usual stand-wise data (about 410 observations). Single-band regression models – exponential in stem volume – produced correlation coefficients of 0.54 and 0.63 in L-band HH- and L-band HV-polarisations, respectively, (0.26, 0.55, and 0.57 in C-band HH-, HV- and VV-polarisations, respectively) between the estimated and measured stem volume.

Castel *et al.* (2001) studied forest stem volume mapping in a French study site using ERS (C-band VV-polarisation, 23° incidence angle), JERS (L-band HH-polarisation, 39° incidence angle), and SIR-C (C- and L-bands, HH- and HV-polarisations, 55° incidence angle) data. The ground dataset consisted of 58 stands (over 2 ha) of Austrian pine (*Pinus nigra nigricans*). The elevation was between 1600 and 1200 m. There were slopes of up to 45°. The stem volume varied between 0 and 700 m^3/ha. Terrain topography effects were corrected using a facet-based method. The terrain corrected σ^o was further modelled and corrected as a function of incidence angle (θ). Linear regression between the logarithm of the backscattering coefficient σ^o and the logarithm of the stem volume was employed. Summer acquisition of SIR-C data produced the highest coefficient of determination (R^2 values of 0.80, 0.71, 0.46, and 0.32 in L-HV, L-HH, C-HV, and C-HH, respectively), followed by JERS (R^2 values of 0.58) and ERS (R^2 values of 0.01).

Santos *et al.* (2001 and 2003) studied air-borne (AeroSensing) P-band SAR data for forest biomass mapping in a tropical study site in Brazilian Amazon. The data set included 17 (2001) and 18 plots (2003). The six primary forest plots measured 10 m x 250 m. The twelve regrowth plots measured 10 m by 100 m. Characteristic species in primary forest included *Carapa guianensis* Aubl., *Eschweilera odorata* (Poepp) Miers, *Syzygiopsis oppositifolia* Ducke, *Trattinickia rhoifolia*, *Tachigalia myrmecophylla* Ducke, *Coumarouma odorata* Aubl., and *Nectandra mollis* Nees. The most common species in regrowth areas were *Tapirira guianensis* Aubl., *Cecropia* spp., *Vismia guianensis* (Aubl) Choisy, *Guatteria poppigiana* Mart., *Didymopanax morototoni* Aubl., *Inga alba* (Sw) Willd., *Murcia bracteata* (Rich) D.C. The biomass was between 8.00 and 271.82 tons/ha. The regression model was logarithmic in biomass. R^2 values of 0.62, 0.65, and 0.47 were obtained for HH-, HV-, and VV-polarisations, respectively (Santos *et al.* 2001). HV-polarisation had the highest dynamic range, (Santos *et al.* 2003). Multiple (HH, HV, and VV) regression did not increase the signif-

icance of R^2 values compared to those obtained with HH- or HV- single-polarisation data.

Israelsson *et al.* (1997) studied CARABAS VHF SAR in forest biomass mapping. The CARABAS operated in the frequency range 20–90 MHz (wavelength 3–15 m) with HH-polarisation. The study site (in Öland, Sweden) was dominated by oak (*Quercus robur*), birch (*Betula sp.*), and alder (*Alnus Glutinosa*). In a dataset of 12 stands (2–12 ha), the forest stem volume varied between 0 and 210 m^3/ha. Incidence angle was between 60° and 65°. The study site had no variation in elevation. Israelsson *et al.* (1997) found that the backscattering coefficient increases with increasing stem volume without saturation in the stem volume range 0–200 m^3/ha.

Smith and Ulander (1998 and 2000) studied CARABAS data for forest biomass mapping in a study site in Finland (Tuusula). Dominant tree species were Scots pine (*Pinus sylvestris*) and Norway spruce (*Picea abies*) with some deciduous trees (most common birch, *Betula pendula*). The study site was generally flat. The dataset included about 140 stands (Smith and Ulander 1998) with size varying between 0.1 and 6 ha. Forest stem volume varied from close to zero to 550 m^3/ha. Disturbing non-forest objects (like power lines, buildings, and fences) were manually excluded from the dataset. In two scenes with incidence angles of 64° and 53°, R^2 values of 0.66 and 0.64 were obtained between the logarithm of σ^o and stem volume (Smith and Ulander 1998). Smith and Ulander (2000) used a regression model of the form $log_{10}(s^o) = c + m \cdot log_{10}(V)$ where s^o is backscattering amplitude and V forest stem volume. The model was determined from a set of 112 stands with stem volume higher than 100 m^3/ha. The inverted model was used to compute stem volume for the stands used. The correlation coefficient between the estimated and measured forest stem volume was 0.82 and 0.81 for the scene with 64° and 53°, respectively. The corresponding RMSE were 89 and 84 m^3/ha.

Fransson *et al.* (2000) studied CARABAS data in forest biomass mapping in a boreal coniferous study site (Tönnershöjden) in southern Sweden. The prevailing tree species were Norway spruce (*Picea abies*) with some Scots pine (*Pinus sylvestris*) and some deciduous species including beech (*Fagus sylvatica*). Elevation varied between 55 and 140 m. Forest stands on relatively flat terrain, larger than 2 ha, and more than 70 percent Norway spruce were selected for analysis. The data set was limited to stands with stem volume 80 m^3/ha or more (average 339 m^3/ha, highest 725 m^3/ha). The 80 m^3/ha limit was applied to avoid problems due to the noise floor of the CARABAS sensor. Disturbing non-forest ob-

jects (like power lines, buildings, and fences) were manually excluded from the dataset. Stands with terrain slope higher than 4° were also excluded. Fransson *et al.* (2000) obtained a correlation coefficient of 0.83 between stem volume and backscattering amplitude in a dataset of 201 stands. In a more limited, objectively inventoried dataset of 30 stands, an R^2 of 0.88 was obtained between the square of stem volume and backscattering coefficient (σ^o). No saturation was observed in either of these datasets.

The sensitivity to environmental factors varies from radar bands to others. Dobson *et al.* (1991) observed that a rain shower had the strongest effect (in a C-, L-, and P-band AIRSAR dataset) on C-band and the weakest effect on the P-band.

The stability of the relation of radar backscatter with forest biomass and environmental factors has been studied among others by Villasenor *et al.* (1993), Ahern *et al.* (1993), Keil *et al.* (1994), Conway & Estreguil (1994), Ranson *et al.* (1995), Quegan *et al.* (2000), Ulander *et al.* (2000), Angelis *et al.* (2001), and Askne *et al.* (2003).

Villasenor *et al.* (1993) studied ERS-1 SAR data (C-band, VV-polarisation, incidence angle 23°) from the commissioning phase of the ERS-1 satellite (the same orbit repeated every 3 days) in a tundra site in Alaska, USA. The elevation in the study site varied typically between 430 and 730 m with some mountains up to 1220 m. Backscatter ratio from scene to scene was used to study the changes in backscatter. The freezing between images acquired on 26 and 29 September caused a drop of backscatter. This drop was over 4 dB higher in dryer, coarse textured soils on upper slopes than on lower, finer textured soils on a flood plain.

Ahern *et al.* (1993) studied HH-polarised data from the Canadian C-band SAR (on-board a Convair-580 aircraft) in a forested study site in Canada. The study site had low relief (generally less than 25 m). The dataset covered 18 forest areas dominated by black spruce (*Picea mariana*), white spruce (*Picea glauca* Voss.), jack pine (*Pinus banksiana* Lamb.), red pine (*Pinus resinosa* Ait.), white pine (*Pinus strobus* L.), tamarack (*Larix laricina*) and some deciduous species. In addition, the dataset included six clear-cut areas. No biomass or stem volume data were reported in Ahern *et al.* (1993) but the age varied between 32 and 100 years, height between 12 and 27 m and diameter at breast height between 12 and 36 cm in the forest areas. Canopy closure was high. The radar dataset of four acquisitions (August, October, February, and May) was not absolutely calibrated but the scenes were scaled to a common mean backscatter value. The dynamic range in the forested areas was highest in May (6 dB) and lowest

in February (3.5 db, temperature -4°, 46 cm of snow in forest). The range of backscatter from open forest land was large. The separation between forested and clear-cut areas was highest in February.

Conway & Estreguil (1994) studied a set of 21 ERS-1 SAR scenes in a tropical study site in Papua New Guinea. The study site was almost flat. Dense evergreen forest had a very stable backscattering coefficient varying less than 1 dB within the year. The backscattering coefficient of savannah varied by 4.5 dB. The contrast between forest and savannah was typically 4 dB in scenes acquired in the dry season and about 1 dB in scenes acquired in the rainy season.

Keil *et al.* (1994) studied four ERS-1 SAR scenes in a tropical study site in Brazil. They also observed that the contrast between rainforest and deforested areas was higher in the scenes that were more within the dry season.

Ranson *et al.* (1995) studied HV-polarised L- and C-band data from the Shuttle imaging radar SIR-C. The topography of the study site was gentle with elevations between 550 and 730 m. The dataset of 13 stands was dominated by jack pine (*Pinus banksiana*) with one spruce stand and one stand of mixture of jack pine and aspen (*Populus tremuloides*). The biomass varied between 6 and 251 tons/ha. Ranson *et al.* (1995) derived two regression models between the logarithm of L-band HV-polarised backscattering coefficient and the forest biomass for scenes acquired on 10 April, 1994 and 1 October, 1994. The April scene was acquired with air temperature around 4° C (after a night with -4°), but the soil (at the depth of 10 cm) still frozen. The October temperature was around +3° both in day and the preceding night, with 1 mm of rain during the 24 hours before the image acquisition. The biomass functions were:

$$y = 5.130 + 0.240x \tag{15}$$

for the April scene and

$$y = 4.540 + 0.201x \tag{16}$$

for the October scene. Here y = logarithm of forest biomass (kg/m^2) and x = backscattering coefficient (dB). The coefficient of determination was 0.863 for the April scene and 0.846 for the October scene. When evaluated at a backscattering coefficient of -20 dB, the April and October functions produce biomass estimates of 21 and 33 tons/ha, respectively. At -16 dB, they produce estimates of 195 and 210 tons/ha.

Quegan *et al.* (2000) studied ERS 1 and 2 data in an English site dominated by Corsican pine using a dataset of 20 SAR scenes. No data on

stem volume or biomass was available, but forest age was used as a variable correlated with biomass. The study site was flat. The soil was porous and dry and contained flints, sand, and chalk. The mean backscatter of Corsican pine first decreased with age, reached then its lowest level around 15–20 years, and then increased to a saturation level around -9 to -10 dB. The decline in backscattering with age (or biomass) arised from increased attenuation. The backscatter level and the slope of the curve depended strongly on ground return, which was time and site dependent. Quegan *et al.* (2000) studied the temporal stability of young forest, old forest, and non-forest areas. Young forest (2–5 years) changed by 7 dB over the year while old forest (13–60 years) changed by 2.5 dB. Non-forest (agricultural) areas changed by at least 5 dB. Quegan *et al.* (2000) used this difference in variability to map mature forest areas. They note that in boreal regions the times of freezing or snow must be excluded because these conditions cause marked changes in the forest backscatter.

Ulander *et al.* (2000) studied the VHF (20–80 MHz) radar CARABAS in a site (Tönnersöhede) in south-western Sweden. The site was dominated by Norway spruce (*Picea Abies*) and had a modest topography with elevations between 55 and 145 m. The backscatter amplitude remained stable over a period of 20 months. Linear regression analysis between the stand-wise averaged backscatter amplitude data from two acquisitions produced a coefficient of determination of 0.91. Ulander *et al.* (2000) also derived regression models between forest stem volume and CARABAS backscatter amplitude in five study sites dominated by conifers in Sweden, Finland, and France. The coefficient of determination in these regression analyses varied between 0.64 and 0.97. The differences in the regression coefficients between sites were due to differences in the ground reflection coefficient.

Angelis *et al.* (2001) studied a set of three ERS-1 scenes (acquired in July 1992, September 1993, and April 1996) in a tropical study site in Brazilian Amazonia. The first two scenes were normalized to the mean backscatter of the last scene. Forests with selective logging had higher backscatter than other forests, forests affected by fire had lower backscatter than other forests, and the undisturbed forest had a stable backscatter.

Askne *et al.* (2003 and 2004) studied JERS and ERS SAR data in forest stem volume mapping in a Swedish study site (Kättöle) dominated by Scots pine (*Pinus sylvestris*) and Norway spruce (*Picea abies*) with some deciduous trees like birch (*Betula pendula*). The topography of the site was relatively flat with elevations between 75 and 110 m. Forest stem

volume data from 42 stands (2–14 ha) varied between 8 and 335 m^3/ha (mean 135 m^3/ha). The ERS dataset consisted of nine tandem pairs (18 scenes) between ERS-1 and ERS-2 from the so called tandem phase (1-day difference between ERS-1 and ERS-2 acquisitions). The JERS dataset included nine scenes. Only one JERS coherence scene (between acquisitions on 15 April and 29 May, 1997) had high enough coherence values to use. Askne *et al.* (2003) found that the ERS backscatter for different acquisitions varied inconsistently from one image to another. Correlation coefficient (against forest stem volume) was typically less than 0.3. The coherence was more consistent and produced correlation coefficients higher than 0.6 in most cases. The RMSE (corrected for ground data sampling error) in forest stem volume mapping with the nine tandem coherence scenes varied between 20.9 and 151.5 m^3/ha. In JERS SAR backscatter data, the correlation coefficient with forest stem volume was generally of the order of 0.8. The (corrected) RMSE values in forest stem volume mapping using JERS backscatter data varied between 36.5 and 140.1 m^3/ha. The multitemporal stem volume mapping using three best JERS backscatter observations and one coherence observation produced (corrected) RMSE values of 27.2 and 38.0 m^3/ha depending on which half of the ground data was used as training and testing set. Using all nine backscatter observations, the RMSE was 36.4 or 59.0 m^3/ha. Askne *et al.* (2004) also made a multiple regression model of the backscatter estimation models of the three best JERS SAR scenes and the coherence estimation model, which produced a correlation coefficient of 0.91 between the estimated and measured stem volume. The use of the four best ERS coherence images (out of the nine pairs acquired) produced a (corrected) RMSE value of 10.0 m^3/ha. In the multitemporal estimation cases, each scene was weighted by its scene-specific RMSE value.

Change detection in forested areas using SAR data has been studied among others by Rignot & van Zyl (1993) and Kuntz *et al.* (1999).

Rignot & van Zyl (1993) studied ERS SAR data in two Alaskan sites. Compared to difference between acquisitions, the ratio between acquisitions had the benefit that the detection probability was independent of backscatter level. Rignot & van Zyl (1993) also used temporal decorrelation of speckle. As the decorrelation of speckle helped to detect changes in the position of scatterers the ratio method provided information about the magnitude of the observed changes. Rignot & van Zyl (1993) recommended that both methods should be used in detailed monitoring studies.

Kuntz *et al.* (1999) used colour composites of texture filtered and speckle reduced Radarsat and JERS SAR scenes in mapping clear-cutting, plantation, and shifting cultivation in a tropical rainforest in Kalimantan, Indonesia. Visual interpretation was done after geo-coding in a GIS system. The problems in separating clear-cutting, plantation, and shifting cultivation in undulating terrain could be overcome by using timeseries of images or by using image pairs acquired from ascending and descending orbits at almost the same time. The L-band JERS SAR data discriminated areas of recent clear-cuts and initial regrowth on plantations better than ERS or Radarsat (C-band) data.

1.4 Multi-Temporal L-Band Radar Backscatter in Forest Biomass Mapping

Boreal forest biomass mapping using L-band SAR data has been studied by, among others, Harrell *et al.* (1995), Fransson and Israelsson (1999), and Pulliainen *et al.* (1999). For further references, see the introduction of Paper 6.

Harrell *et al.* (1995) studied JERS SAR data for forest biomass mapping in Alaska in a study area of 14 sites with a minimum size of 25 ha. Dominant tree species were black spruce (*Picea mariana*) and white spruce (*Picea glauca*). The sites were selected avoiding extreme relief. The total biomass ranged between 0.7 and 5.6 kg/m^2. This corresponds to about 12 to 93 m^3/ha (Equation 1). Harrell *et al.* (1995) obtained an R^2 value of 0.40 (14 sites) between the logarithm of total biomass and logarithm of backscattered power in a mosaic acquired in July-August 1992. When recently burned sites were excluded R^2 rose to 0.66 (11 sites).

Fransson and Israelsson (1999) studied JERS SAR data for forest biomass mapping in north-eastern Sweden in a study site of 59 stands. The dominant tree species were Scots pine (*Pinus sylvestris*), Norway spruce (*Picea abies*), and birch (*Betula pendula* and *Betula pubescens*). Elevation varied between 30 and 310 m. The stem volume varied between 0 and 285 m^3/ha. Fransson and Israelsson (1999) obtained R^2 value of 0.57 between the exponential of stem volume and backscattering coefficient σ^o in a scene acquired in June 1992. In a subset of 37 stands (overlap with other scenes), R^2 rose to 0.60. Fransson and Israelsson (1999) also obtained R^2 values of 0.57 an 0.56 in scenes acquired in December 1992 and May 1994, respectively. The regression lines of the December and June scenes

were around 2 dB lower than the one of the May scene. Fransson and Israelsson (1999) also determined the saturation level of the backscatter *vs.* forest volume relation. The method used the backscattering coefficients of mature forest and ground, the slope of the backscattering coefficient *vs.* stem volume ($\partial\sigma^o/\partial V$), and the attenuation coefficient κ. The saturation level was at 136, 130, and 157 m^3/ha for JERS SAR scenes acquired in June 1992, December 1993, and May 1994, respectively.

Pulliainen *et al.* (1999) studied multi-temporal JERS SAR data in a boreal study site in southern Finland. The dominant tree species was Norway spruce (*Picea abies*). Ground data on stem volume was computed from a Landsat-derived forest inventory map and aggregated to six stem-volume classes between 25 and 260 m^3/ha. The scenes were acquired in December 1994, March 1995, April 1995, and May 1993. The backscatter level in frozen conditions was around 2 dB lower than in non-frozen conditions.

In more recent literature, Santos *et al.* (2002) studied biomass mapping with JERS SAR data in two tropical study sites in Brazil. Santos *et al.* (2002) used regression models (logarithm of biomass and a sigmoid function) to model L-band backscatter using a ground data set of 68 plots (2500 m^2 in primary forest, 1000 m^2 in secondary forest). They found that the sigmoid function has a high sensitivity below (above ground) biomass values of 60 tons/ha, where the backscattering coefficient (σ^o) saturates at about -7.45 dB.

Pierce *et al.* (2003) mapped re-growth biomass in two Brazilian (tropical) study sites using a combination of JERS and Radarsat wide-swath SAR data. The radar data were ortho-rectifed using a digital elevation model (DEM). The local incidence angle was also computed and used to calibrate the SAR data to account for the ground area illuminated. The logarithm of biomass was modelled as a linear combination of L- and C-band data. An R^2 value of 0.92 was obtained in a set of 15 ground plots of 10 m by 50 m. The biomass varied between 8 and 160 tons/ha.

Kuplich and Curran (1999) mapped forest biomass in a Brazilian study site using a time-series of ten JERS SAR scenes. The biomass was between 8 and 104 tons/ha for 15 regenerating plots and about 370 tons/ha for three primary forest plots. The size of plots was 10 m by 50 m (Luckman *et al.* 1997). A correlation coefficient of 0.67 (based on 18 plots) was obtained between the logarithm of above-ground biomass and the logarithm of the backscattering coefficient. The biomass-backscatter relation saturated at around 60 tons/ha.

Castel *et al.* (2000 and 2002) studied biomass mapping in Venezuela using a mosaic of six JERS SAR scenes. The stem volume varied between 0 and 200 m^3/ha in a dataset of 78 (76 in 2002) stands of Caribbean pine (*Pinus caribaea var. Hondurensis*) plantations. Using a semi-empirical forest backscattering model, a correlation coefficient of 0.85 (Castel *et al.* 2000) was obtained between the estimated and measured stem volume (0.92 in Castel *et al.* 2002).

Tsolomon *et al.* (2002) studied a site in Mongolia. Elevation varied between 1100 and 1600 m. They derived regression models between biomass (dependent variable) and the backscattering coefficient (independent variable) from JERS SAR data. The form of the regression model was a quadratic polynomial. Tsolomon *et al.* (2002) obtained R^2 values of 0.55, 0.68, and 0.72 for larch (10 to 30 tons/ha, *Larix sibirica*), pine (15 to 25 tons/ha, *Pinus sibirica*), and poplar (3 to 6 tons/ha, *Populas*) stands, respectively. The data set consisted of one scene and ground data for approximately 25 stands per species.

Kellndorfer and Ulaby (2003) studied JERS and ERS SAR data for biomass mapping in a boreal study site with 17 jack pine (*Pinus banksiana*) stands. The biomass varied between 1 and 90 tons/ha. R^2 values of 0.93 and 0.80 were obtained for JERS and ERS SAR data, respectively, between logarithm of biomass and logarithm of σ^o.

Askne *et al.* (2004) studied forest stem volume mapping with JERS SAR data in a boreal study site in Sweden (Kättböle). The data set included 42 stands between 2 and 14 ha in size. Elevation varied between 75 and 110 m. The dominant tree species were Scots pine (*Pinus sylvestris*) and Norway spruce (*Picea abies*) with some deciduous trees (most common birch, *Betula pendula*). The highest stem volume was 350 m^3/ha and the mean 135 m^3/ha. The backscatter model was exponential in stem volume. Askne *et al.* (2004) obtained stem volume estimation errors (RMSE, corrected for errors in *in situ* data) that varied between 36.5 m^3/ha and 85.4 m^3/ha in nine scenes. Askne *et al.* (2004) found only one interferometric pair (in a dataset of nine scenes) to be useful for stem volume estimation. Askne *et al.* (2004) made a multiple regression model of the backscatter estimation models of the three best scenes and the coherence estimation model, which produced a correlation coefficient of 0.91 between the estimated and measured stem volume.

Santoro *et al.* (2004) studied forest stem volume mapping with JERS SAR data in a boreal study site in Russia near the city Krasnoyarsk. The dominant tree species were spruce (*Picea sibirica*), fir (*Larix dahurica* and *Larix*

sibirica), and birch (*Betula spp*). The study site consisted of four compartments. In one compartment, elevation varied between 220 and 260 m, whereas other compartments had an elevation variation of several hundred metres. SAR backscatter data were corrected for topographic effects using the GTOPO30 elevation model (resolution about 800 m). The terrain correction did not produce significant improvements in stem volume estimation. Forest stem volume varied between 5 and 470 m^3/ha in the study site. In the subset (used in analysis) of stands of 8 ha or larger, the stem volume varied between 5 and 410 m^3/ha. The backscatter model was exponential in stem volume. One third of the data was used for determination of the coefficients of the backscatter model and two thirds for validation. The best R^2 values (in a set of 13 SAR scenes) were 0.71, 0.52, 0.35, and 0.70 for compartments 1 (91 stands), 2 (146 stands), 3 (113 stands), and 4 (156 stands), respectively. The corresponding RMSE values were 57, 74, 87, and 63 m^3/ha, respectively.

If various physiological properties affect the backscatter in various seasonal conditions multi-temporal techniques can benefit from efficient use of data from various seasons. The year can be divided (Paper 6) into the following periods and image acquisition conditions:

G1: the peak bio-chemical activity during the first half of the growing season,

G2: the second half of the growing season before the drop of the leaves of deciduous trees,

G3: the leaves-off period before the first snow,

WD: dry winter conditions, and

WW: wet winter conditions.

2 Materials and Methods

2.1 Study Sites and Data

The selection of study sites in the papers of this thesis was based on the availability of the necessary data, primarily the availability of SAR data, but also of ground data.

Study sites were located in three European countries (Sweden, Germany, and Finland) and in Africa. SAR data were used from the satellites Seasat and JERS and the airborne AIRSAR sensor.

2.1.1 Site and Data for Incidence Angle Study

The study site where topography and incidence angle effects on radar backscatter (Paper 1) were studied was in northern Sweden close to the village Arjeplog. The centre co-ordinates of the site were 66°.0 N (northern latitude) and 17°.3 E (eastern longitude relative to Greenwich).

The site includes mixed forests (mainly pine dominated), plantations of Norway spruce (*Picea abies*) and Scots pine (*Pinus sylvestris*), clear-cut areas, marshes, and lakes. In this northern study site, forest stem volume ranges form zero to about 100 m^3/ha. The soil type is mainly till (glacial drift). The soil contains stones and boulders up to 50 cm in diameter. The elevation varies between 420 and 780 m above mean sea level. The area can be considered as hilly or mountainous.

The Seasat SAR image of the site was acquired on 20 August 1978. Seasat SAR was an L-band, HH-polarised radar with a nominal mid-swath incidence angle of 23 degrees (Pravdo *et al.* 1983). The incidence angle varied between 20° (near range) and 26° (far range). The nominal (4-look) ground resolution was 25 m. The Seasat image was SAR processed by FOA (National Defence Research Establishment, currently FOI, Swedish Defence Research Agency, in Linköping, Sweden).

A digital elevation model (DEM) was used to geo-code the SAR image into the Swedish national grid (“rikets nät”) and to compute incidence angles and resolution cell areas (A in Equation 7). The DEM (grid cell size 25 m by 25 m) was derived from the contour lines of Swedish topographic maps to a scale of 1:100 000 (contour interval 10 m). The DEM was generated by the Institute for Image Processing and Computer Graphics, Joanneum

Research Centre, Graz, Austria. The DEM covered an area of 19 km by 21 km. The terrain slopes in the area are smaller than 23 degrees. No accuracy estimate of the DEM were available. If half of the contour interval is used to describe the accuracy of the interpolated DEM – like in the case of a Finnish DEM (see section 2.1.4) – the vertical accuracy of the DEM in the Arjeplog study site can be assumed to be of the order of 5 m.

Estimation of forest stem volume and forest type classification were derived from an analysis of a Landsat Thematic Mapper scene (world reference system identifier 197-14) acquired on 25 June 1986. The RMSE of the stem volume model was 17.8 m^3/ha (R^2 of 0.67) in the training data. Since the model was applied to another TM scene, the estimation error can be much worse, perhaps of the oder of 30...40 m^3/ha.

2.1.2 Site and Data for SAR Mosaicking Study

The study site where JERS SAR mosaicking techniques (Papers 2 and 3) were studied comprised the whole forest belt of Africa. The mosaic area covers latitudes 10° S to 10° N and longitudes 14° W to 42° E. The mosaic includes large areas of tropical rain forest, with tree and grass savannah along the northern and southern borders of the area. Most of the area is flat or gently undulating below 500 m, but the eastern part of the area includes high mountains (*e.g.* Mount Kilimanjaro 5985 m).

SAR scenes (Paper 2) that were acquired for the GRFM African mosaic were divided in two acquisition layers: low water layer and high water layer. Two acquisitions were made in the GRFM project to allow the use of multitemporal techniques in analysis of the mosaic images. The naming of these layers was based on the water level of the most important river system in the mosaic area, the Congo river. The low water layer covered the whole area as described above. The high water layer covered only longitudes 8° E to 36° E. The two layers included a total of 3624 JERS SAR scenes. The low water layer was acquired in January–March 1996. The high water layer was acquired in October–November 1996.

Each JERS SAR scene covered an area of 80 km by 80 km. The images were SAR processed by the Japanese Space Agency NASDA (currently JAXA) using the so-called NASDA processor. The pixel spacing in the 3-look images was 12.5 m. The images were standard level 2.1 products with geo-location data in Universal Transverse Mercator (UTM) co-ordinates. The images were down-scaled to 100 m pixel spacing by a wavelet-based technique (Simard *et al.* 1998).

Two types of cartographic data were used for geometric control of the mosaic:

- shore line polygons from the World Vector Shoreline database, and
- raster images of topographic maps.

The World Vector Shoreline database (NOAA 2005) was compiled by the Defense Mapping Agency (DMA) of the US (currently NIMA, National Imagery and Mapping Agency). The database was intended for use in a scale of 1:250 000 or smaller. The database was derived mainly from Joint Operations Graphics and coastal nautical charts produced by DMA. The accuracy requirement in this database is that 90 percent of identifiable features are within 500 m from their true position. The (preferred) datum is WGS-84.

The topographic maps were digitized raster images of 1:200 000 topographic maps in the Central African Republic and in the Republic of Congo. The maps were produced by the French mapping agency IGN and digitized by the Belgian company I-Mage in a World Bank program. The accuracy of these maps is not known.

2.1.3 Site and Data for Wavelength and Polarisation Study

The wavelength and polarisation aspects of forest biomass mapping (Papers 4 and 5) were studied in a study site in Schwarzwald, Germany. The study site (centre 48°03' N, 8°23' E) is located near the town of Villingen-Schwenningen. The site was the German study site (named Freiburg study site) in the MAESTRO-1 program (Churchill and Attema 1991) organized by the Joint Research Centre (JRC) of the European Union and the European Space Agency (ESA).

Due to the fairly high elevation (750 to 970 m) the site is dominated by tree species that are typical in boreal forest. Norway spruce (*Picea abies* Karst.) covers 1370 ha, Scots pine (*Pinus sylvestris* L.) 280 ha, and Silver fir (*Abies alba* Mill.) 200 ha. Forest stem volume varied between 0 and 830 m^3/ha.

The SAR data in Paper 4 consisted of two AIRSAR scenes (Held *et al.* 1988) acquired on 18 August 1989. Each scene had three bands: C, L, and P (wavelengths 6 cm, 23 cm, and 63 cm, respectively). The data

were SAR processed by Jet Propulsion Laboratory (JPL). Each pixel in each band contained the full scattering matrix: HH-, HV-, VH-, and VV-polarisations as complex numbers. The scattering matrix AIRSAR data were 1-look data (with nominal ground resolution of 4 m in azimuth and 14 m in range at 45° incidence).

The data were uncalibrated, but a number of 1.8 m trihedral corner reflectors were deployed in the study site during image acquisition. The incidence angle varied between 35° and 55° in scene 1105 and between 48° and 55° in scene 1107, which covered the study site only partially.

The SAR data in Paper 5 consisted of (in addition to the MAESTRO-1 scene 1105) two new AIRSAR scenes acquired on 15 June 1991 (scene 3169) and 16 July 1991 (scene 3275). These data were also SAR processed by JPL. These data were 16-look compressed Stokes matrix data (nominal ground resolution of 16 m in azimuth and 14 m in range at 45° incidence).

A number of 1.8 m trihedral corner reflectors were also deployed in the study site during the 1991 acquisitions. The author of this thesis (assisted by JRC personnel) constructed a 5 m trihedral corner reflector (of chicken wire) for the calibration of P-band data. The July 1991 scene was already calibrated by JPL, but the June 1991 scene was uncalibrated.

Meteorological data for the AIRSAR scenes of the study site is scarce. On 18 August 1989, temperature was 22 degrees C and air humidity 36 percent. Cloud cover was 4/8. There was no rain up to 24 hours before the image acquisitions (JRC 1990). There were some slight rain a few days before 15 June 1991. The day of image acquisition was without rain. The weather was partly cloudy (the AIRSAR aircraft was visible from the study site most of the image acquisition time) and the wind was weak. No meteorological data are available for 16 July 1991. High contrast between agricultural fields and forests suggest that vegetation has not at least been soaked with rain water.

DEM was used in the geo-coding of SAR data. The DEM was made in the MAESTRO-1 program by Universität Stuttgart/Instut für Navigation. The DEM (grid spacing 30 m) was produced using contour lines from German topographic maps of a scale of 1:50 000. An evaluation of the accuracy of the DEM was made against a more accurate topographic map in scale 1:25 000. Horisontal displacements in contour line positions of up to 45 m were found between the DEM and the 1:25 000 topographic map. The maximum vertical difference (in a set of three controlled points) in hill-top elevations was 8.9 m.

Forest inventory ground data in Papers 4 and 5 covered 230 forest stands totaling 1 920 ha (19.2 km^2). The inventory was made in 1981. The accuracy of this stand-wise inventory data is not known. An average RMSE in stand-wise stem volume inventory in Finland has been estimated to be of the order of 24.1 percent (Haara & Korhonen 2004). As the forest inventory data in the Freiburg study site was 8 and 10 years old at the time of SAR data acquisitions, it can be assumed that the forest inventory ground data in Papers 4 and 5 was less accurate than the ground data in the Ruokolahti study site in Paper 6. The forest inventory data consisted of a stand map in a scale of 1:10 000 and stand-wise data sheets (situation 1 October 1981). An attempt was made to take tree growth into account. Forest stem volume was plotted against stand age and a piece-wise linear regression model was fitted with the data. The forest stem volume of the forest inventory dataset was then updated with this simple "growth model" over the 8 year time before the first AIRSAR acquisition. The updated forest stem volume data were compared to ground measurements (June 1991, Rauste 1991) in eight stands. The difference between the updated forest stem volume data and the ground measurements were more random than the difference between the 1981 forest stem volume and the ground measurements. For this reason, the updating approach was abandoned and data from the 1981 forest inventory was used in analysis of the AIRSAR data.

2.1.4 Site and Data for Multi-Temporal L-Band Radar Backscatter Study

The study site (centre 61°31' N, 28°46' E) for the multi-temporal L-band study was located in south-eastern Finland within the municipalities Puumala and Ruokolahti (Paper 6). The most common tree species in the site were Scots pine (*Pinus sylvestris* L.), Norway spruce (*Picea abies* Karst.), and birch (*Betula pendula* and *Betula pubescens*). The dominant soil type was till (glacial drift). Forest stem volume varied between 0 and 364 m^3/ha.

The SAR data included six JERS SAR scenes. The JERS SAR is an L-band, HH-polarisation SAR with a nominal incidence angle of 39°and 3-look ground resolution of 18 m. The JERS SAR scenes were acquired on 20 February 1993, 25 January 1995, 20 July 1995, 2 September 1995, 16 October 1995, and 14 March 1998. These scenes are later referred to as scenes Dry93Feb, Wet95Jan, S95Jul, S95Sep, S95Oct, and Dry98Mar, respectively. All scenes were acquired on the same nominal orbit path so that the imaging geometry is identical from scene to scene. Summer

scenes were acquired in fairly dry conditions. The precipitation on the acquisition day varied between 0.1 and 1.5 mm and on the preceding day between 0.1 and 2.4 mm. The dry winter scenes were acquired in cold conditions. The temperature had been below zero for four days before the scene Dry93Feb and for 13 days before the scene Dry98Mar. The scene Wet95Jan was acquired on a day when the maximum temperature was 0.2° C and the minimum -2.1. The precipitation (as snow) on the acquisition day of the scene Wet95Jan was 1.4 mm and on the previous day 9.7 mm.

The first JERS scene was SAR processed by ESA. The 1995 scenes were SAR processed by NASDA using the so called new NASDA processor. The last scene was processed by NASDA using the Sigma-SAR processor. The first scene was uncalibrated. For the other five scenes NASDA provided calibration factors (Shimada 1996, Shimada and Isoguchi 2002).

The DEM (25 m grid spacing) used in the geo-coding of the SAR data was produced by the Finnish National Land Survey. Contour lines of topographic maps of the scale of 1:20 000 were used in the DEM production. The DEM covered an area of 38 km by 51 km. The vertical accuracy of the DEM is considered to be 2.5 m (half of the contour interval of the topographic map material, Haggrén & Honkavaara 2004).

Forest inventory ground data were available from two sources:

- the forest management information system of Stora Enso Ltd. (the forest owner), and
- measurement of a grid of plot data by the Finnish Forest Research Institute.

The stand-wise data were inventoried in 1997. The stand-wise forest inventory dataset did not include accuracy estimate of the data. Haara and Korhonen (2004) have studied the reliability and accuracy of stand-wise forest inventory data that were made using similar inventory methods. Haara and Korhonen (2004) found the RMSE of stand-wise forest stem volume data to be 21.4 percent (of the stem volume). They also found that the RMSE in stem volume inventory varied from 10.6 to 33.9 percent depending on the person who made the inventory. The stand-wise forest management data included – after elimination of stand boundary areas and stands smaller than 2 ha – 206 stands that covered a total of 845 ha.

The plot data (covering an area of 1 km by 1 km inside the area covered

by the stand-wise inventory data) were measured in a regular grid with 50-m spacing between grid points. The diameter of a plot was about 25 m. The plot data were measured in 2000. The plot size is of the order of one (3-look) pixel in JERS SAR data. This means that very little averaging can be done in SAR data to obtain accurate backscattering coefficient data for each plot. For this reason, the plot data was used in Paper 6 as an independent but less representative data source to verify results obtained using the stand-wise data.

2.2 Methods

2.2.1 Methods for Incidence Angle Study

Pre-processing of Seasat SAR data in Paper 1 included ortho-rectification using a DEM and manually measured ground control points (Rauste 1988). The SAR data were averaged to 75 m pixel size to reduce speckle before statistical analysis.

Linear regression analysis was used to determine the amount of variation in the SAR data explained by terrain topography (including topography-simulated SAR data, resolution cell area, slope and aspect) or forest stem volume.

A simulated SAR scene that depends only on terrain topography was made. Using only land pixels (water masking by Landsat TM data), each pixel value (backscattering amplitude in the SAR scene) was divided by the square root of the area of the resolution cell A. The data were then cross-tabulated against the incidence angle. A second-degree polynomial was then fit to the cross-tabulated data. This polynomial gives the backscattering coefficient σ^o as a function of incidence angle. In the simulation stage, the incidence angle was computed from the DEM. A σ^o value was then computed using the polynomial. The σ^o was then multiplied by the area of the resolution cell A, which was also computed using the DEM.

In the computation of the simulated SAR scene, the so-called thermal noise floor was first subtracted from Seasat SAR data. The noise floor was estimated from the SAR data using the darkest water areas of the scene.

The double-bounce backscattering mechanism is illustrated in Figure 7. When the ground is flat and horizontal (Figure 7 a), vertically growing tree

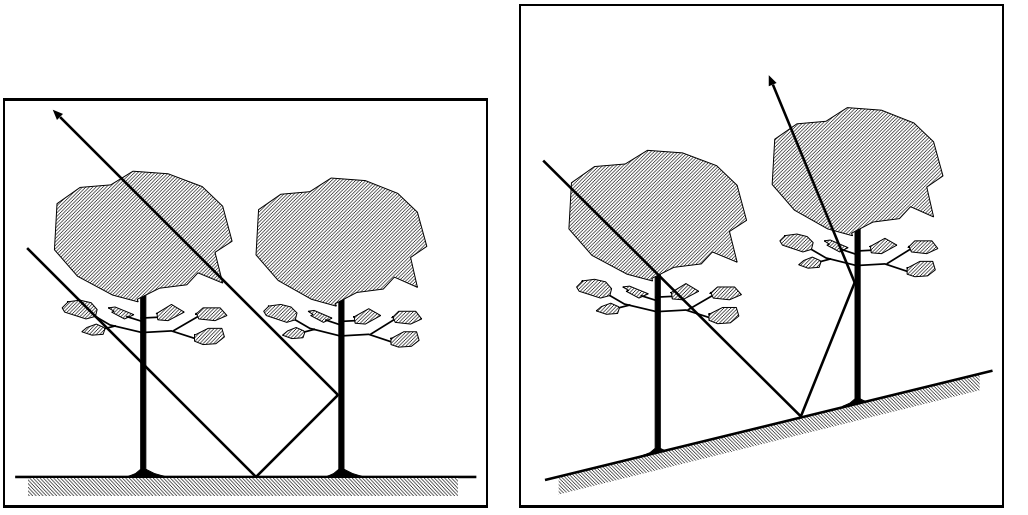

Figure 7. Double-bounce scattering with horizontal ground, a) and with sloping ground, b).

stems form a 90 degree angle to the ground. This geometry forms a corner reflector: the incoming radar signal reflects from the ground and the tree stems in such a way that it always returns back to the direction it came from – independent of the incidence angle. If the ground is tilted and the tree stems vertical (Figure 7 b), there is no 90 degree angle between the ground and tree stems. The double-bounce signal is then reflected in a direction away from the radar.

The following hypothesis was proposed: If the double-bounce component is important in the SAR data of a study site, the backscattering coefficient (σ^o, corrected for the scattering area effects as described above) of horizontal flat pixels should be higher than the σ^o of pixels where the terrain slope is higher. For the testing of this hypothesis, the dataset was divided into two parts:

- pixels with a slope of between 0 and 2 degrees, and
- pixels with a slope of between 2 and 5 degrees.

Pixels with very high slopes were excluded because very steep slopes tend to have sparse forest cover and outcrops, which could influence the analysis.

In the absence of forest inventory data from the study site of Arjeplog, forest stem volume was estimated using a Landsat TM scene and a regression model developed in a northern Finnish study site by Tomppo (1986). A forest type classification was also made.

The dependence of σ^o on incidence angle was studied using linear regression. The σ^o values were cross-tabulated against incidence angle (θ) separately for various forest types. A linear regression model σ^o *vs.* θ was derived for each forest type. The slope of these linear models was then used to study differences in the σ^o *vs.* θ relation between forest types. The slope terms were compared in pair-wise students t-tests between forest types.

2.2.2 Methods for SAR Mosaicking Study

The SAR mosaicking methodology is described separately for scene geometry and scene radiometry.

Geometric Methodology for SAR Mosaicking The image geometry revision method adopted in the mosaicking of JERS SAR data (Papers 2 and 3) is based on automatic correlation-generated tie points and on the use of least squares adjustment over the whole set of SAR scenes. In addition to the global adjustment as described by Siqueira *et al.* (2000) this approach includes the multi-temporal dimension, which guarantees the multi-temporal consistency between mosaics acquired at different times.

Since the scene geo-location data of JERS SAR level 2.1 products can be considered to describe the internal image geometry well, these data were used as the starting point in mosaic geometry revision. Like in Rosaz *et al.* (1994) and Siqueira *et al.* (2000), the similarity transformation (Figure 8) was chosen as the geometric model of scene revision.

Unlike in Rosaz *et al.* (1994) and Siqueira *et al.* (2000), the co-ordinates x and y are not image co-ordinates (azimuth-range) but cartographic co-ordinate differences relative to the scene centre. The map projection of the northing-easting co-ordinates (N and E in Figure 8) can be chosen. The Mercator projection had been chosen in connection with the definition of the GRFM project.

Also unlike in Rosaz *et al.* (1994) and Siqueira *et al.* (2000), the rotation angle α is not a heading difference between orbits but a deviation from

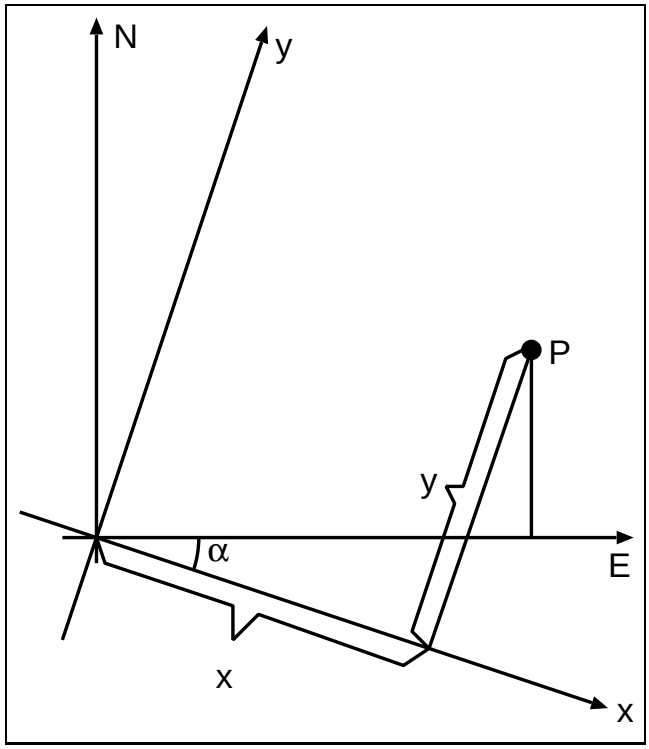

Figure 8. Image co-ordinate systems centred at scene centre.

the scene orientation as estimated by the SAR processor. Therefore, the expected value of α is zero, and its variance can also be expected to be small because the orbit heading can be reliably estimated from orbit data.

In the least squares adjustment (*e.g.*, Hirvonen 1965), observations are expressed as a function of unknown parameters (vector $\mathbf{x}$):

$$v_i = f(\mathbf{x}). \tag{17}$$

Here $f(\mathbf{x})$ is a function of the form where the observed quantity is subtracted from the theoretically calculated value of that quantity.

The number of observations n must be greater than the number of parameters m. Linearizing Equation 17 gives:

$$v_i = \sum_{j=1}^{m} \frac{\partial f}{\partial x_j} \delta x_j + f0_i. \tag{18}$$

Here δx_j is the improvement to the initial value $x0_j$. $f0_i$ is the estimated value of observation i with initial values of vector $\mathbf{x}$. Equation 18 can be written in vector form:

$$\mathbf{v} = \mathbf{A}\mathbf{x} + \mathbf{l} \tag{19}$$

where $\mathbf{v}$ = residual vector of n elements, $\mathbf{l}$ = vector of n $f0$ values (before-adjustment discrepancies), and $\mathbf{A}$ is an n by m matrix of partial derivatives:

$$a_{i,j} = \frac{\partial f_i}{\partial x_j}, \tag{20}$$

evaluated at the point corresponding to observation i.

If the observations have different weights ($\mathbf{P}$ is a diagonal weight matrix with $p_{i,i}$ the weight of observation i) the weighted square sum of errors is:

$$\mathbf{v^T P v} = \mathbf{x^T A^T P A x} + \mathbf{2 x^T A^T P l} + \mathbf{l^T P l}. \tag{21}$$

Using the following notations:

$$\mathbf{N} = \mathbf{A^T P A} \tag{22}$$

and

$$\mathbf{u} = \mathbf{A^T P l}, \tag{23}$$

the minimum of the weighted square sum of errors can be found by solving (Hirvonen 1965)

$$\mathbf{N x} + \mathbf{u} = \mathbf{o} \tag{24}$$

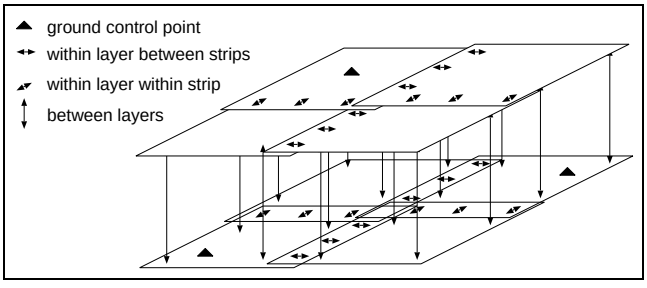

Figure 9. Ground control points and types of tie points with respect to acquisition layers and image strips (orbits).

for $\mathbf{x}$. Matrix $\mathbf{N}$ is called the normal equation coefficient matrix. The vector $\mathbf{o}$ is a vector of m zeroes.

In the block adjustment method adopted in Papers 2 and 3, the observation Equations (17) are of three different types:

1. tie point equations between scenes,
2. ground control point equations between a scene and the cartographic co-ordinate system, and
3. orbit data equations.

Tie points can be further divided into three groups (Figure 9):

1. tie point within a single acquisition layer between two adjacent strips,
2. tie point within a single acquisition layer within a strip between two consecutive frames, and
3. tie point between two acquisition layers.

If scenes of an orbit are acquired on the same day, tie points within strips (type 2 above) are special in the sense that these points can be correlated without strong contrast in the scene. This is due to the fact that the speckle pattern is identical in both scenes in the overlap area (due to common raw data in SAR processing). Other tie point types require a contrast-rich feature that remains stable over the image acquisition interval. From the point of view of observation equations, all tie point types are identical.

In the following observation equations, the unknown parameters that are solved in the least squares adjustment are:

δN^c = translation in northing of the scene,
δE^c = translation in easting of the scene, and
α = rotation of the scene.

For tie point observation equations, we can read in Figure 8:

$$N^p = N^c + \delta N^c + y * cos(\alpha) - x * sin(\alpha) \quad (25)$$
$$E^p = E^c + \delta E^c + x * cos(\alpha) + y * sin(\alpha) \quad (26)$$

where

N^p = northing of point P,
E^p = easting of point P,
N^c = northing of the scene centre,
E^c = easting of the scene centre,
x, y = image co-ordinates relative to scene centre (see Figure 8).

For a tie point observed in two scenes, the observation equations are:

$$\begin{aligned} V_{N^p} &= N_1^p - N_2^p \\ &= N_1^c - N_2^c + \delta N_1^c - \delta N_2^c + y_1 * cos(\alpha_1) - y_2 * cos(\alpha_2) - \\ &\quad x_1 * sin(\alpha_1) + x_2 * sin(\alpha_2) \end{aligned} \quad (27)$$

and

$$\begin{aligned} V_{E^p} &= E_1^p - E_2^p \\ &= E_1^c - E_2^c + \delta E_1^c - \delta E_2^c + x_1 * cos(\alpha_1) - x_2 * cos(\alpha_2) + \\ &\quad y_1 * sin(\alpha_1) - y_2 * sin(\alpha_2), \end{aligned} \quad (28)$$

where V_{N^p} and V_{E^p} are the residual error of the tie point co-ordinates in northing and easting, respectively.

For ground control points with known geodetic co-ordinates N_g and E_g and estimated co-ordinates N_e and E_e, the observation equations are:

$$\begin{aligned} V_{N^g} &= N_e^p - N_g^p \\ &= N^c + \delta N^c + y * cos(\alpha) - x * sin(\alpha) - N_g^p \end{aligned} \quad (29)$$

and

$$\begin{aligned} V_{E^g} &= E_e^p - E_g^p \\ &= E^c + \delta E^c + x * cos(\alpha) + y * sin(\alpha) - E_g^p, \end{aligned} \quad (30)$$

where V_{N^g} and V_{E^g} are the residual error of the ground control point coordinates in northing and easting, respectively.

The orbit data equations are:

$$v_{N^c} = \delta N^c, \tag{31}$$

$$v_{E^c} = \delta E^c, \text{ and} \tag{32}$$

$$v_\alpha = \alpha. \tag{33}$$

In the linearization of observation equations (computation of partial derivatives needed in the matrix $\mathbf{A}$) the following approximations were made because the angle α is always very small:

$$sin(\alpha) \approx \alpha \approx 0 \tag{34}$$

and

$$cos(\alpha) \approx 1 \tag{35}$$

The partial derivatives needed in matrix $\mathbf{A}$) were derived from Equations (27) through (33).

Residual errors after least squares block adjustment can be used as a diagnostic tool to evaluate the geometry of the resulting SAR image mosaic. An additional tool for the evaluation is a diagram of error ellipses of the estimated scene centres. The semi-major (m_{uu}) and semi-minor (m_{vv}) axes of the error ellipses are (Hirvonen 1965):

$$m_{uu} = m_o\sqrt{Q_{uu}} \tag{36}$$

$$m_{vv} = m_o\sqrt{Q_{vv}} \tag{37}$$

where m_o is the mean square error of a unit weight observation and

$$Q_{uu} = \frac{1}{2}(Q_{NN} + Q_{EE} + W) \tag{38}$$

$$Q_{vv} = \frac{1}{2}(Q_{NN} + Q_{EE} - W). \tag{39}$$

Here Q_{NN} and Q_{EE} are the main diagonal elements (of the inverse of the normal equation coefficient matrix) corresponding to the northing and easting translations of the scene in question and

$$W = \sqrt{(Q_{NN} - Q_{EE})^2 + 4Q_{NE}^2} \tag{40}$$

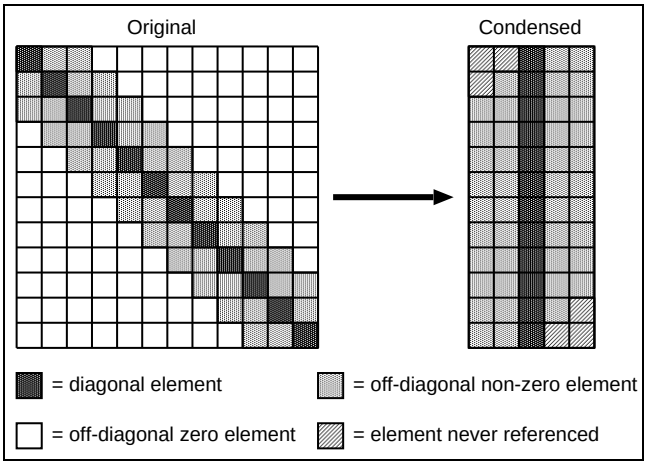

Figure 10. Condensed form of the normal equation coefficient matrix $\mathbf{N}$.

where Q_{NE} is the off-diagonal element corresponding to the northing and easting co-ordinates of the scene in question.

The orientation angle t of the semi-major axis can be solved from:

$$sin(2t) = \frac{2Q_{NE}}{W} \tag{41}$$

$$cos(2t) = \frac{Q_{NN} - Q_{EE}}{W}. \tag{42}$$

The dimension m of the normal equation coefficient matrix $\mathbf{N}$ is three times the number of scenes in the adjustment. If thousands of scenes are included, the $\mathbf{N}$ matrix becomes large. If the scenes are numbered systematically, the $\mathbf{N}$ matrix is a block diagonal matrix with a limited band-width w. The band-width depends on the order in which the various indices grow in the mapping from indices to image number. If scene numbering is such that the fastest growing index (of acquisition layer, strip, and scene within strip) is scene within strip, then acquisition layer, and slowest strip, the band-width is:

$$w = (2 * s_m + 1) * n_l * 3 \tag{43}$$

where s_m is the maximum number of scenes in a single strip (in an acquisition layer) and n_l the number of acquisition layers.

The $\mathbf{N}$ matrix was stored in the condensed form (Figure 10). Matrices $\mathbf{A}$ and $\mathbf{P}$ were not constructed, but the contribution to the matrix $\mathbf{N}$ (and to the $\mathbf{u}$ vector) of each observation equation was summed up directly to the

condensed-form $\mathbf{N}$ matrix (and $\mathbf{u}$ vector) when processing tie point and ground control point observations.

The conjugate gradient method (Press *et al.* 1992) was used to solve the normal equation system (24).

Radiometric Methodology for SAR Mosaicking The radiometric calibration revision was carried out in two phases:

1. removal of constant range dependent artifacts, and
2. radiometric adjustment in overlap areas.

The constant range dependent artifacts result from the sensor antenna pattern, the sensor STC (Sensitivity Time Control) pattern, and the uncertainties connected with the removal of these effects in the SAR processor. The STC is a technique that aims at keeping the recorded signal level approximately constant despite the changes in antenna gain and spreading loss across the image swath. A major source of uncertainty in these corrections is the uncertainty of satellite attitude sensors (roll in particular) because the antenna gain changes rapidly with varying look angle close to the margins of the (vertical) antenna pattern.

An average range pattern was determined over all scenes in the mosaic (Paper 3). Each scene was then scaled (using the average range pattern) so that the average range pattern of the scaled scenes was a linear function of range.

As in Rosaz *et al.* (1994), the scene radiometry was adjusted using least squares adjustment. Unlike the pairwise processing of Rosaz *et al.* (1994), the least squares adjustment (in Paper 3) determined the calibration revision parameters for all scenes of the mosaic in a single adjustment.

The use of calibration tie points in scene-overlap areas and the aiming at identical radar responses in both scenes is justified because the backscattering coefficient γ^o can be expected to

1. be constant over the incidence angle range of JERS SAR , and
2. stay constant over the image acquisition interval.

The first assumption has been confirmed by scatterometer measurements in C-band (Lecomte and Attema 1992) and by JERS SAR data (Shimada

1996). The second assumption can be made because the African JERS SAR data of adjacent orbits were acquired on consecutive days for the major part of the mosaic area.

A bi-linear multiplicative calibration model was adopted in Paper 3 between the original backscattering amplitude r_o and the calibrated backscattering amplitude r_c:

$$\begin{aligned} r_c &= f * r_o && (44) \\ &= (f_0 + x * f_1 + y * f_2 + x * y * f_3) \cdot r_o && (45) \end{aligned}$$

where x and y are the normalized centred image coordinates.

Denoting:

$$\begin{aligned} f_0 &= 1 + \delta f_0, \\ f_1 &= (0+)\delta f_1, \\ f_2 &= (0+)\delta f_2, \text{ and} \\ f_3 &= (0+)\delta f_3 \end{aligned}$$

the observation equation for a calibration tie point P was:

$$\begin{aligned} V^P = r_1^P * \delta f_0^1 + x_1 * r_1^P * \delta f_1^1 + y_1 * r_1^P * \delta f_2^1 + x_1 * y_1 * r_1^P * \delta f_3^1 + r_1^P - \\ r_2^P * \delta f_0^2 - x_2 * r_2^P * \delta f_1^2 - y_2 * r_2^P * \delta f_2^2 - x_2 * y_2 * r_2^P * \delta f_3^2 - r_2^P \quad (46) \end{aligned}$$

where V^P is the error (difference between the backscattering amplitudes in the two overlapping scenes) at point P. Here

r_1^P = observed backscattering amplitude in scene 1,
r_2^P = observed backscattering amplitude in scene 2,
δf_0^1 = improvement of term f_0 for scene 1,
δf_1^1 = improvement of term f_1 for scene 1,
δf_2^1 = improvement of term f_2 for scene 1,
δf_3^1 = improvement of term f_3 for scene 1,
δf_0^2 = improvement of term f_0 for scene 2,
δf_1^2 = improvement of term f_1 for scene 2,
δf_2^2 = improvement of term f_2 for scene 2,
δf_3^2 = improvement of term f_3 for scene 2.

Corresponding to the orbit data Equations (31) to (33) in geometric block adjustment, the calibration adjustment included the following observation equations for the calibration parameters:

$$V_{f0} = \delta f_0 \quad (47)$$

$$V_{f1} = \delta f_1 \quad (48)$$
$$V_{f2} = \delta f_2 \quad (49)$$
$$V_{f3} = \delta f_3. \quad (50)$$

where V_{f0} to V_{f3} are the errors of calibration revision coefficients f_0 to f_3, respectively.

2.2.3 Methods for Wavelength and Polarisation Study

Polarimetric AIRSAR data were used when studying the optimal wavelengths and polarisations for forest biomass mapping (Papers 4 and 5). Those AIRSAR scenes that were not already calibrated were calibrated using the methods described by van Zyl (1990) and Zebker and Lou (1990). The August 1989 scenes, which were stored in scattering matrix format, were converted to Stokes matrix format. A linear correction was made to the range pattern of the June 1991 scene to correct for a calibration anomaly in that scene.

The Stokes matrix scenes were ortho-rectified using ground control points and a digital elevation model. Averaging was done in ortho-rectification to reduce speckle. Gaussian weights were used in the resampling of Stokes matrix elements of the ortho-rectified scenes. The amount of speckle reduction was controlled by the standard deviation of the Gaussian weight function. In the ortho-rectification of the August 1989 scenes, the standard deviation was 0.8 pixels in slant range and 0.8 pixels in azimuth (about 70 percent of the 12.5 m pixel spacing of the ortho-rectified scenes). In the ortho-rectification of the 1991 scenes (with lower speckle due to 16-look format), the standard deviation of the Gaussian weight function was 0.35 pixels in slant range and 0.5 pixels in azimuth.

The Stokes matrix elements, which were proportional to received power quantities, were corrected for topographic effects:

$$P_c = P_o \frac{tan(\theta_r)}{tan(\theta_n)} \quad (51)$$

where P_c is the terrain-corrected Stokes matrix element, P_o is the original Stokes matrix element, θ_r is the incidence angle in range (depending on the local topography), and θ_n is the nominal incidence angle (which varies across the image swath) assuming a flat earth. This form of terrain-correction means that the corrected Stokes matrix elements are proportional to γ^o of Equation (9).

Stokes matrix data were averaged per forest stand using a digital stand mask derived from the forest inventory map.

A systematic search was used to find the polarisation combination that maximised the correlation between backscattering amplitude and forest stem volume. Starting with the stand-wise averaged Stokes matrix data and forest stem volume data for stands:

- the received power was computed for each stand using polarisation synthesis (van Zyl *et al.* 1987),
- correlation coefficient was computed between the forest stem volume and the backscattering amplitude over all stands.

The above optimisation was computed over the 4-dimensional space of polarisation combinations (receive orientation, transmit orientation, receive ellipticity, and transmit ellipticity) in a grid with a grid spacing of 10 degrees in all dimensions.

Visual comparison of correlation coefficient diagrams was used to analyse the temporal stability of the forest biomass *vs.* backscattering amplitude relation. Multiple linear regression analysis was used to study the relation between forest stem volume and backscattering amplitude. The form of the regression function was:

$$V = \alpha_o + \alpha_1 \cdot x_1 + \alpha_2 \cdot x_2 + \alpha_3 \cdot x_3 (+\epsilon) \tag{52}$$

where V was forest stem volume, independent variables x_1 to x_3 were the AIRSAR acquisitions of August 1989, June 1991, and July 1991, respectively, α_o to α_3 were regression coefficients, and ϵ was the random error. Scatter plots between backscattering amplitude data from two acquisitions were used for change detection.

2.2.4 Methods for Multi-Temporal L-Band Radar Backscatter Study

Multi-Temporal L-band SAR data in forest biomass mapping were studied in the Ruokolahti study site (Paper 6). JERS SAR scenes were orthorectified using a DEM, manually measured ground control points, and tie points between scenes.

The JERS SAR data, which were in backscattering amplitude format, were corrected for terrain effects on image radiometry:

$$r_c = r_o \sqrt{\frac{tan(\theta_r)}{tan(\theta_n)}} \tag{53}$$

where r_c is the terrain-corrected backscattering amplitude, r_o is the original backscattering amplitude, θ_r is the incidence angle in range, and θ_n is the nominal incidence angle (39 degrees for JERS SAR; since the study site was only 40 km wide a constant θ_n could be used for a space-borne sensor). This form of terrain-correction means that the corrected backscattering amplitude is proportional to $\sqrt{\gamma^o}$ of Equation (9). Since the terrain correction is made relative to the nominal incidence angle, the average level of the backscattering amplitude does not change from the original level. The calibration factors presented by Shimada (2001) are therefore also applicable to the terrain-corrected backscattering amplitude data. The result of the calibration equations in Shimada (2001) is called σ^o. Because all radar-biomass relations published in the literature have been described in terms of σ^o (not γ^o) the notion of σ^o was used in Paper 6 also.

JERS SAR data were averaged (in power format) per forest stand using a stand mask from forest inventory data. The stands were first eroded by one (25 m) pixel, and only those stands were included in analyses where the stand was 2 ha or more after the erosion step.

Regression analysis, both simple regression and multiple regression, were used to analyse the relation between forest stem volume and L-band backscattering amplitude. Regression analyses were made for various datasets limited by the stem volume range. In these analyses, the number of observations (stands) varied between 19 and 206. In Paper 6, the adjusted R_A^2 (Rudner *et al.* 2002) was used to take this variation into account:

$$R_{A_1}^2 = R^2 - \frac{(1 - R^2) \cdot p}{n - p + 1} \tag{54}$$

where R^2 is the coefficient of determination, n = number of observations, and p = number of independent variables (1 to 6 SAR scenes). There are at least two other variations of the adjusted R_A^2 (Wulder 2005):

$$R_{A_2}^2 = R^2 - \frac{(1 - R^2) \cdot (p - 1)}{n - p} \tag{55}$$

and (Jensen 2005):

$$R_{A_3}^2 = 1 - \frac{(1 - R^2) \cdot (n - 1)}{n - p - 1}. \tag{56}$$

The R_A^2 values of these definitions are also listed in section 3.5.

3 Results and Discussion

3.1 Incidence Angle Effects on L-band Radar Backscatter in Forests

Incidence angle effects – due to local topography – were studied in the Arjeplog study site in northern Sweden. Five independent variables were used in regression analysis where the dependent variable was the Seasat SAR-measured (not corrected for any topographic effects) backscattering amplitude:

topo: topography-simulated SAR image in amplitude as described in section 2.2.1,

vol: forest stem volume estimated from Landsat TM data,

area: (square root of the) area A of the resolution cell computed using DEM data, as described in section 1.1 (Equation 7),

slope: terrain slope computed using DEM data, and

aspect: azimuth of steepest slope with respect to the SAR illumination direction.

Table 2 shows the coefficient of determination (the proportion of total variance accounted for by the independent variables) and the correlation coefficient from linear regression. The correlation coefficient in Table 2 can be considered as the correlation coefficient between a predicted and observed backscattering amplitude when using the independent variables as predictors. In the single-variable cases this is equal to the correlation coefficient between the independent variable and the observed backscattering amplitude (the dependent variable).

The terrain topography is the strongest single factor contributing to the variation in backscattering amplitude in the study site. The topography-simulated SAR image explained 63.1 percent of the total variance in the SAR scene. It is possible that a more detailed and accurate DEM would have increased the proportion of variation that is accounted for by terrain topography. Visual inspection of the SAR scene and the DEM suggested that the SAR scene contained fine-scale topographic variation that was poorly described by the DEM. However, the averaging of the SAR scene to 75 m pixel spacing reduced this fine-scale variation.

Table 2. Regression analysis results in the Arjeplog study site. Dependent variable is the digital number (backscattering amplitude) in a Seasat SAR scene. See section 3.1 for the independent variables. The number of observations (pixels) was 23446 (Paper 1).

Independent variables	Coefficient of determination (%)	Correlation coefficient
topo + vol	65.4	0.81
topo	63.1	0.80
vol	0.3	0.05
area + vol	62.4	0.79
area	60.8	0.78
slope + aspect	3.4	0.19

When adding the (Landsat-derived) stem volume, the proportion of explained variance rose to 65.4 percent. When correlating the stem volume against SAR data that has not been corrected for topographic effects, stem volume is almost uncorrelated to SAR data (the correlation coefficient is only 0.05).

Most of the topography influence comes from the variation of the area of the resolution cell because this (the variable 'area' in Table 2) alone explained 60.8 percent of the total variance. Adding the dependence of the backscattering coefficient σ^o on the incidence angle (variable 'topo' in Table 2), increased the coefficient of determination to 63.1 percent.

Terrain slope and aspect do not explain well (in linear regression analysis) the effects of topography on backscattering amplitude. This can be understood because an increasing terrain slope on fore-slopes (slopes toward the radar) increases the backscattering amplitude whereas an increasing terrain slope on back-slopes (slopes away from the radar) decreases the backscattering amplitude (see Equations 4 and 9).

The proportion explained by terrain topography in Foody (1986) was significantly lower than the 60 percent accounted for by scattering area in Table 2. The main reasons for this might be the higher nominal incidence angle of the Convair-580 sensor (32° to 63° *vs.* 23° of Seasat), which reduces the topographic effects, and a study site (undulating) with less topographic variation. The proportion of variation explained by slope and aspect in Foody (1986) was on the average higher than the 3.4 percent in Table 2. The reason for the higher R^2 in Foody (1986) is most likely the

different statistical analysis techniques (multiple linear regression in Paper 1 *vs.* computation using zero and first order partial correlations in Foody, 1986).

The hypothesis on the double-bounce scattering component was tested with flat (slope 0 to 2 degrees) and non-flat (slope 2 to 5 degrees) forested pixels. The flat average backscattering amplitude was 104 (in arbitrary units) while the non-flat average backscattering amplitude was 106. This suggests that the double-bounce component is not very important in the study site. The reason may be rough (in terms of the 23 cm wavelength of the Seasat SAR) ground (glacial drift with stones and boulders). Rough ground reduces the ground reflection of the double-bounce component (in flat pixels) and also increases the direct backscattering component (both in flat and sloping pixels). Pulliainen *et al.* (1999) also found in a Finnish study site that the stem-ground reflection is small compared to the direct backscattering from forest canopy.

Figure 11 shows the square root of backscattering coefficient (σ^o) as a function of incidence angle in the Arjeplog study site and linear regression functions for the following forest types:

- spruce-dominated mixed forest,
- pine-dominated mixed forest,
- deciduous-dominated mixed forest, and
- clear-cut areas.

The independent variable in the regression analysis was $cos(\theta)$ and the dependent variable $\sqrt{\sigma^o}$. The forest types were mapped using a Landsat TM scene (section 2.2.1). When using tens of thousands of pixels as observations, the slope terms of the regression functions differed significantly (at a 5 percent significance level) between all possible pairs of forest types. The slightly different backscatter-dependence on incidence angle is probably due to different stem volumes in different forest types. On average, spruce-dominated mixed forests had the highest average stem volume in the study site. Also many other factors can have an influence such as understory, soil type, and tree structure.

Even though the regression functions were different for different forest types the σ^o data of forest types overlapped. At 30° incidence angle, where the forest type differences were largest, the average L-band backscattering

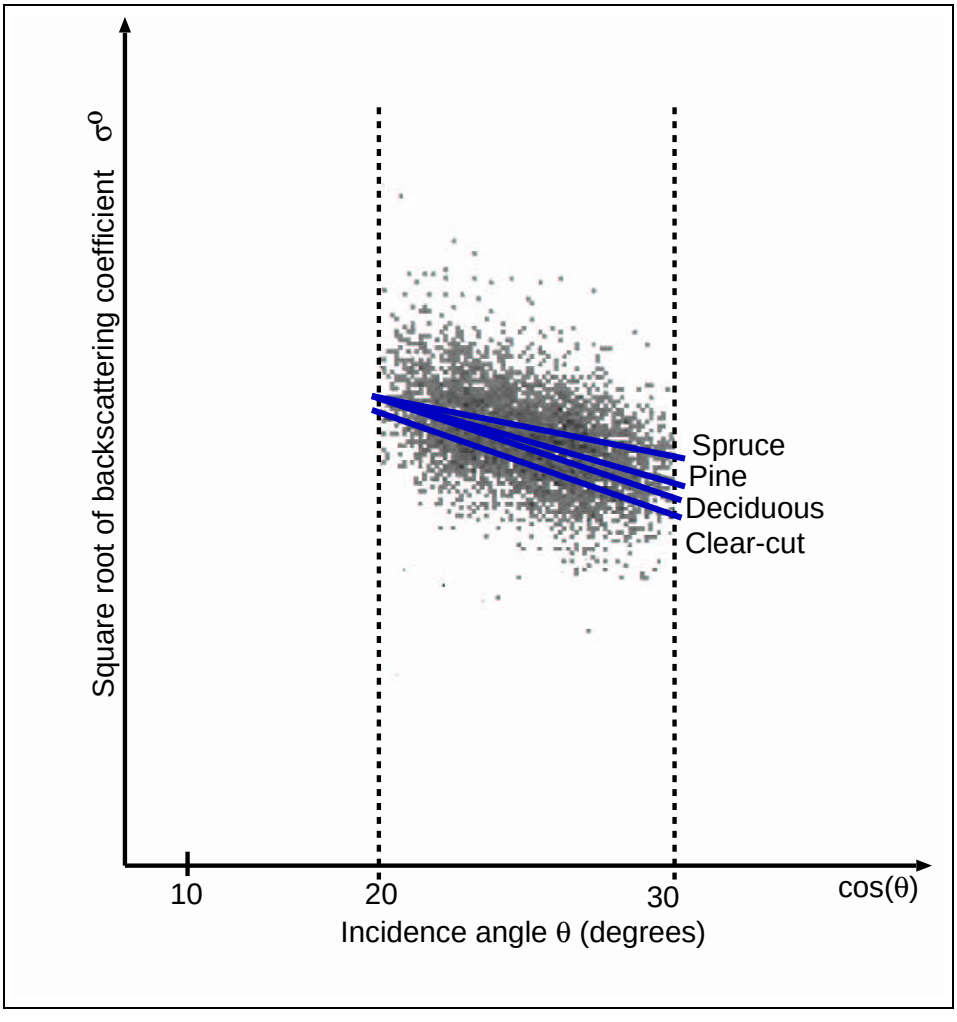

Figure 11. Backscattering coefficient (σ^o) in L-band Seasat SAR data as a function of incidence angle (θ) for various forest types in the Arjeplog study site. Total number of observations (pixels) = 23 446.

amplitude for spruce-dominated mixed forests was only 17 percent higher than that of clear-cut areas and 11 percent higher than the deciduous-dominated mixed forest.

3.2 Geometry in SAR Mosaicking

The geometry revision approach described in Papers 2 and 3, and in section 2.2.2 was applied to the GRFM African dataset of JERS SAR scenes. A total of about 62 000 tie points were produced using an automatic image correlation method. A set of 248 ground control points (GCPs) were measured using an interactive method by displaying shoreline polygons on top of JERS SAR scenes from the World Vector Shoreline database. A set of about 50 GCPs were measured from topographic maps. Water areas and outlines of land features were displayed as opaque colours (other areas as transparent) on top of JERS SAR data.

Table 3 shows the root mean square error (RMSE) statistics when the tie point and GCP datasets were used in block adjustment. The column 'Tie point' gives RMSE computed over all 62 000 tie points in the adjustment, separately for easting and northing. The column 'Scene centre' gives the square average of all scene translations (a scene translation is considered as an error, Equations 31 and 32), separately in easting and northing. The column 'GCP' gives RMSE computed over the set of GCPs, separately in easting and northing. The column 'p_g' gives the weight assigned to GCP observations. The weight of a tie point observation was always 1. The weight of the scene centre Equations (31 and 32), was always $\frac{1}{1000}$. The $\frac{1}{1000}$ weighting of scene centre positions from scene header data corresponds approximately to the estimated variance ratio between these data and the tie point measurements as estimated in some problem scenes in connection with preliminary mosaicking attempts.

When compiling the GRFM African mosaic, obtaining accurate and reliable cartographic data for geometric validation was difficult. The strategy for evaluating the geometric accuracy of the mosaic was to use the tie point and GCP datasets in different combinations. Table 3 shows the RMSE statistics for three adjustments:

1. the adjustment where only tie points and orbit data were used to determine the mosaic geometry,

2. the adjustment where tie points, orbit data, and GCPs from the World

Table 3. Root mean square error statistics of the geometric block adjustments of the GRFM African JERS SAR mosaic. All values are in metres. N = northing, E = easting (Paper 2).

Case	Tie point		Scene centre		GCP		p_g
	N	E	N	E	N	E	
1	33.2	34.8	477.5	751.7	503.0	1021.4	0
2	35.5	40.8	532.0	736.2	193.7	201.6	2
3	40.1	39.7	543.3	758.0	173.2	166.3	2

Vector Shoreline database were used to determine the mosaic geometry, and

3. the adjustment where tie points, orbit data, and GCPs from the World Vector Shoreline database and topographic maps were used to determine the mosaic geometry.

In the first adjustment (case 1 in Table 3) GCPs from the World Vector Shoreline database were included but their weight was zero. The GCPs served as independent validation data. The tie point RMSE values of 33.2 and 34.8 m (in easting and northing) indicate that the mosaic internal consistency is good at sub-pixel level. The pixel size of the scenes to mosaic was 100 m. The RMSE values in GCPs (503.0 m in northing and 1021.4 m in easting) show that absolute geo-location accuracy is (on average) of the order of 10 pixels if no GCPs are used. The scene centre Figures (477.5 m in northing and 751.7 m in easting) tell how large relative movements (from the scene positions given in scenes' geo-location data) are needed to compile a spatially consistent JERS SAR mosaic when using SAR scenes from the so-called new NASDA processor.

In the second adjustment (case 2 in Table 3), GCPs from the World Vector Shoreline database were included in the determination of the mosaic geometry also. The tie point RMSE increased slightly compared to the tie-points-only case, but the RMSE is still within a sub-pixel of the mosaic. The mosaic was shifted by about 0.5 to 1 km with respect to the location derived from the scenes' geo-location data. This shift decreased the RMSE values of GCPs to about 200 m. This value is smaller than the accuracy requirement of the World Vector Shoreline polygons (90 percent of features within 500 m of its true location).

In the third adjustment (case 3 in Table 3), GCPs from topographic maps

(in the Central African Republic and Republic of Congo) were also added. This shifted the mosaic only slightly, and the RMSE values did not change much from case 2. This suggests that adding new GCPs would not change the mosaic geometry much. The mosaic geo-location accuracy (Paper 2) was therefore considered to be most likely within a few hundred meters throughout the mosaic.

The accuracy figures of Table 3 cannot be directly compared to accuracy figures from other studies. This is due to the differences in SAR systems, SAR processors, and orbital data used in the SAR processors. Rosaz *et al.* (1994) presented no geometric accuracy figures for the compiled ERS-1 SAR mosaic. Siqueira *et al.* (2000) estimated the mean geo-location error of the JERS-1 SAR mosaic of Amazon to be 38 m in latitude and 32 m in longitude, when applying average geo-location correction to clusters of 1 degree by 1 degree. This error describes the internal accuracy of the mosaic. When the mosaic was transformed using similarity transformation (rotation and shifts in latitude and longitude) the residuals in GCPs (27 used to tie down the mosaic, 30 used to estimate geo location accuracy) were estimated to be within +/- 400 m. Shimada and Isoguchi (2002) estimated the geometric accuracy of the Southeast Asian JERS-1 SAR mosaic to be 406 m. Hutton *et al.* (2000) estimated the geometric accuracy of the Radarsat-1 mosaic of Canada to be in the order of one pixel or 250 m. Noltimier *et al.* (1999) estimated the absolute geometric accuracy of the Radarsat-1 mosaic of Antarctica to be 150 m or better.

The error ellipses (for case 3 in Table 3) were computed using Equations (36) to (42) and shown in Figure 1 of Paper 2. The semi-major axis of the error ellipse (for a scene centre) varied between 6 and 55 m (median 11 m). The semi-minor axis varied between 6 and 30 m (median 10 m).

Most of the error ellipses were almost circular, which indicates that the uncertainty in the geo-location in these areas is approximately equal in all directions. Most of the ellipses were also of the average dimension, which indicates that the uncertainty in geo-location in these areas is approximately uniform over the area. In sea areas, where tie points were impossible to find between neighbouring strips (orbits), the error ellipses increased in dimension and became elongated. Other such areas where larger and less regular error ellipses indicated worse geo-location accuracy were found along the northern and southern margin of the mosaic area. These were areas where the closest GCPs were distant. Irregular shaped “extensions” of the mosaic area also produced large error ellipses. This phenomenon was especially prominent in the north-western and north-eastern corners of the mosaic.

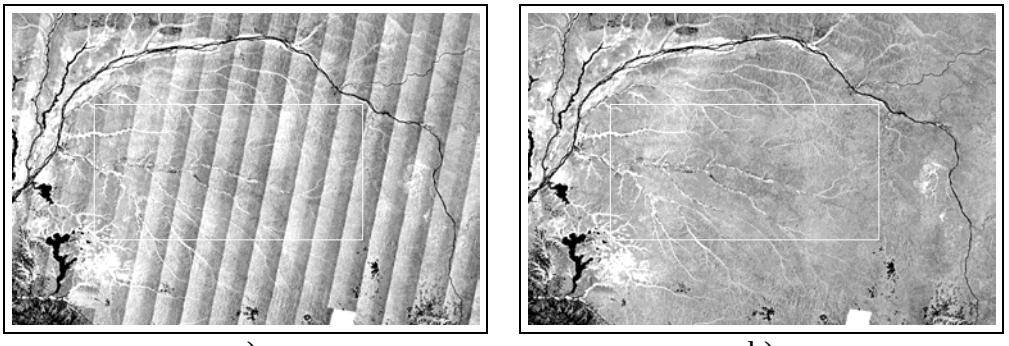

a) b)

Figure 12. A subset of the high-water acquisition layer of the GRFM African mosaic before a), and after b) calibration revision. The area covered is about 1000 km in east-west direction and about 670 km in north-south direction (Paper 3).

The geometric methods of mosaicking that were applied in the compilation of the GRFM African mosaics can be applied to other similar SAR data sets. This requires that the SAR data has associated geo-location data the describes the internal geometry of SAR scenes reliably even though absolute locations may include random or systematic errors of hundreds of meters or even kilometres.

3.3 Radiometry in SAR Mosaicking

No simultaneous calibration measurement were made for validation of the calibration level of the GRFM African mosaic. Removal of visible artifacts were used as an indication of the calibration revision in Paper 3.

Figure 12 shows an example of the calibration approach. There is a clear calibration artifact in the mosaic before calibration (Figure 12 a). As the look direction of the JERS SAR was from east to west, the backscatter increases with increasing range (all scenes were acquired in descending orbits). The calibration method has removed this artifact completely (Figure 12 b).

Figure 13 shows a profile computed cross the white rectangle in Figure 12. The profiles were computed summing all pixels within the rectangle along lines parallel to the orbit direction of JERS. The near-range to far-range increase in backscattering amplitude is about 1 dB (Figure 13 a).

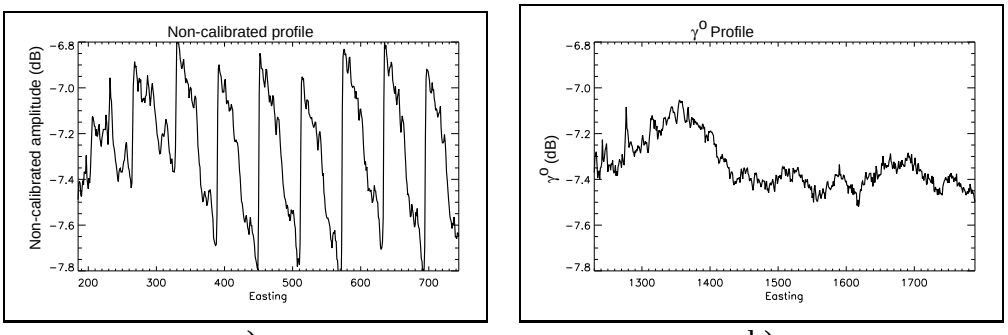

a) b)

Figure 13. A range profile in the GRFM African mosaic extract before a), and after b) calibration revision (Paper 3).

The calibration has clearly removed the artifact. The remaining variation in backscattering amplitude in Figure 13 b) is due to variation in land cover type and vegetation characteristics.

In addition to the validation techniques discussed above, mosaic data can be used in computerized image analysis algorithms to evaluate the possible existence of calibration artifacts. In Paper 3, a land-cover classification was made (not by the author of this thesis) using the calibrated mosaic data. This classification (Figure 12 in Paper 3) does not show visible calibration-related artifacts, which indicates that the calibration method is suitable for producing mosaics for land-cover classification.

As with geometric accuracy, the comparison of mosaic methods in terms of radiometric accuracy is not feasible due to differences in SAR sensor, SAR processors, and available verification data for radiometric accuracy.

The radiometric methods of mosaicking that were applied in the compilation of then GRFM African mosaics can be applied to other similar SAR datasets. The assumption of stable backscattering between neighbouring scenes in the overlap areas must be valid. In SAR systems where the acquisition interval between neighbouring orbits is longer than one day the validity of this assumption can be less probable than in the case of the JERS-1 SAR system. Also higher-frequency SAR systems can have less stable backscattering as a result of changes in weather conditions.

3.4 Radar Wavelength and Polarisation in Forest Biomass Mapping

Multi-band polarimetric AIRSAR data were studied in the Freiburg study site (Papers 4 and 5). Table 4 shows the correlation coefficient between backscattering amplitude and the forest stem volume for the August 1989 scene. There were two scenes of August 1989 (1105 and 1107). Only scene 1105 is included in Table 4 because scene 1107 covered the study site only partially. Table 4 was computed using the stand-wise averaged Stokes matrices of all 230 stands of the study site except for those cases where stem volume range was limited to 0–170 m^3/ha. When computed over the whole range of stem volumes (0–830 m^3/ha) the correlation coefficients in C- and L-bands are negative. This is because the radar backscatter *vs.* stem volume relation saturates at fairly low stem volume levels in C- and L-bands as seen in Figure 14, which shows the HV-polarised backscattering amplitude as a function of forest stem volume for all AIRSAR bands. In L-band, the saturation level is somewhere between 120 and 150 m^3/ha. Figure 14 cannot be said to be in disagreement with the saturation values (130 to 157 m^3/ha) reported by Fransson and Israelsson (1999).

Even though the saturation point is somewhere between 120 and 150 m^3/ha, the backscattering amplitude does not drop rapidly after the saturation point. Fairly high linear correlation coefficients can be obtained up to about 170 m^3/ha. When including only those stands where the stem volume is 170 m^3/ha or less, the L-band correlation coefficients turn positive and the magnitude increases to about 0.45. The highest correlation coefficient (0.73) between backscattering amplitude and stem volume was obtained using P-band HV-polarised data.

Estimation RMSE was computed in Paper 4 for those regression models whose correlation coefficient was larger than 0.40. In the L-band analysis of the 0–170 m^3/ha stem volume range, the dataset included only 72 stands. The RMSE was estimated from the same dataset that was used for the development of the regression model. The RMSE values were 41.7, 40.9, and 42.5 m^3/ha for the HV, HH, and VV models, respectively. The 0–830 m^3/ha dataset that was used for the P-band model included 230 stands. This dataset was split in two equally sized subsets, one for model development and one for computing an estimation RMSE. For P-band HV-polarisation data, the estimation RMSE was 141.7 m^3/ha (in a data set where the forest stem volume varied between 0 and 830 m^3/ha).

The correlation coefficients in P-band (0.73, 0.31, and 0.21 in HV-, HH-, and VV-polarisations, respectively) are lower than those obtained by Le Toan *et al.* (1991) in a French study site (R^2 values of 0.95, 0.90, and 0.88). Two reasons have probably contributed to the lower correlations in the Freiburg study site:

1. Species composition: in the French study site, pine is practically the only tree species in evenly-aged stands whereas the forest in the Freiburg study site includes spruce, fir, pine, and some deciduous species. The age distribution within a stand is also wide in the Freiburg study site.

2. The 8-year old forest inventory data in the Freiburg study site may have lowered the correlation coefficients.

Table 4. Correlation coefficient between AIRSAR backscattering amplitude and forest stem volume for C-, L-, and P-bands in various polarisations in the Freiburg study site. The AIRSAR data were acquired in August 1989 (scene 1105). The number of observations (stands) was 230 for the stem volume range 0-830 and 72 for the range 0-170 (Paper 4).

Band and polarisation	Stem volume (m^3/ha)	Correlation coefficient
C-HV	0-830	-0.37
C-HH	0-830	-0.33
C-VV	0-830	-0.06
L-HV	0-830	-0.19
L-HV	0-170	0.47
L-HH	0-170	0.50
L-VV	0-170	0.43
P-HV	0-830	0.73
P-HH	0-830	0.31
P-VV	0-830	0.21

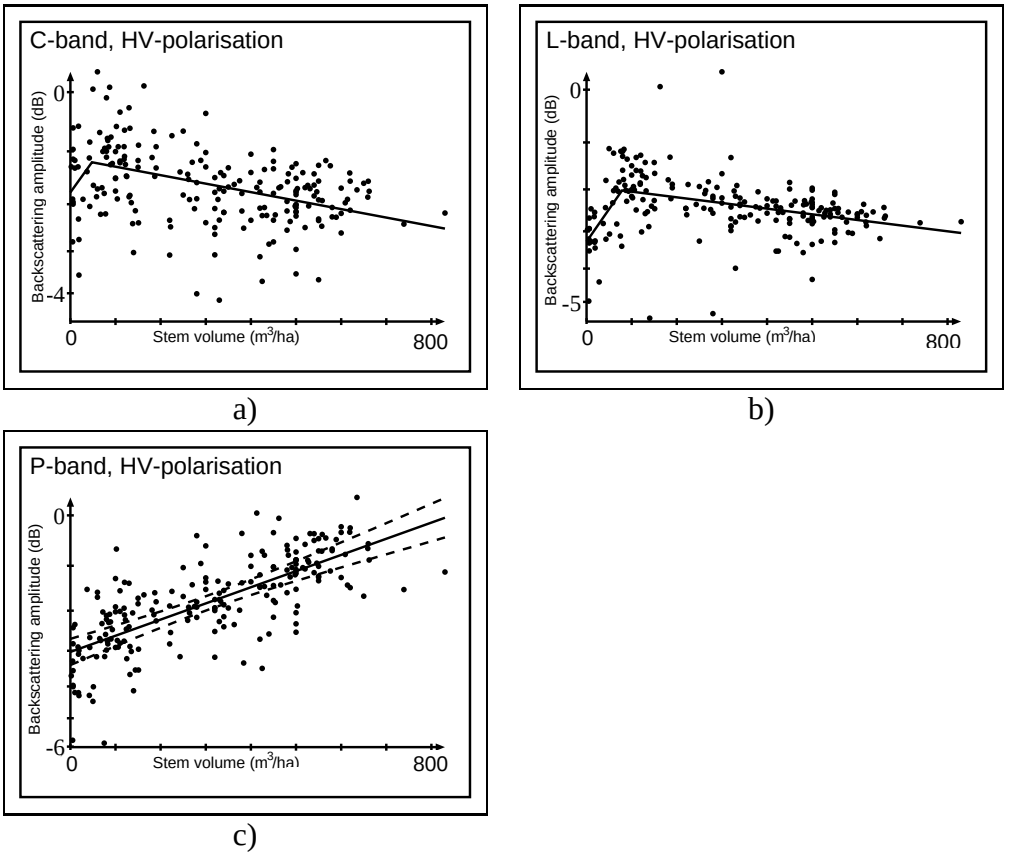

Figure 14. AIRSAR HV-polarised backscattering amplitude as a function of forest stem volume in the Freiburg study site: a) C-band, b) L-band, c) P-band. The 99 percent confidence limits of the regression function are shown as dashed lines for the P-band regression function. The AIRSAR data were acquired in August 1989 (scene 1105, Paper 4).

The search for optimal polarisation for stem volume mapping was conducted separately for each radar band in the 4-dimensional space of polarisation combinations using the search method described in section 2.2.3. The optimal polarisation combination was always at, or close to, the original linear polarisations measured by the radar (HH, HV, VV, VH).

Figure 15 shows the correlation coefficient between the backscattering amplitude and forest stem volume as a function of polarisation combination. Two sub-spaces of the 4-dimensional space of polarisation combinations are shown (in Figure 15): the co-polarised (receive orientation equals transmit orientation, receive ellipticity equals transmit ellipticity) and the cross-polarised (receive orientation is orthogonal to transmit orientation, receive ellipticity is the transmit ellipticity multiplied by -1). In Figure 15 a and b, only those stands were included where stem volume is 170 m^3/ha or lower.

In L-band, the correlation coefficient between backscattering amplitude and stem volume varied very little with the polarisation combination (Figure 15 a and b). In P-band, on the other hand, the correlation has a strong and narrow peak at HV- and VH-polarisations, while the rest of the co-polarisation and cross-polarisation sub-spaces are in the 0.3 to 0.4 range.

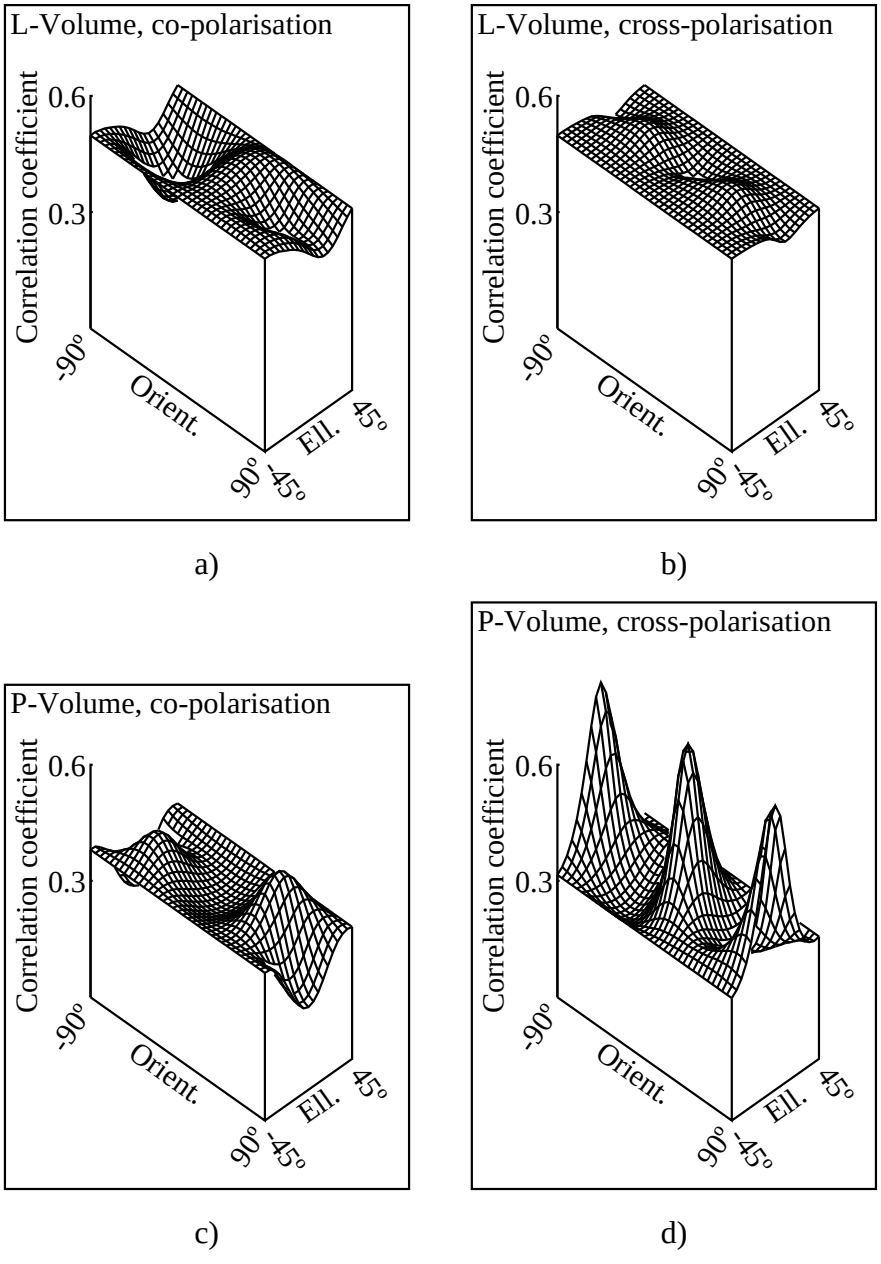

Figure 15. Correlation coefficient between backscattering amplitude and forest stem volume as a function of polarisation combination for AIRSAR data (August 1989, scene 1105) in the Freiburg study site: a) L-band, co-polarisation, b) L-band, cross-polarisation, c) P-band, co-polarisation, and d) P-band, cross-polarisation. In the L-band figures, only those stands were included where stem volume is 170 m^3/ha or lower. Number of observations (stands) was 230 in P-band and 72 in L-band (Paper 4).

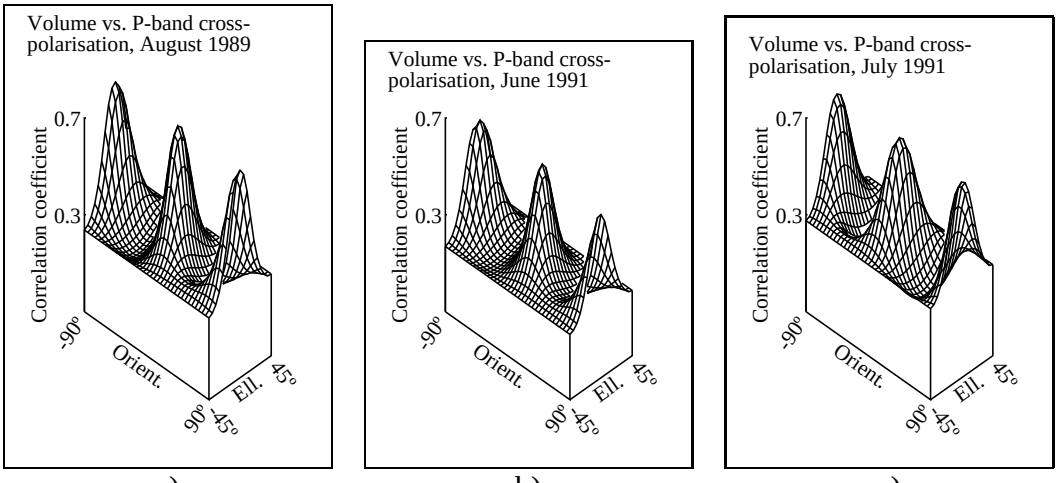

a) b) c)

Figure 16. Correlation coefficient between backscattering amplitude and forest stem volume as a function of polarisation combination for P-band AIRSAR data in the Freiburg study site: a) August 1989 (scene 1105), b) June 1991, and c) July 1991. Only stands of 1 ha or larger were included. The number of observations (stands) was 182, 176, and 179 for August 1989, June 1991, and July 1991, respectively (Paper 5).

The temporal stability of the relation between stem volume and radar backscatter was also studied in the Freiburg study site (Paper 5). Figure 16 (Paper 5) shows the correlation coefficient between the P-band backscattering amplitude and forest stem volume as a function of polarisation combination for three dates:

a) August 1989,

b) June 1991, and

c) July 1991.

All sub-figures of Figure 16 correspond to the same cross-polarised subspace of the 4-dimensional space of polarisation combinations as Figure 15 d). Figure 16 a) was computed from the same data as Figure 15 d), but only stands of 1 ha or larger were included in Figure 16. As can be seen in Figure 16 a) to c), the relation between the stem volume *vs.* backscattering amplitude is fairly constant over time. The corresponding correlation surfaces of C- and L-bands have a lower level of the correlation coefficient and irregular shape. This is in agreement with the observation by Dobson

et al. (1991) that rain shower had the weakest effect on P-band (out of C-, L-, and P-bands).

Table 5 illustrates the development of the correlation coefficients between stem volume and backscattering amplitude for AIRSAR C- and L-band data. As the C-band saturation limit is about 60 m^3/ha and the L-band limit somewhere between 120 and 150 m^3/ha, 100 m^3/ha has been used in Table 5 as compromise between these two values. This choice also allowed the C-band dataset to include more stands than a limit of 60 m^3/ha. Only stands of 1 ha or larger were included in Table 5. The number of such stands varied between 35 and 37. The C-band correlation coefficients varied widely except in VV-polarisation. The L-band correlations were constantly between 0.5 and 0.7.

Table 5. Correlation coefficient between AIRSAR backscattering amplitude and forest stem volume for C- and L-bands in various polarisations in the Freiburg study site in three acquisition times. Only stands of 1 ha or lager with stem volumes 100 m^3/ha or less were included. The number of observations (stands) was between 35 and 37 (Paper 5).

Scene	Band	Correlation coefficient		
		HH	VV	HV
August 1989	C	0.315	0.575	0.215
June 1991	C	0.107	0.631	0.491
July 1991	C	-0.062	0.667	0.386
August 1989	L	0.539	0.674	0.671
June 1991	L	0.635	0.584	0.637
July 1991	L	0.684	0.679	0.699

In addition to the stability of of the relation between stem volume and radar backscatter, the temporal stability of the backscattering was also studied in Paper 5. As the meteorological and soil moisture data were limited, no conclusions could be drawn on the reasons of changes in backscatter between image acquisition times.

In Figure 17, forest stem volume is plotted against the estimated stem volume using AIRSAR P-band HV-polarised data from three dates. The model of the regression function was of the form:

$$V = ax_1 + bx_2 + cx_3 + d\ (+\epsilon\ ) \tag{57}$$

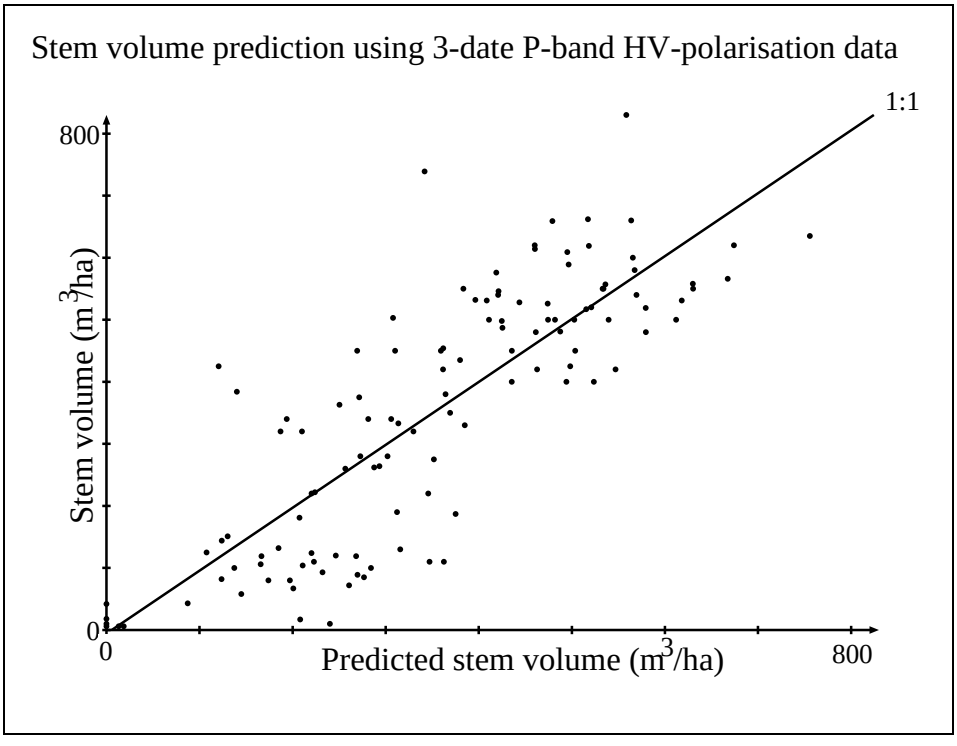

Figure 17. Multi-date regression analysis results for forest stem volume using AIRSAR P-band HV-polarised data in the Freiburg study site. The number of observations (stands) was 120 (Paper 5).

where

V	=	forest stem volume
x_1	=	backscattering amplitude in the August 1989 scene (1105),
x_2	=	backscattering amplitude in the June 1991 scene,
x_2	=	backscattering amplitude in the July 1991 scene,
$a, b, c,$ and d	=	regression coefficients, and
ϵ	=	random error.

The multiple correlation coefficient (the correlation coefficient between the predicted stem volume and the true stem volume) was 0.82, which is higher than any of the single-date correlations (0.79, 0.60, and 0.75). Only stands of 2 ha or larger were included in this multiple regression model (120 observations).

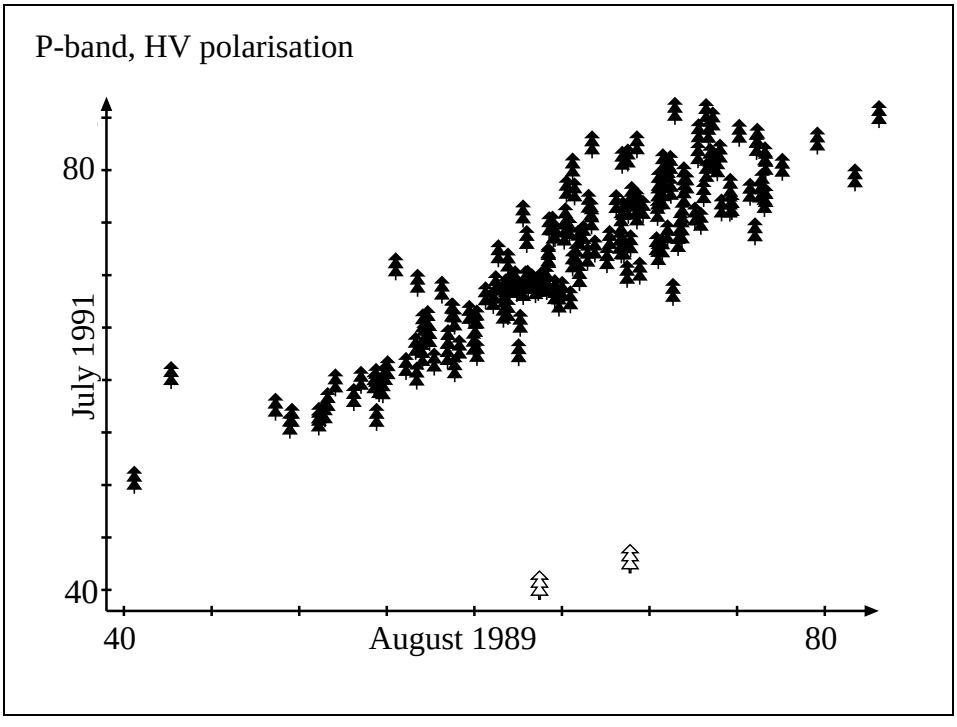

Figure 18. Change detection in the Freiburg study site using stand-wise AIRSAR P-band HV data. Backscattering amplitude of August 1989 (scene 1105) is shown on the horizontal axis and the backscattering amplitude of July 1991 on the vertical axis. The number of observations was 179. The filled symbols are forest stands that were not clear-cut between 1989 and 1991. The two outlined symbols are stands that were clear-cut between August 1989 and July 1991 (Paper 5).

Figure 18 shows a change detection example using AIRSAR P-band HV-polarised data. The figure shows the stand-wise backscattering amplitude of July 1991 plotted against the backscattering amplitude of August 1989. The two stands (open symbols) that have been logged between image acquisitions are clearly separable from other stands.

3.5 Multi-Temporal L-Band Radar Backscatter in Forest Biomass Mapping

Multi-temporal L-band JERS SAR data were studied in the Ruokolahti study site. Table 6 shows single-date regression results for the six SAR scenes that were available (Paper 6). Columns A and B give the slope and intercept of a linear regression model of the form:

$$V = A \cdot r_c + B \ (+ \epsilon \ ) \tag{58}$$

where V is forest stem volume (m^3/ha), r_c is backscattering amplitude corrected for topography (relative to the σ^o calibration factor 68.2 dB, $\sigma^o = 10 \cdot log(r_c^2) - 68.2$ dB, all scenes were scaled to this calibration standard before regression analyses), and ϵ is random error. Column RMSE gives the the root mean square error of the estimated forest stem volume. The RMSE values of Table 6 were computed using the leave-one-out method.

The correlation coefficient is highest (0.63 to 0.81) for the summer scenes. One of the winter scenes (Wet95Jan), had also a correlation coefficient similar to those of the summer scenes. This was a scene acquired in conditions where a layer of moist new snow was present on top of older snow layers, which also were thawed. The other two winter scenes, which were acquired in cold and dry conditions, had low correlations. This is in agreement with the observation by Santoro *et al.* (2004) that frozen conditions were least suitable for forest biomass retrieval.

The level of the summer-time correlation coefficients and the scene Wet95Jan in Table 6 is in agreement with the correlation coefficients of Askne *et al.* (2003) who found the correlation coefficients to be generally of the order of 0.8. The RMSE values of Table 6 are generally lower than the RMSE values of single-date JERS SAR results (69.5–140.1 m^3/ha) in Askne *et al.* (2003) even though the RMSE values in Table 6 have not been corrected for uncertainty of the ground data. The main reason for this is most likely the lower average stem volume in the Ruokolahti study site (100 m^3/ha) compared to that in the Kättböle study site (140 m^3/ha).

Summer Scenes As the summer-time response of L-band backscattering amplitude to forest stem volume is stable from scene to scene, a general L-band model was proposed in Paper 6 for approximative mapping of forest stem volume and biomass. The general function was computed from the three summer scenes combined, leaving out clear-cut areas. The function

Table 6. Correlation coefficients (r) and parameters of linear regression functions (A = slope, B = intercept) between forest stem volume and JERS backscattering amplitude at various times of the year in the Ruokolahti study site. The RMSE was computed using the leave-one-out method. There were 206 observations in all six cases. The regression was significant at 5 % confidence level in all cases except the Dry98Mar. See section 2.1.4 for scene identifiers (Paper 6).

Scene	A	B	r	RMSE (m^3/ha)
S95Jul	0.60	-562	0.81	44.79
S95Sep	0.72	-743	0.70	56.18
S95Oct	0.87	-894	0.63	61.25
Dry93Feb	3.22	-3239	0.40	72.93
Wet95Jan	0.71	-560	0.78	49.22
Dry98Mar	-30.33	26896	-0.05	79.27

was derived from Equation (58):

$$V = 0.65 \cdot r_c - 634 \tag{59}$$

or

$$V = 0.65\sqrt{10^{(\sigma^o+68.2)/10}} - 634 \tag{60}$$

where V is forest stem volume in m^3/ha and r_c is L-band backscattering amplitude (relative to calibration factor 68.2 dB). This function is valid for VV-polarised L-band radar scenes (with a nominal incidence angle of about 39°) that are acquired in summer conditions similar to the conditions of the three scenes used in Paper 6 (i.e., no heavy rain in the weeks preceding radar data acquisition).

In Paper 1, forest stem volume was correlated against L-band Seasat backscattering amplitude that had not been corrected for topography effects. The very low correlation coefficient (0.05) shows that stem volume mapping is not feasible without terrain corrections in a hilly or mountainous area. One reason why forest stem volume estimation was not attempted in Paper 1 after radiometric correction of terrain effects (as done in Paper 6) was the coarse ground data and DEM. Another reason was the poor (Landsat derived) stem volume data in the Arjeplog site.

The summer-time correlations in Table 6 (0.81, 0.70, and 0.63) are slightly higher than the correlations obtained for young stands in the Freiburg study

site using AIRSAR L-band HH-polarised data (0.54, 0.64, and 0.68, Table 5). The reasons for the slight difference can be:

- less accurate ground data in the Freiburg study site (8- or 10-years old inventory in an area where forest growth is fast) than in the Ruokolahti study site (2-year time difference between forest inventory and SAR image acquisition in 1995), and
- a narrower range of stem volumes (restricted to stands with 0 to 100 m^3/ha) in the Freiburg study site than in the Ruokolahti study site (stands with 0 to 364 m^3/ha), which tends to lead to lower correlation coefficients in regression analysis; correlation coefficients in scenes S95Jul, S95Sep, and S95Oct were 0.78, 0.62, and 0.45, respectively, when computing over the 95 stands with stem volume of 100 m^3/ha or less.

Differences in tree species composition, understory, and soil conditions may also have contributed to the differences on correlation coefficients between the Freiburg and Ruokolahti study sites.

Figure 19 shows regression functions and stand-wise observations between backscattering amplitude and forest stem volume for all six scenes. In addition to similar correlation coefficients, the linear regression functions are also similar between all summer scenes.

Winter Scenes In the dry winter scenes (Figure 19), the average backscatter is about 2 dB lower than in the summer scenes. This is in agreement with the well known phenomenon of backscatter drop when the forest canopy freezes. Kwok *et al.* (1994) observed a drop of 3 dB in L-band HH-polarised data when the forest canopy and ground froze. Ranson and Sun (2000) reported a difference of about 2.5 dB between the frozen and thawed state in non-water areas. Santoro *et al.* (2004) found an increase of approximately 4 dB in spring when the forest went from frozen winter conditions to snow-free summer conditions. Santoro *et al.* (2004) mentioned that the calibration error was 1–2 dB.

The dry winter scenes are almost uncorrelated with stem volume. One explanation of this could be that the forest canopy – in areas with average stem volume of about 100 m^3/ha – in a frozen state is almost transparent to L-band radar, and therefore the ground backscattering dominates the radar image.

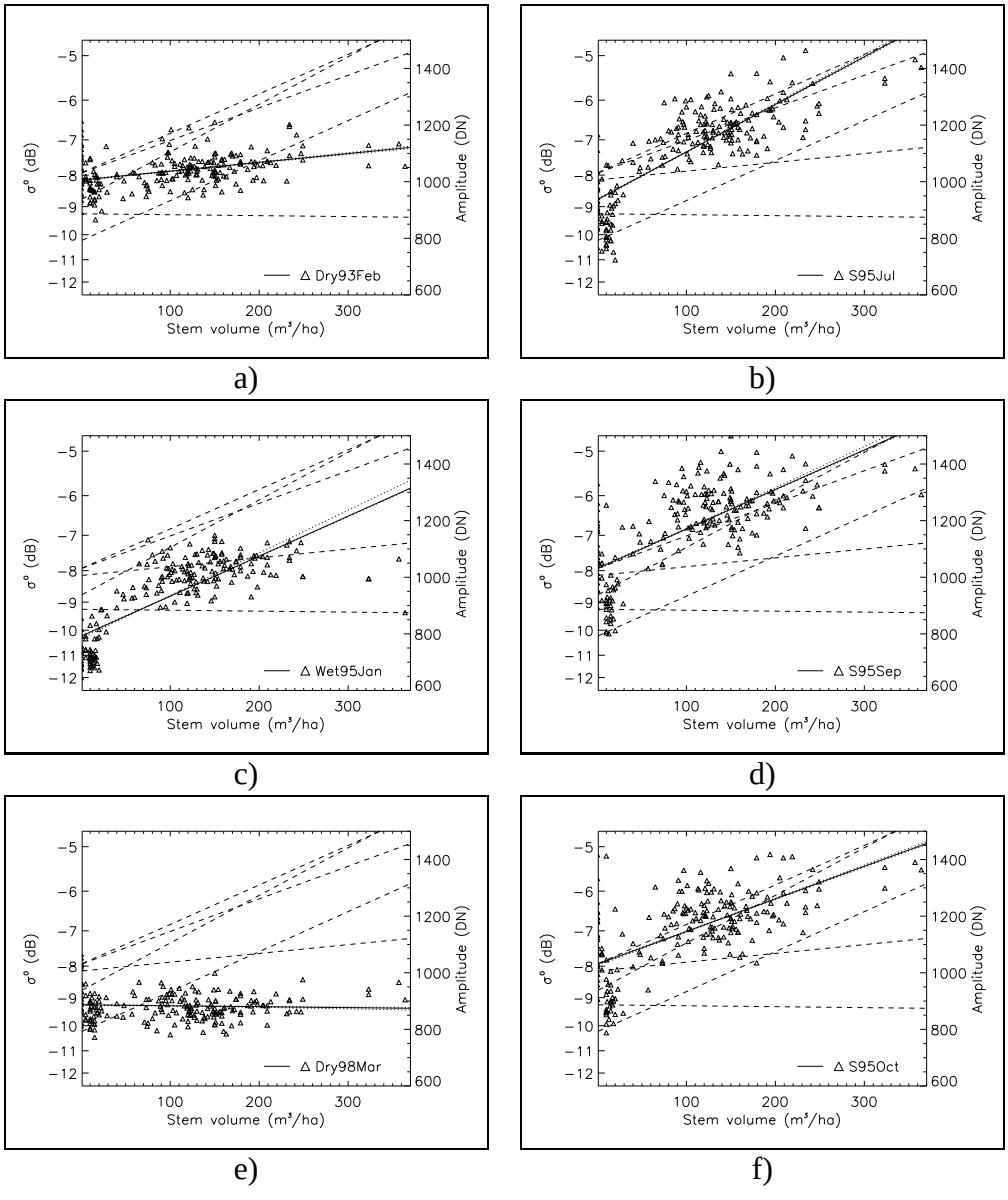

Figure 19. Regression functions between JERS backscattering amplitude and forest stem volume for winter (left) and summer (right) scenes in the Ruokolahti study site. The solid line shows the regression line computed for the observation data in the diagram. The dashed lines show the regression lines for the other five scenes. The dotted lines around the solid line show the variation of the regression function in the leave-one-out testing method (Paper 6).

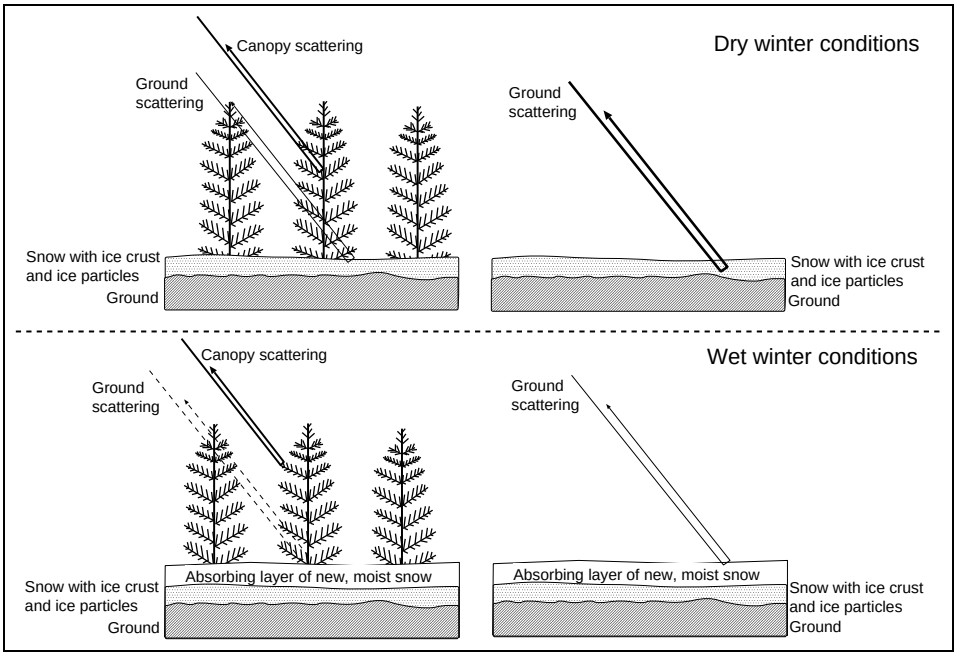

Figure 20. Forest and clear-cut backscatter (schematically) in dry and wet winter conditions (Paper 6).

The wet winter scene Wet95Jan (Figure 19) has a regression function with a similar slope to those of the summer scenes, but the backscatter level is about 2 dB lower than in the summer scenes. This can be an indication that forest canopy and soil included very small amount of liquid water during the acquisition of the scene Wet95Jan, when the temperature had risen to about 0 C in January. The scene Wet95Jan also discriminates well between clear-cut areas and forested areas.

Figure 20 shows a possible explanation for the high correlation coefficient between backscattering amplitude and forest stem volume in wet winter conditions. In dry, frozen winter conditions, the backscatter from the forest canopy is not notably higher than the backscatter from open areas – from the ice particles in the snow pack and from stones and other scattering sources under the snow. If a wet snow layer absorbs the backscatter from ground and lower snow pack, open area backscatter becomes very low. The backscatter from the forest canopy may increase if the liquid water contents of canopy components increases. This increases the correlation coefficient between backscattering amplitude and forest stem volume and also increases the separation between open and forested areas.

Multi-Date Regression Analysis Multiple linear regression analyses (dependent variable forest stem volume, independent variables six JERS SAR scenes) were made in a series varying the stem volume range included in the dataset (Paper 6). Table 7 shows the results of these regression analyses. Column 'R^2' gives the coefficient of variation. Columns '$R^2_{A_1}$' to '$R^2_{A_3}$' give the adjusted R^2 as computed using Equations (54) to (56). Column 'RMSE' gives the root mean square error of the multiple linear regression model as computed by the leave one out method. The column 'RelE' gives the RMSE as a percentage of the width of the forest stem volume range included in the analysis.

Table 7. Multiple regression analysis results as a function of forest stem volume range. The dependent variable was forest stem volume. The independent variables were the six JERS scenes (1 = Dry93Feb, 2 = Wet95Jan, 3 = S95Jul, 4 = S95Sep, 5 = S95Oct, 6 = Dry98Mar). RelE = relative RMSE = RMSE/(Vol$_{max}$ - Vol$_{min}$). S = significant at 5 % risk level, - = not significant (Paper 6).

Vol-Rg	n	R^2	$R^2_{A_1}$ eq 54	$R^2_{A_2}$ eq 55	$R^2_{A_3}$ eq 56	RMSE (m^3/ha)	RelE (%)	1	2	3	4	5	6
0-360	206	0.71	0.70	0.70	0.70	42.8	11.7	S	S	S	-	-	S
50-360	139	0.37	0.34	0.35	0.34	47.2	15.0	S	-	S	-	-	-
100-360	112	0.35	0.31	0.32	0.31	44.8	16.9	S	-	S	-	-	-
150-360	59	0.43	0.37	0.38	0.36	44.6	20.7	-	S	S	-	-	-
200-360	19	0.53	0.33	0.35	0.30	68.8	41.7	-	-	-	-	-	-
0-300	202	0.77	0.76	0.76	0.76	35.2	11.7	S	S	S	-	-	S
0-250	202	0.77	0.76	0.76	0.76	35.2	14.1	S	S	S	-	-	S
0-200	187	0.79	0.78	0.78	0.78	30.1	15.0	-	S	S	-	-	S
0-150	152	0.83	0.82	0.82	0.82	22.9	15.3	-	S	S	-	-	S
0-100	95	0.83	0.82	0.82	0.82	15.5	15.5	-	S	-	-	-	S
0-50	67	0.64	0.61	0.61	0.60	7.6	15.2	-	S	-	-	-	S

In the first set of cases (the upper end of the stem volume range, increasing the lower bound of the range), the coefficient of determination decreases with decreasing range of stem volumes (and decreasing number of stands). The number of significant variables also decreases – the last case with only 19 stands makes the whole regression insignificant at 5 percent significance level. The RMSE increases with decreasing range of stem volumes. Only one (S95Jul) summer scene out of three is significant. This is because sumer scenes are highly correlated among themselves.

In the second set of cases (the lower end of the stem volume range, decreasing the upper bound of the range), the coefficient of determination increases with decreasing range of stem volumes (and decreasing number of stands) until 0–150 or 0–100 m^3/ha. In other words, the highest coefficient of determination (in the lower range of stem volumes) is obtained when including data below the saturation zone only. The RMSE decreases with decreasing range of stem volumes. Also in this set of cases, the scene S95Jul is the only summer scene with a significant contribution to the regression.

A two-piece multi-temporal stem volume estimator was derived from the multiple regression analyses. This estimator is a combination of two multiple linear regression models having three independent variables:

W = backscattering amplitude in the wet winter scene, Wet95Jan,

D = backscattering amplitude in the dry winter scene, Dry98Mar, and

S = average backscattering amplitude in the three summer scenes (S95Jul, S95Sep, and S95Oct).

The two piece-wise estimates are (e_L for the lower stem volume range, e_H for the upper stem volume range):

$$e_L = -118.8 + 0.243 \cdot W - 0.056 \cdot D \tag{61}$$

and

$$e_H = -174.9 + 0.183 \cdot W - 0.239 \cdot D + 0.273 \cdot S. \tag{62}$$

The combined estimate is computed:

$$\begin{aligned} \text{if } e_H > 120: &\quad e = e_H \\ \text{if } e_H < 80: &\quad e = e_L \\ \text{if } e_H \geq 80 \text{ and } e_H \leq 120: &\quad e = \frac{120 - e_H}{40} e_L + \frac{e_H - 80}{40} e_H. \end{aligned} \tag{63}$$

It was decided to split the forest stem volume range at 100 m^3/ha and not at 150 m^3/ha which is closer to the saturation point of L-band backscattering amplitude. This decision, which was based on experimentation, aimed at stronger correlation in the lower stem volume range. The regression coefficients of the upper stem volume range were determined using the whole stem volume range of 0–360 because the function for the upper

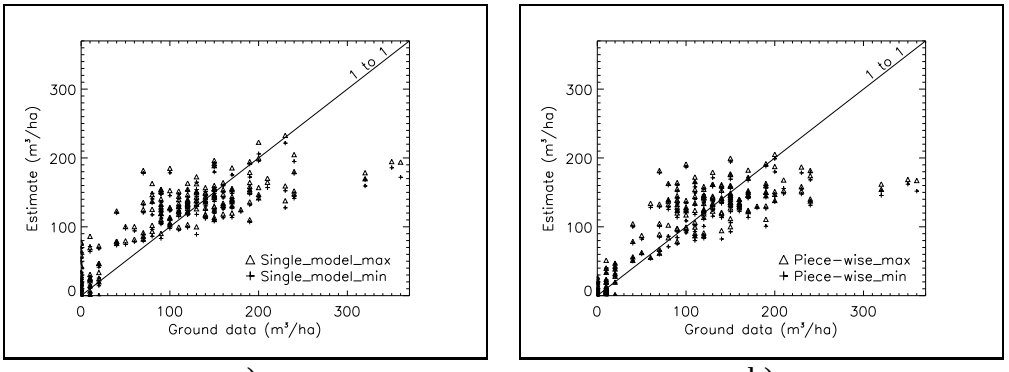

a) b)

Figure 21. Estimated stem volume for multi-date regression models in the Ruokolahti study site. All six JERS SAR scenes were used as independent variables of a linear model in a). The 2-piece model (see section 3.5) was used in b). There were 208 observations in both cases. A triangle marks the maximum estimated stem volume in the leave-one-out method. A plus sign marks the corresponding minimum estimate.

stem volume range was used to select between the pieces of the two-piece estimator. All regression coefficients in Equations (61) and (62) were significant at 5 percent risk level.

Figure 21 shows the estimated *vs.* true forest stem volume for a 6-date linear multiple regression model (a) and the 2-piece model described above. Both models had very similar RMSE figures (41.3 m^3/ha for 6-date linear, 41.6 m^3/ha for the 2-piece model) as estimated by the leave-one-out method. The 2-piece model, which depends more on the wet winter scene, reduces the bias at the lower end of the forest stem volume range. The RMSE value (41.3 m^3/ha) of the six-date estimation is lower than the RMSE obtained by Askne *et al.* (2003) in the Kättböle study site with nine-date JERS backscatter data (36.4 or 59.0 m^3/ha, depending on the selection of training and test datasets) when taking into account that no uncertainty figures for ground data has been subtracted from the RMSE value in the Ruokolahti site. If a similar reduction was made in the RMSE value of the Ruokolahti study site, it would be about on the level (27.2–38.0 m^3/ha) of the RMSE of the model that used three backscatter observations and one coherence observation in Askne *et al.* (2003). The reason for smaller RMSE values in the Ruokolahti study site is most likely the lower mean stem volume in Ruokolahti.

In addition to the two-piece estimator of Equations (61) and (62), another

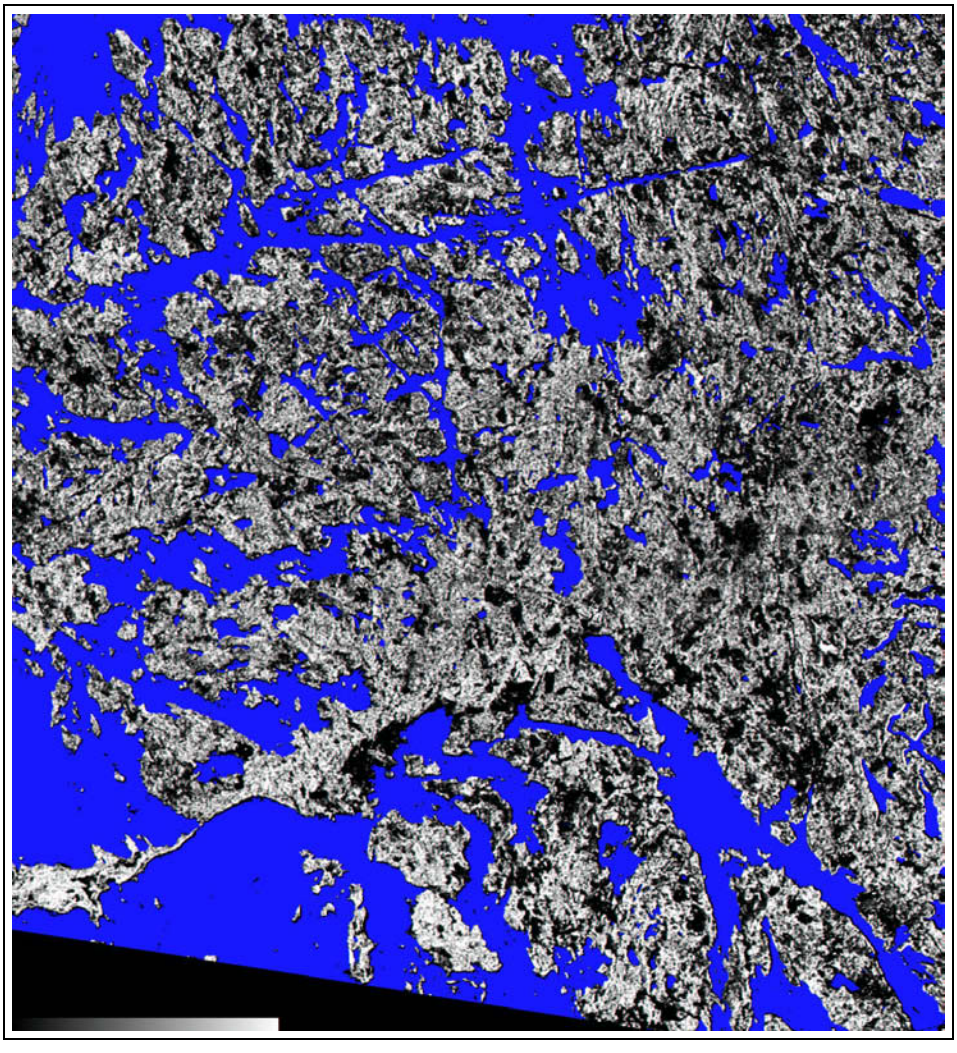

Figure 22. JERS-estimated forest stem volume for a 38 km by 38 km area in the Ruokolahti-Puumala region. Black corresponds to a stem volume of 0 m^3/ha and white to 200 m^3/ha. Compact blue is water. For a colour version, see the front cover of this publication (Paper 6).

estimator was derived using those original scenes (not the averaged summer scene) that produced significant regression coefficients. The upper stem volume range model was determined using only data from the stem volume range of its validity, not over the whole range 0–360 m^3/ha. This estimator produced a better correlation coefficient between the estimated and ground-measured forest stem volume and also a smaller RMSE[2]. This model was abandoned because it produced very poor estimates outside the area of the stands that were used in its derivation.

Figure 22 shows the combined multi-temporal stem volume estimate (two-piece estimate, Equations 61 and 62) computed over an area of 38 km by 38 km around the Ruokolahti study site.

[2]It appears that the RMSE figure of the 2-piece model that was reported in Paper 6 (28.5 m^3/ha) was computed using this model, not the one described by Equations (61) and (62). This was an error in Paper 6.

4 Summary of Papers and Contribution

In Paper 1, the incidence angle effects due to local topography on L-band Seasat SAR data in a forested area were analyzed using a digital elevation model. Topographic effects accounted for over 60 percent of the total variation in the L-band Seasat SAR scene in a hilly and mountainous study site in northern Sweden. The most important topographic factor was the size of the resolution cell, which varies with varying incidence angle components. This was the first study where topographic effects – in the form of the size of a resolution cell – were analysed in quantitative terms in a large study site in boreal forest.

In Paper 2, a methodology for the revision of the geometry of SAR scenes for mosaicking multi-temporal sets of SAR scenes was presented. JERS scenes of the GRFM African mosaic were used as SAR data. Sub-pixel internal consistency of the mosaic was obtained. Absolute geometric accuracy was estimated to be within a few hundred meters. This was the first time that a rigorous least squares adjustment was applied to a multi-temporal SAR mosaic dataset of over 3000 scenes. Error ellipses were used to evaluate the spatial distribution of the uncertainty in scene locations.

In Paper 3, the geometric mosaicking method was described in more detail. A methodology for improving the calibration of SAR scenes when a large number of scenes are mosaicked was also presented. The same set of JERS SAR scenes was used as SAR data as in Paper 2. The calibration artifacts before the calibration revision were about 1 dB or even higher. The calibration revision method produced mosaics that enabled image analysis without scene boundary effects.

In Paper 4, the characteristics of various radar wavelengths and polarisations were analysed in mapping forest biomass. AIRSAR data were used in a German study site. A systematic method was presented to find the optimal combination of transmit and receive polarisations for forest biomass mapping. The method uses stand-wise averaged Stokes matrix data and a polarisation synthesis algorithm. This method maximises the correlation coefficient between forest stem volume and SAR backscattering amplitude. P-band HV-polarisation was the optimal single radar dataset in mapping forest stem volume. In stands with stem volumes less than 170 m^3/ha, L-band also had a strong correlation between stem volume and backscattering amplitude. Paper 4 was the first study where optimal polarisation was systematically analysed – using the correlation

coefficient between forest stem volume and backscattering amplitude – over the whole transmit-receive polarisation space in a dataset of over 200 conifer-dominated forest stands.

Paper 5 extended the wavelength-polarisation analysis of Paper 4 to a multi-temporal AIRSAR dataset. In P-band, the HV-polarisation was the optimal single radar dataset in all three scenes acquired in August 1989, June 1991, and July 1991. The form of the correlation surface (between forest stem volume and backscattering amplitude) in the P-band cross-polarised sub-space was also similar from scene to scene. Also in L-band, the correlation coefficients between forest stem volume and backscattering amplitude were almost constant from scene to scene when the analysis was restricted to stands with stem volumes less than 100 m^3/ha. In C-band, the stem volume correlations varied from scene to scene in HH- and HV-polarisations.

In Paper 6, a multi-temporal JERS SAR dataset was studied in a site in south-eastern Finland. The dataset included three scenes acquired in summer (July to October), two scenes acquired in freezing winter conditions, and one scene in winter conditions with a moist new snow layer on top of old snow. The forest inventory ground data included 206 stands of boreal forest. In the JERS SAR scenes that were acquired in freezing winter conditions the correlation between stem volume and backscattering amplitude was low. The relation between forest stem volume and backscattering amplitude was so similar in summer scenes that one regression model could be proposed for forest stem volume mapping in wide areas if accuracy requirements are not high.

5 Conclusions

An optimal tool – among weather independent microwave sensors – for space-borne forest biomass mapping is a P-band HV-polarised SAR. This is due to its strong relation with forest biomass as shown in Paper 4 and the literature (*e.g.*, Le Toan *et al.* 1991). The P-band relation with forest biomass is also sTable as shown in Paper 5.

In the absence of a space-borne P-band SAR in the foreseeable future, summer-time L-band SAR data can be used for approximate forest biomass mapping in areas where biomass is not very high, *e.g.*, in the northern part of the boreal forest zone. The L-band has a stable relation with forest biomass in areas with fairly low biomass as shown in Papers 5 and 6. This stability of the relation between L-band backscattering amplitude and forest biomass was observed in a dataset that only included SAR scenes acquired in fairly dry conditions. The L-band biomass mapping – using the biomass function derived in Paper 6 – may require that SAR scenes are not degraded by excessive amounts of rain that could decrease the contrast between high and low biomass areas. The results of Conway & Estreguil (1994) and Keil *et al.* (1994) suggests that rain has an impact on the contrast between open and forested areas in C-band SAR data. The relation between L-band backscattering amplitude and forest biomass in rainy SAR scenes was not studied in Paper 6 because the dataset did not include scenes acquired in very rainy conditions.

L-band forest biomass mapping in wide areas requires accurate mosaicking of a large number of SAR scenes. This can be achieved using geometry revision techniques like that described in Paper 2. Application of forest biomass estimation models to a mosaic of SAR data requires good relative calibration from scene to scene. Such calibration can be obtained by calibration revision techniques, for example the technique that was described in Paper 3.

In all forest biomass mapping using SAR backscattering amplitude, the effects of terrain topography must be corrected from the SAR scenes before forest biomass estimation models are used. Terrain topography can account for more than 60 percent of the variation in SAR backscattering amplitude in hilly forested areas as shown in Paper 1.

6 Future Research

The future space-borne SAR systems – especially the Japanese ALOS PALSAR, which operates in L-band – will enhance the potential for wide area forest biomass mapping. The results of Paper 6 suggest that the derived biomass function can be used in forest biomass mapping in wide boreal forest areas with L-band HH-polarised SAR. As these results were verified in a single study site, the biomass function should be validated in a larger set of study sites with wider variation in forest types and forest management practices.

Polarimetric interferometry has been proposed for forest biomass mapping. As this technique requires fully polarimetric data acquisitions, the technique may turn out too demanding in terms of data acquisition and area coverage. In fully polarimetric mode, the SAR sensors of the near future have an image swath width that is only half of the nominal single-polarisation swath. The so called dual-polarisation configuration, which includes simultaneous HH- and HV-polarised data, covers the whole swath of the single-polarisation mode. Therefore, the use of HV-polarisation – alone or in addition to the HH-polarised data – is a central research topic in the coming years.

The forest biomass function derived in Paper 6 is valid in forested areas. Mapping of forest and non-forest land cover types should be made prior to forest biomass mapping to avoid gross errors and mis-interpretation of mapped biomass values. Even though forest area mapping has been studied for a long time reliable discrimination between forest and various non-forest land cover types is challenging in wide areas that include wide variation in climatic and topographic conditions. When forest biomass is mapped in country-wide or continent-wide areas mapping of forest and non-forest land cover types requires research on reliable and accurate methods and on earth observation data that can be used in this task.

A digital elevation model (DEM) was a key element in geometric and radiometric processing of SAR scenes in Papers 1 and 4 through 6. In all these cases, the DEM-based processing was done on single SAR scenes. In wider areas, a mosaicking process hides the growth direction of the range co-ordinate, which is essential for both geometric and radiometric DEM-based processing of SAR scenes. Use of DEMs in geometric and radiometric processing of SAR mosaics requires further research.

References

Ahern, F., Leckie, D., and Drieman, J. 1993. Seasonal changes in relative C-band backscatter of northern forest cover types, *IEEE Transactions on Geoscience and Remote Sensing*, **31(3)**, p. 668–680.

Angelis, C., Freitas, C., Dutra, L., and Valeriano, D. 2001. ERS-1 multitemporal backscatter analysis of different types of land cover in Brazilian Amazonia, Proceedings of the International Geoscience and Remote Sensing Symposium IGARSS 2001, Sydney, Australia, 9–13 July, 2001, IEEE, Piscataway, NJ, USA, Vol. 5, p. 2019–2021.

Askne, J., Santoro, M., Smith, G., and Fransson, J. 2003. Multitemporal repeat-pass SAR interferometry of boreal forests, *IEEE Transactions on Geoscience and Remote Sensing*, **41(7)**, p. 1540–1550.

Askne, J., Smith, G., and Santoro, M. 2004. L-band observations of boreal forest stem volume, Proceedings of the 23rd Symposium of the European Association of Remote Sensing Laboratories, Ghent, Belgium, 2–5 June 2003, Millpress Science Publishers, Rotterdam, the Netherlands, p. 159–165.

Balzter, H., Baker, J., Hallikainen, M., and Tomppo, E. 2002. Retrieval of timber volume and snow water equivalent over a Finnish boreal forest from airborne polarimetric synthetic aperture radar, *International Journal of Remote Sensing*, **23(16)**, p. 3185–3208.

Bayer, T., Winter, R., and Schreier, G. 1991. Terrain influences in SAR backscatter and attempts to their correction, *IEEE Transactions on Geoscience and Remote Sensing*, **29**, p. 451–462.

Castel, T., Beaudoin, A., Stach, N., Stussi, N., Le Toan, T., and Durand, P. 2001. Sensitivity of space-borne SAR data to forest parameters over sloping terrain – Theory and experiment, *International Journal of Remote Sensing*, **22(12)**, p. 2351–2376.

Castel, T., Guerra, F., Caraglio, Y., and Houllier, F. 2000. Retrieval biomass of a large Venezuelan pine plantation using JERS-1 SAR data, Proceedings of the International Geoscience and Remote Sensing Symposium IGARSS 2000, Honolulu, USA, 24–28 July, 2000, IEEE, Piscataway, NJ, USA, Vol. 1, p. 396–398.

Castel, T., Guerra, F., Caraglio, Y., and Houllier, F. 2002. Retrieval biomass of a large Venezuelan pine plantation using JERS-1 SAR data, Analysis of

forest structure on radar signature, *Remote Sensing of Environment*, **79**, p. 30–41.

Churchill, P. and Attema, E. 1991. The European airborne polarimetric SAR campaign MAESTRO 1, Proceedings of the International Geoscience and Remote Sensing Symposium IGARSS'91, Helsinki University of Technology, Espoo, Finland, 3–6 June, 1991, IEEE, Piscataway, NJ, USA, Vol. II, p. 327–328.

Conway, J. and Estreguil, C. 1994. Evaluation of multi-temporal ERS-1 SAR data for tropical forest mapping in Papua New Guinea, Proceedings of the Second ERS-1 Symposium – Space at the Service of our Environment, Hamburg, Germany, 11–14 October, 1993, ESA SP-361 (January 1994), p. 481–484.

Dobson, C., Mc Donald, K., Ulaby, F., and Sharik, T. 1991. Relating the temporal change observed by AIRSAR to surface and canopy properties of mixed conifer and hardwood forests of Northern Michigan, Proceedings of the 3rd Airborne Synthetic Aperture Radar (AIRSAR) Workshop, May 23–24, 1991, JPL Publication 91–30, p. 34–43.

Drieman, J. 1987. Evaluation of SIR-B imagery for monitoring forest depletion and regeneration in western Alberta, *Canadian Journal of Remote Sensing*, **13(1)**, p. 19–25.

ESA 1988. ERS-1 – A keen eye on the earth, ESA F12, 2nd edition, European Space Agency, the Netherlands, August 1988, 6 p.

Foody, G. 1986. An assessment of the topographic effects on SAR image tone, *Canadian Journal of Remote Sensing*, **12(1)**, p. 124–131.

Fransson, J. and Israelsson, H. 1999. Estimation of stem volume in boreal forests using ERS-1 C- and JERS-1 L-band SAR data, *International Journal of Remote Sensing*, **20(1)**, p. 123–137.

Fransson, J., Walter, F., and Ulander, L. 2000. Estimation of forest parameters using CARABAS-II VHF SAR data, *IEEE Transactions on Geoscience and Remote Sensing*, **38**, p. 720–727.

Goering, D., Chen, H., Hinzman, L., and Kane, D. 1995. Removal of terrain effects from SAR satellite imagery of arctic tundra, *IEEE Transactions on Geoscience and Remote Sensing*, **33**, p. 185–193.

Goyal, S., Seyfried, M., and O'Neill, P. 1999. Correction of surface roughness and topographic effects on airborne SAR in mountainous rangeland areas, *Remote Sensing of Environment*, **67**, p. 124–136.

Haara, A. and Korhonen, K.T. 2004. Kuvioittaisen arvioinnin luotettavuus (Reliability of stand-wise forest inventory data, in Finnish), *Metsätieteen aikakauskirja*, publ. Metsäntutkimuslaitos and Suomen Metsätieteellinen Seura, 4/2004, p. 489–508.

Haggrén, H. and Honkavaara, E. 2004. Luento 10: Topografinen peruskartoitus, 'http://ns.foto.hut.fi/opetus/220/luennot/10/L10_2004.pdf', checked 21 October 2005.

Harrell, P., Bourgeau-Chavez, L., Kasischke, E., French, N., and Christensen, N. 1995. Sensitivity of ERS-1 and JERS-1 radar data to biomass and stand structure in Alaskan Boreal forest, *Remote Sensing of Environment*, **54**, p. 247–260.

Held, D., Brown, W., Freeman, A., Klein, J., Zebker, H., Sato, T., Miller, T., Nguyen, Q., and Lou, Y. 1988. The NASA/JPL multifrequency, multipolarization airborne SAR system, Proceedings of the International Geoscience and Remote Sensing Symposium IGARSS'88, 12–16 September, Edinburgh, Scotland, UK, IEEE, Piscataway, NJ, USA, p. 345–350.

Hinse, M., Gwyn, Q., and Bonn, F. 1988. Radiometric correction of C-band imagery for topographic effects in regions of moderate relief, *IEEE Transactions on Geoscience and Remote Sensing*, **26**, p. 122–132.

Hirvonen, R. 1965. Tasoituslasku. Teknillisten tieteiden Akatemia, Helsinki, Finland, 240 p.

Hoekman, D. and Quinones, M. 1998. Land cover type and biomass classifications using AirSAR data for evaluation of monitoring scenarios in the Colombian Amazon, Proceedings of the 2nd International Workshop on Retrieval of Bio- and Geophysical Parameters from SAR Data for Land Applications, 21–23 October, 1998, ESTEC, Noordwijk, The Netherlands, 'www.estec.esa.nl/conferences/ 98c07/review_open/papers/99mb04.pdf', checked 12 May 2005, 9 p.

Hoekman, D. and Quinones, M. 2000. Land cover type and biomass classifications using AirSAR data for evaluation of monitoring scenarios in the Colombian Amazon, *IEEE Transactions on Geoscience and Remote Sensing*, **38**, p. 685–696.

Hussin, Y., Reich, R., and Hoffer, R. 1991. Estimating slash pine biomass using radar backscatter, *IEEE Transactions on Geoscience and Remote Sensing*, **29(3)**, p. 427–431.

Hutton, C., Adair, M., Forest, C., and Parashar, S. 2000. Radarsat-1 mo-

saic of Canada, Proceedings of the 22nd Canadian Symposium on Remote Sensing, Victoria, B.C., Canada, 21–25 August, 2000, National Resources Canada, 7 p.

Häme, T., Salli, A., and Lahti, K. 1992. Estimation of carbon storage in boreal forest using remote sensing data, Pilot study, in: The Finnish programme on climate change, Progress report, edited by M. Kanninen and P. Anttila, Publications of the Academy of Finland 3/92, Helsinki, Finland, p. 250–255.

Häme, T., Salli, A., Andersson, K., and Lohi, A. 1997. A new methodology for the estimation of biomass of conifer-dominated boreal forest using NOAA AVHRR data, *International Journal of Remote Sensing*, **18(15)**, p. 3211–3243.

Häme, T., Sirro, L., Rauste, Y., Ahola, H., van Brusselen, J., Schuck, A., Wegmüller, U., Wiesmann, A., and Hippi, I. 2003. Treaty enforcement services using earth observation (TESEO) theme carbon – Main results, Proceedings of the International Geoscience and Remote Sensing Symposium IGARSS 2003, Toulouse, France, 21–25 July, 2003, IEEE, Piscataway, NJ, USA, Vol. III, p. 1480–1482.

Israelsson, H., Ulander, L., Askne, J., Fransson, J., Frölind, P., Gustavsson, A., and Hellsten, H. 1997. Retrieval of forest stem volume using VHF SAR, *IEEE Transactions on Geoscience and Remote Sensing*, **35**, p. 36–40.

Jensen, A., 2005. Adjusted R_square, California State University, Sacramento, College of Business Administration, 1 p., "http://www.csus.edu/indiv/j/jensena/mgmt105/adjustr2.htm", checked 14.10.2005.

JRC 1990. MAESTRO 1, Airborne synthetic aperture radar (SAR) campaign 1989, Data report, Report number IRSA/MWT/1.90, version 2.0, June, 1990, Commission of the European Communities, Joint Research Centre, Ispra, Italy, 210 p.

Kauppi, P., Tomppo, E., and Ferm, A. 1995. C and N storage in living trees within Finland since 1950s, *Plant and Soil*, **168–169**, p. 633–638.

Keil, M, Winter, R., and Hönsch, H. 1994. Tropical rainforest investigation in Brazil using ERS-1 SAR data, Proceedings of the Second ERS-1 Symposium – Space at the Service of our Environment, Hamburg, Germany, 11–14 October, 1993, ESA SP-361 (January 1994), p. 481–484.

Kellndorfer, J. and Ulaby, F. 2003. Forest biomass inversion from SAR

using object oriented image analysis techniques, Proceedings of the International Geoscience and Remote Sensing Symposium IGARSS 2003, Toulouse, France, 21–25 July, 2003, IEEE, Piscataway, NJ, USA, Vol. 6, p. 3465–3467.

Koskinen, J., Pulliainen, J., Hyyppä, J., Engdahl, M., and Hallikainen, M. 2001. The seasonal behavior of interferometric coherence in boreal forest, *IEEE Transactions on Geoscience and Remote Sensing*, **39**, p. 820–828.

Kuplich, T. and Curran, P. 1999. Temporal analysis of JERS-1/SAR images over regenerating forests in Brazilian Amazonia, Proceedings of the International Geoscience and Remote Sensing Symposium IGARSS'99, Hamburg, Germany, 28 June – 2 July, 1999, IEEE, Piscataway, NJ, Vol. 4, p. 1895–1897.

Kuntz, S., Siegert, F., and Rücker, G. 1999. ERS SAR images for tropical rainforest and land use monitoring: change detection over five years and comparison with Radarsat and JERS SAR images, Proceedings of the International Geoscience and Remote Sensing Symposium IGARSS'99, Hamburg, Germany, 28 June – 2 July, 1999, IEEE, Piscataway, NJ, Vol. 2, p. 910–912.

Kwok, R., Rignot, E., Way, J., Freeman, A., and Holt, J. 1994. Polarization signatures of frozen and thawed forests of varying environmental state, *IEEE Transactions on Geoscience and Remote Sensing*, **32**, p. 371–381.

Leberl, F. 1975. Sequential and simultaneous SLAR block adjustment, *Photogrammetria*, **31**, p. 39–51.

Leclerc, G., Beaulieu, N., and Bonn, F. 2001. A simple method to account for topography in the radiometric correction of radar imagery, *International Journal of Remote Sensing*, **22(17)**, p. 3553–3570.

Lecomte, P. and Attema, E. 1992. Calibration and validation of the ERS-1 wind scatterometer, Proceedings of the First ERS-1 Symposium – Space at the Service of our Environment, Cannes, France, 4–6 November, 1992, European Space Agency, Paris, p. 19–29.

Lewis, J., Schnapf, A., Diesen, B., Martin, P., Schwalb, A., and Bandeen, W. 1983. Meteorological satellites, in Manual of remote sensing, Volume I, eds. Simonett, D. and Ulaby, F., American Society of Photogrammetry, Falls Church, Virginia, USA, p. 651–679.

Louet, J. 2001. The Envisat mission and system, *ESA bulletin* 106, June 2001, http://www.esa.int/esapub/bulletin/bullet106/bul106_1.pdf, checked 3.5.2005, p. 14–25.

Luckman, A., Baker, J., Kuplich, T., Yanasse, C., and Frery, A. 1997. A study of the relationship between radar backscatter and regenerating tropical forest biomass for spaceborne SAR instruments, *Remote Sensing of Environment*, **60(1)**, 1–13.

Menges, C., van Zyl, J., Hill, G., and Ahmad, W. 2001. A procedure for the correction of the effect of variation in incidence angle in AIRSAR data. *International Journal of Remote Sensing*, **22(5)**, p. 829–841.

Moore, R., Chastant, L., Porcello, L., and Stevenson, J. 1983. Imaging radar systems, in Manual of remote sensing, Volume I, eds. Simonett, D. and Ulaby, F., American Society of Photogrammetry, Falls Church, Virginia, USA, p. 429–474.

Morain, S. and Simonett, D. 1967. K-band radar in vegetation mapping, *Photogrammetric Engineering*, **33**, p. 730–740.

NASDA 1988. Earth Resource Satellite-1, National Space Development Agency of Japan, Tokyo, Japan, 1988, 4 p.

NOAA 2005. World Vector Shoreline, 'http://rimmer.ngdc.noaa.gov/mgg/coast/wvs.html', checked 26 April 2005.

Noltimier, K., Jezek, K., Sohn, H., Li, B., Liu, H., Baumgartner, F., Kaupp, V., Curlander, J., Wilson, B., and Onstott, R. 1999. Radarsat Antarctic mapping project – Mosaic construction, Proceedings of the International Geoscience and Remote Sensing Symposium IGARSS'99, Hamburg, Germany, 28 June – 2 1999, IEEE, Piscataway, NJ, USA, Vol. 5, p. 2349–2351.

Pierce, L., Liang, P., Dobson, C., Kellndorfer, J., Barros, O., dos Santos, J., and Soares, J. 2003. Regrowth biomass estimation in the Amazon using JERS-1/Radarsat SAR composites, Proceedings of the International Geoscience and Remote Sensing Symposium IGARSS 2003, Toulouse, France, 21–25 July, 2003, IEEE, Piscataway, NJ, USA, Vol. 3, p. 1933–1935.

Pravdo, S., Huneycutt, B., Holt, B., and Held, D. 1983. Seasat synthetic-aperture radar data user's manual, JPL Publication 82-90, Jet Propulsion Laboratory, California Institute of Technology, Pasadena California, 1 March, 1983, 113 p.

Press, W., Teukolsky, S., Vetterling, W., and Flannery, B. 1992. Numerical recipes in C: The art of scientific computing, Cambridge University Press, Cambridge, U.K., 2nd edition, p. 83–85.

Pulliainen, J., Kurvonen, L., and Hallikainen, M. 1999. Multitemporal behaviour of L- and C-band SAR observations of boreal forest, *IEEE Transactions on Geoscience and Remote Sensing*, **37**, p. 927–937.

Pulliainen, J., Engdahl, M., and Hallikainen, M. 2003. Feasibility of multitemporal interferometric SAR data for stand-level estimation of forest stem volume, *Remote Sensing of Environment*, **85**, p. 397–409.

Quegan, S., Le Toan, T., Yu, J., Ribbes, F., and Floury, N. 2000. Multitemporal ERS SAR analysis applied to forest mapping, *IEEE Transactions on Geoscience and Remote Sensing*, **38(2)**, p. 741–753.

Ranson, K. and Sun, G. 1994. Mapping biomass of a northern forest using multifrequency SAR data, *IEEE Transactions on Geoscience and Remote Sensing*, **32(2)**, p. 388–396.

Ranson, K., Saatchi, S., and Sun, G. 1995. Boreal forest ecosystem characterization with SIR-C/XSAR, *IEEE Transactions on Geoscience and Remote Sensing*, **33(4)**, p. 867–876.

Ranson, K. and Sun, G. 2000. Effects of environmental conditions on boreal forest classification and biomass estimates with SAR, *IEEE Transactions on Geoscience and Remote Sensing*, **38**, p. 1242–1252.

Rauste, Y. 1988. Rectification of spaceborne SAR images using polynomial rectification and a digital elevation model, *Photogrammetric Journal of Finland*, **11**, p. 53–67.

Rauste, Y. 1991. Results of measurements on forest geometric parameters of the Freiburg site 12–18 June 1991, VTT, Espoo, unpublished project report, 9 p.

Richards, J., Sun, G., and Simonett, D. 1987. L-band radar backscatter modeling of forest stands, *IEEE Transactions on Geoscience and Remote Sensing*, **25(4)**, p. 487–498.

Rignot, E. and van Zyl, J. 1993. Change detection techniques for ERS-1 SAR data, *IEEE Transactions on Geoscience and Remote Sensing*, **31(4)**, p. 896–906.

Rosaz, J., Maitre, H., and Rudant, J. 1994. Mosaicking ERS-1 images: Difficulties, solutions and results on the French Guyana, Proceedings of the Second ERS-1 Symposium – Space at the Service of our Environment, Hamburg, Germany, 11–14 October, 1993, ESA SP-361 (January 1994), p. 1221–1226.

Rosenqvist, A. 1996. The global rain forest mapping project by JERS-1 SAR, International Archives of Photogrammetry and Remote Sensing, ISPRS, Vienna, Austria, Vol. 31, Part B7, p. 594–598.

Rosenqvist, A., Shimada, M., Chapman, B., Freeman, A., De Grandi, G., Saatchi, S., and Rauste, Y. 2000. The Global Rain Forest Mapping project – a review, *International Journal of Remote Sensing*, **21(6&7)**, p. 1375–1387.

Rosenqvist, A., Shimada, M., Chapman, B., McDonald, K., De Grandi, G., Jonsson, H., Williams, C., Rauste, Y., Nilsson, M., Sango, D., and Matsumoto, M., 2004. An overview of the JERS-1 SAR Global Boreal Forest Mapping (GBFM) project, Proceedings of IGARSS 2004, Anchorage, Alaska, USA, Sept. 20–24, 2004, p. 1033–1036.

Rosisch, B. and Meadows, P. 2004, Absolute calibration of ASAR level 1 products generated with PF-ASAR, Technical Note, European Space Agency, ESA/ESRIN, Frascati, Italia, 23 January, 2004, 23 p.

Rudner, L., Glass, G., Evartt, D., and Emery, P. 2002. A user's guide to the meta-analysis of research studies, ERIC Clearinghouse on Assessment and Evaluation, University of Maryland, College Park, chapter 9, 7 p. "http://www.erdres.org/meta/chap9/chap9.htm", checked 14.10.2005.

Saatchi, S. and Moghaddam, M. 2000. Estimation of crown and stem water content and biomass of boreal forest using polarimetric SAR imagery, *IEEE Transactions on Geoscience and Remote Sensing*, **38**, p. 697–709.

Sader, S. 1987. Forest biomass, canopy structure, and species composition relationships with multipolarization L-band synthetic aperture radar, *Photogrammetric Engineering and Remote Sensing*, **53(2)**, p. 193–202.

Sader, S., Waide, R., Lawrence, W., and Joyce, A. 1989. Tropical forest biomass and successional age class relationships to a vegetation index derived from Landsat TM data, *Remote Sensing of Environment*, **28**, p. 143–156.

Santoro, M., Eriksson, L., Schmullius, C., and Wiesmann, A. 2004. Seasonal and topographic effects on growing stock volume estimates from JERS-1 backscatter in Siberian forests, Proceedings of the 23rd Symposium of the European Association of Remote Sensing Laboratories, Ghent, Belgium, 2–5 June 2003, Millpress Science Publishers, Rotterdam, the Netherlands, p. 151–158.

Santos, J., Araujo, L., Freitas, C., Sant'Anna, S., Dutra, L., Mura, J., Gama,

F., and Hernandez Filho, P. 2001. Inventory of forest biomass in Brazilian Amazon: A local approach using airborne P-band SAR data, Proceedings of the International Geoscience and Remote Sensing Symposium IGARSS 2001, Sydney, Australia, 9–13 July, 2001, IEEE, Piscataway, NJ, USA, Vol. 2, p. 786–788.

Santos, J., Pardi Lacruz, M., Araujo, L., and Keil, M. 2002. Savanna and tropical rainforest biomass estimation and spatialization using JERS-1 data, *International Journal of Remote Sensing*, **23(7)**, p. 1217–1229.

Santos, J., Freitas, C., Araujo, L., Dutra, L., Mura, J., Gama, F., Soler, L., and Sant'Anna, S. 2003. Airborne P-band SAR applied to the above ground biomass studies in the Brazilian tropical rainforest, *Remote Sensing of Environment*, **87**, p. 482–493.

Shimada, M. 1996. Radiometric and geometric calibration of JERS-1 SAR, *Advances in Space Research*, **17(1)**, p. 79–98.

Shimada, M. 2001. User's guide to NASDA's SAR products ver. 2, NASDA, Tokyo, Japan, 9 August, 2001, 23 p.

Shimada, M. and Isoguchi, O. 2002. JERS-1 SAR mosaic of Southeast Asia using calibrated path images, *International Journal of Remote Sensing*, **23(7)**, p. 1507–1526.

Shimada, M., Tadono, T., and Matsuoka, M. 2002a. Calibration and validation of PALSAR, Proceedings of the International Geoscience and Remote Sensing Symposium IGARSS 2002, Toronto, Canada, 24–28 June, 2002, IEEE, Piscataway, NJ, USA, Vol. 1, p. 384–386.

Shimada, M., Tadono, T., Rosenqvist, A., and Shakil, A. 2002b. Incidence angle dependence of the L-band Pol-In-SAR sensitivity at forestry region – Alos PALSAR study using the Pi-SAR, Proceedings of the International Geoscience and Remote Sensing Symposium IGARSS 2002, Toronto, Canada, 24–28 June, 2002, IEEE, Piscataway, NJ, USA, Vol. 1, p. 632–634.

Shimada, M., Rosenqvist, A., Watanabe, M., and Tadono, T. 2005. The polarimetric and interferometric potential of ALOS PALSAR, Proceedings of POLinSAR 2005, 17–21 January 2005,

'earth.esa.int/workshops/polinsar2005/ participants/213/paper_Polarimetric_paper_S271587.pdf', checked 3.5.2005, 6 p.

Simard, M., de Grandi, G., Thompson, K., and Bennie, G. 1998. Analysis of speckle noise contribution on wavelet decomposition of SAR images,

IEEE Transactions on Geoscience and Remote Sensing, **36**, p. 1953–1962.

Siqueira, P., Hensley, S., Shaffer, S., Hess, L., McGarragh, G., Chapman, B., and Freeman, A. 2000. A continental-scale mosaic of the Amazon basin using JERS-1 SAR, *IEEE Transactions on Geoscience and Remote Sensing*, **38**, p. 2638–2643.

Small, D., Jehle, M., Meier, E., and Nüesh, D. 2004a. Radiometric terrain correction incorporating local antenna gain, Proceedings of EUSAR 2004, Ulm, Germany, 25–27 May, 2004, VDE Verlag, Frankfurt am Main, Germany, p. 929–932.

Small, D., Meier, E., and Nüesch, D. 2004b. Robust radiometric terrain correction for SAR image comparisons, Proceedings of the International Geoscience and Remote Sensing Symposium IGARSS 2004, Anchorage, Alaska, USA, 20–24 September, 2004, IEEE, Piscataway, NJ, USA, p. 1730–1733.

Smith, G. and Ulander, L. 1998. Forest biomass retrieval using VHF SAR. Retrieval of Bio- and Geophysical Parameters from SAR data for Land Applications, Symposium held in ESTEC Noordwijk, 21–23 October 1998, 'www.estec.esa.nl/conferences/98c07/papers/P027.PDF', checked on 13 May 2005, p. 301–307.

Smith, G. and Ulander, L. 2000. A model relating VHF-band backscatter to stem volume of coniferous boreal forest, *IEEE Transactions on Geoscience and Remote Sensing*, **38**, p. 728–740.

Sun, G. and Simonett, D. 1988. A composite L-band HH radar backscattering model for coniferous forest stands, *Photogrammetric Engineering and Remote Sensing*, **54**, p. 1195–1201.

Sun, G., Ranson, K., and Kharuk, V. 2000. Forest biomass estimation in Western Sayani mountains, Siberia from SAR, Proceedings of the International Geoscience and Remote Sensing Symposium IGARSS 2000, Honolulu, USA, 24–28 July, 2000, IEEE, Piscataway, NJ, USA, Vol. 1, p. 435–437.

Sun, G., Ranson, K., and Kharuk, V. 2002. Radiometric slope correction for forest biomass estimation from SAR data in the Western Sayani mountains, Siberia, *Remote Sensing of Environment*, **79**, p. 279–287.

Teillet, P., Guindon, B., Meunier, J., and Goodenough, D. 1985. Slope-aspect effects in synthetic aperture radar imagery, *Canadian Journal of Remote Sensing*, **11**, p. 39–49.

Le Toan, Beaudoin, A., Riom, J., and Guyon, D. 1991. Relating forest parameters to SAR data, Proceedings of the International Geoscience and Remote Sensing Symposium IGARSS'91, Helsinki University of Technology, Espoo, Finland, 3–6 June, 1991, IEEE, Piscataway, NJ, USA, Vol. 2, p. 689–692.

Tomppo, E. 1986. Stand delineation and estimation of stand variates by means of satellite images, Proceedings of the Seminars on Remote Sensing-Aided Forest Inventory, Hyytiälä, Finland, 10–12 December, 1986, Helsingin Yliopiston Metsänarvioimistieteen laitoksen tiedonantoja No. 19 (Research Notes No. 19, University of Helsinki, Department of Forest Mensuration and Management), p. 59–76.

Tsolomon, R., Tateishi, R., and Tetuko, J. 2002. A method to estimate forest biomass and its application to monitor Mongolian taiga using JERS-1 SAR data, *International Journal of Remote Sensing*, **22(22)**, p. 4971–4978.

Ulaby, F., Moore, R., and Fung, A. 1982. Microwave remote sensing, active and passive, Vol. II, Radar remote sensing and surface scattering and emission theory, (Addison Wesley Publishing Company, Reading, Massachusetts, USA), p. 457–1064.

Ulander, L. 1996. Radiometric slope correction of synthetic-aperture radar images, *IEEE Transactions on Geoscience and Remote Sensing*, **34**, p. 1115–1122.

Ulander, L. Askne, J., Fransson, J., Gustavsson, A., Le Toan, T., Manninen, T., Martinez, J-M. Melon, P., Smith, G., and Walter, F. 2000. Retrieval of stem volume in coniferous forest from low VHF-band SAR, Proceedings of the International Geoscience and Remote Sensing Symposium IGARSS 2000, Honolulu, USA, 24–28 July, 2000, IEEE, Piscataway, NJ, USA, Vol. 1, p. 441–443.

Villasenor, J., Fatland, D., and Hinzman, L. 1993. Change detection on Alaska's north slope using repeat-pass ERS-1 SAR images, *IEEE Transactions on Geoscience and Remote Sensing*, **31(1)**, p. 227–236.

Wagner, W., Luckman, Vietmeier, J., Tansey, K., Balzter, H., Schmullius, C., Davidson, M., Gaveau, D., Gluck, M., Le Toan, T., Quegan, S., Shvidenko, A., Wiesmann, A., and Yu, J. 2003. Large-scale mapping of boreal forest in SIBERIA using ERS tandem coherence and JERS backscatter data, *Remote Sensing of Environment*, **85**, p. 125–144.

Williamson, M. 1990. Radar in space, *Space*, **6**, p. 26–32.

Wulder, M. 2005, Correlation coefficient and coefficient of variation, Natural Resources of Canada, Canadian Forest Service, 1 p., "http://www.pfc.forestry.ca/profiles/wulder/mvstats/correl_coef_e.html", checked 14.10.2005.

Zebker, H. and Lou, Y. 1990. Phase calibration of imaging radar polarimeter Stokes matrices, *IEEE Transactions on Geoscience and Remote Sensing*, **28**, p. 246–252.

van Zyl, J., Zebker, H., and Elachi, C. 1987. Imaging radar polarisation signatures: Theory and observation, *Radio Science*, **22**, p. 529–543.

van Zyl, J. 1990. Calibration of polarimetric radar images using only image parameters and trihedral corner reflector responses, *IEEE Transactions on Geoscience and Remote Sensing*, **28**, p. 337–348.

PAPER 1

Incidence-angle dependence in forested and non-forested areas in Seasat SAR data

In: International Journal of Remote Sensing 1990.
Vol. 11, No. 7, pp. 1267–1276.
Reprinted with permission from the publisher.

INT. J. REMOTE SENSING, 1990, VOL. 11, NO. 7, 1267–1276

Incidence-angle dependence in forested and non-forested areas in Seasat SAR data

YRJÖ RAUSTE

Technical Research Centre of Finland, Itatuulentie 2 A,
SF-02100 Espoo, Finland

Abstract. A major part of the variation in a Seasat SAR scene originates from terrain topography. Quantitative evaluation of the topography-induced variation was carried out. Differences in the slope of backscatter curve (sensitivity of radar to changes in incidence angle) between spruce-dominated mixed forests, pine-dominated mixed forests, deciduous forests and regenerated (pine plantations) areas were determined. Contribution of the corner reflector backscatter mechanism (a radar pulse is reflected from ground and tree trunks back to radar) to the total backscatter was evaluated.

Results of the analysis showed that:

65 per cent of the total variation in land pixels can be attributed to terrain topography;

Differences in the slope of backscatter curve were found to be significant (at 0·05 significance level) between spruce-dominated mixed forests, pine-dominated mixed forests, deciduous forests, and regenerated (pine plantations) areas;

The corner reflector backscatter mechanism does not constitute a significant part in the backscatter in the test site, where the ground surface (till) is relatively rough in terms of the radar wavelength.

1. Introduction

The application of microwave remote-sensing techniques in forestry applications has been studied for more than two decades (Morain and Simonett 1967, Sieber 1985, Teillet *et al.* 1985, Hoekman 1985, Hirosawa *et al.* 1987, Mougin *et al.* 1987, Westman and Paris 1987). Although the dominance of topographic effects has been identified as a limiting factor in the interpretation of synthetic-aperture radar (SAR) images of forests (Drieman 1987), only a few attempts have been made to evaluate the topography-induced variation in SAR images in quantitative terms (Foody 1986).

The spectral signature of an object can be defined as the reflectance of the object as a function of wavelength. By analogy, the angular (radar) signature of an object is defined as the backscattering coefficient of the object as a function of incidence angle. The incidence angle is defined as the angle between the surface normal and the direction of illumination by radar. Different forest types have different angular radar signatures due to different canopy structures and different surface roughness. Scattering from thick forest canopies is dominated by diffuse scattering, so the backscattering coefficient depends only slightly on incidence angle. In clear-cut areas, the specular scattering also contributes to the total backscatter. As a consequence, the backscattering coefficient drops with increasing incidence angle and so the slope of the backscatter curve is steeper. If a classification algorithm makes use of a known incidence angle, computed from an existing digital elevation model (DEM), it is essential to know at which incidence angle the backscatter curves cross each other.

Corner reflector backscattering or soil–trunk reflection occurs when a radar pulse is reflected by the soil surface to tree trunks and from trunks back to radar or *vice*

versa. The combination of soil surface and tree trunk, which are at right angles to each other, functions as a corner reflector. Corner reflector backscattering may in some cases be the dominant backscattering contribution (Ulaby *et al.* 1982, Richards *et al.* 1987, Sun and Simonett 1988 a,b).

The objectives of this study are to assess the impact of strong topographic effects on classification algorithms, to study differences in angular signatures of various types of forest cover, and to assess the significance of corner-reflector scattering. The ultimate goal of the study is to develop a computer-based interpretation algorithm making explicit use of known terrain topography.

2. Test site and data

The area covered by the digital elevation model and SAR data consists of mixed forests (mainly pine dominated), pine and spruce plantations, clear-cut areas, marshes and bodies of water. The tree-stem volume of forest varies typically between zero and about $100\,m^3\,ha^{-1}$ (not measured). In this area, spruce-dominated mixed forest usually has the densest canopy and the largest stem volume per hectare. Pine-dominated forest has the second largest stem volume per hectare and deciduous forest has the smallest. The height of the tallest trees varies typically between 10 and 15 m. The lower end of the crown in the tallest pine trees is usually four or five metres above ground. There are very few houses in the test site. Agricultural fields are present in only one spot in the area. Soil is predominantly till with some boulders. The diameter of these boulders seldom exceeds 50 cm. The terrain elevation varies between 420 and 780 m above mean sea level.

The SAR image data consists of a Seasat scene acquired on 20 August 1978. The wavelength of the Seasat SAR is 23 cm (L-band). The image, centred at 66·0°N, 17·3°E, covers an area of about 42 km by 40 km near the village of Arjepolog in Northern Sweden (figure 1). The image has a resolution of 25 m with four looks. In the SAR processing (processing of the raw SAR signal to an image, done by FOA 3 in Linköping, Sweden) a pixel size of approximately 16 m (in ground range) was used. The Landsat thematic mapper image, used as a reference, is quadrant number 2 (north-east) of scene 197-14 acquired on 25 June 1986.

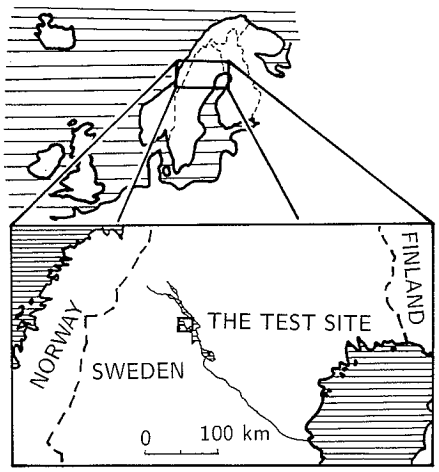

Figure 1. Location of the test site in northern Sweden.

The digital elevation model was generated by digitizing contours of a Swedish 1:100 000 topographic map. The digital elevation model covers an area of about 19 km (north) by 21 km (east) with a cell size of 25 m. The digital elevation model was generated by the Institute for Image Processing and Computer Graphics, Graz Research Centre, Graz, Austria. The SAR image was geocoded using the digital elevation model and a polynomial rectification method (Rauste 1988 a).

3. Methods of analysis

3.1. *Quantitative analysis of topographic effects in SAR data*

Linear regression was used to quantify the topographic effects on backscatter. In these analyses, the digital number in the SAR image was the dependent variable. The form of regression function is the sum of independent variables (each multiplied by its regression coefficient) and a constant term. A set of independent variables was computed for each pixel: simulated SAR image; stem volume per hectare; area of resolution cell; slope angle; and aspect angle.

The simulated SAR image was computed using a digital elevation model. A reference backscatter curve was generated by modelling the backscattering coefficient of land pixels with a second-degree polynomial of the incidence angle (Rauste 1988 b). This modelling was done by dividing each digital number of the Seasat SAR image by the area of the resolution cell and then generating a two-dimensional histogram (or scatter plot) of the backscattering coefficient against the incidence angle. In the simulation stage, the reference backscatter curve was used to assign an output value based on the pixel's incidence angle. This value was then multiplied by the area of the resolution cell.

The noise floor was subtracted from the SAR data before the modelling and simulation. Estimation of the noise floor was based on the darkest water areas in the image. Analysis of the digital elevation model showed that there were no radar shadows in the SAR image.

Stem volume per hectare was estimated using Landsat thematic mapper data and a regression model developed by Tomppo (1986). The regression model was developed for forests in northern Finland using an extensive forest inventory data set. The histograms of the thematic mapper image were normalized to match those of the image for which the regression model was developed. The standard deviation of the regression model is $17{\cdot}8\ m^3\ ha^{-1}$. The accuracy of the model for the test site is poorer than for the original scene, but the spatial variation of the estimated stem volume seemed to fit the real situation as checked visually on site.

The area of the resolution cell, slope angle and aspect angle (figure 2 (*a*)) were computed using the digital elevation model. The slope angle is defined as the angle between the plane of the surface element and a horizontal plane. The aspect angle is defined as the angle between the vertical plane containing the sensor and the centre of the surface element and the vertical plane in the direction of steepest slope of the surface element. The aspect angle is measured clockwise.

Speckle reduction was applied to SAR data prior to regression analysis. In the rectification of the SAR data, a weight function was used in which the weight fades to zero at six (input) pixels from the centre of the output pixel. Then pixel spacing of the image was reduced to 75 m by averaging over a window of 3×3 pixels.

The coefficient of determination (Robinson 1981) was used as a measure of the topographic effects. The coefficient of determination is defined as the variance

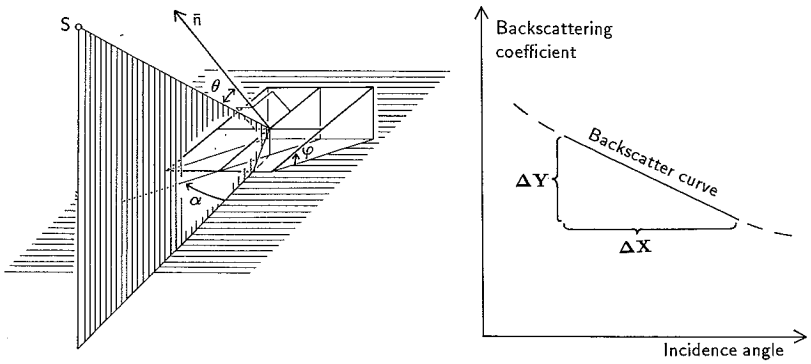

Figure 2. Definition of angles. Incidence angle θ, slope angle φ, aspect angle α, and the slope of the backscatter curve $\Delta y/\Delta x$.

accounted for by the linear regression model divided by the total variance of the dependent variable.

3.2. *Analysis of differences in incidence-angle dependence between forested and non-forested areas*

A two-dimensional histogram (scatter plot of the backscattering coefficient against the incidence angle) was generated for the following forest cover classes: spruce-dominated mixed forest; pine-dominated mixed forest; deciduous forest; and regenerated area.

A two-dimensional histogram (for all forest classes combined) is shown in figure 4. The classes were obtained by maximum likelihood classification of Landsat thematic mapper data. Border pixels (pixels adjacent to water or other non-forested areas) were excluded from the classification result. Starting with the two-dimensional histograms, a linear regression analysis was carried out using all the observations within the selected range of incidence angles (from 20° to 30°). Differences in the slopes of the regression lines (figure 2(*b*)) were tested using the test statistic (Hines and Montgomery 1980, p. 289)

$$t=\frac{x_1-x_2}{\left(\frac{s_1^2}{n_1}+\frac{s_2^2}{n_2}\right)^{1/2}} \tag{1}$$

where x_1 is the slope of the backscatter curve of the first forest cover class, x_2 is the slope of the backscatter curve of the second forest cover class, s_1 is the standard deviation of x_1, s_2 is the standard deviation of x_2, n_1 is the number of observations in the first forest cover class, and n_2 is the number of observations in the second forest cover class.

In the generation of the two-dimensional histograms, each pixel value was divided by the square root (amplitude image) of the area of the resolution cell. Therefore, the ordinate of the histograms is proportional to the square root of the backscattering coefficient. The abscissa is proportional to the cosine of incidence angle.

3.3. *Evaluation of the corner-reflector effect in forests.*

The backscattering from sparse forest canopies can be expressed as a sum of three components: direct backscattering from the vegetation; direct scattering from the soil; and multiply-reflected forward scattering involving both the soil and the vegetation (Ulaby *et al.* 1982, p. 865). The third component is strongest when tree trunks are at right angles to the ground surface (i.e. in flat areas).

It is assumed that the magnitude of this component drops rapidly when the angle between the tree trunks and the ground deviates from a right angle. Under this assumption, the backscattering coefficient of a uniform forest should be much higher for flat areas than for slopes. To test the presence of the corner-reflector effect, a simple experiment was carried out. The data was divided into two groups:

(*a*) flat pixels, where the surface normal deviated from the local vertical by less than 2°; and
(*b*) slope pixels, where the surface normal deviated from the local vertical more than 2°, but less than 5°.

The average slope was 1·2° in the flat group and 3·4° in the non-flat group. If it is assumed that this difference could cause a drop of 6 dB in the corner-reflector component and if this component dominated the backscatter, the expected backscatter (in an amplitude image) in the non-flat group should be about half that of the backscatter of the flat group.

Average backscattering coefficient and its standard deviation were computed for the flat and non-flat group. The difference in backscattering coefficients was tested using the test statistic (1). This test was carried out separately for spruce-dominated mixed forest, pine-dominated mixed forest, deciduous forest, and all forests combined.

4. Results

4.1. *Topographic effects in Seasat SAR data*

The number of observations (pixels) in the regression analyses was 23 446. Six cases were analysed. The independent variables in these analyses were simulated SAR data and stem volume, simulated SAR data only, stem volume only, area of resolution cell and stem volume, area of resolution cell only, and slope and aspect angles.

The results are shown in table 1. The correlation is significant in all six cases. The

Table 1. Regression analysis: SAR versus topography (=simulated SAR) and stem volume.

	Coefficient of determination (in per cent)	Correlation coefficient	F-ratio
Topography + Stem volume	65·4	0·808	22 121
Topography only	63·1	0·795	40 155
Stem volume only	0·3	0·052	64·3
Pixel area + Stem volume	62·4	0·790	19 469
Pixel area only	60·8	0·780	36 430
Slope + aspect	3·4	0·185	408

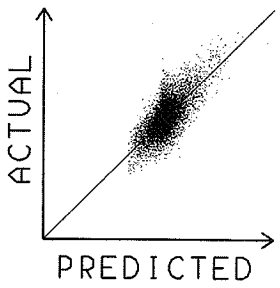

Figure 3. Residual errors of the regression: SAR digital number versus simulated SAR (topography) and stem volume.

aspect angle was the only single variable that did not contribute significantly to the correlation (the computed *t*-statistic was 0·09 while the critical value at 0·05 significance level is 2·0).

Figure 3 shows the residual errors when actual SAR data is regressed against simulated SAR data (topography) and stem volume. As can be seen, there is no need for higher-order polynomials in the regression.

The terrain topography is clearly the greatest constituent in the total variation of the SAR data. The stem volume alone, which is approximately proportional to the total biomass of the forest, could explain only 0·3 per cent of the total variance. Though the correlation was statistically significant using a sample of 23 446 observations, the correlation coefficient was very low. On the other hand, taking into account the stem volume improved the coefficient of determination by 2·3 percentage points (from 63·1 to 65·4) when used in conjunction with terrain topography. Thus, if the topography is not accounted for, it masks out most of the forest-canopy-induced variation in backscatter.

The residuals of the second regression (SAR data against the simulated SAR) were displayed in image form. Because the residual pattern is rather random, and because it does not conform to vegetation changes in the TM classification, it is probable that at least a part of the residual variance is due to small-scale topography, which is not depicted in the contour lines of a 1:100 000 topographic map. Therefore, the value of 63·1 per cent should be considered as a lower bound of the topographic effects (in an area like the test site).

The area of the resolution cell can explain almost as large a part (60·8 per cent) of the total variance as the simulated SAR (63·1 per cent). Because variation in the area

Table 2. Slope of the regression line: SAR versus incidence angle for various land-cover types.

Land cover	Slope	Standard deviation of slope
Spruce-dominated	−0·19	0·03
Pine-dominated	−0·27	0·02
Deciduous	−0·34	0·02
Clear-cut	−0·35	0·02

Table 3. Test of separation of the slopes of regression lines: t statistic for pairwise tests.

	Spruce	Pine	Deciduous
Pine-dominated	86		
Deciduous	153	148	
Clear-cut	167	195	32

of a resolution cell depends only on the imaging geometry, and not on the wavelength, this variation will be present also in the data from the future ERS-1 satellite. However, the proportion of the total variance explained by the area of the resolution cell will be smaller due to increased vegetation-related variation in the C-band.

4.2. *Differences in incidence-angle dependence between forested and non-forested areas*

The slope of the linear regression line was used as a measure of the incidence-angle dependence of radar backscatter. The slopes of the regression lines (the square root of the backscattering coefficient as a linear function of the cosine of the incidence angle) are shown in table 2. Results from the tests of separation of the slopes are shown in table 3. A scatter plot with regression lines is shown in figure 4.

All differences between the slopes of regression lines are significant since the critical value for the t-statistic at 0·05 significance level is 1·96. The incidence-angle dependence is weakest in spruce-dominated mixed forests, which have the oldest trees and densest canopy. The incidence-angle dependence is strongest in clear-cut and regenerated areas where the canopy contribution to backscatter is minimal. The forest canopy has a relatively uniform backscatter level relative to ground backscatter, which depends strongly on incidence angle.

The separation of regression lines in figure 4 increases with increasing incidence angle. This is probably due to the fact that in the L-band, at low incidence angles, most of the backscatter comes from ground (Hoekman 1987) and only at higher incidence angles does the forest canopy contribute significantly to the backscatter. At low incidence angles, the relatively uniform ground component in each forest-cover class masks out the small differences in backscatter originating from the canopy.

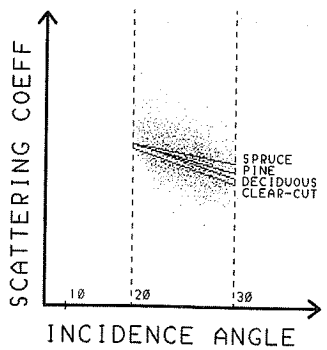

Figure 4. Regression lines adjusted to SAR versus incidence-angle data for spruce-dominated mixed forest, pine-dominated mixed forest, deciduous forest, and regenerated area.

Table 4. Average backscattering for flat and non-flat pixels. Arbitrary units, proportional to the square root of the backscattering coefficient.

	Flat	Non-flat
Spruce-dominated	104	107
Pine-dominated	102	107
Deciduous	105	105
Forests combined	104	106

4.3. *The corner-reflector effect in forests*

Table 4 shows average backscattering coefficients for flat (deviation from horizontal less than 2°) and non-flat (deviation from horizontal more than 2° but less than 5°) pixels for the following land-cover classes: spruce-dominated mixed forest, pine-dominated mixed forest, deciduous forest, and forest in general. Only pixels with incidence angle between 22·5° and 27° were included in the computation, to reduce the effect of incidence-angle change.

Because the average backscattering coefficient for flat pixels is always smaller than that for non-flat pixels, the corner-reflector effect seems not to dominate the backscattering from forest in the test site.

The average values of backscatter in table 4 are not directly comparable due to differences in the amount of stem volume per hectare (table 5). Table 6 shows the regression coefficient for stem volume for flat and non-flat pixels. The correlation (radar backscatter as a linear function of stem volume and terrain topography) was not significant for spruce-dominated flat areas. The regression coefficients are higher for non-flat areas (i.e. the dependence of radar backscatter on stem volume is higher on hill slopes than in flat areas). This phenomenon would be difficult to explain if the corner-reflector mechanism were the dominant component of backscatter in flat areas.

5. Discussion

The dependence of backscatter on terrain topography was high. The amount of variance accounted for by topography was 63·1 per cent. This is much higher than that determined by Foody (1986) for the airborne SAR-580 data, namely 5–25 per cent (with one exception of almost 50 per cent). The main reason for this difference is the difference in the method of analysis. The independent variables used by Foody

Table 5. Stem volume for flat and non-flat pixels ($m^3\,ha^{-1}$)

	Flat		Non-flat	
	Average	Standard deviation	Average	Standard deviation
Spruce-dominated	142	62	176	60
Pine-dominated	106	52	120	42
Deciduous	110	38	132	50
Forests combined	110	22	132	50

Table 6. Regression coefficient for stem volume for flat and non-flat pixels.

	Flat	Non-flat
Spruce-dominated	(0·044)	0·044
Pine-dominated	−0·039	0·058
Deciduous	0·060	0·109
Forests combined	0·020	0·087

(1986) were slope angle and aspect angle, which explained only 3 per cent of the total variance in the current study. If the main factor affecting radar backscatter is the area of resolution cell (60·8 per cent of the total variance), a linear combination of slope and aspect angles cannot be expected to explain the total variance well.

Sun and Simonett (1988 b) note that, at higher incidence angles, the volume scattering term tends to become dominant. Because this term is almost the same for many stands, it follows that discrimination between different forest stands is correspondingly reduced (at higher incidence angles). However, analysis of the incidence-angle dependence of forest-cover type showed that the separation between forest canopy types increases with increasing incidence angle. This was also confirmed using separability tests (Rauste 1988 b). The different behaviour of the discrimination capability as a function of the incidence angle comes from the fact that the trunk–ground term was insignificant in the test site of the current study and, consequently, it could not improve the discrimination capability at low incidence angles. Use of the increased discrimination power due to the tree–ground term at lower incidence angles in applications is complicated because variation in soils and small-scale topography affect this term strongly.

It was shown that the corner-reflector mechanism (or tree–ground term) does not contribute significantly to the backscatter in the test site. Richards *et al.* (1987) and Sun and Simonett (1988 a,b) proved that this term is the dominant contributor to the backscatter. The main reason for this difference is probably the ground surface. In the test site of this study, the prevalent soil is till (glacial drift) with stones and boulders of up to 50 cm diameter. This surface is rather rough, even in L-band wavelengths (23 cm). The underlying surfaces studied by Sun and Simonett (1988 a,b) were very level. Other factors decreasing the trunk–ground term in this study were low tree height and the branched canopy.

Acknowledgments

The study reported in this paper is part of the project SLARSAR funded mainly by the Technical Research Centre of Finland as a part of the research programme of space technology. In its earlier stages, the project has received support from the Academy of Finland and Nesté Ltd.

References

DRIEMAN, J. A., 1987, Evaluation of SIR-B imagery for monitoring forest depletion and regeneration in western Alberta. *Canadian Journal of Remote Sensing*, **13**, 19–25.

FOODY, G. M., 1986, An assessment of the topographic effects on SAR image tone. *Canadian Journal of Remote Sensing*, **12**, 124–132.

HINES, W. W., and MONTGOMERY, D. C., 1980, *Probability and Statistics in Engineering and Management Sciences*, 2nd edn (New York: John Wiley).

HIROSAWA, H., MATSUZAKA, Y., DAITO, M., and NAKAMURA, H., 1987, Measurement of backscatter from conifers in the C and X bands. *International Journal of Remote Sensing,* **8,** 1687–1694.

HOEKMAN, D. H., 1985, Radar backscattering of forest stands. *International Journal of Remote Sensing,* **6,** 325–343.

HOEKMAN, D. H., 1987, Multiband-scatterometer data analysis of forests. *International Journal of Remote Sensing,* **8,** 1695–1707.

MORAIN, S. A., and SIMONETT, D. S., 1967, K-band radar in vegetation mapping. *Photogrammetric Engineering,* **33,** 730–740.

MOUGIN, E., LE TOAN, T., LOPES, A., BORDERIES, P., and SARREMEJEAN, A., 1987, Backscattering measurements at X-band on young coniferous trees. *Proceedings of IGARSS'87 Symposium, held in Ann Arbor, Michigan, on 18–21 May 1987,* edited by M. C. Dobson (New York: I.E.E.E.) pp. 287–292.

RAUSTE, Y., 1988 a, Rectification of spaceborne SAR images using polynomial rectification and a digital elevation model. *Photogrammetric Journal of Finland,* **11,** 53–67.

RAUSTE, Y., 1988 b. DEM-based image processing methods for SAR images. *International Archives of Photogrammetry and Remote Sensing,* **27,** Part B3, Commission III, 696–705.

RICHARDS, J., SUN, G., and SIMONETT, D. S., 1987, L-band radar backscatter modeling of forest stands. *I.E.E.E. Transactions on Geoscience and Remote Sensing,* **25,** 487–498.

ROBINSON, E. A., 1981, *Least Squares Regression Analysis in Terms of Linear Algebra* (Houston, Texas: Goose Pond Press).

SIEBER, A. J., 1985, Forest signatures in imaging and non-imaging microwave scatterometer data. *E.S.A. Journal,* **9,** 431–448.

SUN, G., and SIMONETT, D. S., 1988 a, Simulation of L-band and HH microwave backscattering from coniferous forest stands. A comparison with SIR-B data. *International Journal of Remote Sensing,* **9,** 907–925.

SUN, G., and SIMONETT, D. S., 1988 b, A composite L-band HH radar backscattering model for coniferous forest stands. *Photogrammetric Engineering and Remote Sensing,* **54,** 1195–1201.

TEILLET, P. M., GUINDON, B., MEUNIER, J.-F., and GOODENOUGH, D. G., 1985, Slope-aspect effects in synthetic aperture radar imagery. *Canadian Journal of Remote Sensing,* **11,** 39–49.

TOMPPO, E., 1986, Stand delineation and estimation of stand variates by means of satellite images. *Proceedings of the Seminars on Remote Sensing-aided Forest Inventory held in Hyytiälä, Finland, on 10–12 December 1986. Helsingin Yliopiston metsänarvioimistieteen laitoksen tiedonantoja* No 19 (Research Notes No. 19) (Helsinki: University of Helsinki, Department of Forest Mensuration and Management), pp. 59–76.

ULABY, F. T., MOORE, R. K., and FUNG, A. K., 1982, *Microwave Remote Sensing, Active and Passive,* Vol. II (Reading, Massachusetts: Addison Wesley).

WESTMAN, W. E., and PARIS, J. F., 1987, Detecting forest structure and biomass with C-band multipolarization radar: physical model and field tests. *Remote Sensing of Environment,* **22,** 249–269.

PAPER 2

Compilation of a bi-temporal JERS SAR mosaic over the African rain forest belt in the GRFM project

In: Proceedings of IGARSS'99, Hamburg, Germany, 28 June – 2 July, 1999. IEEE 1999. Pp. 750–752.

COMPILATION OF A BI-TEMPORAL JERS SAR MOSAIC OVER THE AFRICAN RAIN FOREST BELT IN THE GRFM PROJECT

Y. Rauste (1), G.F. De Grandi (1), T. Richards (1), A. Rosenqvist (1), G. Perna (1), E. Franchino (1), F. Holecz (2), P. Pasquali (2)
(1) European Commission Joint Research Centre - Space Applications Institute - 21020 Ispra (VA) Italy
Tel.: +39 332 789823 Fax: +39 332 789073 Email: frank.de-grandi@jrc.it
(2) SARMAP 6981 Banco, TI, Switzerland, sarmap@bluewin.ch.

ABSTRACT

The Global Rain Forest Mapping project GRFM is an international collaborative effort promoted by the National Space Development Agency of Japan NASDA. Main goal of the project is to produce a wall to wall map of the entire tropical rain forest using the L-band SAR on board the JERS-1 spacecraft. Within the GRFM project the European Commission Joint Research Centre acts as main processing node for the assemblage and validation of the radar mosaics related to the African continent. In this paper we give an overview of the techniques used for the compilation of these wide area radar mosaics, with emphasis on the scene geo-referencing. A global optimization technique is used based on a least squares estimation of the scene geometry parameters given observations which comprise intra-scenes correlation measures, ground control points and nominal scene position derived by orbital parameters and the range-doppler equation. Two acquisitions at different dates are simultaneously included in the estimation process, thus assuring optimal co-registration between dates. A similar technique is used for radiometric calibration of the mosaic. Validation of the multi-temporal radar map's geometry with respect to existing cartographic data - a key issue in view of certain thematic applications - is also discussed. A RMSE (Residual Mean Squared Error) of 56 m was obtained when using tie-points between scenes only. This error characterizes the mosaic internal consistency for scenes down-sampled to a pixel spacing of 100 m. A RMSE of 240 m was obtained when using ground control points (GCP) derived from digital cartographic data. This figure characterizes the absolute geo-location accuracy of the GRFM Africa mosaics.

INTRODUCTION

The Global Rain Forest Mapping project (GRFM) [1][2] Africa data sets consists of two blanket coverages of the Central Africa tropical region $10°S-10°N\ \ 8°E-36°W$,acquired during January-March and October -November 1996. A one date continuous coverage of an area in West Africa between $14°E-8°W$ and the island of Madagascar are also included. The overall data set comprises approximately 4000 scenes acquired by the NASDA JERS-1 L-band synthetic aperture radar (SAR). The SAR raw data were correlated into ground range detected images by the NASDA EORC centre in Japan; processing at the JRC entailed a multi-resolution (from 100 m to 1.6 Km) decomposition using wavelets into radiometry and texture maps, and the generation of wide area mosaics with good radiometric and geometric accuracy. This challenging job required the set up of suitable techniques and processing chains, a full description of which is given in [3]. Given the scope of this short communication, we will focus here on the geo-referencing aspects of the mosaicking procedure.

MULTI TEMPORAL BLOCK ADJUSTMENT

Internal geometric consistency and between dates co-registration of the mosaics for the multi-temporal analysis require that the location accuracy of individual scenes is better than the pixel dimension (100 m). The standard deviation of the scene geo-location data was estimated to be several hundreds of meters. Discontinuities of up to 600 m were detected in early mosaicking experiments without geometric corrections. Methods for revising the geo-location data had therefore to be applied in the mosaic compilation.

A global optimization technique was developed based on a linear least squares estimation (LLS) [4] of the scene geometry parameters given observations which comprise intra-scenes correlation measures, ground control points and nominal scene position derived by orbital parameters and the range-doppler equation.

The two acquisitions at different dates are simultaneously included in the estimation process, thus assuring optimal co-registration between dates.

The scene geometry model used in the LLS includes two translations and a rotation in a Northing Easting (Mercator) coordinate system with origin at the scene centre. This model relies on the - confirmed - assumptions that there is no internal deformation in the JERS products. For observations based on tie-points between scenes this model gives for instance:

$$V_{N^p} = N_1^p - N_2^p = N_1^c + dN_1^c - \left(N_2^c + dN_2^c \right) + y_1 \cos(\alpha_1) \qquad (1)$$
$$-y_2 \cos(\alpha_2) - x_1 \sin(\alpha_1) + x_2 \sin(\alpha_2)$$

0-7803-5207-6/99/$10.00 © 1999 IEEE.

where N^P is the Northing of point P; x, y are the image coordinates; N^C is the Northing of the scene centre; dN^C is the translation in Northing of the scene. A similar equation applies for the Easting direction. The observation equations are linearized for small α.

Tie point measurement is based on image correlation performed at 100 m pixel spacing between adjacent scenes belonging to the same date mosaic, or between scenes at two different dates. For scenes acquired along the same orbit the correlation peak is well defined even without high-contrast features; even homogeneous areas can be correlated successfully because the same speckle pattern is present in both scenes. The points within one date and between strips require always the presence of a high-contrast feature that remains stable during the interval between the SAR acquisitions of the adjacent strips. The same applies to the points between dates, but here the overlap area to search for candidate features is larger because the scenes (same node or path-row position) cover the same area.

To increase the probability of a high correlation maximum, a simple interest operator was implemented. A small area around the centre point of a correlation block is searched for candidate templates. The template that produces the highest value of the interest operator is then selected to be used in the correlation.

The structure of the LLS normal equations coefficient matrix **N** is block diagonal, with bandwidth:

$$w = (2s_{path} + 1) \cdot n_{dates} \cdot n_{par} \qquad (2)$$

where s_{path} is the maximum number of scenes in a single path (fast row index), n_{dates} is the number of dates (SAR coverages), and n_{par} is the number of parameters in the geometric model.

A conjugate gradient method can be used efficiently for the solution of linear systems with a block diagonal coefficient matrix. In the implementation of the multi-temporal block adjustment applied to the JERS SAR data the elements of the **N** matrix within the bandwidth are taken into account when computing the conjugate gradient iterations.

VALIDATION

In order to validate the geo-referencing accuracy, a sequence of block adjustments using different sources for the observations in the LSS were performed, and the relative residual mean square errors (RMSE) measured. The hierarchy of tests included: 1) observations based only on tie-points (see previous section); 2) additional observations based on ground control points (GCP) located on the coast lines; 3) additional observations based on GCP located inland in the Central Africa continent.

All three adjustments included 3624 scenes and 62006 tie-points.

Digital data from the World Vector Shoreline data base was used for the GCPs along coastlines. The World Vector Shoreline data covers fairly well West Africa, the Western coastal zone of Africa down to Angola, and the part of the Tanzanian-Kenyan coast that is included in one of the mosaics. Digital topographic maps scale 1:200000 in the Central African Republic and the Republic of Congo (Congo/Kinshasa) were used in test case 2. The maps were produced by IGN/France mainly in the 1950s. The maps were scanned and digitized by I-Mage Consult, Namure, Belgium within the framework of the Regional Environmental Information Management Project on Central Africa (REIMP-CA), initiated under the PRGIE program of the Worldbank.

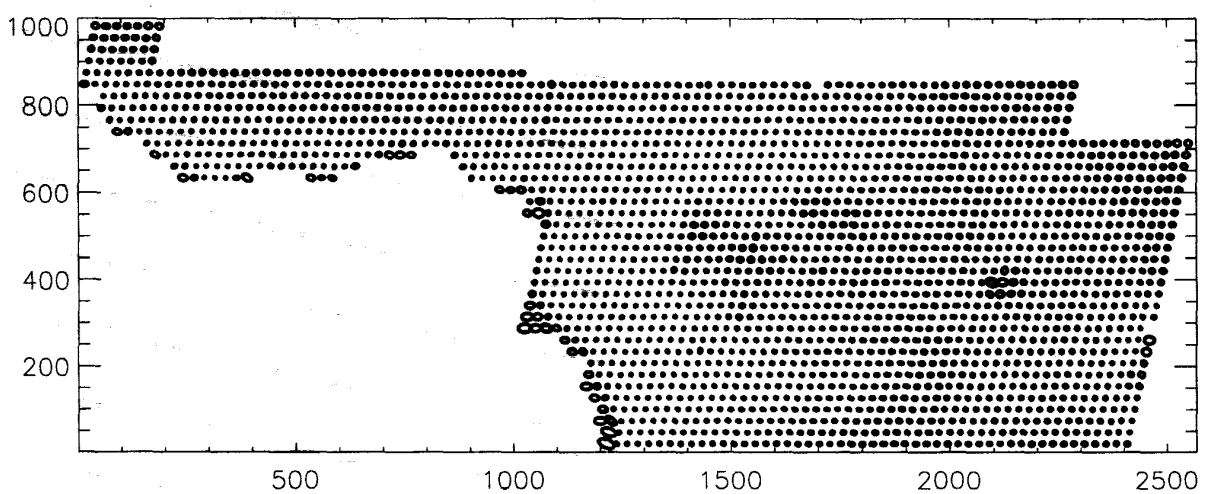

Fig. 1 - Error ellipsis of the scene centres in the whole Central Africa 100 m mosaic after the multi-temporal adjustment using GCPs.

TABLE 1. Residual mean square error statistic (in meters) in the block adjustment of the Central Africa GRFM mosaic

Test case	*Tiepoint N*	*Tiepoint E*	*Centre N*	*Centre E*	*GCP N*	*GCP E*	*Mean dN*	*Mean dE*
1	33.2	34.8	477.5	751.7	503.0	1021.4	26.6	-289.7
2	35.5	40.8	532.0	736.2	193.7	201.6	18.6	-69.3
3	40.1	39.7	543.3	758.0	173.2	166.3	24.3	-46.8

Results of the validation process are reported in Table 1. The columns *Centre N, Centre E* are scene translations in Northing and Easting. The column *Mean dN*, *Mean dE* give the average relative translations between the two dates mosaics. The GCP RMSE in case 1 indicates the mean squared error computed when the 248 coastline GCPs are not considered in the LLS estimator; they are only used to check the error.

As to case 2, the inclusion of GCPs in the LLS degrades the tie-points RMSE by a few metres. On the other hand, it greatly reduces the discrepancy between the mosaic and external control data (from 500 m to less than 200 m in Northing and from 1000 m to less than 200 m in Easting). In case 3 about 50 GCPs located in the Central African Republic and the Republic of Congo were added to the observations, but the RMSE statistics is not change significantly.From this fact we can infer that these GCPs are compatible with the coast line GCPs at the scale of the mosaic pixel size (100 m).

Another interesting way of characterizing the error budget in the scene geometry revision is to plot the local mean and variance of the LLS estimator in Northing and Easting (associating to each scene centre an error ellipse). An example for the whole Central Africa mosaic after the block adjustment using GCPs is shown in Fig. 1. In this case, the semi-major axis of the error ellipse varies between 6 and 55 m with a median at 11 m. The semi-minor axis varies between 6 and 3 m with a median at 10 m. Larger error ellipses correspond to scenes where the number of tie points is reduced because of lack of inter-scene correlation.

CONCLUSIONS

Registration in the sub-pixel range between two dates GRFM Africa mosaics with a sampling interval of 100 m was achieved using the multi-temporal block adjustment described in this paper. A figure of the internal geometric consistency and the between dates registration accuracy is given by a RMSE of 40 m for the tie points.

Adding ground control point data (derived from the World Vector Shoreline data set) shifted the mosaic on the average by a distance between 0.5 and 1 km with respect to the geo-location data from scene headers. Adding more ground control points defined in the central part of the African continent shifted the mosaic only by order of 100 m. Therefore we are confident that the absolute geo-location accuracy is within a couple of hundred metres throughout the whole mosaic that extends from the Western coast of Africa in Sierra Leone to the Eastern coast in Kenya and Tanzania.

A rigorous multi-temporal least squares block adjustment was applied to a semi-continental SAR mosaic consisting of over 3600 scenes and extending over a distance of more than 6000 km. In this respect, the GRFM Africa data set probably represents a milestone in wide area radar mapping of the earth ecosystems.

ACKNOWLEDGMENTS

The GRFM project is an initiative of the National Agency for Space Development of Japan NASDA. The authors, on behalf of their Institutions, would like to express their gratitude to the Agency for having given them the opportunity to participate in the project, and for the support received by the Agency in terms of a very generous data policy.

Also the staff members of the NASA JPL radar science group involved in GRFM Africa are acknowledged for their precious contribution.

REFERENCES

[1] A. Rosenqvist, "The Global Rain Forest Mapping Project by JERS-1 SAR"", *Inter. Archives of Photogrammetry and Remote Sensing", Vol. 31, Part B7, pp. 594-598, ISPRS, Vienna, Austria, 1996.*

[2] A. Rosenqvist, V. Taylor, B. Chapman, M. Shimada, A. Freeman, F. De Grandi, S. Saatchi, and Y. Rauste, *"The Global Rain Forest Mapping Project - A Review", Int. Journal of Remote Sensing,* in press.

[3] Y. Rauste, F. De Grandi, T. Richards, et. alt., "Compilation of JERS SAR Mosaics over Africa Using Multi-temporal Block Adjustment", NASDA Report on the GRFM project, 1999, in press.

[4] S.M. Kay, "Fundamentals of Statistical Signal Processing", *Prentice Hall Int. Ed. 1993, pp. 219,-288.*

PAPER 3

The global rain forest mapping project JERS-1 radar mosaic of tropical Africa: development and product characterization aspects

In: IEEE Transactions on Geoscience and Remote Sensing 2000. Vol. 38, No. 5, September, pp. 2218–2233.

The Global Rain Forest Mapping Project JERS-1 Radar Mosaic of Tropical Africa: Development and Product Characterization Aspects

Gianfranco De Grandi, *Senior Member, IEEE*, Philippe Mayaux, Yrjo Rauste, Ake Rosenqvist, Marc Simard, and Sasan S. Saatchi

***Abstract*—The Global Rain Forest Mapping Project (GRFM) is an international collaborative effort initiated and managed by the National Space Development Agency of Japan (NASDA). The main goal of the project is to produce a high resolution wall-to-wall map of the entire tropical rain forest domain in four continents using the L-band SAR onboard the JERS-1 spacecraft. The processing phase, which entails the generation of wide area radar mosaics from the raw SAR data, was split according to the geographic area. In this paper, the focus is on the part related to Africa. The GRFM project's goal calls for the coverage of a continental scale area of several million km^2 using a sensor with the resolution of tens of meters. In the case of the African continent, this entails the assemblage of some 3900 high resolution SAR scenes into a bitemporal mosaic at 100 m pixel spacing and with known geometric accuracy. While this fact opens up an entire new perspective for vegetation mapping in the tropics, it presents a number of technical challenges. In this paper, we report on the solutions adopted in the GRFM Africa mosaic development and discuss some quantitative and qualitative aspects related to the characterization and validation of the GRFM products. In particular, the mosaic geolocation and its validation are discussed in detail. Indeed, the internal geometric consistency (subpixel accuracy in the coregistration of the two dates), and the absolute geolocation (residual mean squared error of 240 m with respect to ground control points) are key features of the GRFM Africa mosaic. Other important aspects that are discussed are the multiresolution decomposition approach, which allows for tracking the evolution of natural phenomena with scale; the internal semi-automatic radiometric calibration, which minimizes artifacts in the mosaic; and the thematic information content for vegetation mapping, which is illustrated by a few examples elaborated by visual interpretation. Experience gained so far indicates that the GRFM products constitute an important source of information for global environmental studies.**

***Index Terms*—Calibration, geometric modeling, image classification, radar applications, radar cross sections, radar data processing, radar signal analysis, synthetic aperture radar (SAR), tropical regions, vegetation mapping, wavelet transforms.**

I. Background

THE GLOBAL Rain Forest Mapping Project (GRFM) [1], [2] is an international collaborative effort initiated and managed by the National Space Development Agency of Japan (NASDA), Hatoyama. The main goal of the project is to produce a high resolution wall-to-wall map of the entire tropical rain forest domain in four continents (South America, Africa, Asia, and Australia) using the L-band synthetic aperture radar (SAR) onboard the JERS-1 spacecraft.

The adequate monitoring of Earth ecosystems is a prerequisite to the sustainable management of renewable resources. Tropical and boreal forests are a case in point because they represent important pools of economical, biological, and ecological resources. These ecosystems are furthermore threatened by the rapid increase, worldwide, in the demand for new agricultural land and for new products.

Another important aspect related to these ecosystems is their role in the exchange processes between the atmosphere and the geo-, biosphere, and in particular for the carbon cycle and for fluxes of green house gases (GHGs) such as carbon dioxide and methane. In turn, this issue is linked to global climate change, a problem of major concern for all mankind on spacecraft Earth, and hence of great political and scientific relevance. The Protocol to the U.N. Framework Convention agreed to in Kyoto, Japan, has stressed the severity of the problem and confirmed the general awareness and political will to take action toward a long term solution. The Kyoto protocol makes provision for the use of biological GHG sources and sinks to meet commitments, and understandably requires inventory of resources such as forestry and land use change as a basis on which decisions will be taken for future action to account for anthropogenic disturbances. Space provides a unique vantage point and Earth observations by satellite, a unique technology to acquire such information.

An important requirement in the case of ecosystem-wide monitoring is the combination of timeliness, completeness, and spatial resolution of the observations. The NASDA GRFM project is a possible answer to this requirement, based on the recognition that the JERS-1 L-band spaceborne SAR characteristics are ideally suited for mapping and monitoring the vegetation distribution of an entire ecosystem at continental scale, at several spatial resolutions, and with no weather or time of day constraints.

The sheer size and complexity of the project (some 13 000 radar images covering some 50 million km^2) demanded international cooperation from an early stage. Among the main institutions that take part in the project worldwide, we cite the Earth Remote Sensing Data Analysis Centre of Japan (ERSDAC),

Manuscript received August 31, 1999; revised April 24, 2000.

G. De Grandi and P. Mayaux are with the Joint Research Centre, European Commission, Global Vegetation Monitoring Unit, Space Applications Institute, (VARESE), Ispra, Italy (e-mail: frank.de-grandi@jrc.it).

A. Rosenqvist was with the Space Applications Institute, Joint Research Centre (JRC), Ispra, Italy, and is now with NASDA, Tokyo, Japan.

Y. Rauste was with the Space Applications Institute, Joint Research Centre (JRC), Ispra, Italy, and is now with VTT Automation, Espoo, Finland.

M. Simard and S. Saatchi are with the Jet Propulsion Laboratory, Pasadena, CA 91109 USA.

Publisher Item Identifier S 0196-2892(00)08911-7.

Tokyo, Japan, the National Aeronautics and Space Administration (NASA), Washington, DC, the Jet Propulsion Laboratory (JPL), Pasadena, CA, the Alaska SAR facility (ASF), Fairbanks, AK, the European Commission Joint Research Centre (EC JRC), Ispra, Italy, the National Institute for Space Research of Brazil (INPE), São Jose Dos Campos, Brazil, the National Institute for Amazonian Research of Brazil (INPA), Manaus, Brazil, and the University of California, Santa Barbara (UCSB).

Certainly, this strategic vision, which brought together the expertise of major space-related institutions in Japan, the U.S., and Europe and the knowledge and skills of scientists all around the world, was one of the major assets that assured the so far very successful outcome of the project. The GRFM is also, in our opinion, a good example of how the study of global environmental problems requires a concerted effort at the international level.

The project includes a technology part related to the satellite operations, data acquisition and processing for the generation of the wide area radar mosaics, and a science program to support global or local area thematic studies of the tropical ecosystems. As far as the technology part is concerned, the following task structure and allocation was adopted. The SAR data downlink and correlation was performed at the NASDA Earth Observation Center, Hatoyama, Japan, and at the ASF, Fairbanks, Alaska. The latter effort was funded by NASA.

The SAR high resolution detected images were then distributed to a number of main processing nodes for the postprocessing phase involving low resolution product generation and wide area radar maps compilation, suitable for further automatic processing and thematic information extraction. The load was shared according to a geographic area criterion. The South America data set was assigned to the Jet Propulsion Laboratory, California Institute of Technology (funded by NASA), the Africa data set to the EC JRC Space Applications Institute (SAI), the Asia and Australia part to NASDA Earth Observations Research Center EORC. Each center was responsible for developing its own processing algorithms and software, since due to the project's requirements no off the shelf solution was available.

In this paper, the focus is on the Africa postprocessing part of the GRFM project. The postprocessing baseline product consists of a georeferenced, calibrated, bitemporal SAR wide area mosaic at 100 m pixel spacing, comprising radiometric and textural information. Additional products are also generated including multiresolution maps and texture measures (from 200 m down to 1.6 km). In particular, we will describe the main technical and engineering issues of the processor that was developed for the generation of the GRFM Africa products and will discuss some quantitative and qualitative aspects related to the characterization and validation of the products.

The paper is structured as follows. In the next section, we highlight the project's main characteristics and novel aspects. The generation of the Africa mosaic products entails several data sets, software and hardware components, that we collectively indicate as the Africa mosaic engine. These components are described in Section III. In Section IV, a statistical characterization of some baseline products is given. The next Section V deals with the core issue of the mosaic compilation and georeferencing, with particular emphasis on the geometric validation process (Section VI). In Section VII, the problem of correcting radiometric distortions is tackled. In Section VIII, we give a first assessment of the mosaic information content *vis-a-vis* the theme of tropical vegetation mapping. This step, which is conducted at this stage by visual inspection, is an important prerequisite to characterize the potential of the GRFM products for future automatic classification pursuits. Finally, we summarize the current status of the project and hint at the ongoing and future activities within the GRFM Africa project.

II. Project's Highlights

The GRFM approach calls for the coverage of a continental scale geographic area (a linear distance of some 6000 km in the case of the Africa mosaic) using a SAR sensor which acquires a scene within a swath of some 75 km and with a ground resolution of approximately 18 m. This is obtained by tiling together several acquisitions which are not taken instantaneously but still within a short time frame (two months). Moreover due to the orbital characteristics of the JERS-1 spacecraft contiguous swaths are imaged within two consecutive days, which assures a smooth time evolution through the whole coverage.

The resulting product is a spatially continuous radar map, which can eventually be degraded to lower resolutions for studying scale dependent natural phenomena, or to extract thematic information at the most suitable resolution. In the case of the tropical ecosystems, the merit of the approach lies therefore in the possibility of estimating some geophysical parameters of interest (e.g., biomes distribution, deforestation) globally and at unprecedented resolution.

Previous approaches relying on optical sensors were either producing wide area continuous sampling but low resolution maps (e.g., the EC Tropical Ecosystem Environment monitoring by Satellites TREES project vegetation maps based on NOAA AVHRR 1 km data [3]) or high resolution but random coverage data sets [4]–[6] (e.g., LANDSAT TM data). In this case, some global geophysical parameters were then estimated by extrapolation using statistical sampling techniques.

The combination of continuous coverage, short acquisition time, and high resolution is a unique asset of the GRFM approach. Experience gained so far lets us confidently say that data sets such as the GRFM ones will bring forth entirely new paradigms for the remote sensing of wide area terrestrial phenomena and will add enormously to our knowledge of the tropical and other poorly documented earth ecosystems. However the benefit comes at the cost of a number of technical hurdles.

First the end to end process from the satellite down link to the generation of several layers of lower resolution products entails a staggering data volume, and a high processing complexity. Experience in handling large data volumes was certainly not lacking among the major GRFM processing nodes. For instance, a wide area radar mosaic of Central Africa using the ESA ERS-1 SAR data had already been generated at the JRC SAI [7]. Still, the GRFM project introduced one more shift in complexity, due to the geographically distributed processing, and the layers of low resolution products (multitemporal, multiresolution). To give a flavor, the GRFM Africa mosaic consists of some 3900 SAR scenes which is tantamount to 312 Gb of high

resolution ground range data, and 4.8 Gb for one 100 m baseline product, without accounting for all the intermediate and special purpose lower resolution products. This level of data volume already poses some problems even for simple operations like data ingestion if the available off-the-shelf computer technology in the high end Unix servers and workstation class is used.

Second, since the coverage is not obtained in one snapshot, perturbation of the imaging system nominal values (e.g., the satellite attitude) affect the images that compose the mosaic according to their position differently (e.g., radiometric and geometric distortions). These effects must be taken in due account and corrected for. Moreover, the problem of parameters estimation is exacerbated by the data volume issue, because most manual techniques, like tie-pointing, must be ruled out.

Third, even a self-consistent measure of a physical parameter still requires a comparison with independent estimates to be validated. Validation of the image characteristics and, as a second step, of the thematic information that can be eventually extracted (e.g., a vegetation map), is in our opinion one of the central issues in the generation and exploitation of wide area high resolution remote sensing data sets. The validation of a measurement that is spatially dependent and extends over a wide area requires a reference set of known and suitable accuracy and must be dense enough to assure the correct sampling of the signal to validate. The problem is compounded by the fact that ad hoc ground experiments are nowadays difficult to set up in areas of the world like Central Africa, which are plagued by high social and political unrest. Historical data sets are in this case the only source for benchmarks.

In the context of the GRFM Africa postprocessing the validation of the georeferencing accuracy was of particular relevance, because clearly it constitutes a prerequisite to the use of the GRFM radar maps for cartographic applications. These peculiar connotations needed to be taken into account in the GRFM development process and constituted the rationale for the development of suitable processing techniques and tools, which are reported in this paper.

III. The GRFM Africa Mosaic Engine

The GRFM Africa processing chain can be seen from a purely computational point of view as an ensemble of data sets and processes that perform a transformation from the input data sets (the JERS-1 imagery supplied by NASDA) to the output data sets, which are referred to as the GRFM Africa multiresolution products. We indicate this ensemble of data sets, software, and the hosting hardware devices as the "GRFM engine." In this section, we give an overview of the engine main components and their interactions (see diagram in Fig. 1).

A. Input Data Sets

The JERS-1 SAR data acquisitions of the GRFM Africa project include two blanket coverages of the Central Africa tropical region between 10°S and 10°N. The first coverage was acquired during January–March 1996 and extends from 8°E to 42°E. The second during October–November 1996 and extends from 8 to 36°E. In the following, the two data sets will be dubbed the "low water" and "high water" data sets, with reference to the perceived

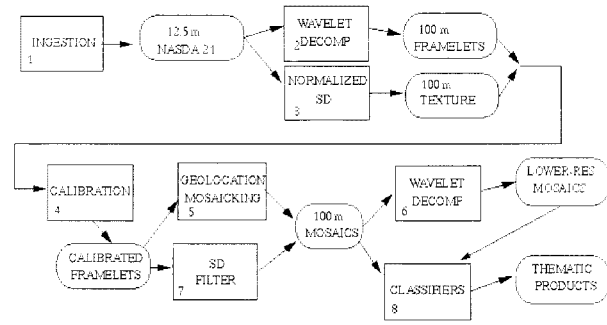

Fig. 1. Diagram of the main components of the GRFM Africa processing chain. The ensemble of the hardware, software processes (square boxes), the digital products (curved boxes), and their interconnections (arrows) is referred to as the GRFM Africa engine. The main processes are numbered for reference in the description of the data flow given in Section III.

hydrological state of the main river network in the region, the Congo river and its tributaries. In addition, the low water data set covers West Africa from 14°W to 8°E and the island of Madagascar (acquired on January 1997).

The SAR raw data corresponding to these acquisitions were correlated at NASDA Earth Observations Center EOC. The output of this processing phase is a product defined by NASDA as a standard geocoded image in a Universal Transverse Mercator (UTM) projection and dubbed Level 2.1 product. However, the rows and columns of the Level 2.1 raster file are aligned with the slant range and azimuth directions and not with the Mercator reference system.

The low water acquisition comprises 2173 scenes, the high water acquisition 1460 scenes in continental Africa, and 263 scenes for the Madagascar island. All the scenes were acquired on descending orbits.

B. Data Flow

Proper management of the data flow in terms of hardware resource allocation, operation synchronization, and housekeeping information is an issue of primary importance in a complex processing system like the GRFM one. Typically the following data flow takes place. The NASDA level 2.1 high resolution images are ingested in batches into the system. The data ingestion step is the most time critical in the overall chain of operations; in our configuration it required approximately two calendar months for all the GRFM data sets.

The high resolution data are then processed by the wavelet decomposition block (block 2 in Fig. 1 and Section III-C), which generates images and texture measures downsampled at 100 m. This product is the basic building block for all successive operations needed to build the mosaic. Products at this resolution will be called framelets.

The framelets are radiometrically calibrated (block 4 in Fig. 1) and geolocated and tiled together (block 5 in Fig. 1). This step produces the baseline products at 100 m resolution (bitemporal mosaics and texture measures).

Larger scale (lower resolution) maps and texture measures are generated again by wavelet decomposition from the baseline products (block 6 in Fig. 1). The multiscale radiometric and texture products are finally used to support further analysis, data

distribution, visual interpretation, and automatic thematic information extraction (block 8 in Fig. 1).

C. Wavelet Multiresolution Decomposition

A multiresolution signal decomposition based on the wavelet transform is used to generate the GRFM Africa products. The rationale for using this approach instead of a classical downsampling method such as block averaging, stems from several considerations.

1) Multiresolution is an intrinsic concept in the wide area radar mapping approach, where a high resolution sensor is used for wide area mapping. The wavelet pyramid gives the possibility of generating approximations of the original radar imagery at several spatial scales (at each stage in the pyramid, the pixel size is double with respect to the previous level). Therefore, it is possible to generate a set of products that best match the thematic analysis requirements for a certain application in terms of resolution, SNR, and data volume.
2) The wavelet coefficients at a scale j carry information on the "details" of the signal that were present in the approximation at a finer scale $j-1$ and were lost in the approximation at scale j. The wavelet coefficients can therefore be interpreted as texture measures at that scale and the wavelet decomposition provides at the same time the approximated image, and information on spatial structures that exist in the image at a certain scale. This fact opens up several possibilities for the automatic extraction of structural and textural information [11], a definite advantage over other multiresolution techniques.
3) The existence of fast discrete wavelet transform algorithms, which require only a number of operations proportional to the size N of the original data, makes this approach ideal in the case of high data volume (in contrast for instance, fast Fourier transforms (FFTs) are typically $N \log N$ algorithms).

The basic theory behind the wavelet based decomposition used in the GRFM engine was developed by Mallat [8]. Details on the adaptation of the theory in the case of SAR imagery and multiplicative speckle noise and on the retrieval of textural and singularity information can be found in [9]–[13].

D. Multiresolution Products

The wavelet decomposition generates from each high resolution level 2.1 image and for each scale three products: 1) the smooth signal; 2) the wavelets coefficients (horizontal, vertical, oblique); and 3) the scalogram. The scalogram at scale j as defined in [10] is the quadratic sum of the wavelet coefficients normalized by the squared smooth signal at that scale to compensate for the wavelet amplitude modulation due to multiplicative speckle noise in stationary areas. Scalograms are useful for constructing multiscale texture maps [11].

It is important to notice that the low pass and high pass filters in the decomposition are applied after a square law detector. In this way, over stationary areas, the intensity mean value is preserved after low pass filtering and therefore, an unbiased estimation of the radar backscattering coefficient is still possible at higher scales (lower resolution).

In parallel to the main pyramid another texture measure product is generated by computing the normalized standard deviation (sample standard deviation normalized by the sample mean) SD_N of the high resolution amplitude signal over contiguous blocks of 8×8 pixels. This texture measure is intuitively proportional to the one point signal variations (namely independent of the spatial ordering) within a resolution element of 100 m. For an homogeneous area with constant underlying radar reflectivity, they are entirely due to speckle noise. SD_N will therefore assume the nominal value for a 3-look amplitude image with correlated fully developed speckle. Deviations from this nominal value indicate that other variations are occurring in the signal within the 100 m resolution cell. See the next section for some statistical considerations on this texture measure.

It is important to realize that the normalized standard deviation SD_N is complementary and bears different information with respect to the wavelet scalogram SW^j. The scalogram at resolution j contains the details that were lost from the higher resolution $j-1$ in approximating the signal, and therefore contains variations that were detectable at scale $j-1$ but that were wiped out at scale j. For instance, SW^j at 100 m contains textural information at the 50-m scale. By contrast, the SD_N measure contains texture at all scales from 12.5 m up to 100 m.

IV. Statistical Considerations

A. Speckle Strength in the Low Resolution Products

The baseline radiometric products at 100-m pixel size are derived from the high resolution level 2.1 data by low pass filtering, the intensity signal, and by decimation. Speckle noise, which is present in the original data, will therefore be attenuated at larger scales but still be present. This has to be taken into account in the development of postprocessing analysis tools such as classifiers and edge detectors.

A quantitative estimation of the speckle strength for a stationary area with fully developed correlated speckle can be obtained considering a simple theoretical model. In the discrete wavelet decomposition, the two-dimensional (2-D) smooth signal at each scale is generated by convolution with a separable (rows and columns) low pass filter and by decimation. Relationships between the input and output random processes statistical parameters (expectations and correlation functions) at each stage in the decomposition can be obtained using the theory of stable, time-invariant linear filters.

Assuming that at the first stage (highest resolution), the input signal x will be correlated only up to 1 lag, the normalized second moment of the output process z can be expressed as

$$m_2(z) = m_2(x)c^2[0] + 2c[1]m_2(x) \cdot (\rho_r c[0] + \rho_a c[1]) + 2(c[0]+1)\sum_{l=2}^{\infty} c[l] \qquad (1)$$

where

$m_2(x) = (E[x^2]/E^2[x])$ normalized second moment of the random process x and indicator of the speckle strength;

$c[l]$ autocorrelation sequence of the wavelet low pass filter impulse response;

ρ normalized autocovariance at 1 lag.

Typical values for JERS-1 level 2.1 data are $\rho = 0.355$ in azimuth and $\rho = 0.4$ in range.

Since the decimation process after both convolutions (by rows and columns) decorrelates the signal, we can assume white speckle noise from the second scale downward. Then, cascading n such filter stages, a relationship between the normalized second moment $m_2[x]$ at the input of the wavelet decomposition and the normalized moment $m_2[x_n]$ at stage n can be obtained

$$m_2[x_n] = m_2[x]c^{n-1}[0] + 2\sum_{l=1}^{\infty} c[l] \sum_{k=0}^{n-2} c^k[0]. \quad (2)$$

Since there are two filters in the decomposition the scale level s is linked to n by $n = 2s+ 1$. Substituting numerical values for the low pass filter coefficients used in the wavelet decomposition in (1) and (2) and considering at the input a stationary random process drawn from intensity data with an equivalent number of looks $ENL = 2.6$ (as in a level 2.1 product), we obtain at the output of the pyramid $ENL = 59$ for the 100 m product and $ENL = 154.2$ for the 200 m product. For comparison a block average of 8×8 pixels would generate a product at 100 m pixel size with $ENL = 46.6$.

B. Variance of the Normalized Standard Deviation Estimator

We now turn to the statistical characterization of the texture measure based on the normalized standard deviation of the high resolution level 2.1 amplitude data. As explained in Section III-D, a local estimator is implemented in the GRFM processing by computing the sample normalized standard deviation of the data (three looks, 12.5 m pixel size) using an N × N window. The window is moved blockwise in the image.

This estimator turns out to be a good discriminator for some thematic forest classes of interest such as the swamp and the lowland rain forest, because it is sensitive to the upper canopy structure. It is therefore important to estimate the variance of the estimator in order to assess the SNR (or in other words the class separability).

The estimator can be expressed as a function of the statistics T_1 and T_2

$$S\hat{D}_n = \frac{\sqrt{\frac{1}{N}\left(\sum_i (x_i - \overline{x})^2\right)}}{\frac{1}{N}\left(\sum_i x_i\right)} = g(T_1, T_2) \quad (3)$$

$$T_1 = \frac{1}{N}\left(\sum_i x_i^2\right), \quad T_2 = \frac{1}{N}\left(\sum_i x_i\right) \quad (4)$$

where x_i are the observations and in this case, the amplitude values of the level 2.1 radar image.

Performing a first order Taylor expansion around the mean values $\overline{T}_1$ and $\overline{T}_2$, we have [14]

$$\begin{aligned}\operatorname{var}\left(S\hat{D}_n\right) = {} & \operatorname{var}(T_1)\left(\frac{\partial g}{\partial T_1}\right)^2_{T_1=\overline{T_1}} \\ & + \operatorname{var}(T_2)\left(\frac{\partial g}{\partial T_2}\right)^2_{T_2=\overline{T_2}} \\ & + 2\operatorname{cov}(T_1, T_2)\left(\frac{\partial g}{\partial T_1}\right)_{T_1=\overline{T_1}}\left(\frac{\partial g}{\partial T_2}\right)_{T_2=\overline{T_2}}.\end{aligned} \quad (5)$$

Equation (5) can be expanded as a function of the moments of the observables x_i, of the estimation window size, and the of normalized autocovariance function of x at 1 lag. All of these quantities can be computed from a theoretical probability distribution function and a correlation model of the SAR data. A detailed derivation is given in [25].

Numerical evaluation of (5) for K-distributed 3-looks amplitude data as a function of the order parameter ν of the $K(\nu, \overline{I})$ distribution and the estimator window size gives the results reported in Table I.

For a stationary area with Rayleigh or K-distributed speckle, the expected value of $S\hat{D}_n$ is a constant, which we consider the signal. The noise component is due to the estimator variance. In this sense, the standard error in Table I can be interpreted as the SNR of the texture measure. This analysis indicates how an improvement of the S/N can be traded off against the spatial resolution. Alternatively, the texture measure signal can be filtered to improve the SNR before the classification engine.

The theoretical estimator variance is the basis for the construction of such a filter (block 7 in Fig. 1). The filter uses the local statistics in the neighborhood of a pixel in the image to detect stationary areas where the statistical regime described above is present. This is achieved using the theoretical estimator variance (5) as a function of the mean value. If the variance threshold is exceeded, an adaptive window algorithm is entered, similar to the one proposed in [15]. If a stationary area is not detected even at this second level, then the original value is stored in the filtered set. Otherwise, the local sample mean is substituted for the current pixel.

The scope of the filter is therefore to smooth the texture measure in stationary areas with constant or Gamma distributed radar cross section and to preserve fine and strong features in nonstationary areas of the texture signal.

V. Geolocation

The geolocation of the individual scenes (framelets) is a fundamental step in the mosaic compilation. The problem can be explained as follows. If each framelet were to be positioned in a Mercator reference system relying only on the scene coordinates given in the NASDA product ancillary data, geometric inconsistencies would arise with respect to other framelets. Points belonging to the same feature on the ground would be displaced as seen in a framelet or in a neighboring one. This is due to errors in the sensor's position and uncertainty in the estimation of the Doppler centroid frequency that propagate in the solution of the range Doppler equations used by NASDA to rectify the geolocated level 2.1 product. The standard deviation of the

TABLE I
THEORETICAL VARIANCE OF THE SAMPLE ESTIMATOR $S\hat{D}_n$ (NORMALIZED STANDARD DEVIATION) FOR AMPLITUDE STATIONARY K-DISTRIBUTED SAR DATA AS A FUNCTION OF THE ORDER PARAMETER ν OF THE $K(\nu, \bar{I})$ DISTRIBUTION. THE ESTIMATOR VARIANCE AND STANDARD ERROR ARE REPORTED FOR AN ESTIMATOR MOVING WINDOW OF 8 × 8 PIXELS AND 16 × 16 PIXELS

		8x8 window		16x16 window	
$S\hat{D}_n$	ν	$\sqrt{var(S\hat{D}_n)}$	Std. Error%	$\sqrt{var(S\hat{D}_n)}$	Std. Error%
0.30	77.68	0.037	12.34	0.019	6.27
0.35	7.66	0.042	12.12	0.021	6.15
0.40	3.80	0.047	11.99	0.024	6.07

scene geolocation data was experimentally estimated to be several hundreds of meters, and discontinuities of up to 600 m were detected. On the other hand, internal geometric consistency and between dates coregistration of the mosaics for the multitemporal analysis require that the location accuracy of individual scenes is better than the pixel dimension (100 m). Methods for revising the geolocation data must therefore be applied in the mosaic compilation. A global optimization technique was developed based on a linear least squares estimation (LLS) of the scene geometry parameters given observations that comprise interscenes correlation measures, ground control points, and nominal scene position. The two acquisitions at different dates are simultaneously included in the estimation process, thus assuring optimal coregistration between dates.

From an intuitive point of view, the internal mosaic geometric consistency would be assured if the same features in different neighboring images were to match perfectly. Now the same feature on the ground is indeed imaged twice in the overlap area of two adjacent framelets. This fact can be exploited to get a measure of the relative discrepancies in the positions of the two framelets. The next problem is to move one framelet relative to the other in such a way as to be consistent with the positions of the other neighboring framelets and to avoid the propagation of errors in one direction as a function of the order in which the relative displacements are considered. The solution is to look for a global minimization of all the observed discrepancies.

This kind of global optimization technique has been studied in an application area of linear algebra which is called the calculus of observations [17]. The principle that underpins the calculus of observations can be summarized as follows. Suppose we experimentally perform M observations (e.g., coordinates of a point P in two images) that are linked to N parameters to be adjusted by a linear system of equations. In matrix form, $Ax + b = 0$, where x is a vector of N parameters, and A is an M by N matrix.

If no error were present in the observations the linear system would be consistent. Otherwise, we would have a discrepancy $\delta = Ax + b$ that we would want to minimize in the least square sense. This requires [17] that $\delta^T\delta$ be a minimum or

$$\frac{\partial}{\partial x}\left(\delta^T\delta\right) = 2A^TAx - 2A^Tb = 0. \tag{6}$$

These are the so-called normal equations and can be solved for the parameters vector x if the $N \times N$ matrix A^TA is nonsingular. Weighting factors can be also introduced in the error criterion $\delta^T\delta$ in order to emphasize the samples that are deemed more reliable. Then the error to be minimized becomes $\delta^TW\delta$, where W is a positive definite $N \times N$ weighting matrix.

The application of this global optimization technique to the case of image block adjustment requires the definition of a geometric model or in other words the definition of the observation equations $\delta = Ax + b$. We use a model [18] where, given a framelet in the Mercator projection, the scene center translation $\nabla N_C \nabla E_C$ and the rotation angle α are considered as parameters. This model relies on the confirmed assumption that there is no internal deformation in the NASDA level 2.1 products. Working the problem in a conformal mapping projection minimizes the risk of introducing projection-dependent systematic deformations. Also, the rotation angles are kept small and therefore, the block adjustment can be simplified by linearizing the observation equations.

With the aid of an auxiliary reference system with origin at the scene center, the relationship in the Mercator reference system between one point P in the image and the unknown parameters can be derived where

$$\begin{aligned} N^P &= N_C + y\cos\alpha - x\sin\alpha \\ E &= E_C + x\cos\alpha + y\sin\alpha \end{aligned} \tag{7}$$

N^PE^P Mercator coordinates of point P;
x, y image coordinates in the auxiliary reference system and N^CE^C are the coordinates of the scene center;
α rotation angle of the auxiliary system with respect to the Mercator system.

The observations equations $\delta = Ax + b$ based on tie-points between scenes are

$$\begin{aligned} \delta N^P &= N_1^P - N_2^P = N_1^C - N_2^C + y_1\cos(\alpha_1) \\ &\quad - y_2\cos(\alpha_2) - x_1\sin(\alpha_1) + x_2\sin(\alpha_2) \end{aligned} \tag{8}$$

$$\begin{aligned} \delta E^P &= E_1^P - E_2^P = E_1^C - E_2^C + x_1\cos(\alpha_1) \\ &\quad - x_2\cos(\alpha_2) - y_1\sin(\alpha_1) + y_2\sin(\alpha_2). \end{aligned} \tag{9}$$

These equations are put into the suitable linear form in the parameters $N_1^CN_2^CE_1^CE_2^C\alpha_1\alpha_2$ by a Taylor's series and retaining only first order terms. Thus, for example for the Northing term

$$\begin{aligned} \delta N^P &= f\left(N_1^C, N_2^C, \alpha_1, \alpha_2\right) \\ &= \delta N_0^P + \nabla N_1^C - \nabla N_2^C + \frac{\partial f}{\partial \alpha_1}\nabla\alpha_1 + \frac{\partial f}{\partial \alpha_2}\nabla\alpha_2 \end{aligned} \tag{10}$$

where

$\nabla N_1^C \nabla N_2^C$ translations in Northing of the scene;
$\alpha_1\alpha_2$ rotations of the scenes with respect to their local reference systems;
δN_0^P initial Northing discrepancy at point P.

The elements of the matrix A in the observations equations are the partial derivatives with respect to the parameters, and the vector b corresponds to the initial discrepancies before the adjustment. Tie-point measurement is based on image correlation performed at 100 m pixel spacing between adjacent scenes belonging to the same date mosaic or between scenes at two different dates. For scenes acquired along the same orbit, the correlation peak is well defined even without high contrast features. Even homogeneous areas can be correlated successfully,

because the same speckle pattern is present in both scenes. The points within one date and between strips always require the presence of a high contrast feature that remains stable during the interval between the SAR acquisitions of the adjacent strips. The same applies to the points between flood season, but here the overlap area to search for candidate features is larger because the scenes (same node or path-row position) cover the same area.

Measurements related to tie points between two neighboring scenes assure only control over the internal consistency and the coregistration of the bitemporal mosaic. However, in order to improve the absolute geolocation accuracy also ground control points (GCPs) derived by external cartographic data were introduced. In this case, the observation equations for a GCP of known geodetic coordinates $N_{true}E_{true}$ are

$$\begin{aligned}\delta N^P &= N^P_{computed} - N^P_{true} \\ &= N^C + y\cos\alpha - x\sin\alpha - N^P_{true} \end{aligned} \tag{11}$$

$$\begin{aligned}\delta E^P &= E^P_{computed} - E^P_{true} \\ &= E^C + x\cos\alpha + y\sin\alpha - E^P_{true}. \end{aligned} \tag{12}$$

Finally, information on the image location derived from the SAR ancillary data was added to the LLS adjustment. This last information is by far less accurate than the one derived by tie points between images but is still useful in establishing a bound on image rotation and translation with respect to the original position.

The structure of the LLS normal equations coefficient matrix $N = A^T W A$ is block diagonal with bandwidth

$$w = (2s_{path} + 1) \cdot n_{dates} \cdot n_{par} \tag{13}$$

where

- s_{path} maximum number of scenes in a single path (fast row index);
- n_{dates} number of dates (SAR coverage);
- n_{par} number of parameters in the geometric model.

A conjugate gradient method [19] can be used efficiently for the solution of linear systems with a block diagonal coefficient matrix. In the case of the bitemporal Africa mosaic, the matrix size is 10 875 × 10 875, which is also an indicator of the processing complexity.

VI. Geolocation Validation

In order to validate the georeferencing accuracy, a sequence of block adjustments using different sources for the observations in the LLS were performed, and the relative residual mean square errors (RMSE) measured. The hierarchy of tests included: 1) observations based only on tie-points between neighboring scenes; 2) additional observations based on GCPs located on the coast lines; and 3) additional observations based on GCPs located in the interior of the continent. All three adjustments included 3624 scenes and 62 006 tie-points.

Digital data from the World Vector Shoreline data base was used for the GCPs along coastlines. The World Vector Shoreline data covers fairly well West Africa, the Western coastal zone of Africa down to Angola, and the part of the Tanzanian–Kenyan coast that is included in one of the mosaics. Digital topographic maps with scale 1 : 200 000 in the Central African Republic and the Republic of Congo (Congo/Kinshasa) were used in test case 2. The maps were produced by IGN/France mainly in the 1950s. The maps were scanned and digitized by I-Mage Consult, Namure, Belgium within the framework of the Regional Environmental Information Management Project on Central Africa (REIMP-CA), initiated under the PRGIE program of the Worldbank.

TABLE II
Residual Mean Square Error (RMSE) Statistic in the GRFM Geolocation Block Adjustment. All Quantities are in Meters. Centre N And Centre E are Scene Translations in Northing and Easting. The Column Mean ∇N And Mean ∇E Give the Average Relative Translations Between the Two Dates Mosaics. Ground Control Point (GCP) N And GCP E are the Coordinates of the Ground Control Points

Test case	*Tiepoint N*	*Tiepoint E*	*Centre N*	*Centre E*	*GCP N*	*GCP E*	*Mean* $\nabla N_{1,2}$	*Mean* $\nabla E_{1,2}$
1	33.2	34.8	477.5	751.7	503.0	1021.4	26.6	-289.7
2	35.5	40.8	532.0	736.2	193.7	201.6	18.6	-69.3
3	40.1	39.7	543.3	758.0	173.2	166.3	24.3	-46.8

Results of the validation process are reported in Table II. The table gives RMS errors in meters for various quantities of interest. The columns *Centre N*, *Centre E* are scene translations in Northing and Easting. The column *Mean* $\nabla N_{1,2}$, *Mean* $\nabla E_{1,2}$ give the average relative translations between the low water and the high water mosaics. The RMS error on GCP's in case 1 indicates the error computed when the 248 coastline GCPs are not included in the LLS adjustment but only used to estimate the error.

As to case 2, the inclusion of GCPs in the least squares estimation LLS degrades the tie-points RMSE by a few meters. On the other hand, it greatly reduces the discrepancy between the mosaic and external control data (from 500 m to less than 200 m in Northing and from 1000 m to less than 200 m in Easting). In case 3, about 50 GCPs located in the Central African Republic and the Republic of Congo were added to the observations, but the RMSE statistic of scene translation vectors did not change significantly. From this fact we can infer that these GCPs are compatible with the coast line GCPs at the scale of the mosaic pixel size (100 m).

In case 1, the GCP data were a completely independent test set. In the error analysis of cases 2 and 3, the same GCP data set is used both to derive the parameters of the model and to test the accuracy of the model. Theoretically, a better error estimate could be obtained using an independent test set. However, to the best of our knowledge, no such set exists for tropical Africa given the error budget and extension required. One solution could have been to divide the GCP population into two sets (one for model derivation and the second for testing), alternating for instance 500-km stretches along the coast line for each set. This approach was not followed for two reasons. First, it was thought that RMS errors of the order of 200 m are already close or below the accuracy specification of the vector shore line data (dividing the population into two sets would still give the same level of RMS errors). Second, the splitting could introduce systematic errors (as a result of differences in origin and quality of the map material used to derive the coast line data) into the analysis depending on the way the partitioning is made.

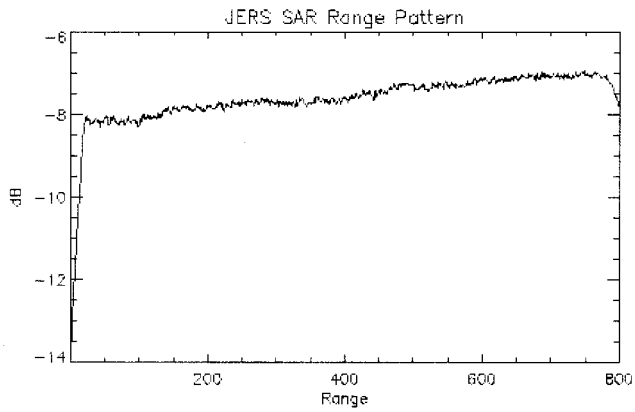

Fig. 2. Typical JERS-1 level 2.1 product range pattern (average backscatter amplitude as a function of the range coordinate). Notice the anomalous behavior where the backscatter increases from near to far range. This pattern cannot be expected for any natural target and is therefore a processing artifact probably due to the sensor's attitude variations. However, since the artifact manifests itself randomly in the set of images composing the mosaic and cannot be characterized by analysis of the SAR ancillary data, an empirical calibration algorithm had to be devised that relied on a global minimization of radiometric discrepancies between the same ground target imaged in two neighboring images.

VII. Radiometric Calibration

A. Calibration Algorithm

The calibration of most spaceborne SAR sensors is based on the use of the tropical forest as a calibration target [20], [21]. Usually the antenna pattern, determined on the ground before the launch of the satellite, is revised based on the fact that the backscattering coefficient γ° of the tropical forest is constant over a wide range of incidence angles. The revised antenna pattern is then used in connection with SAR processing to produce calibrated SAR products. This approach works well if all the necessary spacecraft (such as platform attitude angles) and processing parameters remain constant or are known with the required accuracy. Uncontrolled drift in these parameters may cause changes in the SAR range pattern and degrade the (relative) calibration accuracy.

Indeed the main calibration artifact that pollutes the JERS-1 level 2.1 products is related to the average backscatter amplitude as a function of the range coordinate in homogeneous areas. In many scenes, the range pattern shows an anomalous behavior whereby the average amplitude increases from near range to far range (see Fig. 2). Typically, the increase is of 1 dB across the image swath. This kind of backscatter curve cannot be expected for natural targets.

Other radiometric problems in the JERS-1 imagery are related to striping in the along track direction due probably to errors in processing the sensitivity time control (STC) data and between scenes gain imbalance.

Since the reasons for these calibration artifacts are not known, and related characterization data cannot be deduced from the header data of the SAR level 2.1 products, an empirical method based on backscatter estimates of the same target in neighboring scenes was devised to remove the artifacts. Also, the procedure requires a minimum amount of manual intervention, a relevant factor in the GRFM Africa context, where a large number of scenes acquired at different times must be processed.

The resulting calibration should be considered accurate only in flat areas. Indeed due to the unavailability of suitable digital elevation models at continental scale in the Africa tropical region, techniques to compensate radiometric errors due to the influence of topography were ruled out. Also, since topography is not accounted for, the term "incidence angle" in the following must be understood under the assumption of flat terrain.

The automatic calibration procedure is based on the following rationale. The dominant land cover type in the area covered by the GRFM project is tropical rain forest. Scatterometer measurements at C-band [20] indicate that this natural target exhibits a constant backscattering coefficient γ° over 50° incidence angle range from 18 to 68°. The same results are confirmed at L-band for the JERS-1 SAR in [21]. For the 4° incidence angle range used (96% of the mosaic pixels have an incidence angle between 37.4 and 41.5° due to the overlap between strips and the far-range-on-top mosaic compilation mode), it is safe to assume that also other land cover types with rough surfaces such as dry wood, land, or open-canopy forest (savanna), have a practically constant γ°.

Assuming a constant γ° for major land cover types over the range of incidence angles means that a pixel observed at far-range incidence angle and near-range incidence angle in an overlap area between strips should have the same backscattering value in both strips provided that no environmental change has influenced the backscatter level between the two acquisitions. Due to its unique orbit, the JERS-1 radar acquired the two adjacent strips on two consecutive days. Therefore, it is reasonable to assume that the γ° of an overlap area remains the same in the relatively weather-insensitive L-band SAR data.

The objective of the calibration procedure is to produce mosaics with minimum radiometric difference between scenes in the overlap areas (and consequently along the seams between scenes), both within a strip and between strips.

This is achieved by using an LLS of the coefficients in a bilinear radiometric correction model

$$DN_{cal} = (1 + f_0 + f_1 x + f_2 y + f_3 x \cdot y) \cdot DN_{orig} \quad (14)$$

where x, y are normalized line and columns coordinates derived from the line and column indices in the SAR image.

The model incorporates a constant gain factor and coordinate dependent gain factors. The main part of the calibration artifact is a function of the range coordinate only (see Fig. 2). Since the reason for this artifact is not known, it cannot be assumed that the calibration artifact would remain constant as a function of time. Azimuth and cross terms are therefore included in the radiometric correction model.

Points in the overlap area between two neighboring scenes are used to derive observations for the LLS adjustment. The observation equation for two scenes is

$$\begin{aligned}\delta = {} & f_0^2 DN_{orig2} + f_1^2 DN_{orig2} \cdot x \\ & + f_2^2 DN_{orig2} \cdot y + f_3^2 DN_{orig2} \cdot xy \\ & - f_0^1 DN_{orig1} - f_1^1 DN_{orig1} \cdot x - f_2^1 DN_{orig1} \cdot y \\ & - f_3^1 DN_{orig1} \cdot xy + DN_{orig2} - DN_{orig1} \end{aligned} \quad (15)$$

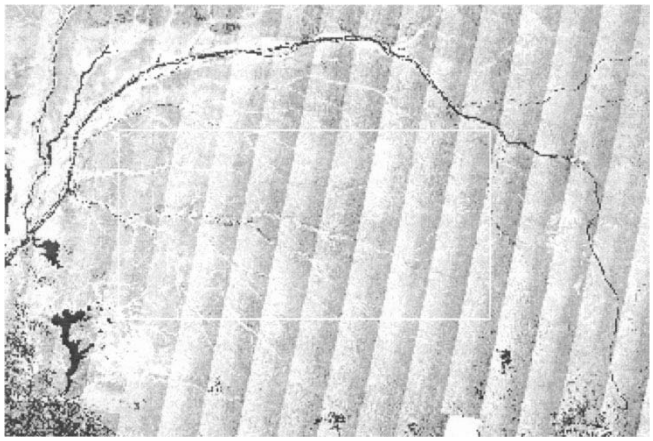

(a)

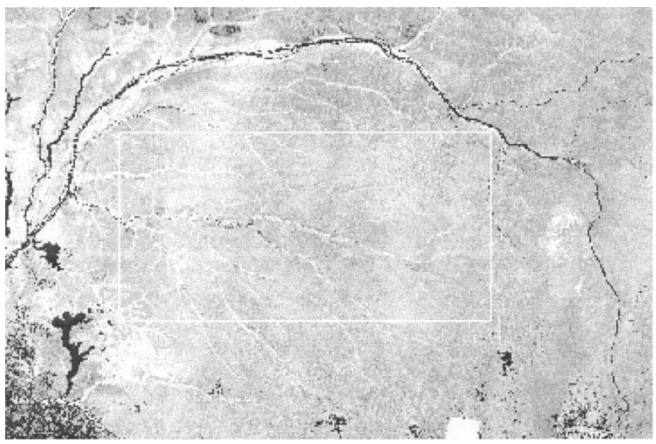

(b)

Fig. 3. (a) Subset of the high water mosaic compiled using the original, noncalibrated 100-m framelets. The effect of the anomalous range pattern is clearly visible and produces what could be called a striping effect in the image. (b) The same mosaic after the bilinear LLS calibration revision. Clearly, the major calibration artifacts have been removed.

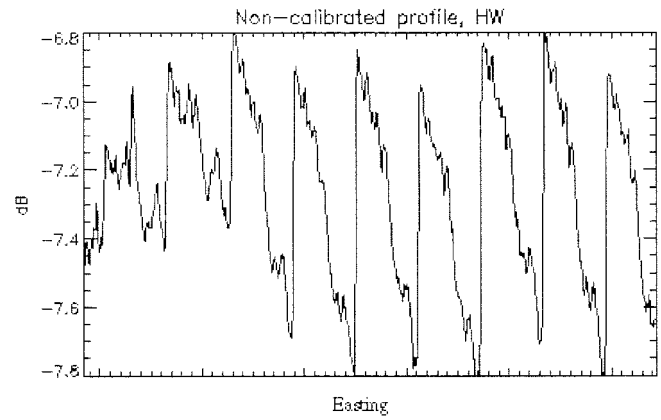

(a)

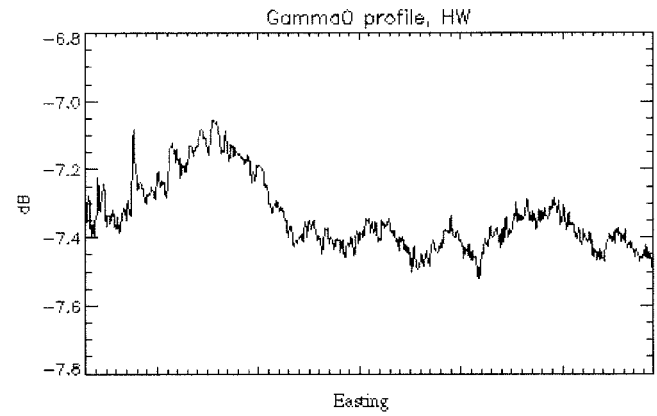

(b)

Fig. 4. (a) Average range profile computed on the noncalibrated mosaic in the window highlighted in Fig. 3. There is a pronounced increase if 1 dB in the backscatter over the image swath. (b) The average range profile of the calibrated image confirms that the calibration artifacts have been corrected for.

where f_j^i is the correction factor for image i and order j, and $DN_{orig1}DN_{orig2}$ are digital values of image 1 and 2 in the overlap area.

B. Calibration Results

This section reports on sample results of the GRFM calibration procedure. A subset of the high water mosaic composed using the original uncalibrated 100-m scenes is shown in frame a) of Fig. 3. An average profile computed over the rectangle highlighted in Fig. 3 is plotted in frame a) of Fig. 4. This profile was computed projecting each pixel to an Easting coordinate along lines parallel to the orbit direction. Because the look direction of JERS-1 in descending orbits is westwards, the range coordinate decreases with increasing Easting coordinate. This graph clearly indicates that there is a pronounced increase of almost 1 dB over the image swath.

The same mosaic subset compiled using the calibrated framelets and the associated range profile are shown in frame b) of Figs. 3 and 4. The calibration anomaly (increasing backscatter with increasing range) has been clearly compensated for.

Analysis of the calibration results for the bitemporal mosaics confirms that the method works in a satisfactory way using automatic (systematic grid sampling) selection of calibration points in forested areas. However in very dynamic environments such as flooding in savanna or in grassland areas, the backscatter may change considerably even during the one-day interval between the acquisition of adjacent strips. These cases can be detected by careful inspection of the calibration factors, and must be handled by a separate semiautomatic procedure. This procedure calls for the removal of the automatically selected calibration points and the interactive selection of points in areas which can be expected to be less prone to meteorological changes in backscatter level (e.g., the primary rain forest).

The GRFM calibration method produces a constant response backscatter curve which corresponds to the constant γ° in forested areas. The calibration coefficient (in the near-range far-range direction) does not change notably when going from a forest area into a savanna area. This confirms the assumption that the backscatter coefficient γ° of savanna can also be considered as constant over the incidence angles present in the mosaic.

Finally, one comment should be made regarding the possibility of retrieving σ° values form the DN values of the Africa mosaics. The assumptions made in the radiometric model for the

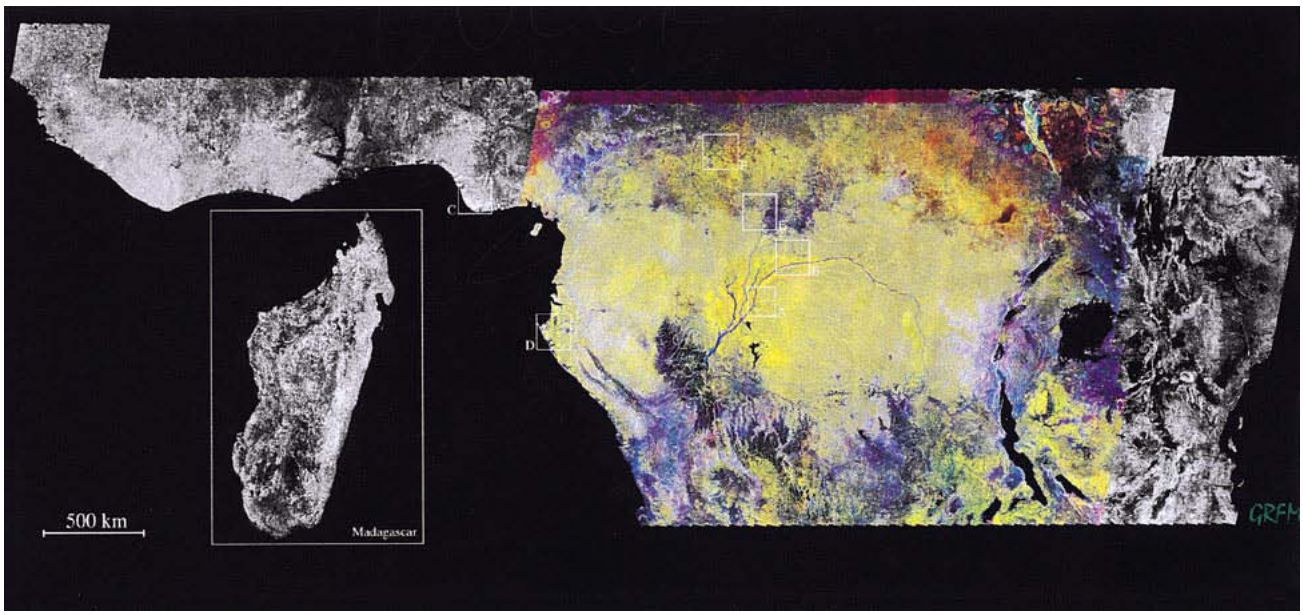

Fig. 5. Synoptic view of the GRFM Africa mosaic. The mosaic extends from the western coast of Africa in Sierra Leone at 14° W to the eastern coast in Kenya and Tanzania at 42° E in longitude and from 10° S to 10° N in latitude. In addition, the island of Madagascar is included (see inset). A blanket coverage of the whole area was acquired in January–March 1996 during the low water season of the Congo river. A second acquisition from 8° E to 36° E was also performed during the high water season in October–November 1996. The area covered by the two acquisitions is shown in false color in the figure. Areas of interest for relevant thematic features are highlighted and enlarged in the next figures.

calibration algorithm, and the several steps needed to compensate for various radiometric artifacts in the NASDA products, suggest (to be on the safe side) the disclaimer that the GRFM Africa mosaic is not suitable for building a radar cross section map. Rather, it is an internally consistent image (an approximation of the radar reflectivity) that is useful as input to supervised classification algorithms, which rely on relative comparisons of the local image amplitude statistics and texture measures.

In particular cases, such as for areas belonging to the lowland rain forest, it is safe to derive estimates of the γ° coefficient from the local statistics of intensity data. Knowledge of the local incidence angle would then allow for the retrieval of σ° values in dB using for instance the equation supplied by NASDA [21].

VIII. Thematic Information Content

The richness in information content is one of the most striking assets of the GRFM Africa wide area radar mosaics. From the first analyses based on visual interpretation, a series of features related mainly to vegetation regional mapping and landcover change studies have already emerged and indicate that these radar maps are of great interest for global vegetation mapping, a major objective of research programs such as the International Geosphere Biosphere Programme (IGBP) and the Global Observation of Forest Cover (GOFC).

In order to give evidence about this statement, a few examples of the thematic content derived by visual inspection of the GRFM products will be reported in the following. A synoptic view of the Africa mosaic derived from the 100 m digital image is shown in Fig. 5.

The colored area corresponds to the bitemporal coverage. Already at this scale it is evident how the mosaic represents a unique cross section of important tropical biomes from the savannah and dry forest in the north through the entire rain forest domain and again through the seasonal formations south of the equator (savannah and edge of the Miombo woodland). The coverage of the mosaic is such that, since it crosses the equator, it contains at the same time dry and rainy season acquisitions with a gradient of wetness in between [23]. This allows a range of observations to be made with respect to the occurrence or to the lack of seasonal contrasts between various vegetation formations.

Areas related to the cases that are discussed are highlighted in the synoptic view and enlarged in the next series of figures.

The first case is related to the swamp forests in the Congo river floodplain. Swamp forests are interesting ecosystems that function as water storage, faunistic and florensis habitat, and fish stock. Moreover, they host a series of biochemical processes such as nitrogen turnover and methane emission. Since methane is a greenhouse gas, this process has a significance in global change issues [24]. Due to the density of the hydrographic network, swamp forests cover large areas in the center of the Congo basin, leaving room for the lowland rain forest in the inter fluvial areas only.

Different types of swamp forests coexist according to the frequency and the duration of the flooding, and they can be discriminated in the radar image by textural and radiometric differences. The L-band SAR onboard the JERS-1 satellite offer unique characteristics to map these ecosystems [25], [26]. Indeed, electromagnetic waves at L-band can penetrate even through the thick closed canopy of the Africa swamp forests and the backscattered signal is thus sensitive to standing water on the terrain through a double bounce scattering mechanism. The upper canopy of the swamp forest is closed and very homogeneous, and the radar reflectivity from direct backscattering

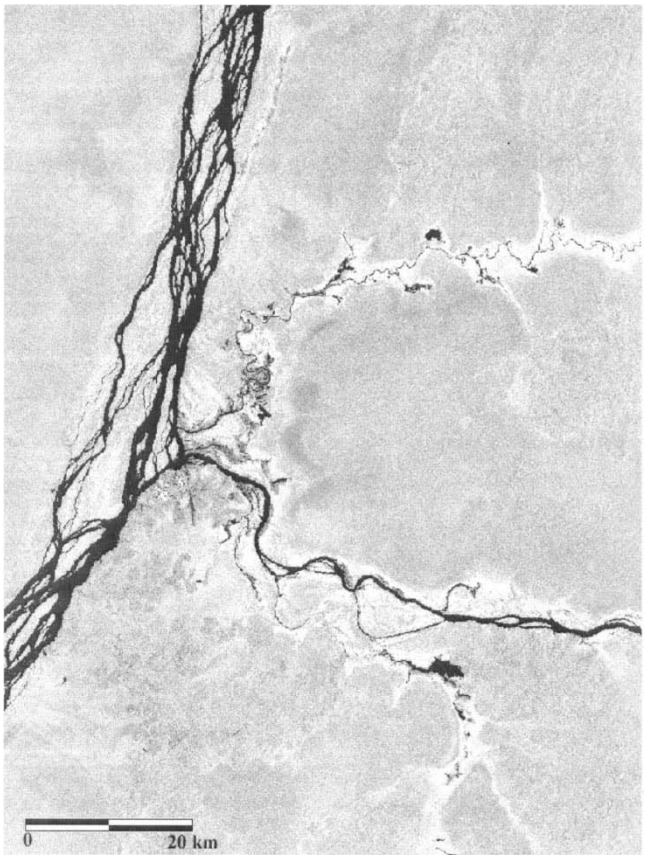

Fig. 6. Flood plains along the Congo river in Central Africa are covered by forests adapted to the soil conditions (area A in Fig. 5). As an example, in this figure, permanently inundated forests are characterized by a brighter tone (strong backscatter due to the double bounce mechanism) because of the presence of standing water. Smooth texture allow us to the distinguish periodically inundated forests to the west of the Congo River or in the large patches at the center of the image.

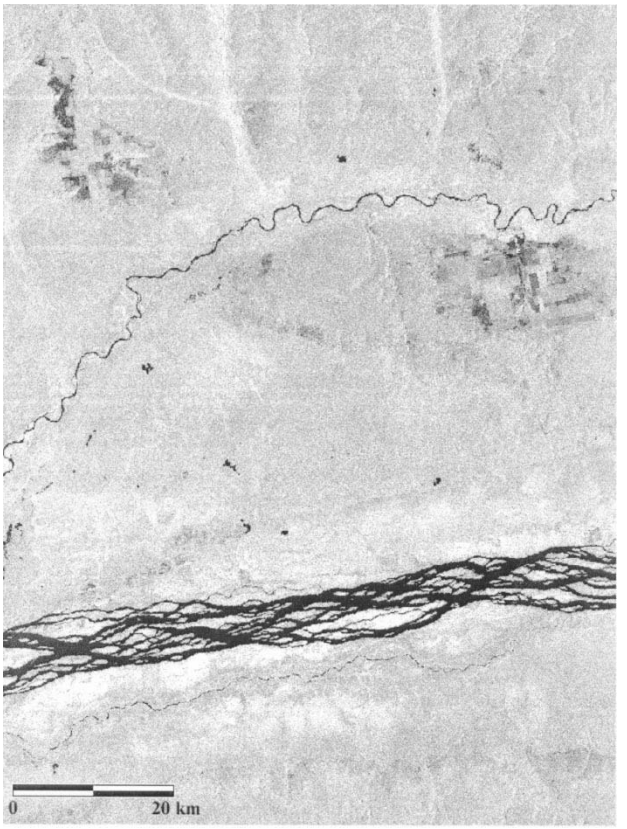

Fig. 7. Large industrial plantations (Hevea, Elaeis) established in colonial times in the proximity of the Congo River and his tributaries are readily detectable in this image due to their regular geometric shape (area B in Fig. 5). The dense network of the Congo River (lower part of the image) is very sharply delineated. The flooded swamp forests are also visible along the river due to the high double-bounce return.

exhibits smooth textural properties (statistically it approximates very well the fully developed speckle Rayleigh regime). On the other hand, species heterogeneity and a higher fragmentation modulates the spatial variations of the thick upper canopy in the lowland rain forest. This produces a microtopography effect that changes the textural properties of the radar backscatter even at L-band. An example is shown in Fig. 6.

Permanently inundated forests are characterized by brighter tone in the image (strong backscatter) because of the presence of standing water. Smooth texture permits the distinction of periodically inundated forests at the west of the Congo River or in the large patches at the center of the image.

Fig. 7 reveals the presence of large industrial plantations (Hevea, Elaeis) established in colonial times in the proximity of the Congo River and his tributaries.

The plantations are characterized by a uniform cover and follow a geometrical layout, clearly identifiable on the center and the right center of the image. The different backscatter responses correspond to different practices used in the plantation management (mainly fires). The dense river network and the numerous branches of the Congo River are very clearly delineated in the image. The capability of monitoring the river configuration, which undergoes continuous modifications, is of primary interest for the local economy of the many villages and settlements along the Congo river.

Coastal ecosystems are the target of ecological pressures by several anthropogenic activities: urbanization, oil extraction, fishing, forest logging, and hunting. In Fig. 8, the Niger Delta is shown. This area is covered by a dense network of mangroves. Mangroves are forest formations associated with marine alluvium, partially steeped in salt water. The survey of the mangrove degradation is particularly crucial in this region where many oil-extraction activities are under way and cause soil pollution.

The coastal part of Gabon, namely the city of Port-Gentil (Fig. 9), is also a site with intensive offshore oil extraction activities. The Ogooué river estuary is covered by a complex of swamp grasslands with gramineae and Papyrus, mangroves and swamp forests, lagoons and coastal savanna, and rain forests.

The city of Bangui in Central African Republic is located on the Oubangui river at the border between the savanna and the forest domains. It is clearly visible as a strong scatterer in Fig. 10. The urban expansion has a major impact since the 1960s on the forest degradation taking place toward South from the city, as attested by many openings in the forest (dark tone in the image). On the other side of the Oubangui river, a reticulated network of gallery forests penetrates into the savanna domain.

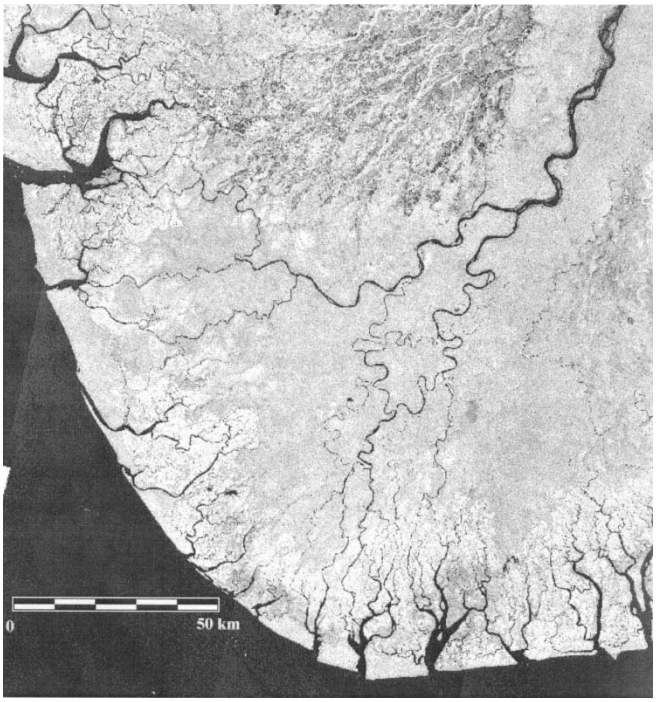

Fig. 8. The Niger Delta is a coastal ecosystem that is the target of ecological pressures by several anthropogenic activities (area C in Fig. 5). This area is covered by a dense network of mangroves (in light gray), easily distinguishable from the surrounding rain forests. A wide ribbon of dense rain forest extends along the Niger River at the North of the image in the middle of savanna and secondary zones. Note the presence of offshore platforms (bright dots in the sea).

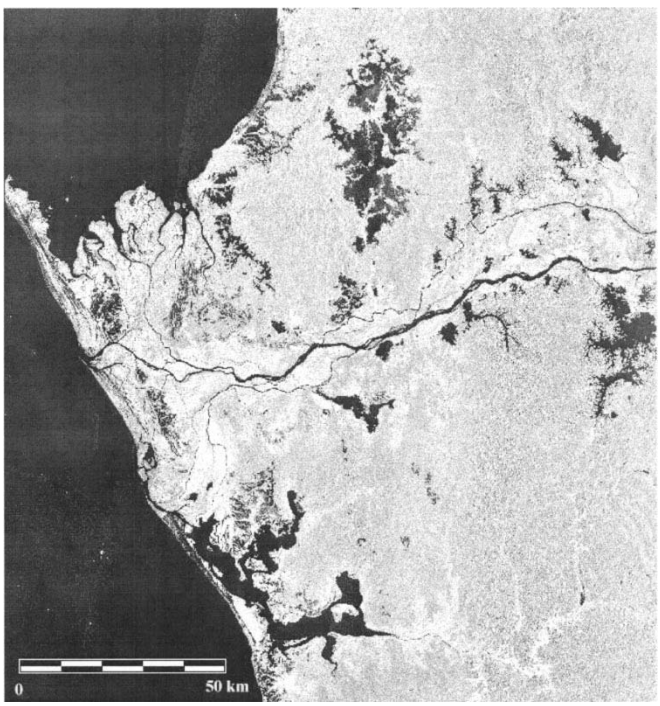

Fig. 9. The Ogooué river estuary, near by the city of Port-Gentil (area D in Fig. 5), is covered by swamp grassland, mangrove, and swamp forests (bright return). Lagoons and coastal savanna appear in black, while rain forests present an intermediate reflectivity.

These gallery forests play a key role in the biodiversity conservation.

Fig. 10. The city of Bangui in the Central African Republic is located on the Oubangui river at the border between the savanna and the forest domains and is clearly visible in this image as a strong scatterer. On the other side of the Oubangui river, a reticulated network of gallery forests penetrates into the savanna domain.

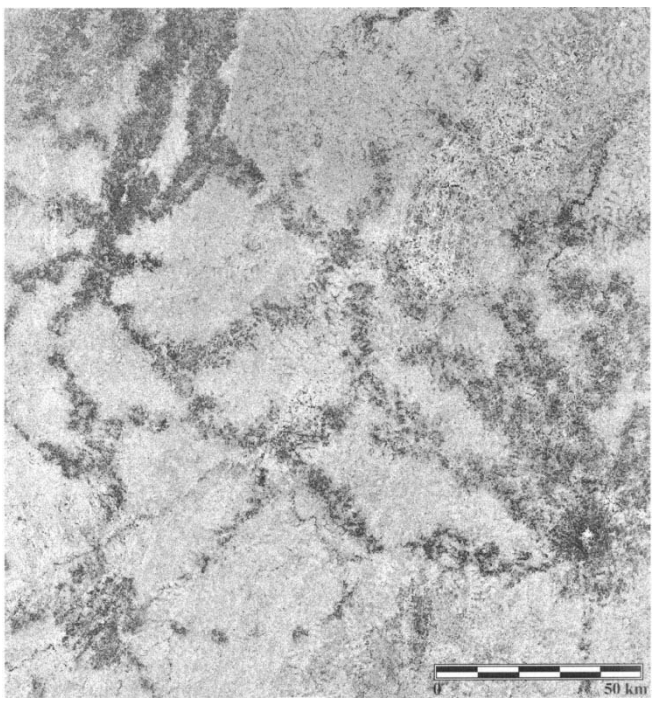

Fig. 11. A reticulated pattern of agricultural fields within the woodland and tree savanna domain in the central part of the Central African Republic.

Fig. 11 shows a reticulated pattern of agricultural fields within the woodland and tree savanna domain in the central part of the Central African Republic.

The relatively low population is concentrated along the road network. Common crops are cassava, maize, and peanuts used

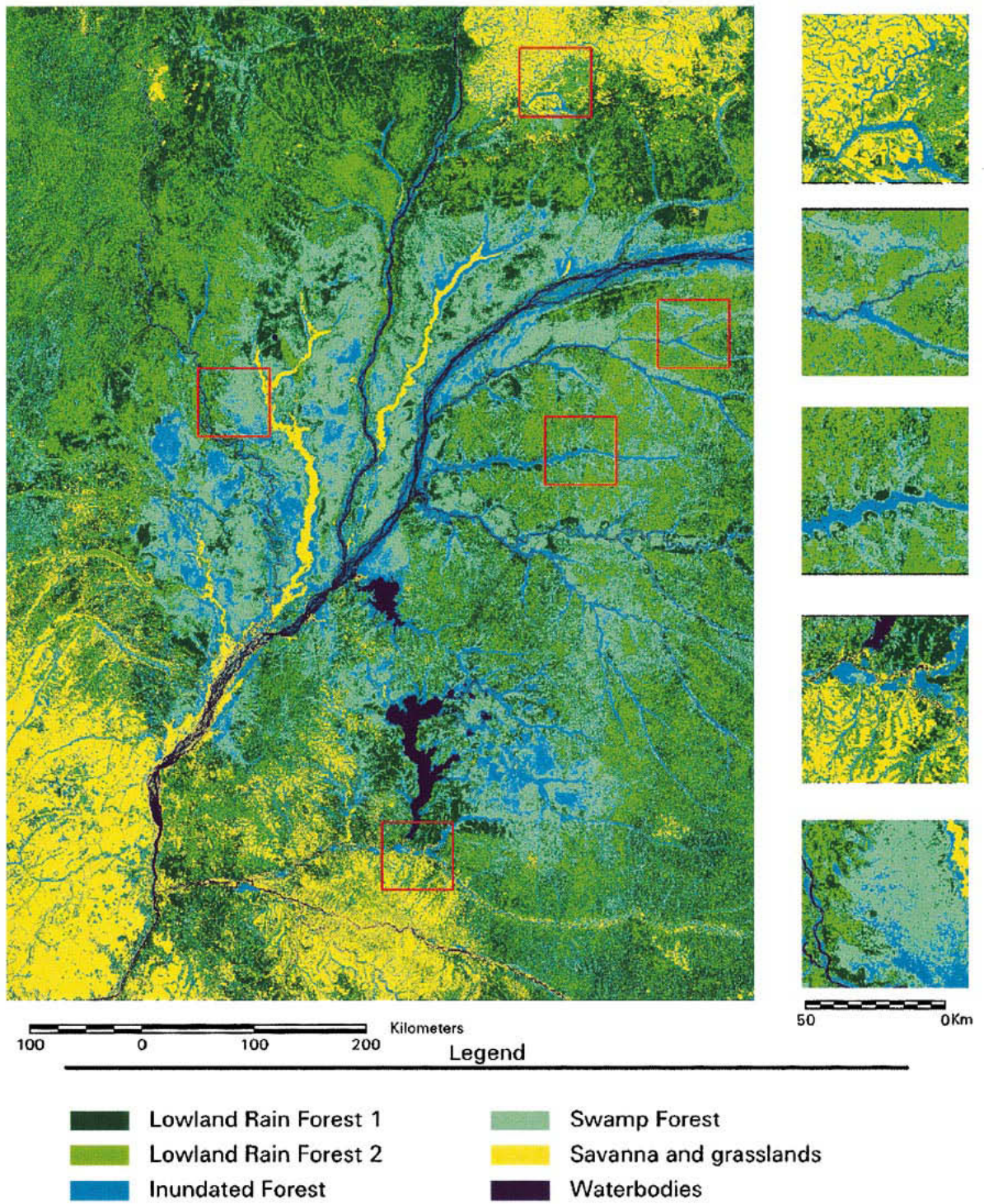

Fig. 12. Classification map of the entire Congo river floodplain at 200 m pixel size. The map was generated from the GRFM Africa high water data set (radiometry and texture) using a maximum likelihood classifier and by stratification with the TREES project GIS data. The insets show the reticulated pattern of gallery forests penetrating into the savanna domain at the south and north of the Congo basin and the presence of swamp forests in the depressions.

locally as food source and cotton for export trading. These fields with bare soil or low biomass vegetation exhibit lower L-band backscatter than the surrounding areas with higher biomass trees. In the northeast area of the picture, very dark patterns correspond to a region with more intensive agricultural practices due to the presence of a development project.

Derivation of regional scale vegetation maps from the GRFM mosaics calls for automatic thematic information extraction techniques. In this direction the first attempts using a simple supervised classification have already produced very promising results. As an example, a thematic map of the swamp and lowland rain forest in the entire Congo river basin at 200 m pixel size is reported in Fig. 12.

The map constitutes a significant update in the information on biomes like the swamp forests in the Congo floodplain that were thus far not well documented at a continental scale. Validation

of the classification accuracy, a topic of central importance in continental scale studies, is under way and will be reported in a future paper.

IX. Summary and Future Perspectives

We have given on overview of the main technical aspects related to the compilation and the validation of the wide-area radar map of the tropical forest domain in Africa, an effort which is part of the GRFM Project.

The most salient characteristics of the GRFM Africa mosaic can be summarized as follows.

- Multitemporal and continental scale data set: Continuous coverage of tropical Africa at two dates from the west coast in Sierra Leone to the east coast in Kenya and Tanzania, covering a distance of some 6000 km, was obtained by the assemblage of more the 3900 JERS-1 SAR scenes.
- Multiresolution approach: Generation of a pyramid of products (reflectivity and texture maps) at different spatial resolutions to accommodate the needs of different types of thematic analyses. Starting from the NASDA level 2.1 SAR images at 12.5 m pixel size, the baseline mosaics are generated at 100 m pixel size, and lower resolution maps at dyadic scales down to 1.6 km.
- High internal geometric consistency of the mosaics: A multitemporal block adjustment algorithm based on tie-pointing between neighboring images gives a figure of 56 m for the RMSE. This also means that coregistration at subpixel accuracy is achieved between the two dates.
- Validated absolute geolocation accuracy: Using ground control points derived from the World Vector Shoreline data in the block adjustment and in the validation process a RMSE of 240 m was measured. This absolute geolocation accuracy probably constitutes a first in wide area radar mapping.
- Revised radiometric calibration to minimize artifact: A semiautomatic calibration method is applied in the mosaic compilation process to correct radiometric artifacts introduced mainly by the sensor's attitude errors. Although the mosaic cannot be considered a radar cross section map, it is still an approximation of the radar reflectivity suitable for the generation of thematic products either by visual interpretation or by automatic supervised image classification.
- Richness in thematic information content: Thanks to the characteristics of the JERS-1 L-band radar a number of very important features of great importance for land applications such as vegetation mapping, geomorphology, and cartography can be readily delineated in the GRFM Africa mosaics. This puts this product in a firm position for its exploitation in global environmental studies.
- Breadth of scope: The breadth of scope of the project, due to the intrinsic global (at ecosystem level) nature of the target and the involvement of several partners in a large international collaborative effort has brought forth several added value consequences. Among these are the arousal of the remote sensing community's awareness and consensus on the potential of wide area high resolution radar mapping for global environmental studies, the development of advanced processing methods, the establishment of a common technological platform through the shared experience of the involved partners, which will be the basis for bridging the GRFM approach over to future pursuits, with more global and operational characteristics.

The GRFM Africa project is now entering a second phase where the focus is on geophysical parameters retrieval and in general on automatic thematic information extraction. Other avenues currently being explored are the fusion with the ERS-1 C-band Africa mosaic and with other optical sensors' data sets. On the other hand, development of more sophisticated classification techniques that would fully exploit the multiresolution properties of the GRFM mosaics is under way, in particular at JPL. The reader is referred to [27], [28] for some preliminary results.

The GRFM Africa data set represents a milestone in wide area radar mapping of the Earth's ecosystems. However, at this stage, it is a foundation whose value will be fully exploited only if on top of it, geoscience applications will be developed by the science community at large for providing adequate information on local and global environmental issues to the policy and decision makers. In this perspective, the availability of the GRFM present and future products will be a key asset. In response to these requirements, a CD-ROM set with the GRFM Africa baseline products is already available for distribution to interested parties.

Acknowledgment

The authors would like to thank NASDA for their fundamental role in the GRFM project, a role that unfolded from the vision of new ways and avenues for the utilization of the JERS-1 capabilities back in 1995 at the time of the project conception through a continuous and excellent technical support at all stages: spacecraft operation, data processing, and the support to the science program through a very generous data distribution policy. All the NASDA staff involved in GRFM is credited with the successful outcome of the project. In particular, we would like to thank T. Tanaka, former NASDA EORC Director, M. Shimada, Chief Architect of the NASDA SAR processing chain, A. Rosenqvist, former GRFM Manager at NASDA. They can probably be considered the project's fathers, together with A. Freeman and B. Chapman of NASA JPL. The authors would also like to thank the Technical Staff involved in GRFM, JRC SAI Global Vegetation Monitoring Unit GVM, and at NASA JPL, who played different, but equally important, roles in the project. In particular, they would like to thank P. Siqueira, NASA JPL, for his suggestions on the block adjustment algorithm, T. Richards, TREES Information System Manager, for his contribution to the geolocation, G. Perna and E. Franchino, A. Tournier, U. Costantini, B. Glenat of the GRFM Africa Software Development Team, P. Janvier for the GIS technology, F. Achard, TREES Project Manager, A. Belward, GVM Unit Manager, and R. Winter SAI Director. They would also like to thank J. M. Gregoire, E. Bartholome, JRC GVM, and M. Leysen, Flemish Institute of Technological Research, for their help in the GRFM thematic validation, and F. Holecz and P. Pasquali, formerly with the Remote Sensing Laboratories University of Zuerich, now with SARMAP Switzerland, for their contribution to the calibration algorithms.

Finally, they would like to thank J. P. Malingreau, the man whose vision was instrumental back in 1994 in setting up the whole wide area radar vegetation mapping activity at the JRC GVM. The anonymous reviewers are also thanked for their valuable suggestions and comments.

REFERENCES

[1] A. Rosenqvist, "The global rainforest mapping project by JERS-1 SAR," *Int. Archives Photogramm. Remote Sensing*, pt. B7, vol. 31, pp. 594–598, 1996.

[2] A. Rosenqvist, M. Shimada, B. Chapman, A. Freeman, G. F. De Grandi, S. Saatchi, and Y. Rauste, "The global rain forest mapping project—A review," *Int. J. Remote Sensing: Special Issue on Global and Regional Land Cover Characterization from Satellite Data*.

[3] P. Mayaux, F. Achard, and J. P. Malingreau, "Global tropical forest area measurements derived from coarse resolution satellite imagery: A comparison with other approaches," *Environ. Conservation*, vol. 25, no. 1, pp. 37–52, 1998.

[4] D. Skole and C. Tucker, "Tropical deforestation and habitat fragmentation in the amazon: Satellite data from 1978-1988," *Science*, vol. 260, pp. 1905–1910, 1993.

[5] J. P. Malingreau and C. Tucker, "Large scale deforestation in the southern amazon basin of Brazil," *Ambio*, vol. 17, pp. 49–55, 1988.

[6] P. Mayaux, G. F. De Grandi, and J. P. Malingreau, "Central Africa forest cover revisited: A multi-satellite analysis," *Remote Sens. Environ.*, vol. 71, pp. 183–196, 2000.

[7] G. F. De Grandi, J. P. Malingreau, and M. Leysen, "The ERS-1 central Africa mosaic: A new perspective in radar remote sensing for the global monitoring of vegetation," *IEEE Trans. Geosci. Remote Sensing*, vol. 37, pp. 1730–1746, May 1999.

[8] S. G. Mallat, "A theory for multi-resolution signal decomposition: The wavelet representation," *IEEE Trans. Pattern Anal. Machine Intell.*, vol. 11, p. 674, July 1989.

[9] S. G. Mallat and W. L. Hwang, "Singularity detection and processing with wavelets," *IEEE Trans. Inform. Theory*, vol. 38, no. 2, pp. 617–642, March 1992.

[10] M. Simard, G. F. De Grandi, K. P. B. Thomson, and G. B. Benie', "Analysis of speckle noise contribution on wavelet decomposition of SAR images," *IEEE Trans. Geosci. Remote Sensing*, vol. 36, pp. 1953–1962, Nov. 1998.

[11] M. Simard, G. F. De Grandi, and K. Thomson, "Adaptation of the wavelet transform for the construction of multi-scale texture maps of SAR images," *Can. J. Remote Sensing*, vol. 24, pp. 264–285, Sept. 1998.

[12] M. Simard, G. F. De Grandi, S. Saatchi, M. Leysen, and K. P. B. Thomson, "Processing and analysis techniques for continental scale radar maps of the tropical forest," in *Proc. IEEE IGARSS'97 Symp.*, Singapore, 1997, pp. 1890–1892.

[13] F. De Grandi, J. S. Lee, D. Schuler, G. Kattenborn, F. Holecz, P. Pasquali, and M. Simard, "Singularity analysis with wavelets in polarimetric SAR imagery for vegetation mapping applications," in *Proc. IEEE IGARSS'99*, Hamburg, Germany, 1999, Paper E05-06.

[14] S. M. Kay, *Fund.Statistical Signal Processing*. Englewood Cliffs, NJ: Prentice-Hall, 1993, pp. 294–299.

[15] J. S. Lee, "Refined filtering of image noise using local statistics," *Comput. Graph. Image Processing*, vol. 15, pp. 380–389, 1981.

[16] A. V. Oppenheim and R. W. Schafer, *Discrete Time Signal Processing*. Englewood Cliffs, NJ: Prentice-Hall, 1989, pp. 63–67.

[17] L. Mirsky, *An Introduction to Linear Algebra*. New York: Dover, 1990, p. 156, 158.

[18] Y. Rauste, T. Richards, G. F. De Grandi, G. Perna, E. Franchino, and A. Rosenqvist, "Compilation and validation of the GRFM Africa SAR mosaics using multi-temporal block adjustment," *JERS-1 Sci. Prog. 99 PI Reps., NASDA EORC*, pp. 99–108, Mar. 1999.

[19] W. H. Press, B. P. Flannery, S. A. Teukolsky, and W. T. Vetterling, *Numerical Recipes in C: The Art of Scientific Computing*. Cambridge, U.K.: Cambridge Univ. Press, 1992, pp. 84–85.

[20] P. Lecomte and E. Attema, "Calibration and validation of the ERS-1 wind scatterometer," in *Proc. First ERS-1 Symp. Space at the Service of our Environment*, Cannes, France, Nov. 4–6, 1992, pp. 19–29.

[21] M. Shimada, "Radiometric and geometric calibration of JERS-1 SAR," *Adv. Space Res.*, vol. 17, no. 1, pp. 79–88, 1996.

[22] A. H. Devol, J. E. Richey, W. A. Clark, and S. L. King, "Methane emissions to the troposphere from the Amazon floodplain," *J. Geophys. Res. 93*, pp. 1583–1592, 1998.

[23] A. Rosenqvist, C. Birket, E. Bartholome, and G. F. De Grandi, "Using satellite altimetry and historical gauge data for validation of the hydrological significance of the JERS-1 SAR (GRFM) mosaics in central Africa," in *Proc. IGARSS'99*, Hamburg, Germany, 1999, EE10_02.

[24] A. Rosenqvist, B. R. Forsberg, T. Pimentel, and J. E. Richey, "Using JERS-1 L-band SAR to estimate methane emissions from the Jau river floodplain," in *IEEE IGARSS'98*, Seattle, WA, July 6–10, 1998, pp. 1623–1625.

[25] F. De Grandi, P. Mayaux, J. P. Malingreau, A. Rosenqvist, S. Saatchi, and M. Simard, "New perspectives on global ecosystems from wide-area radar mosaics: Flooded forest mapping in the tropics," *Int. J. Remote Sensing: Special Issue on Global and Regional Land Cover Characterization from Satellite Data*.

[26] G. F. De Grandi, P. Mayaux, A. Rosenqvist, Y. Rauste, S. Saatchi, M. Simard, and M. Leysen, "Flooded forest mapping at regional scale in the central Africa congo river basin: First thematic results derived by ERS-1 and JERS-1 radar mosaics," in *Proc. Sec. Int. Workshop on Retrieval of Bio- and Geophys. Parameters from SAR Data, ESA ESTEC*, Oct. 21–23, 1998.

[27] S. Saatchi, G. F. De Grandi, M. Simard, and E. Podest, "Classification of JERS-1 image mosaic of central Africa using a supervised multi-scale classifier of texture features," in *Proc. IEEE IGARSS'99*, Hamburg, Germany, 1999, EE10-06.

[28] M. Simard, S. Saatchi, and G. F. De Grandi, "Classification of the Gabon SAR mosaic using a wavelet based rule classifier," in *Proc. IEEE IGARSS'99*, Hamburg, Germany, 1999, EE10-07.

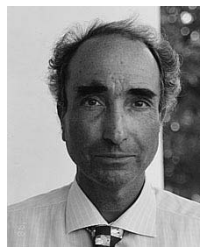

Gianfranco (Frank) De Grandi (M'90–SM'96) received the Ph.D. in physics engineering (with honors) from the Politecnico Milano, Milano, Italy, in 1973.

Since 1977, he has been with the European Commission Joint Research Centre (JRC), Ispra, Italy, where he has performed research in signal processing for application areas such as gamma ray spectroscopy, data communications, and radar remote sensing. In 1985, he was a Visiting Scientist with Bell Communications Research, Morristown, NJ, where he participated in the design of METROCORE, one of the first research projects for Gb rate metropolitan area networks. From 1986 to 1989, he headed the signal processing section of the Electronics Division, JRC, where he introduced VLSI design technology and conducted research, in cooperation with Bellcore, on packet video, and in cooperation with ITALTEL Italy on the European digital mobile phone network. In 1989, he joined the Institute for Remote Sensing Applications [now Space Applications Institute (SAI)], where he started a research activity in radar polarimetry in the Advanced Techniques unit. Since 1994, he has been Principal Scientist for radar remote sensing in the Global Vegetation Monitoring unit. Since 1997, he has been Assistant Professor with the Faculte' de Foresterie et Geomatique, Universite' Laval, Quebec, PQ, Canada. His current research interests span a wide gamut, including global scale forest mapping using high resolution spaceborne SAR, multiresolution analyses based on the wavelet representation for texture measures, backscattering multitemporal estimators, topography sensing using polarimetric SAR data, and the statistics of polarimetric synthesized SAR images.

Dr. De Grandi is a senior member of the IEEE Geoscience and Remote Sensing and Signal Processing Societies and a member of the Planetary Society, Pasadena, CA.

Philippe Mayaux received the engineer degree in agronomy and forestry in 1986, and the degree in land planning and the Ph.D. degree from the University of Louvain, Belgium, in 1999.

He has worked for several field projects in Tanzania and Senegal. Since 1995, he has been Coordinator for Africa within the European Commission Tropical Ecosystem Environment monitoring by Satellites (TREES) project. His work has focused on vegetation mapping at regional scale from optical and microwave data and on the problem of scaling in remote sensing. He is involved in many regional and global projects related to forest cover mapping, such as GRFM or GOFC.

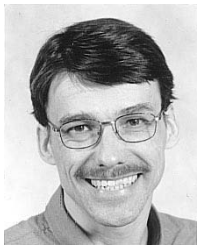

Yrjo Rauste was born in Espoo, Finland, in 1956. He received the M.S. degree in surveying and mapping in 1983 and the Licentiate of Technology in 1989, both from the Helsinki University of Technology, Espoo, Finland.

He has been with Technical Research Centre of Finland (VTT), Espoo, Finland, since 1979, except for visits to other research centers and his military service in 1983. From 1986 to 1987, he was a Visiting Scientist with the Institute for Image Processing and Computer Graphics, Graz Research Center, Graz, Austria. From 1997 to 1999, he was a postdoctoral grant holder with the Joint Research Centre (JRC), European Commission, Ispra, Italy. From 1994 to 1996, he also served as the Secretary of the Finnish Society of Photogrammetry and Remote Sensing. He is currently a Senior Research Scientist in the Remote Sensing group of VTT Automation. His research interests include application of SAR image analysis and processing (especially in forestry applications) and forest fire detection using optical satellite data.

Ake Rosenqvist received the M.Sc. degree from the Royal Institute of Technology, Stockholm, Sweden, in 1988, and the Ph.D. degree in civil engineering from the University of Tokyo, Tokyo, Japan, in 1997.

Since 1997, he has been a Visiting Scientist with the Joint Research Centre, European Commission (JRC SAI), Ispra, Italy, where he is involved in continental scale radar mapping of South America, Africa, and Siberia. He was an Invited Scientist with the National Space Development Agency of Japan (NASDA), Tokyo, Japan, from 1993 to 1997, where he was Project Scientist and Project Coordinator for the JERS-1 SAR Global Rain Forest and Boreal Forest Mapping Projects (GRFM/GBFM). From 1990 to 1993, he was with the Swedish Space Corporation, Stickholm, Sweden, focusing on Dem generation and land cover mapping by optical remote sensing.

Dr. Rosenqvist is currently the Chairman of the ISPRS working group for Global Monitoring (WG VII/5).

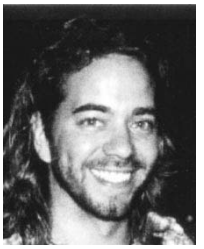

Marc Simard received the B.Sc. degree in physics (with honors) in astrophysics from Queen's University, Quebec, ON, Canada, in 1992, and the M.Sc. and Ph.D. degrees in physics (specializing in radioastrophysics) and geomatic sciences, respectively, from the Universite Laval, Quebec, in 1994 and 1998, respectively.

From 1995 to 1997, he was a Grant Holder with the Space Applications Institute of the Joint Research Center, European Communities (JRC SAI), Ispra, Italy. Since 1998, he has been a National Research Council Research Associate with the Jet Propulsion Laboratory, Pasadena, CA. His research interests include the multiscale analysis and classification of SAR images.

Sasan S. Saatchi received the B.S. and M.S. degrees in electrical engineering from the University of Illinois, Champaign, in 1981 and 1983 respectively, and the Ph.D. degree from the George Washington University, Washington, DC, in 1988 with a concentration in electrophysics and modeling of wave propagation in natural media.

From 1989 to 1991, he was a Postdoctoral Fellow, National Research Council, and worked at the Laboratory for Terrestrial Physics, NASA/Goddard Space Flight Center, Greenbelt, MD, on the hydrological application of active and passive microwave remote sensing. Since April of 1991, he has been a Scientist with the Radar Science and Engineering Section of the Jet Propulsion Laboratory, California Institute of Technology, Pasadena, CA, where he is involved in developing microwave scattering and emission models for soil and vegetated surfaces and retrieval algorithms for estimating geophysical parameters from spaceborne remote sensing instruments. He has been a Principal or Co-Investigator in several interdisciplinary international projects such as FIFE, EFEDA, Magellan, Mac-Hydro, Hapex-Sahel, BOREAS, LCLUC, and LBA. His present research activities include land cover classification, biomass and soil moisture estimation in boreal forests, land use and land cover change, and forest regeneration monitoring over tropical rain forests. His research interests also include wave propagation in disordered/random media and EM scattering theory.

PAPER 4

Radar-based forest biomass estimation

In: International Journal of Remote Sensing 1994.
Vol. 15, No. 14, pp. 2797–2808.
Reprinted with permission from the publisher.

INT. J. REMOTE SENSING, 1994, VOL. 15, NO. 14, 2797–2808

Radar-based forest biomass estimation

Y. RAUSTE, T. HÄME

Technical Research Centre of Finland, Space Technology,
Metallimiehenkuja 10, FIN-02150 Espoo, Finland

J. PULLIAINEN, K. HEISKA and M. HALLIKAINEN

Helsinki University of Technology, Laboratory of Space Technology,
Otakaari 5 A, SF-02150 Espoo, Finland

Abstract. The potential of radar-based tree biomass estimation has been studied using polarimetric SAR data from the Freiburg test site of the MAESTRO 1 Campaign and scatterometer data from a test site in Finland. Using the Freiburg SAR data and polarizaiton synthesis, the most suitable polarization combination was obtained. In *P* band, the maximum correlations, which were found near the linear *HV* polarization, were up to 0·75.

In the Finnish test site, a strong negative correlation (correlation coefficient −0·65) existed between the pine biomass and *X-VV* backscatter. When the combination of *X* and *C* bands (measured by the HUTSCAT scatterometer) was used, a correlation coefficient of 0·81 was obtained.

1. Introduction

The biomass of forests affects the circulation of carbon in the biosphere. Tropical forests are a carbon source, while many temperate and boreal forests are a carbon sink. It has been estimated that the annual build-up of carbon in European forests alone is 50 million tons (Kauppi *et al.* 1992). Forests also produce raw material for a variety of industrial activities. There are large areas in the boreal forest zone where the amount and distribution of forest biomass is poorly known.

Mapping of forest biomass using radar has been studied (e.g., Sader 1987, Hussin *et al.* 1991, Le Toan *et al.* 1991) in recent years. Sader (1987) studied the relationship between *L*-band polarimetric SAR data and the biomass of two pine species (longleaf pine, *Pinus palustris* Mill. and slash pine, *Pinus elliotti* Englem.). The terrain elevation in the study site varied from 3 to 15 m above sea level. Sader found a correlation coefficient of 0·76 between the *L-HV* digital number and biomass in a set of nine stands. The *HH* and *VV* polarizations did not have significant correlation with biomass. The green weight biomass ranged from 25 to 230 t ha^{-1}.

Hussin *et al.* (1991) studied the estimation of slash pine biomass using *L*-band polarimetric SAR data. The age of the stands in the study varied between 4 and 31 years. In a dataset of 35 stands, a coefficient of determination (r^2) 0·97 was obtained with *HV* polarized SAR data. The Box–Cox power transformation was applied to the biomass data before they were used in regression analyses.

Le Toan *et al.* (1991) studied the relationship between multi-band polarimetric SAR data and stem biomass. The study site consisted of homogeneous stands of

0143–1161/94 $10.00

maritime pine (*Pinus pinaster* Ait.). The forest had been planted on flat soil. The age varied from 0 to 42 years and the stem biomass from 0 to 105 t ha^{-1}. High correlations between the stem biomass and the relative backscattering coefficient were obtained for *VH*, *HH*, and *VV* polarizations in *P* band (r^2 values of 0·95, 0·90 and 0·88, respectively). The relationship between the stem biomass and the relative backscattering coefficient was linear throughout the whole biomass range (0–105 t ha^{-1}) and no saturation was observed.

Owing to differences in the species composition or forest management practices, the test sites of these studies are not representative of large natural forests in the Eurasian part of the boreal forest zone.

The study described in this article was carried out in the context of the MAESTRO 1 Campaign, organized jointly by the Joint Research Centre of the European Communities and the European Space Agency.

The possibilities for the use of radar in tree biomass estimation are studied using polarimetric SAR data from the Freiburg test site. Scatterometer data from a test site in Ruotsinkylä in Finland are studied to supplement and enlarge the findings of the study based on SAR data.

Processing and analysis of the SAR data has been carried out mainly by the Instrument laboratory of the Technical Research Centre of Finland. Measurement, processing and analysis of the scatterometer data have been carried out by the Laboratory of Space Technology of the Helsinki University of Technology.

2. Study sites and measurement data

2.1. *Freiburg test site and SAR data*

Data from the Freiburg test site of the MAESTRO 1 Campaign was used in the study. The test site (centre at 48°02′25″ N, 8°22′01″ E) is located near the town of Villingen–Schwenningen in south-west Germany. Terrain elevation at the test site varies between 750 and 970 metres above sea level. The area is dominated by temperate coniferous forests. Norway spruce (*Picea abies* Karst.) covers 1370 ha, Scots pine (*Pinus sylvestris* L.) 280 ha and Silver fir (*Abies alba* Mill.) approximately 200 ha of the 1920 ha study area. Deciduous trees are distributed sparsely in the area. Stem volume in the study area varies between 0 and 830 m^3 ha^{-1}. Age varies from 0 to 180 years.

The ground data from the test site included a forest map at a scale of 1:10 000 and standwise forest inventory data for 230 forest stands. The map and forest inventory data were based on a field inventory in 1980. A trial, based on the average relationship between stand age and stem volume, was made to update the stem volume information. Ground observations in June 1991 revealed that this updating was very unreliable. The original ground data were used in analyses.

Direct measurements of the biomass of the forest were not available. Stem volume was used to represent the forest biomass. According to other studies (Häme *et al.* 1992), the stem volume (in m^3 ha^{-1}) could be approximately converted into dry biomass of trees (in kg ha^{-1}) by multiplying the stem volume by 600. In the absence of more accurate data on the biomass in the test site, this simple transformation has been used in this study where standwise data are analysed. For example, a stem volume of 800 m^3 ha^{-1} corresponds approximately to a dry biomass of 480 000 kg ha^{-1} (48 kg m^2).

Two scenes of the Freiburg SAR data (Churchill *et al.* 1990) were used: scenes 1105 and 1107. The SAR data (fully polarimetric images in *C*, *L* and *P* bands) were

acquired using the AIRSAR sensor (Held *et al.* 1988). The incidence angle in the study site ranged from 35° to 55° in scene 1105 and from 48° to 55° in scene 1107. The SAR data were acquired on 18 August 1989 with no rain on the preceeding two days.

Figure 1 shows the processing steps applied to the data before the data were used in the analyses (Rauste 1992). The topography normalization utilizes the equation:

$$R_{\text{norm}} = \frac{R_{\text{orig}}\sqrt{\tan(\theta_r)}}{\sqrt{\tan(\theta_{\text{nom}})}} \tag{1}$$

where R_{norm} = normalized radar return (amplitude), R_{orig} = original radar return (amplitude), θ_r = incidence angle in range direction, and θ_{nom} = nominal incidence angle. The angle θ_r was computed for each pixel using a digital elevation model. Standwise averaged Stokes matrix data were used in the search for the best band polarization combination for tree biomass mapping.

2.2. *Ruotsinkylä test site and scatterometer data*

The helicopter-borne scatterometer measurements were performed in the Ruotsinkylä research area of the Finnish Forest Research Institute. The test site is located near Helsinki (centre at 60°21′23″ N, 25°00′48″ E). The total length of test lines for helicopter-borne scatterometer measurements was 4 km. The dominant tree species in the test lines were Scots pine and Norway spruce. The test lines were divided into 20 m by 20 m sample plots for the data analysis. The measured forest characteristics of each sample plot included:

(*a*) average tree height,
(*b*) mean tree stem diameter at a height of 1·3 m,
(*c*) mean tree stem diameter at a height of 6 m and
(*d*) density (number of tree stems per hectare).

Detailed information on the ground truth database is given in Hyyppä and Hyyppä (1992). The basal area ($m^3\,ha^{-1}$) was calculated on the basis of stem diameter measurements at a height of 1·3 m. The stem volume was calculated on the basis of stem diameter measurements at 1·3 m and 6 m and tree height measurements.

In this analysis, a total of 150 sample plots were used; 96 of these were pine dominated and the rest were spruce dominated sample plots. The tree height for the sample plots varies from 1 to 27 m, and the stem volume per hectare varies from 0 to 370 $m^3\,ha^{-1}$.

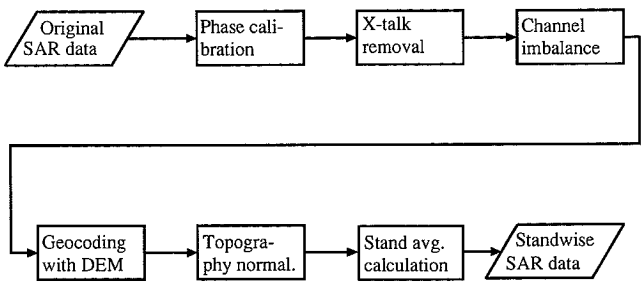

Figure 1. Preprocessing steps applied to SAR data.

The scatterometer data were acquired with the HUTSCAT instrument under winter conditions in December 1991. The ground surface temperature was −5° C, and the thickness of snow-cover was between 0 and 5 cm. The HUTSCAT scatterometer is an 8-channel helicopter-borne non-imaging ranging scatterometer operating at *C* and *X* bands (5 and 10 GHz) at *HH*, *VV*, *VH* and *HV* polarizations (Hyyppä and Hallikainen 1991). The scatterometer measures the backscattered power versus range along the flight line (in 1-m intervals). The backscattering coefficient of the target is calculated from the radar return versus range profiles. A video camera is used for positioning the radar measurements in relation to the corresponding forest sample plots. The application of the HUTSCAT instrument for forest measurements is described in Hallikainen *et al.* (1990).

The HUTSCAT instrument is both internally and externally calibrated. The internal calibration data are recorded for each measurement sequence. The absolute level of internal calibration is determined by external calibration, performed with Luneberg lenses and active radar calibrators.

The HUTSCAT scatterometer is an FM-CW radar that measures the backscattering properties of a target versus range in real time. This is accomplished by performing a 512-point FFT to the intermediate frequency of the radar. The radar cross-section of a target (in dB) is calculated by summing the power received from the target for different intermediate frequencies (ranges), and by using internal calibration. This result is directly comparable with the SAR measurement. The backscattering coefficient (σ^0, expressed in dB) can be determined by dividing the radar cross-sections of different ranges with the illuminated areas corresponding to different ranges.

3. Analysis methods

In the analysis of the polarimetric SAR data, a systematic search was employed to find the best band polarization combination for tree biomass mapping. Starting with the standwise average Stokes matrix data and the standwise stem volume data, the following operations were carried out for each possible polarization combination (combination of transmit orientation, transmit ellipticity, receive orientation and receive ellipticity):

(*a*) the received power was calculated for each stand using polarization synthesis (van Zyl *et al.* 1987),
(*b*) the linear correlation coefficient between the stem volume and the radar amplitude (square root of the received power) was calculated.

The polarization combination that gave the highest correlation with stem volume was considered to be the best for biomass mapping. The space of all possible polarization combinations was processed in a grid with a step of 10°. The polarization optimization described above was carried out separately for each radar band.

Linear regression analysis was used, in the analysis of both SAR and scatterometer data, to estimate the accuracy with which the tree stem volume can be estimated from SAR data. In the analysis of the polarimetric SAR data, the ground data was split into two subsets: one for determination of the linear regression model (the learning set) and another for testing the model. Correlation coefficients were computed for the whole ground dataset. When the correlation coefficient exceeded

0·4, the estimation error E for the linear model was computed:

$$E=\sqrt{\frac{\Sigma(V_{\text{est}}-V_{\text{real}})^2}{n-1}} \tag{2}$$

where V_{est} is the stem volume estimate given by the model, V_{real} is the stem volume in the ground data and n is the number of observations in the testing set.

For the analysis of the HUTSCAT data, the average backscattering coefficient of each forest sample plot was calculated. The average value was taken from 20 scatterometer measurements for a sample plot.

4. Estimation of tree biomass from SAR data

The polarization optimization procedure decribed earlier was applied over the whole 4-dimensional space of receive and transmit orientation and ellipticity. The highest stem-volume–radar correlations were found in P band and close to the original HV polarization. As the highest correlations were found close to the original polarizations (HH, HV and VV) the following concentrates on the original polarizations. Table 1 shows the correlations obtained for each band. The last line of the table was obtained with data from scene 1107 (larger incidence angle) and the other lines with data from scene 1105. The L-band correlations were studied using two datasets: (1) the whole dataset with stem volume 0–830$\text{m}^3\,\text{ha}^{-1}$ and (2) the subset with stem volume 0–170$\,\text{m}^3\,\text{ha}^{-1}$. The L-band amplitude seems to reach its saturation level somewhere close to 150$\,\text{m}^3\,\text{ha}^{-1}$. Thus, the correlation between L-band amplitude and stem volume is higher in the stem volume range 0–170$\,\text{m}^3\,\text{ha}^{-1}$ than in the whole range of 0–830$\,\text{m}^3\,\text{ha}^{-1}$. The size of the 0–170$\,\text{m}^3\,\text{ha}^{-1}$ ground dataset (72 stands) did not allow splitting into the learning and testing sets.

Figure 2 shows the radar HV amplitude as a function of stem volume for C, L and P bands. The dashed lines in the P-band diagram show the confidence limits of the regression model at 1 per cent confidence. As observed in other studies (e.g. Kasischke *et al.* 1991, Dobson *et al.* 1991) the backscatter saturates at a biomass level that depends on the wavelength. The relationship between the stem volume and radar amplitude is linear in P-HV. In L-HV, the radar amplitude first increases with

Table 1. SAR backscatter (amplitude) *vs.* stem volume.

Band-polarization	Stem volume range ($\text{m}^3\,\text{ha}^{-1}$)	Correlation coefficient	Estimation error ($\text{m}^3\,\text{ha}^{-1}$)	
			Learning	Testing
C-HV	0–830	−0·37	—	—
C-HH	0–830	−0·33	—	—
C-VV	0–830	−0·06	—	—
L-HV	8–830	−0·19	—	—
L-HV	0–170	0·47	41·7	—
L-HH	0–170	0·50	40·9	—
L-VV	0–170	0·43	42·5	—
P-HV	0–830	0·73	135·6	141·7
P-HH	0–830	0·31	—	—
P-VV	0–830	0·21	—	—
P-HV (1107)	0–830	0·65	145·9	168·2

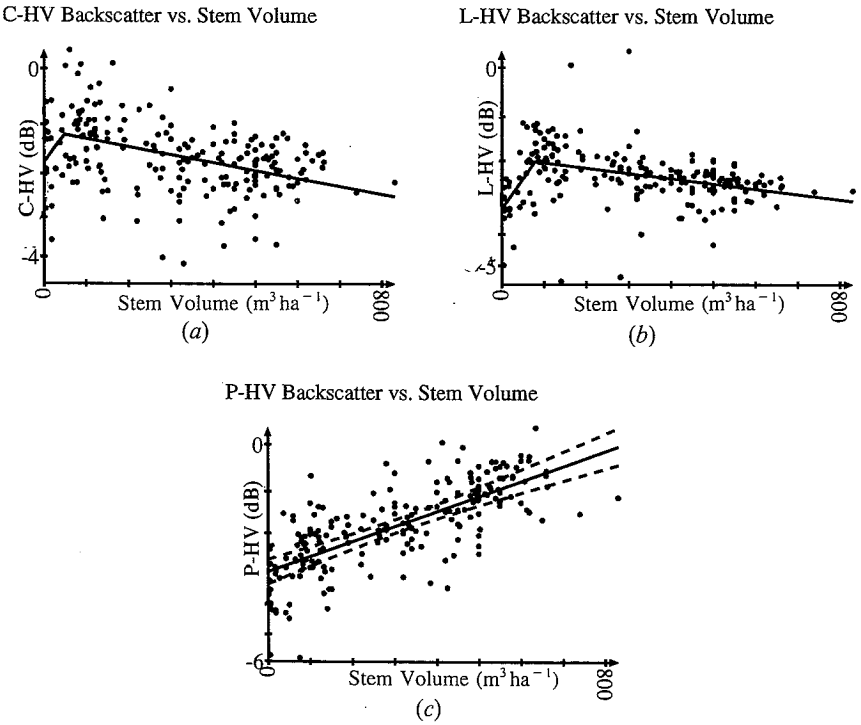

Figure 2. Radar amplitude as a function of stem volume in the Freiburg test site. (*a*) *C*-band; (*b*) *L*-band; (*c*) *P*-band.

increasing stem volume content. After a stem volume of about $120\,m^3\,ha^{-1}$, the radar amplitude decreases with increasing stem volume. A stem volume of $120\,m^3\,ha^{-1}$ corresponds to a dry biomass of about $7\,kgm^{-2}$. In *C* band, the radar amplitude reaches its saturation level at about $60\,m^{-3}\,ha^{-1}$ (about $3{\cdot}5\,kgm^{-2}$ dry biomass).

Figure 3 shows the correlation coefficient between the stem volume and the radar amplitude as a function of the polarization combination. The possible polarization combinations form a 4-dimensional space (receive orientation, receive ellipticity, transmit orientation and transmit ellipticity). Only two 2-dimensional subsets of the 4-dimensional space are shown in figure 3. In the copolarized diagram, the receive orientation equals the transmit orientation and the receive ellipticity equals the transmit ellipticity. In the cross-polarized diagram, the receive orientation is at right angles to the transmit orientation and the receive ellipticity equals the negative transmit ellipticity. In *P* band, the highest correlations form a very narrow peak around the linear *HV* polarization. In *L* band, the correlations are lower but less dependent on the polarization combination. In the *L*-band diagram, only those stands where the stem volume was less than $170\,m^3\,ha^{-1}$ were included.

As no absolute calibration was carried out on the SAR, the coefficients of the linear regression models between the SAR amplitude and stem volume are not reported here. The models were of the form:

$$V_{est} = ax + b, \tag{3}$$

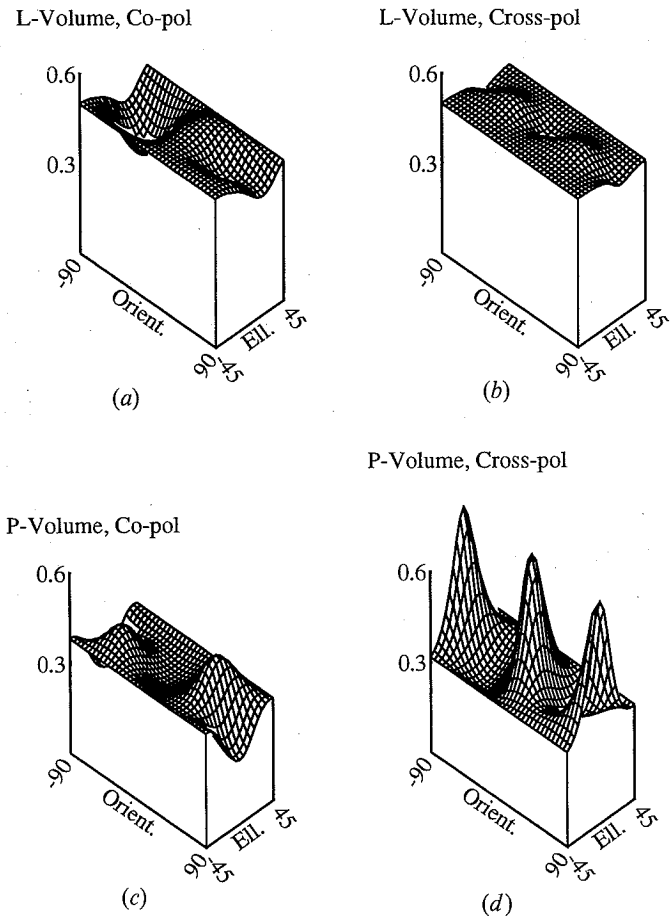

Figure 3. Correlation coefficient between the radar amplitude and stem volume as a function of polarization combination (Freiburg test site). (*a*) *L*-band, co-pol.; (*b*) *L*-band, cross-pol.; (*c*) *P*-band, co-pol.; (*d*) *P*-band, cross-pol.

where a and b are the coefficients of the model and x is the radar amplitude. Figure 4 shows the stem volume estimate using *P-HV* data.

5. Estimation of tree biomass from scatterometer data

Tables 2 and 3 show the correlation coefficients between forest characteristics and different scatterometer channels. The results imply that the response of the *C*-band channels to the changes in forest characteristics is negligible. The channel showing the highest correlation between the stem volume and the backscattering coefficient is *X*-band *VV* polarization (figure 5). The backscattering coefficient decreases with increasing stem volume, except for stem volume values smaller than $50\,m^3\,ha^{-1}$.

Figure 6 demonstrates the feasibility of a multi-channel instrument for stem volume estimation. The results shown in figure 6 were obtained by a multiple linear regression model for the stem volume (only pine sample plots were employed). The

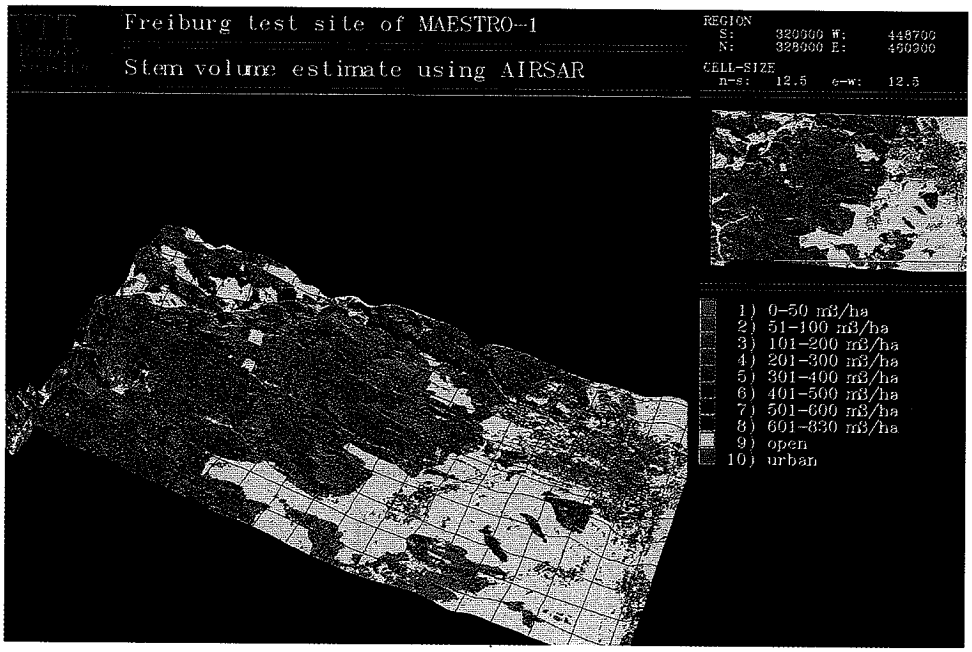

Figure 4. SAR-based (*P-HV*) stem volume estimate of the Freiburg test site.

correlation coefficient is 0·75 ($r^2 = 0{\cdot}56$). The same equation gives a correlation coefficient of 0·81 ($r^2 = 0{\cdot}66$), when two neighbouring sample plots are averaged in both the ground truth data and the scatterometer data.

6. Discussion

The highest correlations between tree biomass and backscatter found in the Freiburg test site were similar but slightly lower than those found by Hussin *et al.* (1991) or Le Toan *et al.* (1991). Several factors may have contributed to the lower correlations. The topography of the Freiburg test site was more pronouncced than that in the French test site studied by Le Toan *et al.* (1991). Residual topographic effects (after topographic normalization) have contributed to the lower correlation in the Freiburg test site. The topography could also explain the lower *HH* correlation, which according to Beaudoin *et al.* (1992) depends strongly on local slope. The stands in the Freiburg test site were mainly mixed stands and not single-

Table 2. Correlation coefficients (r) for the whole Ruotsinkylä dataset (pine- and spruce-dominated sample plots); 150 sample plots.

	C-HH	*C-HV*	*C-VH*	*C-VV*	*X-HH*	*X-HV*	*X-VH*	*X-VV*
Stem volume	−0·08	0·02	0·00	−0·02	−0·37	−0·34	−0·35	−0·57
Basal area	−0·02	0·07	−0·03	−0·03	−0·20	−0·23	−0·22	−0·40
Mean diameter	−0·03	0·03	−0·01	−0·04	−0·30	−0·35	−0·32	−0·49
Density	0·07	0·12	−0·14	−0·01	0·18	0·34	0·33	−0·25
Average height	−0·17	−0·20	−0·12	−0·10	−0·38	−0·40	−0·39	−0·46

Table 3. Correlation coefficients (r) for pine-dominated sample plots in the Ruotsinkylä test site; 96 sample plots.

	C-HH	*C-HV*	*C-VH*	*C-VV*	*X-HH*	*X-HV*	*X-VH*	*X-VV*
Stem volume	−0·03	0·08	0·11	0·08	−0·44	−0·59	−0·55	−0·65
Basal area	0·15	0·30	0·22	0·01	−0·12	−0·24	−0·22	−0·29
Mean diameter	0·12	0·12	0·13	0·03	−0·27	−0·49	−0·40	−0·49
Density	0·03	0·09	0·09	−0·05	0·19	0·36	−0·34	0·33
Average height	−0·07	−0·20	0·02	0·03	0·36	−0·45	−0·40	−0·42

species stands as in Hussin *et al.* (1991) or Le Toan *et al.* (1991). Also, the range of biomass in the Freiburg test site was larger than that in Hussin *et al.* (1991) or Le Toan *et al.* (1991). The relatively low accuracy (due to a 9-year interval between the forest inventory and the SAR image acquisition) may also have contributed to the lower correlation.

In the analysis of the Freiburg SAR data, a positive correlation between *P-HV* backscatter and tree biomass was found in the biomass range of 0–50 kgm^{-2}. In *L*-band, there was a positive correlation at 0–7 kgm^{-2} after which the backscatter decreased slowly with increasing biomass. In *C* band, there was a weak positive correlation in the range 0–3·5 kgm^{-2} after which the backscatter decreased more rapidly than in *L* band.

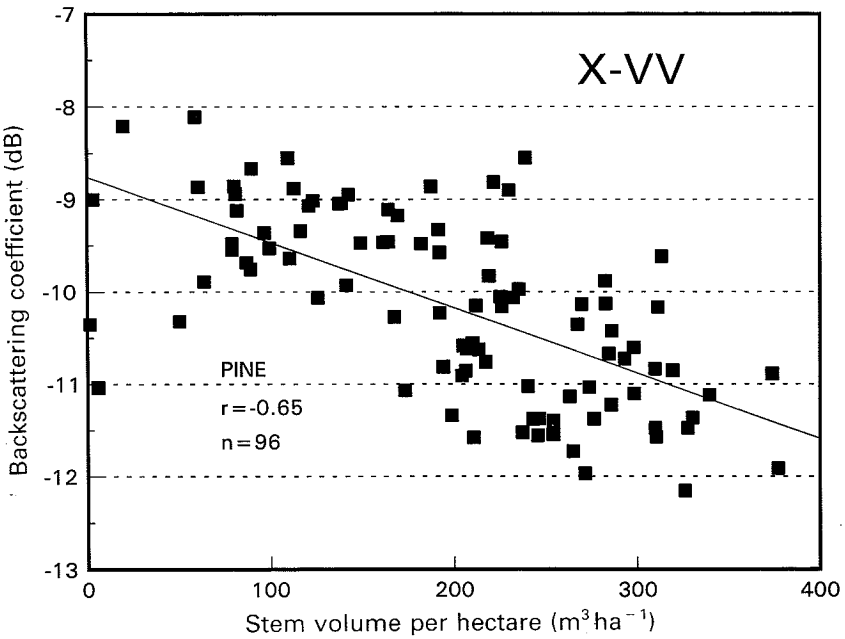

Figure 5. Backscattering coefficient as a function of stem volume per hectare for *X*-band *VV* polarization (Ruotsinkylä test site). Excluding data points with a stem volume below 50 $m^3 ha^{-1}$ increases the correlation coefficient (r) from 0·65 to 0·71. Measurements were made on 17 December 1991.

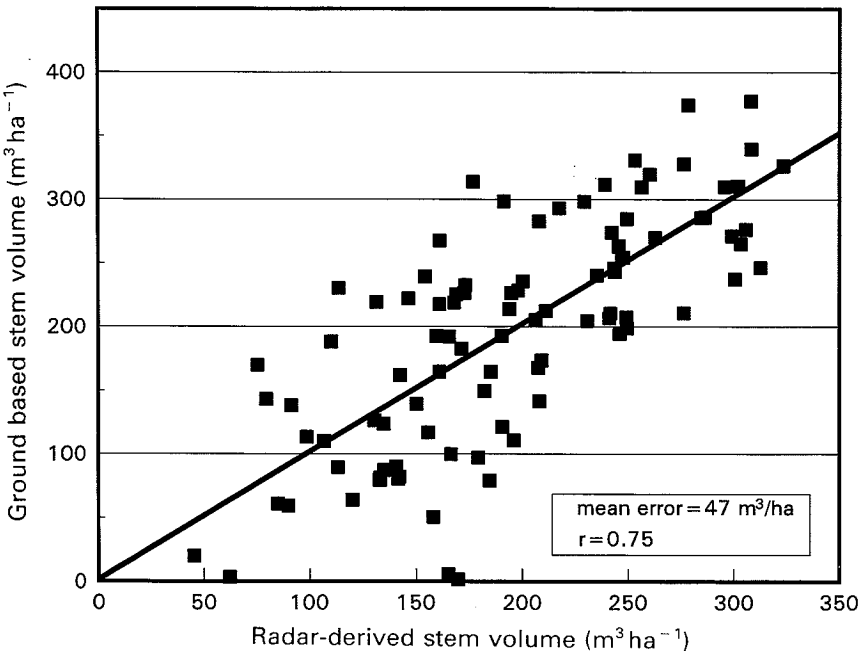

Figure 6. Ground-based volume versus radar-based estimate from multiple linear regression equation employing *X-VV*, and *C*- and *X*-band cross-polarized channels (Ruotsinkylä-test site). Pine forest 17 December 1991. The formula used to calculate the radar-derived stem volume was:

$$V(\mathrm{m^3\,ha^{-1}}) = 657 - 637\frac{\sigma^0_{C\text{-}VH}}{\sigma^0_{X\text{-}HV}} - 165\frac{\sigma^0_{C\text{-}HV}}{\sigma^0_{X\text{-}VH}} - 28\,\sigma^0_{X\text{-}VV}$$

In the analysis of the scatterometer data, the *C*-band backscatter was found to be almost independent of biomass. In *X* band, there was a positive correlation at 0–25 $\mathrm{kgm^{-2}}$ after which the backscatter decreased rapidly with increasing biomass. The decrease is most likely to be due to increased attenuation of the ground–trunk backscattering and increased attenuation of the direct backscattering from the ground. Figure 7 shows a schematic representation of the radar backscatter at *P*, *L*, *C* and *X* bands.

The *C* band of the SAR aboard the ERS-1 satellite does not seem to be very promising for tree biomass estimation. Two types of radar sysems could be used in tree biomass mapping: (1) a system with a long wavelength and cross-polarization (*P-HV*) or (2) a system with a short wavelength (*X-VV*). In the first case, the correlation between backscatter and biomass is positive. In the second case, the correlation is negative. In areas where the biomass level is less than about 10 $\mathrm{kgm^{-2}}$, forest biomass could also be mapped with SAR in *L* band, which is present aboard an existing satellite (JERS-1).

Acknowledgments

The authors would like to thank the Finnish Technology Development Centre TEKES and the Central Association of Finnish Forest Industries (Suomen Metsäteollisuuden Keskusliitto) for funding the study.

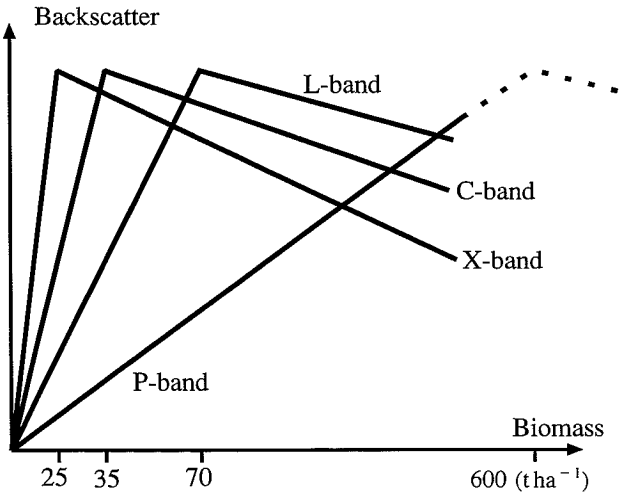

Figure 7. Schematic representation of the radar backscatter as a function of tree biomass at *P*, *L*, *C* and *X* band.

References

BEAUDOIN, A., LE TOAN, T., HSU, C., HAN, H., KONG, J., and SHIN, J., 1992, Simulation of forest backscatter as a function of forest and ground parameters. *Proceedings of IGARSS '92, 22-29 May, Houston, Texas* (Piscataway, New Jersey, USA: Institute of Electrical and Electronics Engineers), pp. 1212-1214.

CHURCHILL P., ATTEMA, E., BAKER, J., BLYTH, K., BIRD, P., BOUMAN, S., UENK, D., VISSERS, M., DROESEN, W., GUYON, D., RIOM, J., HOEKMAN, D., VAN LEEUWEN, H., VAN DER SANDEN, J., KOBRIK, M., SHEN, Y., CARANADE, R., KUNTZ, S., LE TOAN, T., BEAUDOIN, A., MITCHELL, P., WIELOGORSKI, A., and WOODING, M., 1990, MAESTRO 1 airborne synthetic aperture radar (SAR) campaign 1989, Data report, JRC/Ispra and ESA, June 1990 (Ispra, Italy: Joint Research Centre, Institute for Remote Sensing Applications), 198 pp.

DOBSON, M., MCDONALD, K., and SHARIK, T., 1991, Relating the temporal change observed by AIRSAR to surface and canopy properties of mixed conifer and hardwood forests of northern Michigan. *Proceedings of the Third Airborne Synthetic Aperture Radar (AIRSAR) Workshop, 23-24 May,* JPL Publication, 91-30, pp. 34-43.

HALLIKAINEN, M., TARES, T., HYYPPÄ, J., SOMERSALO, E., AHOLA, P., TOIKKA, M., and PULLIAINEN, J., 1990, Helicopter-borne measurements of radar backscatter from forests, *International Journal of Remote Sensing*, **11**, 1179-1191.

HÄME, T., SALLI, A., and LAHTI, K., 1992, Estimation of carbon storage in boreal forests using remote sensing data, Pilot study. In M. Kanninen, and P. Anttila, (editors), *The Finnish research programme on climate change, Progress report* (Helsinki, Finland: Publications of the Academy of Finland 3/92), pp. 250-255.

HELD, D., BROWN, W., FREEMAN, A., KLEIN, J., ZEBKER, H., SATO, T., MILLER, T., NGUYEN, Q., and LOU, Y., 1988, The NASA/JPL multifrequency, multipolarization airborne SAR system, *Proceedings of IGARSS'88 September, Edinburgh, Scotland* (Paris: European Space Agency), pp. 345-350.

HUSSIN, Y., REICH, R., and HOFFER, R., 1991., Estimating slash pine biomass using radar backscatter, *I.E.E.E. Transactions on Geoscience and Remote Sensing*, **29**, 427-431.

HYYPPÄ, J., and HYPPÄ, H., 1992, A database and software tools for developing algorithms in forest inventory, Report 8, Laboratory of Space Technology, Helsinki University of Technology, 40 pp.

HYYPPÄ, J., and HALLIKAINEN, M., 1991, Development of a helicopter-borne 8-channel ranging scatterometer, Report 4, Laboratory of Space Technology, Helsinki University of Technology, 24 pp.

LE TOAN, T., BEAUDOIN, A., RIOM, J., and GUYON, D., 1991, Relating forest parameters to SAR data, *Proceedings of IGARSS'91, Helsinki University of Technology, Espoo, Finland, 3-6 June*, Vol. II (New York, USA: Institute of Electrical and Electronics Engineers), pp. 689-692.

KASISCHKE, E., BOURGEAU-CHAVEZ, L., CHRISTENSEN, N., and DOBSON, C., 1991, The relationship between aboveground biomass and radar backscatter as observed on airborne SAR imagery, *Proceeding of the Third Airborne Synthetic Aperture Radar (AIRSAR) Workshop, 23-24 May*, JPL Publication 91-30 (New York, U.S.A.: Institute of Electrical and Electronics Engineers), pp. 11-21.

KAUPPI, P., MIELIKÄINEN, K., and KUUSELA, K., 1992, Biomass and carbon budget of European forests, 1971 to 1990, *Science*, **256,** 70-74.

RAUSTE, Y., 1992, Geometric/radiometric preprocessing of SAR scattering matrix data, *Proceedings of the final workshop of the MAESTRO 1 and AGRISCATT Campaigns, Noordwijk, The Netherlands, 6-7 February* (Paris: European Space Agency), pp. 113-116.

SADER, S., 1987, Forest biomass, canopy structure, and species composition relationships with multipolarization *L*-band synthetic aperture radar data, *Photogrammetric Engineering and Remote Sensing*, **53**, 193-202.

VAN ZYL, J., ZEBKER, H., and ELACHI, C., 1987, Imaging radar polarization signatures: Theory and observation, *Radio Science*, **22,** 529-543.

PAPER 5

Multitemporal analysis of forest biomass using AIRSAR data

In: Proceedings of the 25th International Symposium, Remote Sensing and Global Environmental Change, Graz, Austria, 4–8 April, 1993. Pp. I-328–I-338.

MULTITEMPORAL ANALYSIS OF FOREST BIOMASS USING AIRSAR DATA*

Yrjö Rauste
Technical Research Centre of Finland
Instrument Laboratory
Espoo, Finland

ABSTRACT

Multitemporal AIRSAR data of the Freiburg test site of the MAESTRO-1 and MAC Europe campaigns were used for forest biomass mapping. Image data acquired in August 1989, June 1991, and July 1991 were geo-coded to the same grid structure. A geocoding residual error less than 2 pixels (less than 20 m) was achieved using a DEM. The HV-polarization of P-band was verified to be the optimal band-polarization combination in forest biomass mapping. A multitemporal regression model produced a higher correlation (0.82) between forest biomass and radar data than the highest single-date correlation (0.79). Clear-cut areas could be identified in multitemporal radar data in all three bands studied: C, L, and P.

1 INTRODUCTION

Accurate knowledge on the amount and spatial distribution of forest biomass is essential in environmental and climatological modelling. In large areas of the world, timber is also a valuable natural resource for paper and sawmill industries and an important source of energy.

Radar has been studied as a tool for forest inventory fairly widely (e.g. Sader 1987, Hussin et al. 1991, Christensen et al. 1990, Kasischke et al. 1991, and Le Toan et Beaudoin 1991). Radar, due to its cloud-penetrating capability, is very suitable for multitemporal analysis. Only few studies (e.g. Rignot et al. 1992) have concentrated on the use of multitemporal radar data in forest inventory applications.

The radar data used in this study have been acquired in two international research campaigns: MAESTRO-1 (1989-1992, organized jointly by the Joint Research Centre of EC and the European Space agency) and MAC Europe (1991, organized mainly by NASA).

The objective of this study is to assess the potential of multitemporal radar data in forest biomass mapping.

*Presented at the 25th International Symposium, Remote Sensing and Global Environmental Change, Graz, Austria, 4-8 April 1993

2 MATERIALS AND METHODS

2.1 Ground data

The forested study site (centre: 48°05'25" N, 8°22'01" E) is in Germany close to the town Villingen-Schwenningen. The main tree species are Norway spruce (*Picea abies*), fir (*Abies alba*), and Scotch pine (*Pinus sylvestris*). Deciduous trees are rare in the study site. The area is relatively flat although the elevation (750 m ... 970 m above mean sea level) is high.

The forest inventory ground data consist of two elements:

- a forest map in scale 1:10 000 showing the stands and
- forest inventory data sheets.

The forest inventory data sheets contain for every stand:

- the area of the stand,
- stem volume, and
- the distribution of the area among tree species.

The forest map and the forest inventory data sheets describe the situation in October 1981. The map was digitized and converted into a raster image. From the forest inventory data sheets, the items mentioned above were input into the computer system used. The forest stem volume data were used as a substitute for biomass data because no data on total biomass was available. The amount of total biomass can be assumed to be directly proportional to the stem volume.

The digital elevation model (DEM) used in geocoding of AIRSAR data was generated by the Universität Stuttgart/Institut für Navigation. Contours from the German topographic maps in scale 1:50 000 were used as input to the DEM generation.

2.2 AIRSAR Data

The SAR data were acquired by the AIRSAR system (Held et al. 1988) operated by NASA/JPL. SAR data from three days were studied:

1. 18 August 1989 (CCT id HR1105C, HR1105L, and HR1105P),
2. 15 June 1991 (CCT id CM3169), and
3. 16 July 1991 (CCT id CM3275).

The first scene was acquired in the MAESTRO-1 campaign (Churchill et Attema 1991) and the other two scenes in the MAC Europe campaign. The first scene is in single-look scattering matrix format, the other two scenes in 16-look compressed Stokes matrix format.

2.3 Preprocessing of AIRSAR Data

2.3.1 Calibration

The August-89 scene was calibrated (Rauste 1992b) using trihedral reflectors and the algorithms described by van Zyl (1990) and Zebker et Lou (1990).

The June-91 scene was phase calibrated using trihedral corner reflectors. For the P-band calibration, a 5-m high trihedral corner reflector was constructed of chicken-wire. Neither cross-talk removal, nor channel balance calibration was applied. In the June-91 scene, the average return power decreased with increasing range much stronger than in the August-89 or July-91 scenes. Because the reason for this steeper decrease was not known (possibly uncertainty in antenna pattern correction in the SAR processor) a very simple correction was applied. A linear regression line was determined for the June-91 and July-91 scenes. The June-91 scene was subsequently multiplied by a range-dependent constant in such a way that the slope of the regression line of the June-91 was forced to that of the July-91 scene.

The July-1991 scene was calibrated (phase calibration, cross-talk, and channel imbalance) by JPL.

2.3.2 Forming of the multitemporal image database

Quantitative analysis of multitemporal remote sensing data is facilitated considerably if the image data are resampled to the same, geo-referenced grid. The geo-coding of the AIRSAR data was done using polynomial rectification with a digital elevation model. The resampling was done on Stokes matrix data, separately for each element of the Stokes matrix. The August-89 scene, which originally was in single-look scattering matrix format, was first converted to Stokes matrix format and compressed using the algorithm described by Dubois et Norikane (1987).

In the polynomial rectification, the relationship between object space (geodetic) co-ordinates and the image co-ordinates (range and azimuth) is expressed in the form of polynomial functions whose coefficients are determined using ground control points (GCP). The relief displacement is treated separately as an elevation-dependent correction to the range co-ordinate. Table 1 summarizes the residual errors in geocoding the AIRSAR images. The geocoding accuracy indicated by table 1 was verified by Visual comparison between the geocoded images and an overlaid transparent copy of the topographic map (in scale 1:25 000).

In the resampling process, a Gaussian weighting function was used to resample each output pixel. In this type of resampling, the amount of speckle reduction is controlled by the width of the weighting function. In resampling of the August-89 scene, the standard deviation of the weighting function was 0.8 pixels in slant range and 0.8 pixels in azimuth. This means that the standard deviation was approximately 70 percent of the pixel spacing (12.5 m) of the geocoded images. In the June-91 and July-91 scenes, less speckle reduction was required due to lower speckle level in the 16-look images. The standard deviation of the weighting function was 0.35 pixels in slant range and 0.5 pixels in azimuth, approximately 25 percent of the pixel spacing of the geocoded images in range and 50 per cent in azimuth.

Table 1. Summary of geocoding accuracy

Scene	Number of GCPs	RMSE (pixels)		RMSE (m)	
		Range	Azimuth	Range	Azimuth
August-89	23	1.6	1.1	14.6	13.3
June-91	28	1.6	1.4	14.6	16.9
July-91	24	1.2	0.8	10.7	9.7

The geocoded Stokes matrix images were normalized for terrain topography:

$$P_{norm} = P_{orig}\frac{\tan(\theta_r)}{\tan(\theta_{nom})} \quad (1)$$

where P_{norm} is the normalized Stokes matrix element, P_{orig} the original Stokes matrix element, θ_r the incidence angle in range direction (depending on the local slope), and θ_{nom} the nominal incidence angle depending only on the range co-ordinate.

Stand-wise average Stokes matrices were computed using the digitized forest map. For stands greater than 100 pixels (approximately 1.7 ha) only those pixels were included in the averaging whose average power (the Stokes matrix element F_{11}) was at most 50 percent smaller and at most 70 percent larger than the stand-wise average power. This was done to eliminate the effects of inhomogeneous stand closure (shadows due to small openings and high return from the far edge of small openings) on the stand-wise average Stokes matrix.

After stand-wise averaging, the stands larger than a threshold (1 ha or 2 ha depending on the analysis) were selected to be used in further analyses.

2.4 Analysis Methods

As previously (Rauste 1992a), polarization synthesis was used to find the optimum polarization for forest biomass mapping. The whole space of all possible polarization combinations (combinations of transmit orientation, transmit ellipticity, receive orientation, and receive ellipticity) were traversed in a grid of 5 to 15 degrees. For each polarization combination:

- the received power was calculated for each stand based on the stand-wise Stokes matrix.
- the correlation coefficient between the received amplitude (square root of the received power) and the forest stem volume was calculated.

Changes in backscattering as a function of time were studied using three techniques:

- plotting the (relative) backscatter amplitudes of forest stands as a function of time,

- scatter plots of data from two dates, and
- visual interpretation of colour composites and principal components made of images of three dates.

In the first technique, the development of each stand was plotted as a line from the first image to the last. Because no absolute calibration was applied to the data, the datasets of different dates were normalized by forcing the average power (computed over all stands of the data set) to the same value.

3 RESULTS

3.1 Radar-Biomass correlation

Table 2 shows the correlation between radar amplitude and forest stem volume. Only stands larger than 1 ha were included in the table. For C and L bands, the correlations (table 3) were computed also for relatively young forests with the stem volume less or equal to 100 m^3/ha. The P-band HV-polarization has the highest correlation. The C and L-bands have also a relatively high correlation with stem volume, especially in forests where the stem volume is relatively small. The C and L-band correlations are higher than what was obtained earlier with the August 1989 data only (Rauste et al. 1992). The difference is explained by the fact that only stands larger than 1 ha were included in this study. Only the basic linear polarizations (HH, VV, and HV) are included in table 2. In the search for optimal polarization (section 2.4), the strongest correlations between the radar backscatter and stem volume were found in P-band and always close to the HV-polarization. The somewhat lower correlations in P-band of the June-91 scene may be due to deficiencies in antenna pattern correction.

Table 2. Correlation between radar amplitude and stem volume

Scene	Band	Stem Volume (m^3/ha)	Number of stands	HH	VV	HV
August-89	C	0 ... 830	179	-0.392	-0.078	-0.429
June-91	C	0 ... 830	183	-0.460	-0.199	-0.349
July-91	C	0 ... 830	181	-0.583	-0.260	-0.507
August-89	L	0 ... 830	182	-0.161	-0.046	-0.268
June-91	L	0 ... 830	184	-0.176	0.134	-0.123
July-91	L	0 ... 830	179	-0.262	0.082	-0.266
August-89	P	0 ... 830	182	0.280	0.210	0.750
June-91	P	0 ... 830	176	0.230	0.216	0.590
July-91	P	0 ... 830	179	0.272	0.234	0.707

Table 3. Correlation between radar amplitude and stem volume for young stands

Scene	Band	Stem Volume (m^3/ha)	Number of stands	HH	VV	HV
August-89	C	0 ... 100	36	0.315	0.575	0.215
June-91	C	0 ... 100	37	0.107	0.631	0.491
July-91	C	0 ... 100	36	-0.062	0.667	0.386
August-89	L	0 ... 100	37	0.539	0.674	0.671
June-91	L	0 ... 100	37	0.635	0.584	0.637
July-91	L	0 ... 100	35	0.684	0.679	0.699

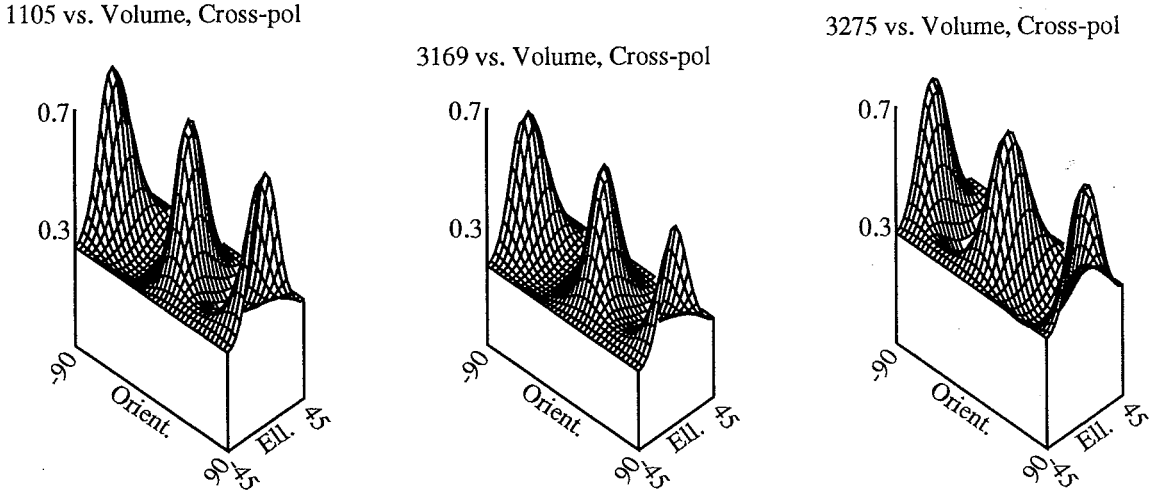

(a) August 1989 (b) June 1991 (c) July 1991

Figure 1. Radar-biomass correlation as a function of polarization (P-band, cross-polarization)

The P-band biomass correlation depends strongly on the polarization as observed in a previous study (Rauste 1992a). Figure 1 shows the correlation coefficient between cross-polarized P-band amplitude and stem volume as a function of polarization. The same pattern can be seen in all 3 diagrams. The highest correlations are found in the vicinity of the original HV polarization.

A linear multiple regression model was determined for the forest stem volume (as dependent variable) with the P-HV radar data of the three dates as the independent variables. Stand-wise average

Stokes matrix data of stands larger than 2 ha were used in the model. A multiple correlation coefficient of 0.82 (coefficient of determination 0.68) was obtained. The correlation was higher than the highest single-date correlation coefficient (August 1989: 0.79, June 1991: 0.60, and July 1991: 0.75) using the same data set. Figure 2 shows the residuals and 5-percent confidence limits of the model.

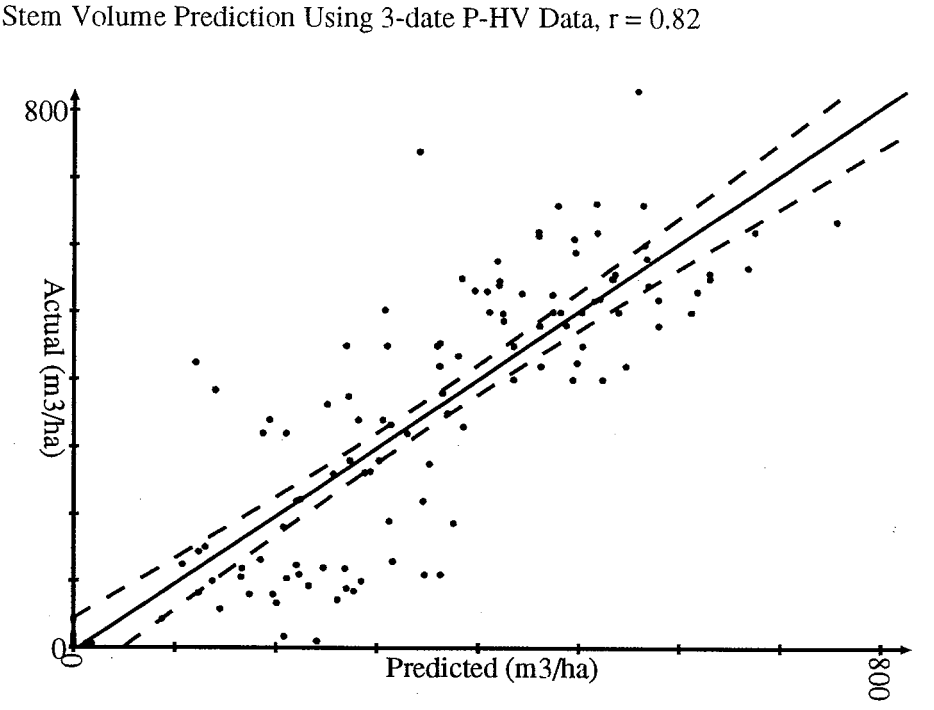

Figure 2. A tri-temporal regression model for forest stem volume

3.2 Backscattering as a function of time

Figure 3 shows the C, L, and P band amplitude as a function of time. In C-band, the June-91 values in HH are higher than the August-89 or July-91 values. In VV, the situation is the opposite. This is most likely due to the lacking channel imbalance calibration of the June-91 scene. Inspection of some corner reflector pixels in the June-91 scene showed that the HH amplitude is some 5 to 10 percent higher than the VV amplitude.

In general, the backscatter changes of forest stands are relatively small. Comparing the direction and magnitude of change with ground data does not reveal an obvious and easily identifiable reason for the change in average backscatter. Clear-cut areas form an exception to this observation. Inspection of the tri-temporal colour composites suggests that the correction of antenna pattern effects in the June-91 scene may have been slightly too cautious.

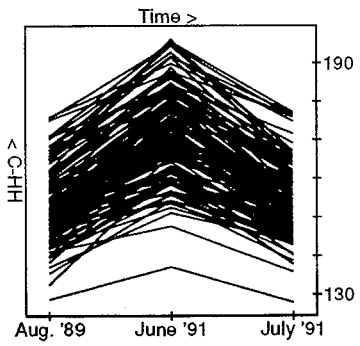

(a) C-HH.

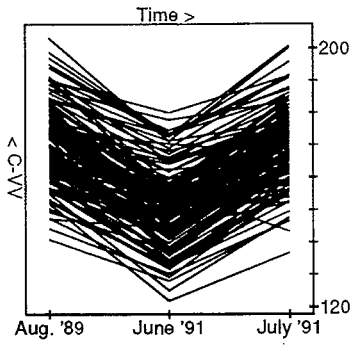

(b) C-VV.

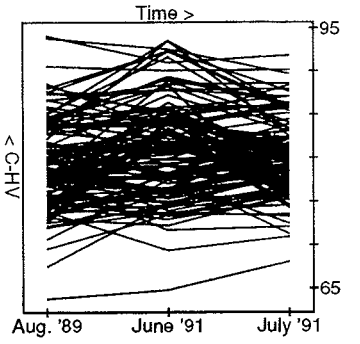

(c) C-HV.

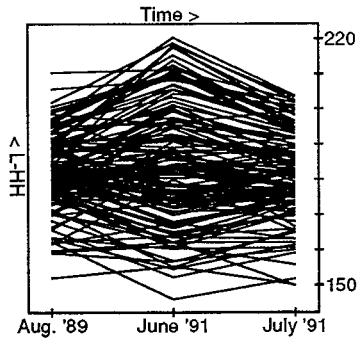

(d) L-HH.

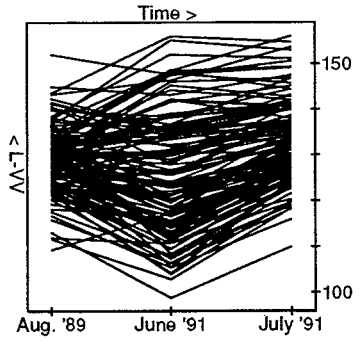

(e) L-VV.

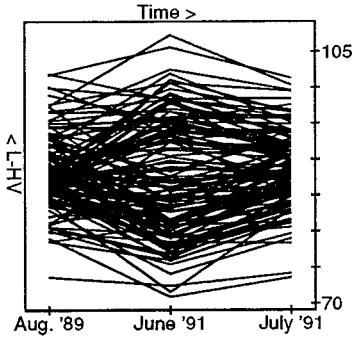

(f) L-HV.

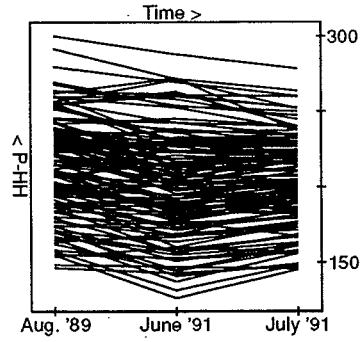

(g) P-HH.

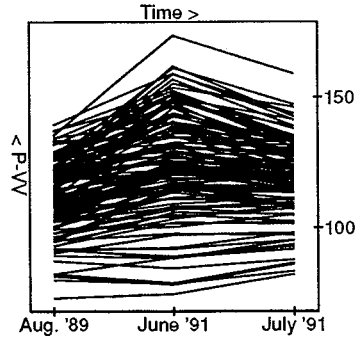

(h) P-VV.

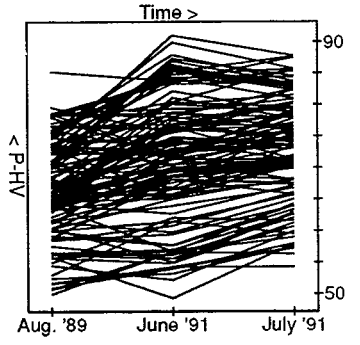

(i) P-HV.

Figure 3. Backscatter amplitude as a function of time

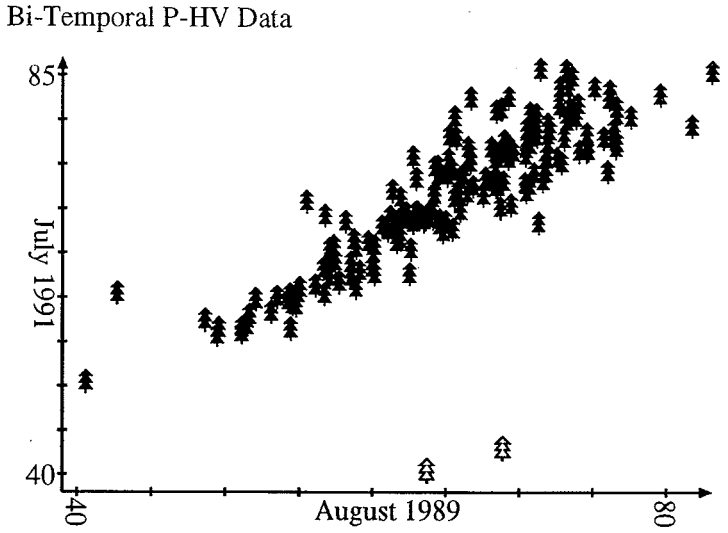

Figure 4. P-HV of July 1991 *vs.* P-HV of August 1989

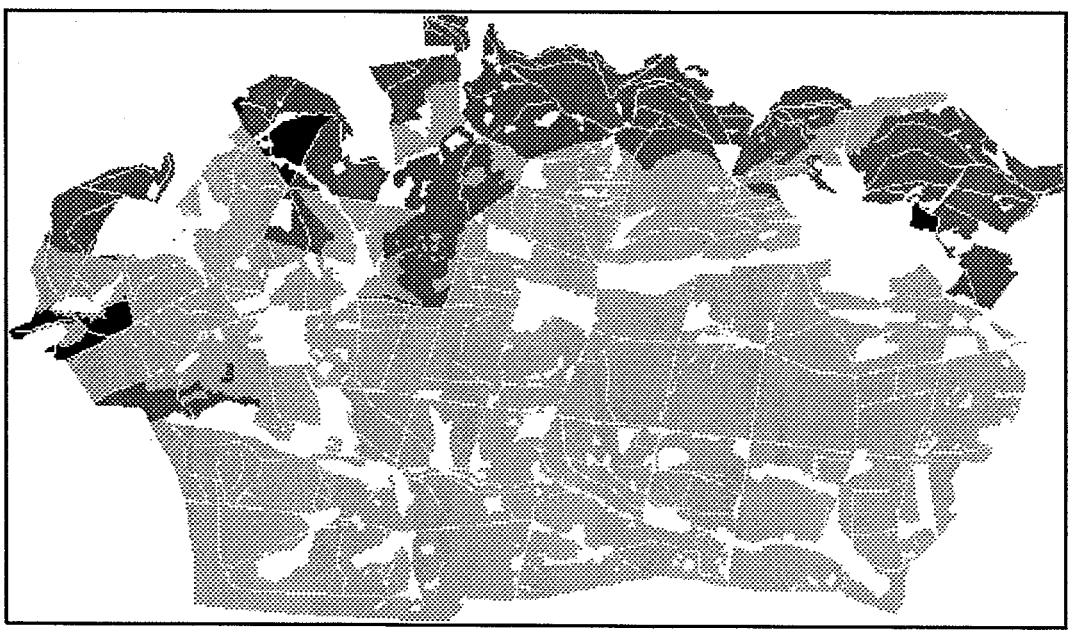

Figure 5. P-HV backscatter change by forest stands

Clear-cut areas can be identified clearly in tri-temporal colour composites in P-band, but also in L and C-bands. By visual evaluation, the contrast between the clear-cut areas and forests is largest in P-band, then in L-band and smallest in C-band. Figure 4 shows a scatter diagram of forested (solid symbols) and two clear-cut stands (outlined symbols). Figure 5 shows the direction of change of the P-HV backscatter in stands larger than 2 ha. Stands where P-HV backscatter of 1989 was higher than that of 1991 are shown in black. This area includes the clear-cut area near the eastern end of the picture. Stands where the P-HV backscatter of 1989 falls between the June and July values of 1991 are shown in dark gray. Stands where both the June and July values of 1991 are higher than that of 1989 are shown in light gray. The areas where the P-HV backscatter has decreased most are concentrated in the northern part of the study site. The reason for this could be more intensive thinning cutting in these areas. This was not verified because no quantitative information on recent thinning cutting were available in this study.

4 DISCUSSION

The high correlations between the mixed-forest biomass and P-HV backscatter obtained earlier (e.g. Rauste 1992a) were verified in this study. Also the strong dependence of the correlation on the polarization was verified. A spaceborne P-band SAR using HV-polarization could be a useful tool in mapping large forested areas in the boreal forest zone.

The results on the development of backscatter with time of the year should be considered preliminary. Further research with more thoroughly calibrated data is needed to obtain information on the development of the backscatter characteristics of different types of forest with different amounts of biomass.

The separability of clear-cut areas could be studied using the same kind of optimal polarization search as used in the correlation analysis. If data on the thinning cutting were available, the potential to map small changes could be studied using the same type of techniques.

5 REFERENCES

Christensen, N., Kasischke, E. and Dobson, M. 1990. SAR-derived estimates of aboveground biomass in forested landscapes, Proceedings of the International Geoscience and Remote Sensing Symposium *IGARSS'90,* University of Maryland, College Park, Maryland, USA, May 20-24, 1990, p. 1209-1212.

Churchill, P. and Attema, E. 1991. The European airborne polarimetric SAR campaign MAESTRO 1, Proceedings of the International Geoscience and Remote Sensing Symposium *IGARSS'91,* Helsinki University of Technology, Espoo, Finland, June 3-6, 1991, Vol. II, p. 327-328.

Held, D., Brown, W., Freeman, A., Klein, J., Zebker, H., Sato, T., Miller, T., Nguyen, Q., and Lou, Y. 1988. The NASA/JPL multifrequency, multipolarization airborne SAR system, Proceedings of the International Geoscience and Remote Sensing Symposium *IGARSS'88,* Edinburgh, September 1988, p. 345-350.

Dubois, P. & Norikane, L. 1987. Data volume reduction for imaging polarimetry, Proceedings of *IGARSS'87* Symposium, Ann Arbor, 18-21 May 1987, p. 691-696.

Hussin, Y., Reich, R., and Hoffer, R. 1991. Estimating slash pine biomass using radar backscatter, *IEEE Transactions on Geoscience and Remote Sensing,* Vol. 29, No. 3, May 1991, p. 427-431.

Kasischke, E., Bourgeau-Chavez, L., Christensen, N., and Dobson, C. 1991. The relationship between aboveground biomass and radar backscatter as observed on airborne SAR imagery, Proceedings of the Third Airborne Synthetic Aperture Radar (AIRSAR) Workshop, May 23-24 1991, *JPL-Publication* 91-30, p. 11-21.

Rauste, Y. 1991. Polarimetric radar signatures of forest as a function of terrain topography. Proceedings of the International Geoscience and Remote Sensing Symposium *IGARSS'91,* Helsinki University of Technology, Espoo, Finland, June 3-6, 1991, Vol. II, p. 341-344.

Rauste, Y. 1992a. Estimation of biomass in mixed forests using polarimetric SAR data, Proceedings of *IGARSS'92,* South Shore Harbour Resort and Conference Center, Houston, Texas, May 26-29, 1992, p. 789-791.

Rauste Y. 1992a. Geometric/radiometric preprocessing of SAR scattering matrix data, Proceedings of the Final Workshop of the MAESTRO/AGRISCATT Campaigns, Noordwijk, 6-7 February 1992, p. 113-116.

Rauste, Y., Heiska, K., and Pulliainen, J. 1992. On forest inventory and elevation determination using polarimetric radar data, Proceedings of the Final Workshop of the MAESTRO/AGRISCATT Campaigns, Noordwijk, 6-7 February 1992, p. 117-121.

Rignot, E., Way, J., Mc Donald, K., Viereck, L., and Adams, P. 1992. Monitoring of environmental conditions in the Alaskan forests using ERS-1 SAR data, Proceedings of *IGARSS'92,* South Shore Harbour Resort and Conference Center, Houston, Texas, May 26-29, 1992, p. 530-532.

Sader, S. 1987. Forest biomass, canopy structure, and species composition relationships with multipolarization L-band synthetic aperture radar data, *Photogrammetric Engineering and Remote Sensing,* Vol. 53, No. 2, February 1987, p. 193-202.

Le Toan, T. and Beaudoin, A. 1991. Relating forest parameters to SAR data, Proceedings of the International Geoscience and Remote Sensing Symposium *IGARSS'91,* Helsinki University of Technology, Espoo, Finland, June 3-6, 1991, Vol. II, p. 689-692.

Zebker, H. and Lou, Y. 1990. Phase calibration of imaging radar polarimeter Stokes matrices, *IEEE Transactions on Geoscience and Remote Sensing,* Vol. 28, No. 2, p. 246-252.

van Zyl, J. 1990. Calibration of polarimetric radar images using only image parameters and trihedral corner reflector responses, *IEEE Transactions on Geoscience and Remote Sensing,* Vol. 28, No. 4, p. 337-348.

PAPER 6

Multi-temporal JERS SAR data in boreal forest biomass mapping

In: Remote Sensing of Environment 2005.
Vol. 97, pp. 263–275.

Available online at www.sciencedirect.com

SCIENCE DIRECT

Remote Sensing of Environment 97 (2005) 263 – 275

Remote Sensing of Environment

www.elsevier.com/locate/rse

Multi-temporal JERS SAR data in boreal forest biomass mapping

Yrjo Rauste

VTT Technical Research Centre of Finland, Finland

Received 28 March 2003; received in revised form 29 March 2005; accepted 19 May 2005

Abstract

Multi-temporal JERS SAR data were studied for forest biomass mapping. The study site was located in South-eastern Finland in Ruokolahti. Pre-processing of JERS SAR data included ortho-rectification and radiometric normalization of topographic effects.

In single-date regression analysis between backscatter amplitude and stem volume, summer scenes from July to October produced correlation coefficients (r) between 0.63 and 0.81. Backscatter level and the slope of the (linear) regression line were stable from scene to scene. Winter scenes acquired in very cold and dry winter conditions had a very low correlation. One winter scene acquired in conditions where snow is not completely frozen produced a correlation coefficient similar to summer scenes.

Multivariate regression analysis with a 6-date JERS SAR dataset produced correlation coefficient of 0.85. A combined JERS–optical regression analysis improved the correlation coefficient to 0.89 and also alleviated the saturation, which affects both SAR and optical data.

The stability of the regression results in summer scenes suggests that a simple constant model could be used in wide-area forest biomass mapping if accuracy requirements are low and if biomass estimates are aggregated to large areal units.

Keywords: Remote sensing; Biomass; Microwave; Boreal forest

1. Introduction

Standing forest biomass forms an essential part of active carbon pool participating in the global carbon cycle. Mapping the amount and geographic distribution of forest biomass – and its change with time – is important for understanding the development of the carbon cycle. Main part of forest biomass in boreal forests is in tree stems, which can be used as raw material in wood and pulp industry. Information on the spatial distribution of forest biomass is therefore important for forest industry and sustainable forestry.

In the GRFM (Global Rain Forest Mapping) project, several continental SAR mosaics were produced for tropical areas. In a follow-on project GBFM (Global Boreal Forest Mapping), similar mosaics are being produced for the whole boreal forest belt of the world (Rosenqvist et al., 2000). These mosaics can serve as a starting point and important input dataset when global forest biomass evaluations are made for carbon cycle studies and other environmental applications. In the context of the GBFM project, a Northern Europe science node was organised by Metria Miljoanalys (Jonsson, 2002) as a "regional exploratory addition to the GBFM programme".

Most of the forest biomass in boreal forests is in tree stems. Since large datasets on biomass measurements in boreal forests are difficult to obtain, stem volume data from forest inventory data bases are widely used instead of forest biomass. As an approximation, forest stem volume (m^3/ha) in boreal forests can be converted into dry biomass (tons/ha) by multiplying the stem volume estimate by 0.6 (Häme et al., 1992).

Active microwave sensors from 10-GHz X-band (e.g., Beaudoin et al., 1992; Le Toan et al., 1992) to 28- to 80-MHz VHF SAR (e.g., Israelsson et al., 1997) have been studied for forest biomass mapping. X-band has the lowest dynamic range and sensitivity to forest biomass (Le Toan et al., 1991). The three-band (C, L, and P) polarimetric AIRSAR sensor has been used in many forest biomass

E-mail address: Yrjo.Rauste@vtt.fi.

0034-4257/$ - see front matter © 2005 Elsevier Inc. All rights reserved.
doi:10.1016/j.rse.2005.05.002

studies (e.g., Green, 1998; Kasischke et al., 1991, 1995; Moghaddam et al., 1994; Ranson & Sun, 1997). The strongest correlation between SAR backscatter and forest biomass has been reported in P-band and the weakest in C-band (e.g., Beaudoin et al., 1992; Dobson et al., 1992; Israelsson et al., 1992; Rauste et al., 1992; Skriver & Gudmandsen, 1992). A spaceborne P-band SAR will not be available in the foreseeable future even though it has been proposed (e.g., Rignot et al., 1995). Despite the very strong backscatter–biomass relation in VHF SAR (Melon et al., 2001, report even a 0.99 correlation), a spaceborne VHF SAR is not practical. Studies using dual-frequency (C- and L-bands) polarimetric SIR-C data (e.g., Dobson et al., 1995; Harrell et al., 1997) point out the importance of L-band data in coniferous forest biomass mapping.

The correlation between forest biomass and the C-band backscatter measured by the ERS-1 and ERS-2 SAR sensors has been reported to be low in tropical forests (e.g., Luckman et al., 1997) and oil palm and rubber plantations (Rosenqvist, 1996). Kasischke et al. (1994) describe the C-band dynamic range due to biomass variation as low in young loblolly pine forests. In boreal forests, the biomass vs. C-band backscatter correlation depends heavily on the soil moisture conditions (Pulliainen et al., 1994, 1997; Wang et al., 1994). Pulliainen et al. (1996) have used a highly multi-temporal ERS dataset and a semiempirical backscatter model for boreal forest biomass estimation. A correlation coefficient (r) of 0.66 was obtained in a test site where the stem volume ranged from 0 to 300 m^3/ha. Since the method includes per-scene soil and vegetation moisture variables (and biomass reference data), its use in wide-area biomass mapping may be difficult.

Repeat-pass interferometry with C-band ERS data has been studied for forest biomass mapping (e.g., Fransson et al., 2001; Luckman et al., 2000). Luckman et al. (2000) obtained a coefficient of determination (R^2) of 0.805 between ERS-1/2 (1-day difference) tandem coherence and the logarithm of forest biomass in regenerating tropical forests (biomass mainly between 0 and 100 tons/ha). Fransson et al. (2001) studied 5 ERS-1/2 interferometric pairs of a test site where stem volume ranges from 0 to 300 m^3/ha. The highest (adjusted) coefficient of determination (R_A^2) between stem volume and ERS coherence was 0.87 while the lowest was 0.06. In a more recent study, Pulliainen et al. (2003) used 14 ERS-1/2 interferometric pairs (1-day difference in scene acquisition) in a Finnish site (stem volume 0...539 m^3/ha, mean stem volume 174 m^3/ha). The correlation coefficient (r) between coherence and stem volume varied mainly between 0.46 and 0.87 while one pair (during snow melting period) had an r value of 0.07. These last two examples suggest, as Pulliainen et al. (2003) note, that the repeat-pass interferometry in forest biomass mapping is influenced by weather conditions.

Even though L-band backscatter is stronger correlated with forest biomass, a limiting factor is the saturation of the backscatter–biomass relationship at some biomass level (Imhoff, 1993). Based on a dataset combined from three test sites (Hawaii/USA: broad-leaved, North Carolina/USA: pine forests, and France: pine forests), Imhoff (1995) reports the L-band saturation level at 40 tons/ha of dry biomass. Luckman et al. (1998) found a saturation of 60 tons/ha in a Brazilian test site. In boreal forests, the 40 tons/ha limit corresponds to a forest stem volume of approximately 70 m^3/ha. Israelsson et al. (1995) found the saturation level of 100 to 150 m^3/ha in a boreal test site in Sweden and Fransson and Israelsson (1999) obtained a saturation level of 143 m^3/ha. Rauste et al. (1994) found an L-band saturation level of about 120 m^3/ha in a coniferous forest site in Germany. Kurvonen et al. (1999) report a saturation level of 225 m^3/ha in two JERS SAR scenes. Toshio et al. (1995) obtained a correlation coefficient (r) of 0.75 between forest stem volume and JERS SAR amplitude in a test site in Japan where the forest stem volume goes up to 900 m^3/ha. So the saturation level may depend on the tree species and forest types as well as the ground surface type. In addition to tree species, the L-band backscatter vs. biomass relationship also depends on forest management practices. Kuplich et al. (2000) found a strong L-band vs. biomass correlation ($r=0.77$) in a Brazilian test site (re-growth after a clear cut) while the correlation was weak in a Cameronian test site (selective logging). Paloscia et al. (1999) report an r^2 value (between the logarithm of woody biomass and logarithm of backscatter power) of 0.77 using a few forested areas in a JERS-1 SAR dataset in Italy. Kellndorfer et al. (2001) report an adjusted R_A^2 values of 0.72 and 0.56 (between the logarithm of biomass and logarithm of backscatter power) for two JERS SAR scenes in Michigan in a stand-wise dataset consisting of 39 pine stands. Smith et al. (1998) report R^2 values of 0.27 and 0.30 for two summer-time JERS SAR scenes (uncalibrated) in a Finnish study site in stands with stem volumes 0...150 m^3/ha.

Fransson and Israelsson (1999) and Harrell et al. (1995) have published regression models between L-band backscatter and forest biomass (see later chapter comparison of new regression models and existing models).

Dobson et al. (1991) observed that a rain shower had the strongest effect (in a C-, L-, and P-band dataset) on C-band data and the weakest effect on the P-band data. The stability of the relation between polarimetric P-band data and forest biomass through the growing season was also confirmed by Rauste (1993). Chipman et al. (2000) observed (in a C- and L-band dataset) that the L-band is likely to be more temporally stable than the C-band. Since boreal forest environment – with low temperatures and seasonal snow cover – has widely variable physical attributes for microwave scattering, the seasonal variations in L-band SAR data can be expected to be pronounced in boreal forests (e.g., Pulliainen et al., 1999).

The literature has documented the relationship of L-band backscatter and forest biomass. Seasonal effects in this relationship have also been observed. These observations are rather occasional. No systematic effort to

exploit these seasonal effects in L-band biomass mapping has been documented in literature. The objectives of the study were:

1. To study seasonal variation in L-band SAR data and the potential of L-band SAR data acquired in various seasons in mapping the biomass of boreal forest;
2. To study the potential of combining L-band SAR data and optical satellite data in boreal forest biomass mapping.

2. Materials and methods

2.1. Ground data

The study site (centre 61°31′N, 28°46′E) was located in Puumala and Ruokolahti in South-eastern Finland. The dominant soil type in the site is glacial drift. The most common tree species was pine (*Pinus sylvestris*). Other common species were spruce (*Picea abies*) and birch (*Betula betula*).

Ground data came from two sources: (1) stand-wise forest inventory data from Stora Enso Ltd., and (2) a set of point-wise measurements made by the Finnish Forest Research Institute.

The stand-wise forest inventory data included one forest stem volume for the whole stand. Since this dataset was compiled for practical forest management purposes, its accuracy is not perfect. The forest inventory was made in 1997. The stand-wise forest inventory data were turned to image format and resampled to 25 m pixels as used in the ortho-rectification of the SAR data. One erosion step (pixels whose all neighbouring pixels are not of the same stand as the pixel itself rejected) was done to the ground data image. Stands smaller than 2 ha (32 pixels) were excluded. The forest inventory dataset finally included 206 stands covering 845 ha. The average stem volume within these 206 stands was 102 m^3/ha (lowest 0 m^3/ha, highest 364 m^3/ha, standard deviation 79 m^3/ha).

The point-wise (plot) ground data covered a 1-km-by-1-km area with a regular grid of points at a distance of 50 m (20 lines by 20 columns). The average stem volume within the point-wise ground dataset was 104 m^3/ha (lowest 0 m^3/ha, highest 355 m^3/ha, standard deviation 68 m^3/ha). Total stem volume measurement data were used as an independent test data for JERS-derived biomass estimates.

A digital elevation model (DEM) was used for ortho-rectification of JERS SAR data. The DEM was produced with contour-line data from 1:20,000 topographic maps. The pixel spacing in the DEM was 25 m and the vertical accuracy about 2 m. The DEM covered an area of 38.15 km (in northing) by 50.85 km (in easting).

2.2. SAR data

The conceptual model of seasonal changes included 5 seasonal configurations based on meteorological and physical conditions controlling overall backscattering and the phenological state of trees:

1. the peak bio-chemical activity during the first half of the growing season (G1),
2. the second half of the growing season before the drop of the leaves of deciduous trees (G2),
3. leaves-off period before the first snow (G3),
4. cold winter conditions (WD), and
5. wet winter conditions (WW).

The aim in image selection was to obtain at least one scene from all seasons defined above. Only those descending-orbit scenes were considered that were acquired on the same track as the first scene (20.02.1993) of the dataset. Some scenes that were listed in JERS SAR catalogues were not of high enough quality for SAR processors. Table 1 shows the scenes that were available for analysis. The first growing season configuration (G1) remained missing due to quality problems of raw SAR data. The meteorological data in Table 1 are from the airport of Lappeenranta 60 km from the study site. Temperatures (min and max) are for the image acquisition day. Precipitation data are for the acquisition day (column Day) and the day preceding the acquisition day (column Prev). The form of precipitation has been snow on 20.2.1993 and 14.3.1998 and water on 20.7.1995, 2.9.1995, and 16.10.1995. On 25.1.1995, the precipitation may have been either water or snow or – most likely – wet snow. The summer and autumn scenes (20.7.1995, 2.9.1995, and 16.10.1995) are all from reason-

Table 1
JERS SAR scenes used and the meteorological conditions (in Lappeenranta airport)

Acquired	Temperature (°C)		Precipitation (mm)		Frost days	Conf	Processor
	Max	Min	Day	Prev			
20.02.1993	−5.8	−11.2	2.4	7.7	4	WD	ESA
25.01.1995	0.2	−2.1	1.4	9.7		WW	NASDA/ERS-DPS/434
20.07.1995	20.4	12.0	0.2	1.6		G2	NASDA/ERS-DPS/434
02.09.1995	17.0	8.0	0.1	2.4		G2	NASDA/ERS-DPS/434
16.10.1995	8.6	0.6	1.5	0.1		G3	NASDA/ERS-DPS/434
14.03.1998	−9.0	−13.6	0.7	2.8	13	WD	NASDA/Sigma-SAR

ably dry conditions. Precipitation of only 0.2... 1.5 mm suggests that the rain has been light, low intensity showers, where the water evaporates from leaves and other canopy components in a matter of an hour or less. Because there has been some precipitation, trees and other plants have not been plagued by drought. Column Frost days gives the number of days during which the maximum temperature has been below 0 °C before the image acquisition day. Column Conf gives the classification of the meteorological conditions to the seasons listed above. Column Processor gives the SAR processor used to generate the SAR image product.

Most of the SAR scenes were within 2 years from the forest inventory (summer 1997). Since the yearly growth in the climatic conditions of the study site is only a few percent, the data can be considered to be from the same time as the SAR data.

A Landsat TM scene acquired on 29 August 1997 was used to study SAR-optical synergy.

2.3. Pre-processing of SAR data

The SAR data that stemmed from 3 different SAR processors were not calibrated to the same standard. The older NASDA processor (ERS-DPS, version 434) was chosen as a reference and the remaining two scenes were scaled to that system. The first scene (acquired on 20.2.1993, no calibration data were supplied with the data) was approximately calibrated. Two sample areas were chosen in mature forest areas and in water areas. Image data ratio (in amplitude) was computed between the average of the 4 scenes of 1995 and the scene of 20.2.1993. An average between the water and forest ratio was calculated. The scene of 20.2.1993 was scaled by this factor to approximately match the scenes of 1995. The scene acquired on 14.3.1998 was scaled (the amplitude values of this scene were multiplied by 0.139) to take into account the difference in calibration factors of the older NASDA processor (68.2 dB, Shimada, 1996, 2001) and the Sigma-SAR processor (85.34 dB, Shimada & Isoguchi, 2002).

The JERS SAR scenes were ortho-rectified to 25-m pixel spacing. The rectification made use of tie points between scenes, ground control points (GCPs) between scenes and topographic maps, and block adjustment by the least squares method (see De Grandi et al., 2000). Affine (6 parameter) geometric model was used in the block adjustment. The tie point RMSE (Residual Mean Square Error) was 19 m in northing and 12 m in easting. The GCP RMSE was 24 m in northing and 22 m in easting.

JERS SAR data were radiometrically normalized in connection with ortho-rectification:

$$\mathrm{DN_{out}} = \mathrm{DN_{in}}{*}\mathrm{sqrt}\left(\tan\left(\theta_R^{\mathrm{local}}\right)/\tan(\theta_o)\right) \quad (1)$$

where $\mathrm{DN_{out}}$ = normalized pixel amplitude, $\mathrm{DN_{in}}$ = input pixel amplitude, $\theta_R^{\mathrm{local}}$ = the local incidence angle in the vertical cross-track plane, θ_o = the nominal incidence angle of the sensor (38°).

This normalization gives a constant response (with respect to incidence angle) for targets whose backscattering coefficient γ° (not σ^{O}) is uniform with respect to incidence angle.

An adaptation of median and average filtering (5-out-of-9 filtering) was used in speckle reduction of JERS SAR scenes. Pixel values in each 3-by-3 window are sorted. The highest 2 values and the lowest 2 values are excluded. A weighted average is computed of the remaining 5 pixels. The weighting function is Gaussian with standard deviation of half a pixel. This filtering was used when producing pixel-wise stem volume maps, not in connection with regression analysis.

2.4. Regression analysis

Regression analysis is an appropriate statistical technique to study the relationship between continuous variables such as forest biomass and radar backscatter. Regression analysis (both single-variable and multivariate regression analysis) was used in stem volume estimation. Stand-wise forest inventory data were used as training data to derive regression models between stem volume (the dependent variable) and various sets of JERS SAR and Landsat TM data as independent variables. The earth observation data were averaged for the 206 stands using a stand mask image to obtain the value of the independent variable(s). The JERS SAR amplitude data were squared before averaging and a square root was taken after the averaging. The stem volume of the stand (just one figure per stand) was used as the value of the dependent variable.

Past studies (e.g., Rauste et al., 1994) have shown that a fairly linear relationship (at least for low biomass levels) can be expected between forest stem volume and radar backscatter amplitude. Since the variable to estimate was stem volume, not the logarithm of stem volume, any non-linear transformations could only be applied to radar backscatter data. The JERS SAR data were supplied by NASDA in the form of backscatter amplitudes. Because amplitude is a widely used form of SAR data distribution, JERS SAR data were input in regression analysis as amplitude values. The form of the regression function in single-date regression analysis was:

$$V = A{*}\mathrm{DN_{JERS}} + B \quad (2)$$

where V = stem volume ($\mathrm{m^3/ha}$), $\mathrm{DN_{JERS}}$ = JERS SAR amplitude scaled as in the scenes used in this study, i.e., $\sigma^{\circ} = 10{*}\log_{10}(\mathrm{DN_{JERS*}}{\cdot}\mathrm{DN_{JERS}}) - 68.2$ dB, A = slope of the regression model, B = intercept of the regression model.

Multivariate regression analysis was used to study the increased potential of multi-temporal L-band SAR data in forest biomass mapping.

The relationship between forest stem volume (or biomass) and L-band radar backscatter saturates somewhere

between 100 m^3/ha and 200 m^3/ha. For this reason, regression analyses were made in a series of steps leaving a part of the stem volume range out. The reference case included all stands (with stem volume range 0...360 m^3/ha). The first set of cases included the upper end of the stem volume range present in the study site. The lower limit of the stem volume range was increased in steps (50, 100, 150 and 200 m^3/ha). The second set of cases included the lower part of stem volume range. In this set of cases, the upper limit of the stem volume range was decreased in steps (300, 250, 200, 150, 100, and 50 m^3/ha). Because the number of observations varied from 19 to 206, an adjusted R^2 was also computed in addition to the usual coefficient of determination:

$$R_A^2 = R^2 - \left(1 - R^2\right)p/(n - p + 1) \quad (3)$$

where R_A^2=adjusted R^2, R^2=coefficient of determination, n=number of observations, and p=number of predictor variables (6 SAR scenes).

The accuracy of JERS-SAR-based stem volume estimate was measured by root-mean-square error:

$$\mathrm{RMSE} = \mathrm{sqrt}\left(\Sigma\left(V_g - V_J\right)^2/(n-2)\right) \quad (4)$$

where RMSE=root-mean-square error, V_g=stem volume in ground data, V_J=stem volume in JERS-based estimate, and n=number of observations.

3. Results and discussion

3.1. Single-date regression models

Table 2 shows regression results for each of the JERS SAR scenes against forest stem volume. Column Vol-Rg shows the range of stem volume of the stands that were included in the analyses. Column n shows the number of stands. The variation by one stand is due to a slightly varying coverage of the scenes. Columns A and B show the coefficients of a linear regression model (Eq. (2)) between JERS SAR amplitude and stem volume. Column r in Table 2 shows the correlation coefficient between SAR amplitude and stem volume. Coefficient of determination is R^2. The scene identifiers in Table 2 are of the form:

CYYMMM

where C=designation of the seasonal configuration: dry for the winter/dry scenes, wet for the winter/wet scene, and S for the summer scenes, YYMMM=acquisition year (YY) and month (MMM). The full acquisition date is shown in Table 1.

Table 2
Regression results between forest stem volume and single-date JERS SAR data

Scene	Vol-Rg	n	A	B	r	R^2
S95Jul	0–360	205	0.60	−562	0.81	0.66
S95Sep	0–360	205	0.72	−743	0.70	0.49
S95Oct	0–360	206	0.87	−894	0.63	0.40
Dry93Feb	0–360	206	3.22	−3239	0.40	0.16
Wet95Jan	0–360	206	0.71	−560	0.78	0.61
Dry98Mar	0–360	206	−30.33	26896	−0.05	0.00
Summer	0–360	616	0.71	−713	0.71	0.50
Summer	10–360	529	0.65	−634	0.73	0.53

The lines titled Summer at the end of Table 2 combine all observations of scenes S95Jul, S95Sep, and S95Oct into a single dataset. The 616 observations in the summer dataset are not completely independent because the stands cover the same area on the ground, and therefore, three observations have the same value of dependent variable. The observations of the SAR backscatter are independent because the speckle and other noise sources are independent from scene to scene.

The regression model of the combined summer dataset can be written:

$$V = 0.65\ \mathrm{sqrt}\left(10^{\left(\left(\sigma^O + 68.2\right)/10\right)}\right) - 634 \quad (5)$$

where σ^O=backscattering coefficient in dB and V=stem volume in m^3/ha. The corresponding model for forest biomass (dry) is:

$$B = 0.39\ \mathrm{sqrt}\left(10^{\left(\left(\sigma^O + 68.2\right)/10\right)}\right) - 380 \quad (6)$$

where B=dry biomass in tons/ha.

Fig. 1 shows the stand average data and regression lines separately for winter and summer scenes. The correlation between stem volume and JERS SAR data is very weak in winter scenes acquired in cold, dry conditions (scenes Dry93Feb and Dry98Mar in Fig. 1). Correlation coefficients are low (0.4 and −0.05). There is a more pronounced relationship between the JERS SAR data and stem volume in summer scenes. Correlation coefficients range from 0.63 to 0.81. The form of the relationship (regression lines in Fig. 1 and A and B coefficients in Table 2) is similar from scene to scene. No significant difference can be seen between the scenes acquired in leaves-on conditions (S95Jul and S95Sep) and the scene acquired in leaves-off conditions (S95Oct). The slope of the regression line is slightly lower in the late-autumn scene and its correlation coefficient is slightly lower than that of the July–September scenes, though. All three estimator lines (S95Jul, S95Sep and S95Oct) are within 60 m^3/ha from each other over the whole range from 0 to 200 m^3/ha. This suggests that a linear model with constant coefficients can be used to produce an estimate of forest stem volume when using L-band SAR data acquired in reasonably dry summer conditions, especially if accuracy requirements are not high.

The scene Wet95Jan forms an exception in the set of winter scenes. Correlation coefficient (0.78) is as high as in

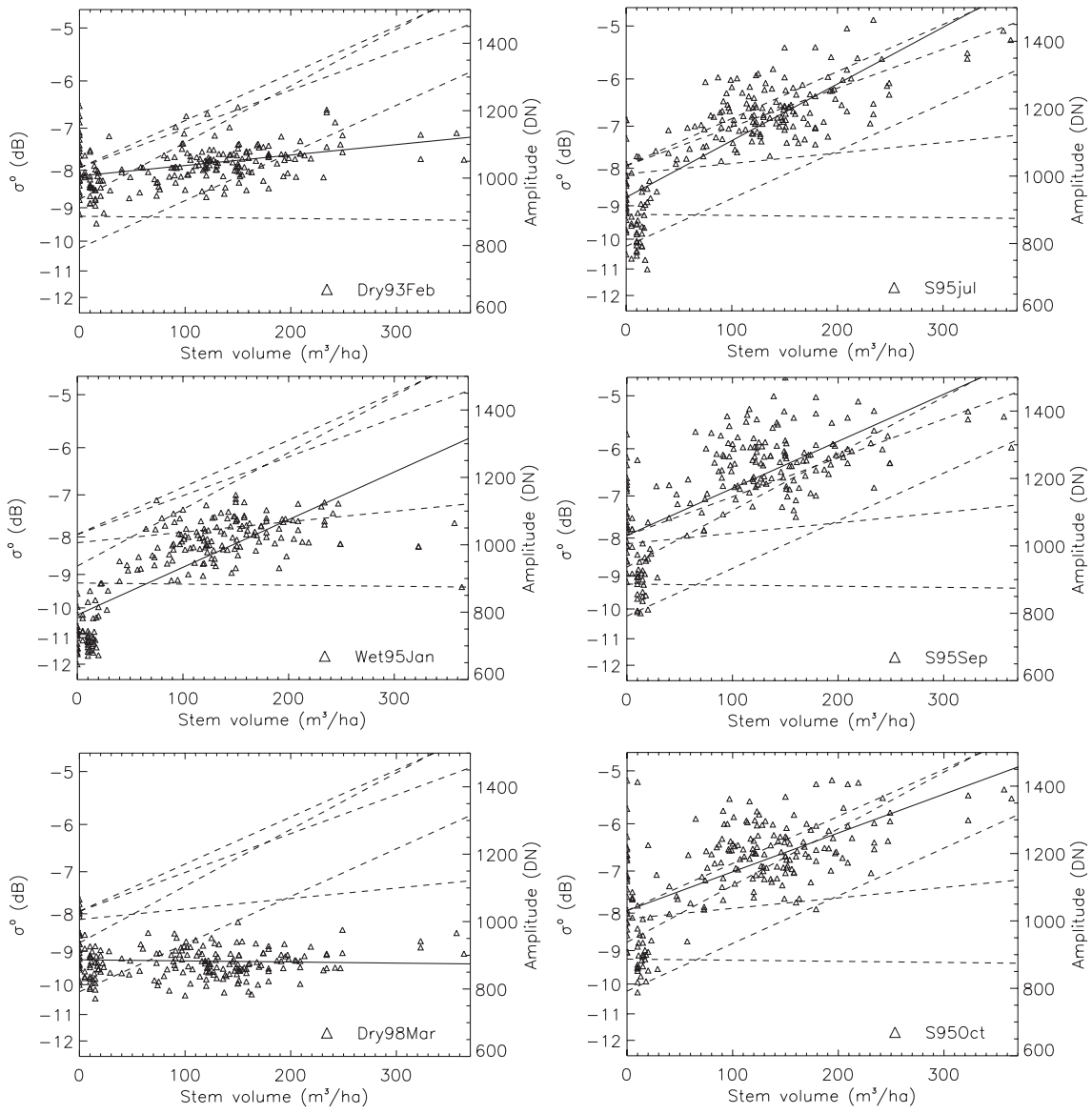

Fig. 1. Regression diagrams between forest stem volume and JERS SAR data for winter (left) and summer (right) scenes. The solid line shows the regression line computed from the observation data in the diagram. The dashed lines are the regression lines from the other 5 scenes.

a typical summer scene. The slope of the regression line is also very similar to the summer scenes, but the overall backscattering level is lower in this winter scene, which was acquired in conditions with a moist layer of new snow on top of older snow layers. In addition to high stem volume vs. backscatter correlation, the scene Wet95Jan discriminates well between clear-cut areas and forest.

Fig. 2 shows one mechanism that can explain the separability of clear-cut areas in scene Wet95Jan. In normal dry winter conditions, the backscatter from the snow pack (with various ice crust layers and other ice objects inside) and from the underlying soil surface (in clear-cut areas) is about as high as the backscatter from various components of forest canopy. If there is a layer of new snow (or snow with a high moisture content in general), the backscatter from the snow pack and underlying soil is absorbed in the clear-cut areas while the canopy backscatter in forested areas remains about the same as in dry winter conditions. This generates a difference between clear-cut areas and forest in the scene in wet winter conditions. The lower the stem volume, the closer a stand is to the clear-cut case, which creates a positive correlation between stem volume and backscatter.

3.2. Comparison of new regression models and existing models

Harrell et al. (1995) found a regression model between total biomass and JERS-1 SAR backscatter:

$$y = 2.555\log(x) - 9.644 \quad (7)$$

where x=total biomass (kg/m^2) and y=backscattering coefficient (dB). The model was derived in an Alaskan test

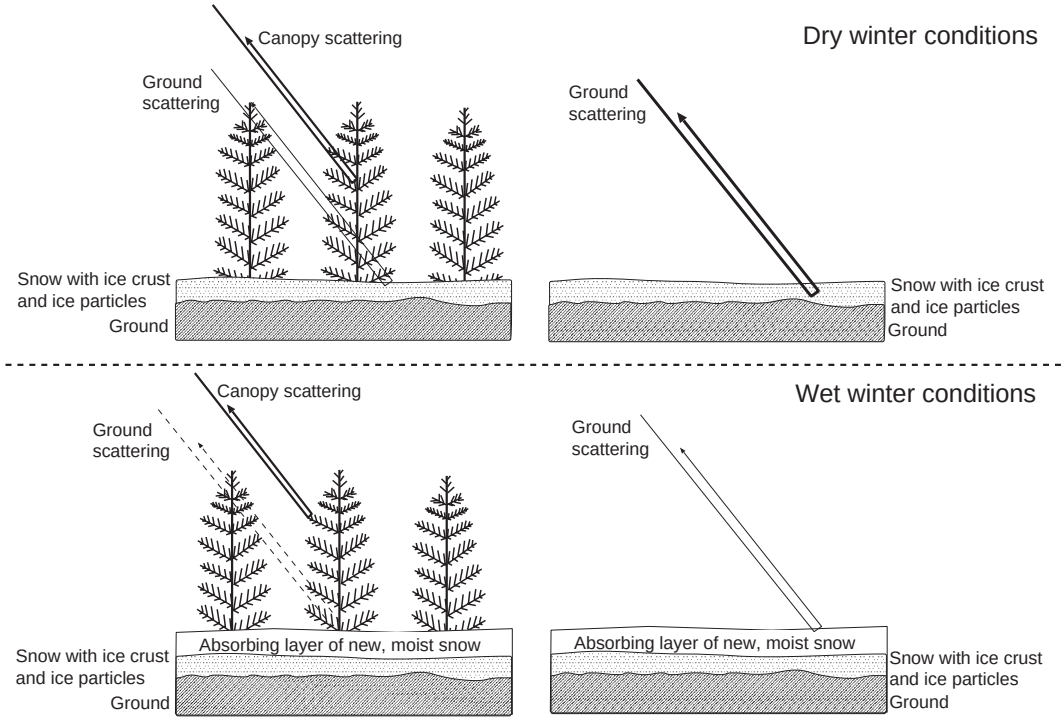

Fig. 2. Forest and clear-cut backscatter (schematically) in dry and wet winter conditions.

site (11 stands) with the total biomass ranging from 1 to 6 kg/m^2 (10 to 60 tons/ha). The JERS SAR data were acquired in July–August 1992.

Fransson and Israelsson (1999) found a regression model between stem volume and JERS-1 SAR backscatter:

$$V = 786 + 79\sigma^O \quad (8)$$

where σ^O=backscattering coefficient (dB) and V=stem volume (m^3/ha). The model was derived in a Swedish study site close to Umeå (37 stands) with the stem volume ranging from 0 to 300 m^3/ha. The JERS SAR data were acquired in June 1992.

Published regression models from literature can be directly compared to regression models derived using calibrated data. Fig. 3 shows the JERS SAR summer data from the Ruokolahti study site. The continuous line is the regression line corresponding to these points. Data for a Finnish Boreal forest study site by Pulliainen et al. (1999) has also been included in Fig. 3. These data were averaged over a JERS image (23 May 1993) for 6 stem volume classes based on a forest map by the Finnish Forest Research Institute. The curvilinear dotted line that ends at 100 m^3/ha is from Harrell et al. (1995). The biomass values have been converted to stem volume by the formula (Häme et al., 1992):

$$V = B/0.6 \quad (9)$$

where V=stem volume (m^3/ha) and B=dry biomass (tons/ha). The JERS SAR data of Harrell et al. (1995) were acquired in July–August 1992. The test site of Harrell et al. (1995) was in Interior Alaska with a fairly low biomass level. The almost linear dashed line in Fig. 3 is from Fransson and Israelsson (1999). This model is based on JERS SAR data acquired on 17 June 1992. The slight curvature of the Fransson–Israelsson model is due to the fact that this model was determined as a linear regression between the logarithm of the backscattering coefficient (σ^O in dB) and stem volume. The Ruokolahti model was determined as a linear regression between the square root of the backscattering coefficient (amplitude) and the stem volume.

The Harrel et al. model in Fig. 3 fits the data from the Ruokolahti site fairly well. The form of the model seems

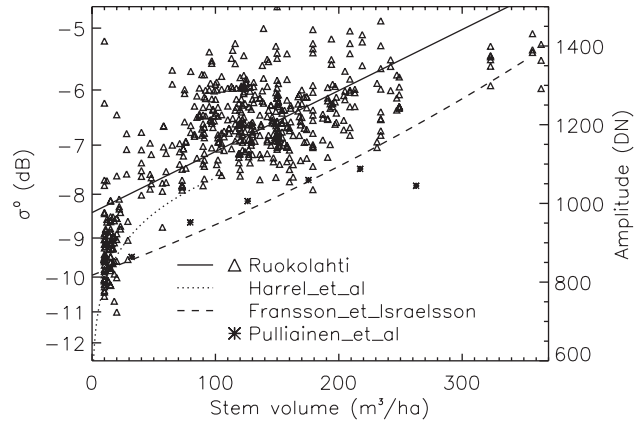

Fig. 3. Summer-time JERS data with the models of Harrell et al. (1995) and Fransson and Israelsson (1999). The observation data of Pulliainen et al. (1999) is also shown. The solid line is the regression model corresponding to line "Summer, 10–360" in Table 2.

appropriate in the narrow stem volume range. Young stands (stem volume less than 30 m^3/ha) are not very well in line with this model. This may be due to soil effects (outcrops and stones in Ruokolahti site).

Fransson and Israelsson (1999) model (dashed line in Fig. 3) and the data by Pulliainen et al. (1999) are about 1.3 dB lower than the Ruokolahti data. The difference is within the limits of calibration accuracy. Shimada (1996) reports a standard deviation of 1.86 dB for the JERS SAR calibration factor. In addition, the Umeå study site used by Fransson and Israelsson (1999) is situated on the West coast of Gulf of Botnia. In this type of area, a descending-orbit JERS SAR scene can include sea area in the near-range part of the scene. Shimada (2001) points out that the NASDA-supplied calibration factor is not valid in this situation because the AGC (Automatic Gain Control), which measures the average backscatter level from the near-range 18 km zone, causes the raw data to saturate. This in turn leads to a reduced backscatter level in the processed scene. The JERS SAR data of 21 May 1994 in Fransson and Israelsson (1999) fit well the Ruokolahti data. The numerical values for the 21 May 1994 regression line were not included in Fransson and Israelsson (1999).

The reason why the backscatter data of Pulliainen et al. (1999) are lower than in the current study may be a higher soil moisture in spring (May) after snow melt. The attempt to obtain JERS data of late spring or early summer failed in the current study.

The regression models derived in this study are valid for stands where the species composition is similar to that in the study site, typically pine or spruce dominated mixed forest. If these models are applied to sites where trees of very different canopy structure (e.g., multi-stem deciduous trees like rowan) are common, the models perform worse. Coniferous and conifer-dominated mixed forests dominate in the boreal forest zone.

3.3. Multi-date regression models

Table 3 shows the results of two sets of multivariate regression analyses. Column R^2 gives the coefficient of determination. Column r gives the correlation coefficient between the estimated stem volume and the ground data (for comparison with the data of Table 2). Column. R_A^2 gives the adjusted R^2, which takes into account the variation in the number of observations (Eq. (3)). The significance columns give the result of the t test that tests the significance of the independent variable in the regression function.

In the first set of cases, the correlation coefficient decreases with decreasing range of stem volume. The number of significant independent variables also decreases with decreasing range of stem volume (and decreasing number of observations). The last case with only 19 observations renders the whole regression insignificant at 5% significance level. Of the scenes acquired during growing season (S95Jul, S95Sep, and S95Oct), which are highly correlated among themselves, only one (S95Jul) has a significant contribution to the multivariate regression. The dry winter scene Dry93Feb, which alone does not correlate well with stem volume, is so uncorrelated with summer scenes that it adds a significant contribution to the multivariate regression in 3 cases out of 5.

In the second set of cases, the correlation coefficient first increases with decreasing range of stem volume. After reaching the saturation zone (somewhere around 50...150 m^3/ha), the correlation coefficient does no longer increase with decreasing range of stem volume (and decreasing number of observations). The number of significant independent variables again decreases with decreasing stem volume range (and decreasing number of observations). Again, the only summer acquisition with a significant contribution is the July scene (S95Jul). Even this scene becomes insignificant at 0–100 m^3/ha (with 95 observations). This is due to the high correlation between the summer scenes and the wet winter scene (Wet95Jan).

An attempt was made to derive an optimal 2-piece linear regression model for stem volume estimation (a) using all three summer scenes in an average summer scene, and (b) using the scenes as independent variables (see Table 4). Use of an average summer scene seems not to improve over the original bands. Computation of two models in image form showed that the 2-piece linear regression model with

Table 3
Multivariate regression results as a function of stem volume range

Vol-Rg	n	R^2	r	R_A^2	Dry93Feb	Wet95Jan	S95Jul	S95Sep	S95Oct	Dry98Mar
0–360	206	0.71	0.85	0.70	S	S	S	–	–	S
50–360	139	0.37	0.61	0.34	S	–	S	–	–	–
100–360	112	0.35	0.59	0.31	S	–	S	–	–	–
150–360	59	0.43	0.65	0.37	–	S	S	–	–	–
200–360	19	0.53	0.73	0.33	–	–	–	–	–	–
0–300	202	0.77	0.87	0.76	S	S	S	–	–	S
0–250	202	0.77	0.87	0.76	S	S	S	–	–	S
0–200	187	0.79	0.89	0.78	–	S	S	–	–	S
0–150	152	0.83	0.91	0.82	–	S	S	–	–	S
0–100	95	0.83	0.91	0.82	–	S	–	–	–	S
0–50	67	0.64	0.80	0.61	–	S	–	–	–	S

S=significant at 5% risk, –=not significant.

Table 4
Multivariate regression results with summer scenes averaged

Vol-Rg	n	R^2	r	Dry93Feb	Wet95Jan	S95Jul	Dry98Mar	Summer
0–360	206	0.70	0.82	–	S	0	S	S
0–100	95	0.83	0.91	–	S	0	S	–
0–150	152	0.82	0.91	–	S	0	S	S
100–360	112	0.24	0.49	–	–	0	–	S
150–360	59	0.38	0.62	–	S	0	–	S
0–150	152	0.82	0.91	0	S	0	S	S
0–150	152	0.83	0.91	0	S	S	S	0
150–360	59	0.36	0.60	0	S	0	0	S
150–360	59	0.40	0.63	0	S	S	0	0

S=significant at 5% risk level, –=not significant, 0=not included in the analysis.

original bands only (the last and third-last lines of Table 4) did not produce reliable stem volume estimates for the test site. In Table 4, column r gives the correlation coefficient between the estimated stem volume and ground data.

A 2-piece linear estimator was designed based on the regression experiments above. Since summer scenes are highly correlated, an average was computed over the 3 summer scenes (S95Jul, S95Sep, and S95Oct). The combined estimator used one winter-time wet-condition scene (scene Wet95Jan), one winter-time dry-condition scene (Dry98Mar), and the average summer scene. Two estimates were computed: e_L for lower volume range and e_H for upper volume range:

$$e_L = -118.8 + 0.243*W - 0.056*D \quad (10)$$

$$e_H = -174.9 + 0.183*W - 0.239*D + 0.273*S \quad (11)$$

where W=amplitude in the winter-wet scene, D=amplitude in the winter-dry scene, and S=amplitude in the summer average scene.

The decision which estimate to use was based on the SAR-derived estimates, not on ground data. This is essential for an estimator that must be applicable also outside study areas with ground data. If $e_H > 100$ m^3/ha, e_H was assigned as the combined estimate, e_L otherwise. The division point was determined by visual analysis of regression data. Within a zone of ±20 m^3/ha around the dividing line of 100 m^3/ha, the combined estimate was computed as a weighted average of e_L and e_H:

$$\begin{aligned} &\text{if } e_H > 120: && e = e_H \\ &\text{if } e_H < 80: && e = e_L \\ &\text{if } e_H \geq 80 \text{ and } e_H \leq 120: && e = ((120 - e_H)/40)e_L + ((e_L - 80)/40)e_H \end{aligned} \quad (12)$$

The application of the 2-piece linear regression model for mapping large forest areas is difficult because acquiring the needed winter-wet scene (and winter dry scene) depends on weather.

Fig. 4 shows the combined estimate against ground data in the stand-wise dataset. The RMSE was 28.5 m^3/ha. As most input SAR data are from the year 1995, the reference year of the estimate is 1995.

The combined estimate of stem volume was computed over the whole area where rectified JERS SAR data existed. To reduce the effects of speckle, JERS SAR scenes were filtered by the 5-out-of-9 filtering technique described earlier. The standard deviation of the Gaussian weight function was set to half a pixel (with 25-m pixel spacing).

Fig. 5 shows the combined estimate for a sub-window (4 km by 4 km) of the study site. The water mask was made with Landsat TM (near-infrared) data. An extract from an Ikonos multispectral (true colour) image is also shown for comparison. Recent clear-cut areas are fairly well presented in the stem volume estimate. Locations of high-estimate areas also correspond well with the locations of mature forests.

Fig. 6 shows the combined stem volume estimate over an area of 38 km by 38 km. The water mask was made with Landsat-TM data. The black triangle at the South-western corner is due to lack of coverage in one of the five JERS SAR scenes used.

The accuracy of the JERS-SAR-based stem volume estimate was tested using the point-wise dataset of stem volume measurements. The root-mean-square error between the JERS estimate and the ground measurement was 59.8 m^3/ha. The average stem volume in the ground dataset was

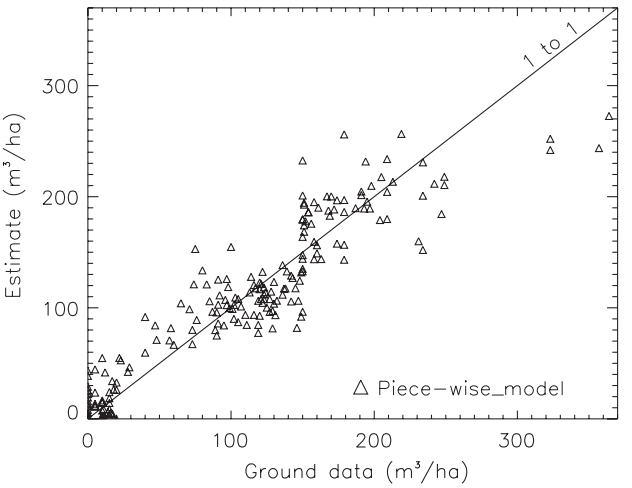

Fig. 4. Regression result: combined stem volume estimate vs. ground-measured stem volume.

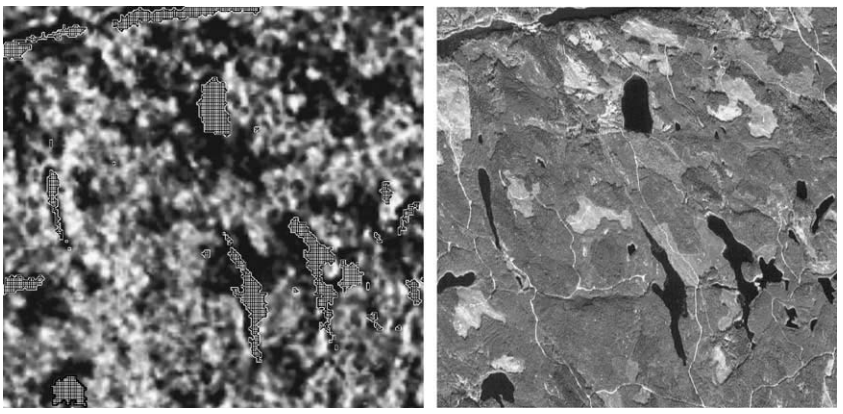

Fig. 5. Stem volume estimate using 5-date JERS SAR data (left) and Ikonos 4-m multispectral image. The scaling of stem volume shows the range 0...200 m^3/ha as black to white. Ikonos image: "Includes material (c) Space Imaging L.P."

104 m^3/ha and the maximum 355 m^3/ha. The average stem volume in the JERS-SAR-based stem volume estimate was 89 m^3/ha and the maximum 218 m^3/ha. The correlation coefficient between the estimated and measured stem volume was 0.57. The correlation in this point-wise dataset is lower than in the stand-wise dataset used as training data. This is partly due to speckle and other noise sources in the SAR data. Averaging SAR data over forest stands reduces speckle and enhances the relationship between forest biomass and SAR backscatter. Stand-wise averaging is a standard technique in studies of forest biomass and SAR. Another reason for the somewhat low accuracy is the difference in spatial scale between the datasets. The diameter of a ground measurement plot is of the order of 25 m. The JERS-based estimate was computed from a dataset where SAR pixels were averaged in a 75-m by 75-m window.

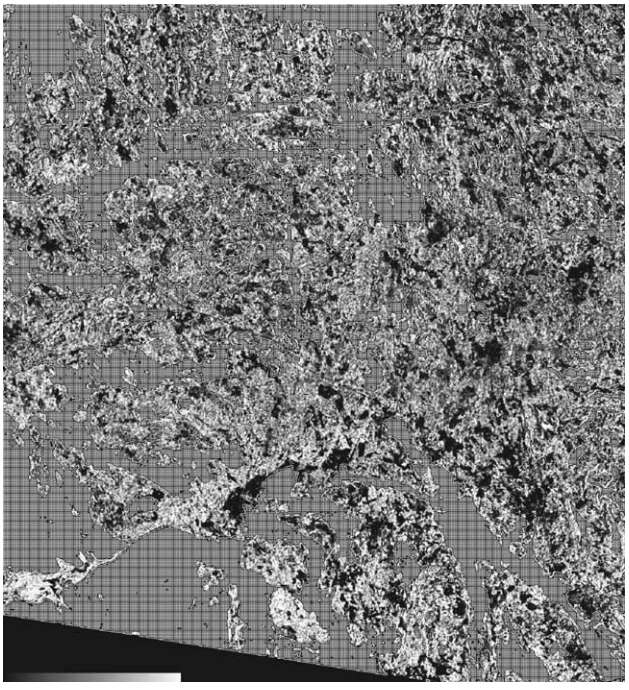

Fig. 6. JERS-based stem volume estimate over a 38-km-by-38-km area in Ruokolahti.

3.4. JERS-TM synergy

Regression analysis and stand-wise averaged JERS SAR and Landsat TM data were used to study the synergy between L-band SAR and optical data in forest biomass estimation. Landsat TM bands 2 (green visible light), 3 (red visible light), 4 (near-infrared), 5 (middle-infrared), and 7 (middle-infrared) were included in the analyses. Atmospheric corrections were applied to Landsat TM data and the pixel values were proportional to surface reflectance. Band 1 (blue visible light) of TM data was left out due to noise and band 6 (thermal band) due to lack of consistency from scene to scene in forest biomass estimation. NDVI (TM4 − TM3)/(TM4 + TM3) was also tested. Because NDVI had a low coefficient of determination (32%), it was left out in further analysis. Table 5 shows the correlation coefficient and coefficient of determination for a number of combinations of JERS acquisition dates and TM spectral bands. Column r in Table 5 gives the correlation coefficient between the estimated stem volume and ground data. The multi-temporal regression results shown on the first row of Table 3 is also shown here for convenience. The JERS regression was made in one unit over the whole range of stem volumes, not using the 2-piece approach defined by Eqs. (10)–(12). Multiple correlation coefficients of the order of 0.85 were obtained both for JERS data and TM data when these datasets were analysed

Table 5
Regression analysis of combined JERS SAR and Landsat TM data

Bands	r	R^2	n
JERS, 6 dates	0.85	0.71	206
TM, 5 bands	0.85	0.73	206
TM, bands 3 and 4	0.85	0.72	206
JERS + TM, all bands	0.89	0.79	206
JERS + TM, significant bands	0.88	0.77	206

separately. The corresponding coefficient of determination (R^2) was about 0.7, i.e., 70%. When combining optical (TM) and microwave (JERS) sensors, the correlation coefficient rose to almost 0.9 and the coefficient of determination to over 0.75 (75%). When restricting to only those bands in the JERS+TM combination that were significant at 5% significant level (TM band 3 and JERS scenes Dry93Feb and S95Jul), the correlation coefficient did not drop much.

Fig. 7 shows some of the regression results in graphical form. Triangles (top left) are Landsat TM estimates, squares (top right) JERS estimates, and diamonds (bottom left) JERS-TM estimates. One of the problems in Earth-observation-based forest biomass estimation is the saturation of the estimate at a fairly low level of biomass both for optical data and for L-band microwave data. Combination of sensors seems to alleviate this problem somewhat because the highest JERS-TM estimates are higher than either of the single-sensor estimate (the upper most dashed regression line at higher stem volumes in the bottom right figure belongs to the JERS-TM estimate). Similarly the lowest biomass estimates are slightly better in the JERS-TM estimate than in the single-sensors estimates. The slope of the regression line (slightly higher for the JERS-TM data) also reflects this phenomenon.

4. Conclusions

The single-date regression analysis showed that the stem volume vs. L-band backscatter relationship is very stable over the summer period. The regression models obtained in Ruokolahti site fit well with the model (for low biomass values) of Harrell et al. (1995). The fit between the Ruokolahti model and the model by Fransson and Israelsson (1999) was not as good, but the difference is within the limits of calibration accuracy of the JERS SAR sensor. The stability of the regression models from scene to scene suggests that a constant regression model could be used in mapping boreal forest biomass using a single summer acquisition. This could be applied, e.g., to wide area mosaics produced in the GBFM project (Rosenqvist et al., 2000) if accuracy requirements are low and if biomass is aggregated to larger units before the data are used in quantitative models. Eqs. (5) and (6) above could be used for stem volume and biomass when the available Earth observation data are from an L-band SAR (HH-polarized, nominal incidence angle 39°) and the scenes have been acquired in summer conditions. This type of wide area biomass estimation would ideally require well-calibrated L-band SAR data. For instance, an increase of 1.86 dB due to calibration error increases the stem volume estimate from

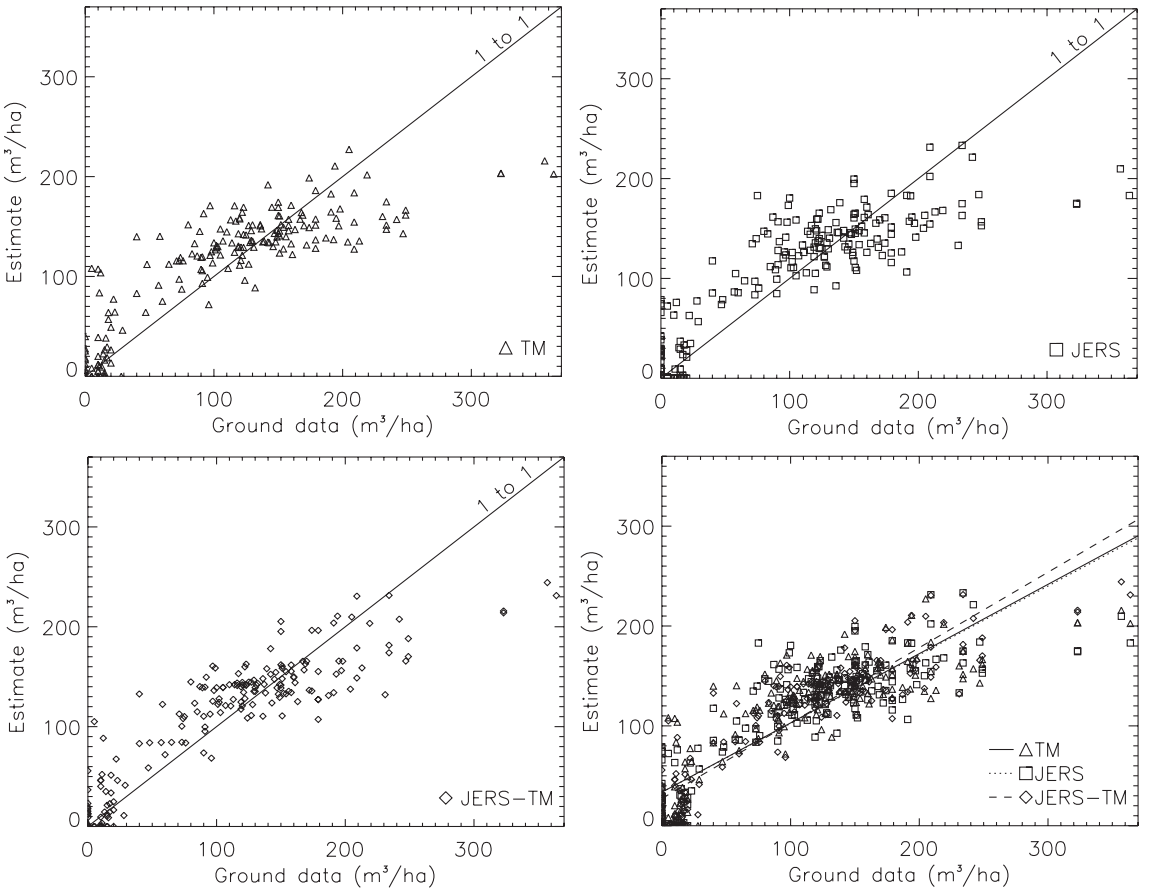

Fig. 7. Estimated vs. ground-observed stem volume for Landsat TM data (top left), JERS data (top right), both datasets combined (bottom left). The last sub-figure (bottom right) shows all three estimates with their linear regression lines in the same diagram.

100 m^3/ha to 275 m^3/ha. A calibration accuracy of 0.7 dB produces an increase from 100 m^3/ha to 162 m^3/ha, which is better in balance with the estimation accuracy (60 m^3/ha).

The high correlation ($r=0.85$) obtained in regression modelling between multi-temporal JERS SAR data and forest stem volume data suggests that multi-temporal L-band SAR data can be used for forest biomass mapping for large stands and forest management units larger than stands. Data from varying winter conditions, in addition to summer data, were used to obtain the correlation coefficient of 0.85. In winter data, the relationship between L-band backscatter and forest biomass varies widely from scene to scene. The regression model is applicable in scenes acquired in the same meteorological conditions as those used to derive the regression model. In practice, this technique requires reference data within each mapped scene. This technique can be efficient for areas that consist of one or a few scenes (along an orbit). For larger areas, e.g., for continental mapping, multi-temporal image acquisitions in uniform meteorological conditions are practically impossible. Even in a local context, the mapping of high-biomass areas (e.g., dry biomass greater than 100 tons/ha) is not accurate.

The use of optical Landsat TM data, in addition to JERS SAR data, improved the biomass estimation accuracy slightly (r increased from 0.85 to 0.89). The inclusion of optical data also improved the saturation of the regression model. Since the only significant optical bands in the SAR-optical regression model were the red and near-infrared bands, data from practically all optical satellites can be used.

A detailed (25-m pixel spacing, 2-m vertical accuracy) DEM was used when analysing the JERS SAR data of the Ruokolahti study site. For wide-area biomass mapping, the acquisition of a DEM of the same standard is costly if such a DEM is available at all. Global DEM data are too coarse for radiometric normalization of topographic effects in JERS SAR data. An accurate and detailed DEM is essential for pixel-wise biomass estimation because even a 5° slope (towards the sensor) causes a change of 63 m^3/ha in the stem volume estimate. If biomass mapping is made for larger areal units, the topographic effects can be expected to cancel out from the averaged biomass estimate if the estimation unit includes equal areas of fore-slopes and back-slopes.

Acknowledgements

The work described in this paper was funded by TEKES in the context of “MODIS biomass” project. JERS SAR data were supplied by NASDA (currently JAXA) in the context of the GBFM North Europe science node. Stora Enso Ltd. supplied the stand-wise forest inventory data. Finnish Forest Research Institute supplied the point-wise ground data. Dr. Ranga B. Myneni (the principal investigator of NASA project NAS 13-98048) is acknowledged for supplying the Ikonos scene of a part of the study site. The author also wants to thank Mrs. Eija Parmes of VTT for re-formatting and processing the forest inventory data, Mrs. Brita Veikkanen of VTT for geo-coding Landsat TM data, and Dr. Hans Jonsson of Metria Miljoanalys for his assistance in ordering JERS SAR data. Dr. Tuomas Häme of VTT provided valuable comments to improve the clarity of the manuscript.

References

Beaudoin, A., Le Toan, T., Goze, S., Hsu, C., Han, H., Kong, J., et al. (1992). Retrieval of forest biomass from SAR data. *Proceedings of the Final Workshop of the MAESTRO/AGRISCATT Campaigns, Noordwijk, 6–7 March 1992* (pp. 123–130).

Chipman, J., Lillesand, T., Gage, J., & Radcliffe, S. (2000). Spaceborne imaging radar in support of forest resource management. *Photogrammetric Engineering and Remote Sensing*, *66*(11), 1357–1366.

De Grandi, G., Mayaux, P., Rauste, Y., Rosenqvist, Å., Simard, M., & Saatchi, S. (2000). The global rain forest mapping project JERS-1 radar mosaic of tropical Africa: Development and product characterisation aspects. *IEEE Transactions on Geoscience and Remote Sensing*, *38*(5), 2218–2233.

Dobson, C., Mc Donald, K., Ulaby, F., & Sharik, T. (1991). Relating the temporal change observed by AIRSAR to surface and canopy properties of mixed conifer and hardwood forests of Northern Michigan. *Proceedings of the Third Airborne Synthetic Aperture Radar (AIRSAR) Workshop, May 23–24, 1991. JPL Publication*, *vol. 91–30* (pp. 34–43).

Dobson, C., Ulaby, F., Pierce, L., Sharik, T., Bergen, K., Kellndorfer, J., et al. (1995). Estimation of forest biophysical characteristics in Northern Michigan with SIR-C/X-SAR. *IEEE Transactions on Geoscience and Remote Sensing*, *33*(4), 877–894.

Dobson, C. K., Ulaby, F., Le Toan, T., Beaudoin, A., Kasischke, E., & Christensen, N. (1992). Dependence of radar backscatter on coniferous forest biomass. *IEEE Transactions on Geoscience and Remote Sensing*, *30*(2), 412–415.

Fransson, J., & Israelsson, H. (1999). Estimation of stem volume in boreal forests using ERS-1 C- and JERS-1 L-band SAR data. *International Journal of Remote Sensing*, *20*(1), 123–137.

Fransson, J., Smith, G., Askne, J., & Olsson, H. (2001). Stem volume estimation in boreal forests using ERS-1/2 coherence and Spot XS optical data. *International Journal of Remote Sensing*, *22*(14), 2777–2791.

Green, R. (1998). Relationship between polarimetric SAR backscatter and forest canopy and sub-canopy biophysical properties. *International Journal of Remote Sensing*, *19*(12), 2395–2412.

Häme, T., Salli, A., & Lahti, K. (1992). Estimation of carbon storage in boreal forest using remote sensing data, Pilot study. In M. Kanninen, & P. Anttila (Eds.), The Finnish programme on climate change, Progress report. *Publications of the Academy of Finland*, *vol. 3/92* (pp. 250–255). Helsinki, Finland: VAPK Publishing.

Harrell, P., Bourgeau-Chavez, L., Kasischke, E., French, N., & Christensen, N. (1995). Sensitivity of ERS-1 and JERS-1 radar data to biomass and stand structure in Alaskan boreal forest. *Remote Sensing of Environment*, *54*, 247–260.

Harrell, P., Kasischke, E., Bourgeau-Chavez, L., Haney, E., & Christensen, N. (1997). Evaluation of approaches to estimating aboveground biomass in Southern pine forests using SIR-C data. *Remote Sensing of Environment*, *59*, 223–233.

Imhoff, M. (1993). Radar backscatter/biomass saturation: Observations and implications for global biomass assessment. *Proceedings of IGARSS'93, 18–21 August 1993, Tokyo, Japan*, *vol. I* (pp. 43–45).

Imhoff, M. (1995). Radar backscatter and biomass saturation: Ramifications for global biomass inventory. *IEEE Transactions on Geoscience and Remote Sensing*, *33*(2), 511–518.

Israelsson, H., Askne, J., Fransson, J., & Sylvander, R. (1995). *JERS-1 SAR analysis of boreal forest biomass, Final report of JERS-1/ERS-1 system verification program, MITI and NASDA, March 1995, vol. II, p. 2–38...2–45.*

Israelsson, H., Askne, J., & Sylvander, R. (1992). Estimation of forest characteristics using multi frequency polarimetric SAR data. *Proceedings of the Final Workshop of the MAESTRO/AGRISCATT Campaigns, Noordwijk, 6–7 March 1992* (pp. 47–51).

Israelsson, H., Ulander, L., Askne, J., Fransson, J., Frölind, P., Gustavsson, A., et al. (1997). Retrieval of forest stem volume using VHF SAR. *IEEE Transactions on Geoscience and Remote Sensing*, *35*(1), 36–40.

Jonsson, H. (2002). GBFM/Northern Europe science node initiation. *Proceedings of the 1st Science Meeting—GBFM/NE, Stockholm, Sweden, 7–8 February 2002*. Metria Miljöanalys. 16 p.

Kasischke, E., Bourgeau-Chavez, L., Christensen, N., & Dobson, C. (1991). The relationship between aboveground biomass and radar backscatter as observed on airborne SAR imagery. *Proceedings of the Third Airborne Synthetic Aperture Radar (AIRSAR) Workshop, May 23–24, 1991. JPL Publication*, *vol. 91–30* (pp. 11–21).

Kasischke, E., Bourgeau-Chavez, L., Christensen, N., & Haney, E. (1994). Observations on the sensitivity of ERS-1 SAR image intensity to changes in aboveground biomass in young loblolly pine forests. *International Journal of Remote Sensing*, *15*(1), 3–16.

Kasischke, E., Christensen, N., & Bourgeau-Chavez, L. (1995). Correlating radar backscatter with components of biomass in Loblolly pine forests. *IEEE Transactions on Geoscience and Remote Sensing*, *33*(3), 643–659.

Kellndorfer, J., Dobson, C., & Pierce, L. (2001). Forest biometrics from ERS and JERS in Michigan. *Proceedings of IGARSS'2001* (pp. 780–782).

Kuplich, T., Salvatori, V., & Curran, P. (2000). JERS-1/SAR backscatter and its relationship with biomass of regenerating forests. *International Journal of Remote Sensing*, *21*(12), 2513–2518.

Kurvonen, L., Pulliainen, J., & Hallikainen, M. (1999). Retrieval of biomass in boreal forest from multitemporal ERS-1 and JERS-1 SAR images. *IEEE Transactions on Geoscience and Remote Sensing*, *37*(1), 198–205.

Le Toan, T., Beaudoin, A., & Guyon, D. (1992). Relating forest biomass to SAR data. *IEEE Transactions on Geoscience and Remote Sensing*, *30*(2), 403–411.

Le Toan, T., Beaudoin, A., Riom, J., & Guyon, D. (1991). Relating forest biomass to SAR data. *Proceedings of the International Geoscience and Remote Sensing Symposium IGARSS'91, Helsinki University of Technology, Espoo, Finland, June 3–6, 1991*, *vol. II* (pp. 689–692).

Luckman, A., Baker, J., Honzak, M., & Lucas, R. (1998). Tropical forest biomass density estimation using JERS-1 SAR: Seasonal variation, confidence limits, and application to image mosaics. *Remote Sensing of Environment*, *63*, 126–139.

Luckman, A., Baker, J., Kuplich, T., Yanasse, C., & Frery, A. (1997). A study of the relationship between radar backscatter and regenerating tropical forest biomass for spaceborne SAR instruments. *Remote Sensing of Environment*, *60*, 1–13.

Luckman, A., Baker, J., & Wegmüller, U. (2000). Repeat-pass interferometric coherence measurements of disturbed tropical forest from JERS and ERS satellites. *Remote Sensing of Environment*, *73*, 350–360.

Melon, P., Martinez, J., Le Toan, T., Ulander, L., & Beaudoin, A. (2001). On the retrieving of forest stem volume from VHF SAR data: Observation and modeling. *IEEE Transactions on Geoscience and Remote Sensing*, *39*(11), 2364–2372.

Moghaddam, M., Durden, S., & Zebker, H. (1994). Radar measurement of forested areas during OTTER. *Remote Sensing of Environment*, *47*, 154–166.

Paloscia, S., Macelloni, G., Pampaloni, P., & Sigismondi, S. (1999). The potential of C-band and L-band SAR in estimating vegetation biomass: The ERS-1 and JERS-1 experiments. *IEEE Transactions on Geoscience and Remote Sensing*, *37*(4), 2107–2110.

Pulliainen, J., Engdahl, M., & Hallikainen, M. (2003). Feasibility of multi-temporal interferometric SAR data for stand-level estimation of boreal forest stem volume. *Remote Sensing of Environment*, *85*, 397–409.

Pulliainen, J., Heiska, K., Hyyppä, J., & Hallikainen, M. (1994). Backscattering properties of boreal forests at the C- and X-bands. *IEEE Transactions on Geoscience and Remote Sensing*, *34*(5), 1041–1050.

Pulliainen, J., Kurvonen, L., & Hallikainen, M. (1997). Effect of temporally varying parameters on L- and C-band SAR observations of boreal forests. *Proceedings of IGARSS'97, 3–8 August 1997, Singapore*, *vol. IV* (pp. 1874–1877).

Pulliainen, J., Kurvonen, L., & Hallikainen, M. (1999). Multitemporal behaviour of L- and C-band SAR observations of boreal forests. *IEEE Transactions on Geoscience and Remote Sensing*, *37*(2), 927–937.

Pulliainen, J., Mikkelä, P., Hallikainen, M., & Ikonen, J. (1996). Seasonal dynamics of C-band backscatter of boreal forests with applications to biomass soil moisture estimation. *IEEE Transactions on Geoscience and Remote Sensing*, *34*(3), 758–770.

Ranson, K., & Sun, Q. (1997). An evaluation of AIRSAR and SIR-C/X-SAR images for mapping northern forest attributes in Maine, USA. *Remote Sensing of Environment*, *59*, 203–222.

Rauste, Y. (1993). Multitemporal analysis of forest biomass using AIRSAR data. *Proceedings of the 25th International Symposium on Remote Sensing and Global Environmental Change, Graz, Austria, 4–8 April 1993*, *vol. I* (pp. 328–338).

Rauste, Y., Häme, T., Pulliainen, J., Heiska, K., & Hallikainen, M. (1994). Radar-based forest bio-mass estimation. *International Journal of Remote Sensing*, *15*, 2797–2808.

Rauste, Y., Heiska, K., & Pulliainen, J. (1992). On forest inventory and elevation determination using polarimetric radar data. *Proceedings of the Final Workshop of the MAESTRO/AGRISCATT Campaigns, Noordwijk, 6–7 March 1992* (pp. 117–121).

Rignot, E., Zimmermann, R., & van Zyl, J. (1995). Spaceborne applications of P band imaging radars for measuring forest biomass. *IEEE Transactions on Geoscience and Remote Sensing*, *33*(5), 1162–1169.

Rosenqvist, Å. (1996). Evaluation of JERS-1, ERS-1 and Almaz SAR backscatter for rubber and oil palm stands in West Malaysia. *International Journal of Remote Sensing*, *17*, 3219–3231.

Rosenqvist, Å., Shimada, M., Chapman, B., Freeman, A., De Grandi, G., Saatchi, S., et al. (2000). The global rain forest mapping project—a review. *International Journal of Remote Sensing*, *21*(6–7), 1375–1387.

Shimada, M. (1996). Radiometric and geometric calibration of JERS-1 SAR. *Advances in Space Research*, *17*(1), 79–88.

Shimada, M. (2001). *User's guide to NASDA's SAR products Ver.2*. Tokyo, Japan: NASDA 2001 (Aug. 9) 23 pp.

Shimada, M., & Isoguchi, O. (2002). JERS-1 SAR mosaics of Southeast Asia using calibrated path images. *International Journal of Remote Sensing*, *23*(7), 1507–1526.

Skriver, H., & Gudmandsen, P. (1992). Analysis of MAESTRO-1 polarimetric SAR data of forest areas at Les Landes. *Proceedings of the Final Workshop of the MAESTRO/AGRISCATT Campaigns, Noordwijk, 6–7 March 1992* (pp. 131–136).

Smith, G., Dammert, P., Santoro, M., Fransson, J., Wegmuller, U., & Askne, J. (1998). Biomass retrieval in boreal forest using ERS and JERS SAR. *Proceedings of the Retrieval of Bio- and Geo-Physical Paramaters from SAR Data for Land Applications Workshop*. Noordvijk, The Netherlands: ESA/ESTEC.

Toshio, S., Takuhiro, N., Takuro, Y., Keiji, O., Sotaro, T., & Toshiro, S. (1995). *Applicability of JERS-1 SAR data for monitoring of forest function and environment: Analysis of forest stand structure using JERS-1 SAR data for forest management, Final report of JERS-1/ERS-1 system verification program, MITI and NASDA, March 1995, vol. II, p. 2–38...2–45.*

Wang, Y., Kasischke, E., Melack, J., Davis, F., & Christensen, N. (1994). The effects of changes in loblolly pine biomass and soil moisture on ERS-1 SAR backscatter. *Remote Sensing of Environment*, *49*, 25–31.

Published by

Series title, number and report code of publication

VTT Publications 591
VTT–PUBS–591

Author(s)
Rauste, Yrjö

Title

Techniques for wide-area mapping of forest biomass using radar data

Abstract

Aspects of forest biomass mapping using SAR (Synthetic Aperture Radar) data were studied in study sites in northern Sweden, Germany, and south-eastern Finland. Terrain topography – via the area of a resolution cell- accounted for 61 percent of the total variation in a Seasat (L-band) SAR scene in a hilly and mountainous study site.

A methodology – based on least squares adjustment of tie point and ground control point observations in a multi-temporal SAR mosaic dataset – produced a tie point RMSE (Root Mean Square Error) of 56 m and a GCP RMSE of 240 m in the African mosaic of the GRFM (Global Rain Forest Mapping) project. The mosaic consisted of 3624 JERS SAR scenes. A calibration revision methodology – also based on least squares adjustment and points in overlap areas between scenes – removed a calibration artifact of about 1 dB.

A systematic search of the highest correlation between forest stem volume and backscattering amplitude was conducted over all combinations of transmit and receive polarisations in three AIRSAR scenes in a German study site. In the P-band, a high and narrow peak around HV-polarisation was found, where the correlation coefficient was 0.75, 0.59, and 0.71 in scenes acquired in August 1989, June 1991, and July 1991, respectively. In other polarisations of P-band, the correlation coefficient was lower. In L-band, the polarisation response was more flat and correlations lower, between 0.54 and 0.70 for stands with a stem volume 100 m^3/ha or less.

Three summer-time JERS SAR scenes produced very similar regression models between forest stem volume and backscattering amplitude in a study site in south-eastern Finland. A model was proposed for wide area biomass mapping when biomass accuracy requirements are not high. A multi-date regression model employing three summer scenes and three winter scenes produced a multiple correlation coefficient of 0.85 and a stem volume estimation RMSE of 41.3m^3/ha. JERS SAR scenes that were acquired in cold winter conditions produced very low correlations between stem volume and backscattering amplitude.

Keywords
wide-area mapping, remote sensing, Synthetic Aperture Radar, forest biomass, SAR, Polarimetry, mosaicking, forests, backscattering

Activity unit
VTT Information Technology, Vuorimiehentie 3, P.O. Box 1000, FI-02044 VTT, Finland

ISBN			Project number
951–38–6694–7 (soft back ed.) 951–38–6695–5 (URL:http://www.vtt.fi/inf/pdf/)			T5SU00716
Date December 2005	Language English	Pages 103 p. + app. 77 p.	Price D
Name of project		Commissioned by	
Series title and ISSN VTT Publications 1235–0621 (soft back ed.) 1455–0849 (URL: http://www.vtt.fi/inf/pdf/)		Sold by VTT Technical Research Centre of Finland P.O. Box 1000, FI-02044 VTT, Finland Phone internat. +358 20 722 4404 Fax +358 20 722 4374	

VTT PUBLICATIONS

574 Juslin, Kaj. A Companion Model Approach to Modelling and Simulation of Industrial Processes. 2005. 155 p. + app. 15 p.

575 Aura, Anna-Marja. *In vitro* digestion models for dietary phenolic compounds. 2005. 107 p. + app. 57 p.

576 Kyllönen, Hanna. Electrically or ultrasonically enhanced membrane filtration of wastewater. 2005. 79 p. + app. 54 p.

577 Monni, Suvi. Estimation of country contributions to the climate change. Viewpoints of radiative forcing and uncertainty of emissions. 2005. 99 p. + app. 76 p.

578 Hämäläinen, Anitta. Applying thermal hydraulics modeling in coupled processes of nuclear power plants. 2005. 103 p. + app. 99 p.

579 Korpipää, Panu. Blackboard-based software framework and tool for mobile device context awareness. 2005. 225 p.

580 Karppinen, Kaarina. Security Measurement based on Attack Trees in a Mobile Ad Hoc Network Environment. 2005. 57 p. + app. 8 p.

581 Urala, Nina. Functional foods in Finland. Consumers' views, attitudes and willingness to use. 2005. 79 p. + app. 109 p.

582 Human practice in the life cycle of complex systems. Challenges and methods. Edited by Maaria Nuutinen & Juha Luoma. 2005. 147 p.

583 Turunen, Erja. Diagnostic tools for HVOF process optimization. 2005. 66 p. + app. 92 p.

584 Measures for improving quality and shape stability of sawn softwood timber during drying and under service conditions. Best Practice Manual to improve straightness of sawn timber. Edited by Veikko Tarvainen. 2005. 149 p.

585 Hyötyläinen, Raimo. Practical interests in theoretical consideration. Constructive methods in the study of the implementation of information systems. 2005. 159 p.

586 Koivisto, Tapio. Developing strategic innovation capability of enterprises. Theoretical and methodological outlines of intervention. 2005. 120 p.

587 Ajanko, Sirke, Moilanen, Antero & Juvonen, Juhani. Kierrätyspolttoaineiden laadunvalvonta. 2005. 59 s.

588 Ebersberger, Bernd. The Impact of Public R&D Funding. 2005. 199 p. + app. 12 p.

589 Kutinlahti, Pirjo. Universities approaching market. Intertwining scientific and entrepreneurial goals. 2005. 187 p. + app. 4 p.

590 Jantunen, Erkki. Indirect multisignal monitoring and diagnosis of drill wear. 2005. 80 p. + app. 110 p.

591 Rauste, Yrjö. Techniques for wide-area mapping of forest biomass using radar data. 2005. 103 p. + app. 77 p.

Tätä julkaisua myy	Denna publikation säljs av	This publication is available from
VTT TIETOPALVELU PL 2000 02044 VTT Puh. 020 722 4404 Faksi 020 722 4374	VTT INFORMATIONSTJÄNST PB 2000 02044 VTT Tel. 020 722 4404 Fax 020 722 4374	VTT INFORMATION SERVICE P.O.Box 2000 FI–02044 VTT, Finland Phone internat. +358 20 722 4404 Fax +358 20 722 4374

ISBN 951-38-6694-7 (soft back ed.)
ISSN 1235-0621 (soft back ed.)

ISBN 951-38-6695-5 (URL: http://www.vtt.fi/inf/pdf/)
ISSN 1455-0849 (URL: http://www.vtt.fi/inf/pdf/)